EFFECTS OF PROTEIN KINASE C PHOSPHORYLATION OF CARDIAC TROPONIN I: AN EXPERIMENTAL AND MODEL-BASED STUDY

by

Jonathan Alder Kirk

B.S., Bioengineering, Washington State University, 2004

Submitted to the Graduate Faculty of

Swanson School of Engineering in partial fulfillment

of the requirements for the degree of

Doctor of Philosophy

University of Pittsburgh

2009

UNIVERSITY OF PITTSBURGH

SWANSON SCHOOL OF ENGINEERING

This dissertation was presented

by

Jonathan Alder Kirk

It was defended on

August 19th, 2009

and approved by

Harvey S. Borovetz, Ph.D.
Distinguished Professor and Chair, Department of Bioengineering;
Robert L. Hardesty Professor, Department of Surgery;
Professor, Department of Chemical & Petroleum Engineering, University of Pittsburgh

Kenneth B. Campbell, D.V.M., Ph.D.
Professor, Department of Veterinary & Comparative Anatomy, Pharmacology & Physiology,
Washington State University

Franklin Fuchs, Ph.D.
Faculty Emeritus, Department of Cell Biology and Physiology, University of Pittsburgh

Barry London, M.D., Ph.D.
Harry S. Tack Professor of Medicine, University of Pittsburgh; Chief of Cardiology, Director
of the Cardiovascular Institute, University of Pittsburgh Medical Center

Guy Salama, Ph.D.
Professor, Department of Cell Biology and Physiology, University of Pittsburgh

Dissertation Director: Sanjeev G. Shroff, Ph.D.
Professor and Gerald McGinnis Chair in Bioengineering; Department of Bioengineering,
University of Pittsburgh

EFFECTS OF PROTEIN KINASE C PHOSPHORYLATION OF CARDIAC TROPONIN I: AN EXPERIMENTAL AND MODEL-BASED STUDY

Jonathan Alder Kirk, Ph.D.

University of Pittsburgh, 2009

This project was aimed at further elucidating the role of protein kinase C (PKC)-induced phosphorylation of troponin-I (cTnI) in cardiac contraction. We created a new transgenic mouse model (TG-E), expressing a mutant cardiac TnI constitutively pseudo-phosphorylated at the three PKC phosphorylation sites (S43, S45, T144 mutated to glutamate). 2D-DIGE (Difference in Gel Electrophoresis) gels indicated 7.2 ± 0.5% replacement, with no change in baseline level of *actual* phosphorylation of cTnI or other myofilamental proteins. Experiments were conducted in perfused isolated mouse hearts, isolated papillary muscles, and skinned fiber preparations. The mechanical measurements were complemented by biochemical and molecular biological measurements, and a mathematical model-based analysis for integrative interpretation. Compared to wild-type mice, TG-E mice exhibited negative inotropy in *in vivo* echocardiographic studies (9% decrease in fractional shortening), isolated hearts (14% decrease in peak developed pressure), papillary muscles (53% decrease in maximum developed force), and skinned fibers (14% decrease in maximally activated force, F_{max}). Additionally, TG-E mice exhibited slowed relaxation in echocardiographic studies, isolated hearts, and intact papillary muscles. The TG-E mice showed no differences in calcium sensitivity, cooperativity, steady-state force-ATPase relationship, and calcium transient (amplitude and relaxation). The four-state model of cardiac contraction was used for a model-based analysis of the data. The model was verified as *a priori* globally identifiable using a differential algebraic approach; however, automated optimization procedures proved to be unreliable. Instead we performed *in silico*

experiments, altering sets of parameters in an attempt to recreate our experimental data. The model-based analysis revealed that experimental observations in TG-E mice could be reproduced by two simultaneous perturbations: a decrease in the rate constant of crossbridge formation and an increase in calcium-independent persistence of the myofilament active state. In summary, a modest increase in PKC-induced cTnI phosphorylation can significantly regulate cardiac muscle contraction: (1) negative inotropy via decreased crossbridge formation and (2) negative lusitropy via persistence of myofilament active state. Based on our data and data from the literature we speculate that the effects of PKC-mediated cTnI phosphorylation are site-specific (S43/S45 *vs*. T144).

TABLE OF CONTENTS

ACKNOWLEDGEMENTS XVI

1.0 BACKGROUND 1

1.1 CARDIAC MUSCLE PHYSIOLOGY 1

1.2 PROTEIN KINASE C CARDIAC SIGNALING 4

1.3 INTRACELLULAR CALCIUM 6

1.4 CARDIAC TNI PHOSPHORYLATION BY PKC 8

1.5 MATHEMATICAL MODEL BASED ANALYSES 13

1.6 CLINICAL RELEVANCE 15

2.0 SPECIFIC AIMS 16

3.0 ANIMAL USE 18

4.0 EXPRESSION OF MUTANT CTNI DNA AND PROTEIN 19

4.1 INTRODUCTION 19

4.2 GENERATION OF TRANSGENIC MICE 20

4.3 METHODS 21

4.3.1 Polymerase Chain Reaction 21

4.3.2 Sequencing 21

4.3.3 Myofibril Isolation 23

4.3.4 Phosphoprotein Stain 24

4.3.5 Phosphoprotein Data analysis 24
4.3.6 Western Blots 27
4.3.7 Hemotoxylin and Eosin Staining 28
4.4 RESULTS 29
4.4.1 PCR Results 29
4.4.2 DNA Sequencing Results 30
4.4.3 Phosphoprotein Stain 31
4.4.4 Western Blots 34
4.4.5 Histology 35
4.5 2D-DIGE 36
4.5.1 Methods 36
4.5.2 Results 37
4.6 SUMMARY 42
5.0 WHOLE ORGAN STUDIES 43
5.1 INTRODUCTION 43
5.2 METHODS 44
5.2.1 Echocardiography 44
5.2.2 Echocardiography: Data Analysis 45
5.2.3 Isolated Heart 47
5.2.4 Isolated Heart: Protocols 48
5.2.5 Isolated Heart: Data analysis 49
5.2.6 Isolated Heart: Statistical Analysis 50
5.3 RESULTS 51

5.3.1 Echocardiography 51
5.3.2 Isolated Heart 53
5.3.2.1 Frank Starling Protocol 53
5.3.2.2 Ischemia-Reperfusion Protocol 56
5.3.2.3 Isoproterenol Protocol 58
5.4 INADVERTENTLY INDUCED HYPOXIA 58
5.5 SUMMARY 61
6.0 FORCE-CALCIUM RELATIONSHIPS 62
6.1 INTRODUCTION 62
6.1.1 Myofibrilar ATPase Measurement 63
6.2 METHODS 64
6.2.1 Isolated Papillary Muscle 64
6.2.2 Isolated Papillary Muscle: Protocols 67
6.2.3 Isolated Papillary Muscle: Data Analysis 68
6.2.4 Isolated Papillary Muscle: Statistical Analysis 68
6.2.5 Skinned Fiber 69
6.2.6 Skinned Fiber: Protocols 70
6.2.7 Skinned Fiber: Data Analysis 71
6.2.8 Skinned Fiber: Statistical Analysis 71
6.3 RESULTS 72
6.3.1 Papillary Muscle: Results 72
6.3.1.1 Muscle Length Protocol 72
6.3.1.2 Acute cTnI Phosphorylation Protocol 77

6.3.2 Skinned Fiber 81
6.4 SUMMARY 83
7.0 MODEL-BASED ANALYSIS 85
7.1 INTRODUCTION 85
7.2 METHODS 86
7.2.1 Model Selection 86
7.2.2 Four-State Model 86
7.2.3 *A Priori* Identifiability 89
7.2.3.1 Model Identifiability Using Differential Algebra: An Example 90
7.2.3.2 DAISY and the Four-State Model 93
7.2.4 Automated Optimization 95
7.3 RESULTS 95
7.3.1 *A Priori* Identifiability 95
7.3.2 Automated Optimization 96
7.3.3 Model-Based Interpretation of Experimental Data 99
7.4 SUMMARY 105
8.0 DISCUSSION 106
8.1 HYPOTHESES 106
8.2 INITIAL CHARACTERIZATION 107
8.3 CONTRACTION AND RELAXATION 109
8.4 ISOLATED HEART AND ECHOCARDIOGRAPHY 110
8.4.1 Heart Rate 110
8.4.2 Response to Ischemia 111

8.4.3 Response to β-adrenergic Stimulation 113
8.5 ISOLATED PAPILLARY MUSCLE 113
8.5.1 Intracellular Calcium Transients 113
8.5.2 Acute Phosphorylation 115
8.6 SKINNED FIBERS 116
8.6.1 Calcium Sensitivity 116
8.6.2 ATPase Activity 118
8.7 INTEGRATIVE AND MODEL-BASED INTERPRETATION 118
8.7.1 Parameter Identifiability Challenges 118
8.7.2 Site Specificity 119
8.7.3 Biophysical Basis for Model-Based Interpretations 120
8.7.4 Functional "Gain" 121
9.0 CONCLUSIONS 123
9.1 TAKE HOME MESSAGES 123
9.2 CLINICAL IMPLICATIONS 124
9.3 FUTURE WORK 125
APPENDIX A 128
APPENDIX B 151
APPENDIX C 157
APPENDIX D 168
APPENDIX E 179
BIBLIOGRAPHY 182

LIST OF TABLES

Table 1. Quantification of Percent Replacement and Protein Phosphorylation..... 41

Table 2. Echocardiographic Intra-Observer Error 46

Table 3. Echocardiographic Indices from WT and TG-E Mice..... 52

Table 4. Effects of Isoproterenol Treatment 58

Table 5. Slope and Intercept Values for Various Relationships in Papillary Muscles 76

Table 6. Summary of Data from Skinned Fiber Protocol 83

Table 7. Results of Identifiability Analysis 95

Table 8. Parameter Estimates from Levenberg-Marquadt Algorithm 96

Table 9. Values for Parameter Estimation on Synthetic Data 98

Table 10. Mechanical Restitution Data..... 138

Table 11. Results of Identifiability Analysis 156

Table 12. Effect of Changes in k_2 169

Table 13. Effects of Changes in k_3..... 170

Table 14. Effects of Changes in k_4..... 171

Table 15. Effects of Changes in g 172

Table 16. Effects of Changes in α_1 173

Table 17. Effects of Changes in β_1..... 174

Table 18. Effects of Changes in α_f..... 175

Table 19. Effects of Changes in β_f 176

Table 20. Effects of Changes in d 177

Table 21. Index Sensitivity to All Parameters 178

LIST OF FIGURES

Figure 1-1. Schematic of Calcium Handling in the Ventricular Myocyte. 2

Figure 1-2. Schematic of PKC Signaling 5

Figure 1-3. The Static and Dynamic Calcium-Force Relationships 7

Figure 1-4. Schematic of cTnI 9

Figure 4-1. Wild type (WT) versus TG-E (TG-E) Mice Mass Comparison. 20

Figure 4-2. DNA Sequence from the TG-E Plasmid. 22

Figure 4-3. Representative PCR Gel 29

Figure 4-4. α-MHC Plasmid Sequence Versus Sequence from TG-E Mouse. 30

Figure 4-5. cTnI Sequence from Plasmid Versus TG-E mouse 31

Figure 4-6. Phosphoprotein Assay on PKA and PKC Treated Samples 32

Figure 4-7. Phosphoprotein Assay on Untreated Samples 33

Figure 4-8. Western blot of TG-E versus WT samples 34

Figure 4-9. H&E Stained Sections from WT and TG-E mice 35

Figure 4-10. 2D-DIGE of PKA and PKC WT Myofibrils 38

Figure 4-11. 2D-DIGE Data from WT and TG-E Samples 40

Figure 5-1. Frank Starling Protocol 48

Figure 5-2. Echocardiographic Images from WT and TG-E mice 52

Figure 5-3. WT and TG-E Frank Starling Raw Data 53

Figure 5-4. Compiled Developed and Diastolic Indices 54
Figure 5-5. Stress-Volume Relationships for WT and TG-E Mice 54
Figure 5-6. Relaxation Indices for WT and TG-E Mice 55
Figure 5-7. Data from Ischemia-Reperfusion Experiments 57
Figure 5-8. Effects of Reduced Oxygenation in an Isolated Heart 60
Figure 6-1. Myofibrilar Maximal ATPase Activity 63
Figure 6-2. Schematic of Intracellular Calcium Imaging Setup 65
Figure 6-3. Raw Fluorescence Data from a WT Papillary Muscle 72
Figure 6-4. Raw Force and Calcium from WT and TG-E Papillary Muscles 73
Figure 6-5. Force - Length Relationships in WT and TG-E Papillary Muscles 74
Figure 6-6. Calcium - Length Relationships in WT and TG-E Papillary Muscles 75
Figure 6-7. Representative Prop./PE Treatment Data 78
Figure 6-8. Effect of Phenylephrine Treatment 79
Figure 6-9. Calcium from Prop./PE Treatment Experiment 80
Figure 6-10. Data from WT and TG-E Skinned Fibers 81
Figure 6-11. Tension Cost for WT and TG-E Skinned Fibers 82
Figure 7-1. Schematic of the Four-State Model 87
Figure 7-2. Schematic of Example Model 91
Figure 7-3. Synthetic and Model-Fit Pressure Waveform 99
Figure 7-4. Experimental and Model Calculated Pressure Waveforms 102
Figure 7-5. Experimental and Model Calculated pCa-Force Plots 103
Figure 7-6. Experimental and Model Calculated Force-ATPase Relationships 104
Figure 8-1. WT vs. TG-A Response to Ischemia-Reperfusion 112

Figure 9-1. Example of Mechanical Restitution Protocol 132
Figure 9-2. Example Pressure and Calcium Waveforms 134
Figure 9-3. Effects of Altered LV Volume 135
Figure 9-4. Effects of Sustained Volume 136
Figure 9-5. Analysis of Mechanical Restitution Data 139
Figure 9-6. Pressure versus Calcium Relaxation 141
Figure 9-7. Determinants of Developed Pressure 142
Figure 9-8. Model-Based Interpretation: Mechanical Restitution Protocol 147
Figure 9-9. Model-Based Interpretation: Frank Starling Protocol 150
Figure 9-10. Windkessel Models 153
Figure 9-11. Schematic of Three-State Model 155
Figure 9-12. Fura Binding to Calcium 179

ACKNOWLEDGEMENTS

There is a long list of people who have contributed to this project. I would like to begin by thanking my advisor, Dr. Sanjeev Shroff. He has supported me in numerous ways over the past five years. It is to him that I owe my successes, and from him that I have learned how to be a scientist and a teacher.

I owe many thanks to my committee: Dr. Harvey Borovetz, Dr. Kenneth Campbell, Dr. Franklin Fuchs, Dr. Barry London, and Dr. Guy Salama. They have helped to shape this work. I owe a special thanks to Dr. Campbell, who has provided me with guidance for the better part of a decade.

I would like to thank all past and present members of the Shroff lab: Dr. Dan Debrah, Dr. Lauren Johnson, Dr. Nick Perrusquia, Dr. Yong He, Dr. Andrzej Janczewski, and Jamie Haney. Particular thanks go to Caroline Evans and Dr. Steve Smith who have provided so much help on the experiments.

I thank the undergraduate students I have mentored over the years: Tahir Zaman, Casey Overby, Rachael Werner, and Russell Bregman. Teaching is one of the best ways to learn.

I owe many thanks to the faculty of the Bioengineering Department at the University of Pittsburgh, as well as the administrative staff: Joan Williamson, Lynette Spataro, Judy Repp, and Mary Grace Wojnar.

I must thank Steve Winowich and Robert Kormos for giving me the opportunity to work at the Artificial Heart Program. I found it fulfilling and a perfect complement to my work in the lab.

There were many individuals who provided helpful discussion, advice, technical help, and collaboration, including (in no particular order) Dr. Guy MacGowan at University of Newcastle upon Tyne, Paul Janssen and Kenny Varian at The Ohio State University, Dr. John Jeremy Rice at IBM, Dr. R. John Solaro and Chad Warren at the University of Illinois in Chicago, Dr. Murali Chandra and Ranganath Mamidi at Washington State University, Dr. Alexandre F.R. Stewart at the University of Ottawa Heart Institute, Dr. Carter Ralphe at the University of Wisconsin-Madison, Dr. Maria Pia Saccomani at the University of Padova (Italy), and Kelly Clause, Partha Roy, Kimimasa Tobita, and John Brigham at the University of Pittsburgh.

I want to thank the funding sources that supported this work: the NIH (T32-HL76124) and the McGinnis Endowed Chair research funds.

Lastly, I owe special thanks to my wife, Erin, and my son, Hayden. You bring me joy every day.

1.0 BACKGROUND

1.1 CARDIAC MUSCLE PHYSIOLOGY

The heart acts as a pump to move blood, the carrier of oxygen and nutrients, to the various tissues of the body. Blood enters the main pumping chambers, the ventricles, which contract, decreasing the volume inside the ventricle. This causes an increase in pressure which forces the blood to the lungs (from the right ventricle) or the rest of the body (from the left ventricle).

This contraction occurs because the heart is essentially a large muscle. The fundamental complete unit of force production is the sarcomere, but its control starts at a more macroscopic level. The electrical conduction system in the heart provides an electrical stimulus, an action potential (AP), to the heart muscle. The AP stimulates L-type calcium channels on the surface of the cell (the sarcolemma) to open, allowing the Ca^{2+} current (I_{Ca}) to carry extracellular calcium into the cell. Additional calcium enters the cell through the Na^{+}-Ca^{2+} exchanger (NCX). This relatively small increase in intracellular calcium concentration is sensed by ryanodine receptors (RyR) on the surface of the sarcoplasmic reticulum (SR), an intracellular organelle analogous to the endoplasmic reticulum in non-muscle cells. Stimulating the RyR triggers the SR to release its vast stores of calcium, thus greatly increasing intracellular calcium concentration. This is referred to as calcium-induced calcium release (CICR). The relative contribution of the L-type

channels, NCX and SR to total intracellular calcium, however, varies between species [1], an important distinction when interpreting experimental data. Overall, there is a 10-20 fold increase in intracellular calcium concentration, from a diastolic concentration of ~ 100nM to a peak systolic concentration of 1000-2000nM [2].

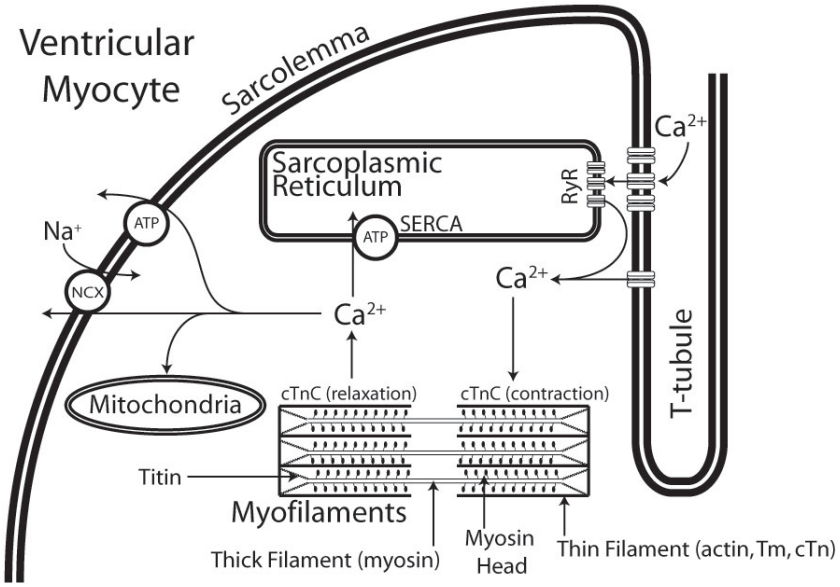

Figure 1-1. Schematic of Calcium Handling in the Ventricular Myocyte.

The rise of intracellular calcium acts as a stimulus to the sarcomere. The sarcomere is highly structured, consisting of overlapping thin and thick filaments. The thick filament is comprised primarily of myosin, which makes up the filament and the head region. The myosin heads protrude from the filament surface at regular intervals. Each myosin has two heads and consists of two myosin heavy chains (MHC, primarily β -MHC in human ventricles, and α -MHC in mouse), and four (two per head) myosin light chains (MLC): two essential light chains (ELC) and two regulatory light chains (RLC). The thin filament consists mainly of actin, which has binding sites for the myosin heads. At diastolic levels of calcium, those binding sites are

sterically blocked by tropomyosin. Tropomyosin is comprised of two α-helical chains arranged in a coiled-coil structure. These structures polymerize to form long strands that wrap around actin [3]. When intracellular calcium rises, the calcium binds to another thin filament associated protein, cardiac troponin (cTn). More specifically, it binds to cardiac troponin C (cTnC), which, along with cardiac troponin T (cTnT) and cardiac troponin I (cTnI), make up the trimeric protein cTn. The binding of calcium to cTnC begins a process that causes tropomyosin to move out of the myosin binding pocket on actin.

Once myosin binds to actin, forming a crossbridge, the myosin head undergoes a conformational change, generating longitudinally perceived torque, producing roughly 10-12 pico-Newtons of force [4]. This movement is often called the powerstroke. Following this work-producing step, myosin-bound ADP is released and replaced by ATP, which causes the myosin head to unbind from actin. When myosin reattaches to actin, the ATP is hydrolyzed by ATPase, and the process begins again [5].

At the end of contraction, calcium is sequestered back into the sarcoplasmic reticulum (by Sarco/Endoplasmic Reticulum Ca^{2+}-ATPase, SERCA) or transported back out of the myocyte by NCXs and ATPase pumps. See **Figure 1-1** for a schematic of cardiac contraction (in the figure, NCX pumps are only shown pumping calcium out of the cell, in reality they move calcium into and out of the cell).

While the stimulatory AP is all-or-nothing, the muscle contraction itself can be tightly regulated by a number of signaling pathways.

1.2 PROTEIN KINASE C CARDIAC SIGNALING

Cardiac function can be modulated through neurohormonal stimulation. Primary signaling messengers such as norepinephrine, epinephrine, bradykinin, angiotensin II (Ang-II), endothelin I (ET-1), and others can activate protein kinase C downstream. These messengers act on cell surface G-protein coupled receptors (GPCRs) such as α_1 adrenergic, ET-1, AT1, muscarinic and bradykinin receptors.

GPCRs have seven transmembrane domains, and are involved in signaling cascades all over the body. These specific receptors are primarily coupled to G_q proteins (a heterotrimeric G protein) which in turn activate phospholipase C (PLC), which is bound to the intracellular portion of the G_q protein. Activated PLC acts on phosphatidylinositol 4,5-bisphosphate (PIP_2), causing its breakdown into inositol triphosphate (IP_3) and diacylglycerol (DAG). IP_3 acts on IP_3 receptors located on the surface of the sarcoplasmic reticulum (SR) to release intracellular calcium. DAG binds to PKC to stabilize its active form and calcium increases the enzyme's affinity for lipids [6, 7]. See **Figure 1-2** for schematic of a PKC signaling.

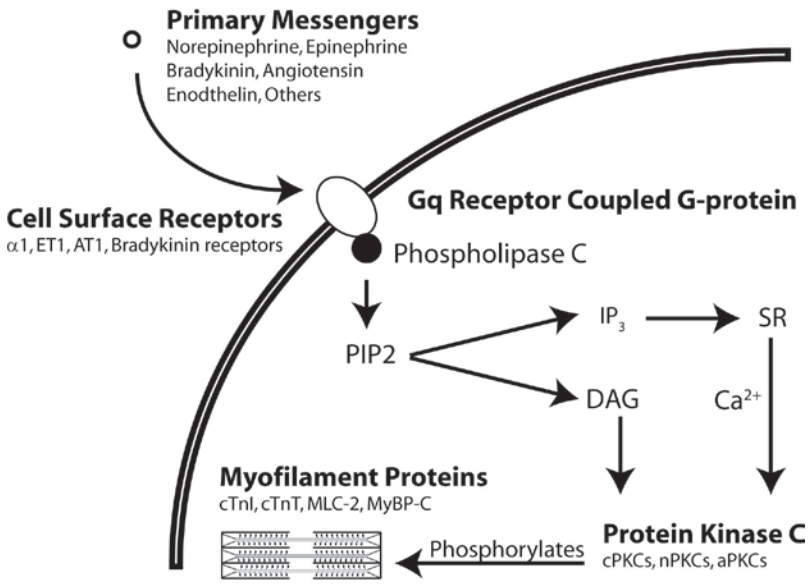

Figure 1-2. Schematic of PKC Signaling

PKC is a serine/threonine kinase and was first described by Takai *et al.* [8] and later identified in the heart by Kuo *et al.* [9]. There are many isoforms of PKC, categorized into three classes [10]: calcium sensitive, novel, and atypical. The calcium sensitive PKCs (cPKCs) have a calcium binding site and require activation by both DAG and calcium. There are four cPKCs: α, β-I, β-II, and γ. The novel PKCs (nPKCs) require only DAG activation; there are five nPKCs: δ, ε, η, μ, and θ. There are two atypical PKCs (aPKCs), ζ and ι/λ, and they are less well characterized, but have recently been implicated in sarcomeric protein phosphorylation [11].

PKC, as a kinase will do, phosphorylates a number of intracellular proteins, including several myofilamental proteins. These include myosin binding protein C (MyBP-C) [12-14], myosin light chain 2 (MLC-2) [15, 16], cTnT [17] and cTnI. PKC-induced phosphorylation of cTnI is the focus of this project, and will be covered in detail. Of the isoforms discussed above, there is evidence that PKC α, β-I, β-II, δ and ε phosphorylate cTnI [18]. However, we are not

looking at the effects of a specific PKC isoform, but the phosphorylation of the sites primarily targeted by all PKC isoforms.

1.3 INTRACELLULAR CALCIUM

Intracellular calcium plays a critical role in regulating normal cardiac mechanical function. Although it was found that calcium rises and falls in contracting muscle more than forty years ago [19], there remains a great deal about its role that is still unclear. Abnormal calcium cycling occurs in heart failure [20-23], dilated cardiomyopathy [24, 25], ischemia-reperfusion [26, 27], and arrhythmias [28]. There is little understanding as to why calcium cycling abnormalities occur, or how to correct them.

The relationship between calcium and generated force in cardiac myocytes is often studied under steady-state conditions. The technique involves enzymatically “skinning” the fiber to remove the membrane and all intracellular structures, effectively isolating the contractile machinery. By changing the concentration of calcium in the bathing solution, calcium is held at a particular concentration and the force produced at that concentration is then measured. This provides a steady-state relationship between calcium and force that is referred to as the force-pCa relationship.

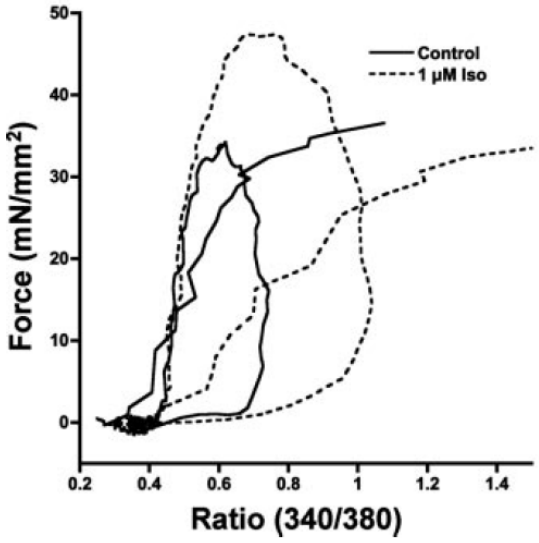

Figure 1-3. The Static and Dynamic Calcium-Force Relationships

Dynamic (loops) and steady-state (sigmoid) force-calcium relationships before and after isoproterenol treatment from the same trabeculae muscle. From Varian K.D. et al, *Am J Physiol Heart Circ Physiol*, 2006 [29]. Used with permission.

If each force-calcium concentration pair determined from the static relationship were the same in the dynamic, physiologic relationship, there would be no need for further study. However, in dynamic measurements of intracellular free calcium, concentration reaches its maximum and falls to near baseline by the time developed tension reaches its peak [19, 30]. This implies that during dynamic conditions, maximum calcium does not produce maximum force as the steady-state force-pCa curve predicts (at calcium levels under saturation). Moreover, there are at least two force levels for a given calcium concentration, one during the rising phase and one during the relaxation phase, and neither are necessarily the same as the force predicted by the force-pCa relationship. These properties can be easily appreciated when the dynamic data are overlaid on the steady-state data as seen in **Figure 1-3**. Therefore, evaluation of the dynamic relationship between force and calcium, in addition to the steady-state relationship, is important to better understand the *in vivo* processes that connect them.

1.4 CARDIAC TNI PHOSPHORYLATION BY PKC

One of the key elements in the physical connection between calcium and force is the troponin complex. The inhibitory subunit, cTnI, has gained particular prominence due the discovery that it is a target for phosphorylation. cTnI has been implicated in a wide array of myofilament property alterations.

Cardiac TnI is a 24kD, 211 amino acid protein. It consists of 6 main regions: 1) a cardiac specific N-terminal extension, 2) a structural domain which binds to the C-lobe of cTnC, 3) a region which binds to the C-terminus of cTnT, 4) an inhibitory region which binds to actin, 5) a regulatory region, and 6) a second actin-binding region. Overall, cTnI has a highly conserved amino acid sequence (especially the inhibitory region). The human and mouse sequences differ in length by one amino acid at the N-terminus; the initiating methionine is present in the mouse, but not in the human. Amino acid positions presented here are for the mouse cTnI, but are shifted one lower for human (i.e., position 23 in mouse is 22 in human). See **Figure 1-4** for a schematic of cTnI.

Cardiac TnI it is a substrate for both protein kinase A (PKA) and PKC. The five amino acid residues on cTnI that can be phosphorylated by PKA and PKC are serines at positions 23, 24, 43 and 45 and threonine at position 144. The serines nearest the N-terminus, in the cardiac specific N-terminal extension, (S23 and S24) are primarily phosphorylated by PKA. PKA-induced phosphorylation has been shown to increase systolic function (i.e. reduction in peak developed force or pressure) [31], enhance relaxation [14, 31, 32], increase crossbridge cycling rate [14, 33], decrease myofilament calcium sensitivity [18, 34], alter ATPase activity [34], and increase length dependent activation [35, 36].

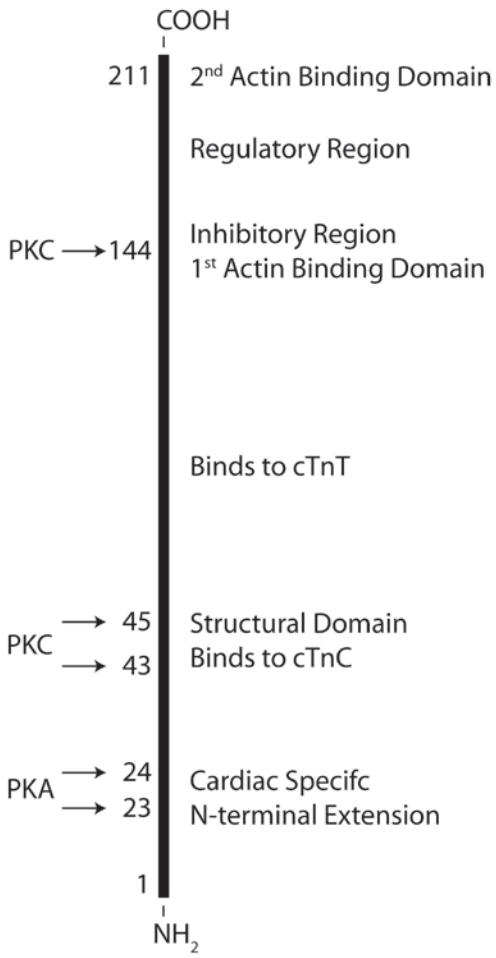

Figure 1-4. Schematic of cTnI

It is important to acknowledge that there may be other phosphorylation sites, including S150 [37] and S76/T77 [38] (in human) as well as other kinases that act on cTnI, including p21-activated kinase (PAK) [37], mammalian sterile 20-like kinase 1 (Mst1) [39], and PKD [40]. The impact of phosphorylation of these sites or these kinases remains unclear.

The focus here, however, will be on PKC due to evidence that its effects are largely dominant over those of PKA [41]. Moreover, the effects of PKA phosphorylation are comparatively well-studied, while there still remains ambiguity and disagreement regarding the effects of PKC-induced phosphorylation of cTnI.

The main targets of PKC are S43, S45 and T144. The serines at position 43 and 45 reside in the structural domain of cTnI which binds to the C-lobe of cTnC. The threonine at 144, however, lies in the inhibitory, actin binding region. PKC is rather promiscuous, however, and it can cross phosphorylate the PKA sites [42, 43], meaning there is some affinity for PKC to phosphorylate S23 and S24.

There are three primary techniques for studying the effects of PKC-mediated phosphorylation of cTnI: chemically or pharmacologically blocking or upregulating PKC, reconstituted fibers, and transgenic animals. The first method involves chemically treating the sample with a PKC blocker or PKC activator like ET-1 [44], propranolol [45], high calcium [46], or with PKC itself [47]. The difficulty with these experiments is the confounding effects that PKC has on other myofilament proteins, as well as its affects on L-type calcium channels [48] and protein expression [49].

A cleaner experimental model involves mutating the PKC phosphorylation sites on cTnI directly, thereby isolating the perturbation to cTnI. This method involves reconstituting the sarcomere with a mutant form of the troponin (Tn) complex [50]. The mutant form is generally created by replacing the endogenous residue (either a serine or a threonine) with either an alanine (which cannot by phosphorylated) or glutamate/aspartate (both of which simulate the charge and steric effect of a phosphate group). The reconstitution technique involves isolating fiber bundles from the heart (often from papillary muscles) and then “skinning” them, removing the membrane by detergent treatment. The fiber is then bathed in an exchange buffer (for approximately 90 minutes, see [51] for details) and the mutant Tn, which over time will begin to replace the endogenous Tn.

These experiments have allowed many perturbations of the phosphorylation sites, including: T144A (threonine at amino acid position 144 mutated to alanine) [52], S43A/S45A (serines at positions 43 and 45 are mutated to alanines) [52], S43A/S45A/T144A[52], T144E[51], S43E/S45E[51], S43E/S45E/T144E [51], and T144P (proline is the residue in the equivalent position in slow skeletal TnI, ssTnI) [53, 54]. The limitation of this technique is obvious: the muscle is already skinned, and so the type of experiments that can be performed is quite limited.

The third method involves mutant cTnI expressed in a whole transgenic animal. Using these mice, many types of experiments are possible, including whole animal *in vivo* techniques like echocardiography. The same constructs that are used to create reconstituted fibers can be used to create transgenic animals, but the time and cost have limited the strains of transgenic mice created. The cDNA for the mutant protein is attached to a cardiac specific promoter (such as the α-myosin heavy chain promoter) for conditional expression. The strains of transgenic mice that have been created are: S23D/S24D/S43D/S45D/T144D [41], S23A/S24A/S43A/S45A/T144A [55], S23A/S24D/S43D/S45D (an attempt to mimic changes in phosphorylation during heart failure) [56], and S43A/S45A [57], and a PKC overexpressing mouse [58].

Despite, or perhaps because of, the number of experimental methods that exist, there has been disagreement and ambiguity regarding the effects of PKC phosphorylation of cTnI. There is evidence suggesting that PKC-activated phosphorylation of cTnI serines at positions 43 and 45 has a negative ionotropic effect [41]. However, it has been shown PKC activation produces a positive inotropic response [45], depending on the species. Regarding relaxation, there is

evidence of negative [59] and positive lusitropic [53] effects as well. Previous data from our lab suggested negative inotropy with no change in relaxation [60].

Based on the negative inotropic and lusitropic effects, it has been suggested that crossbridge cycling is decreased [51]. Given the uncertainty involving these functional effects, it is difficult to be certain of the state of crossbridge cycling under cTnI phosphorylation. Moreover, the changes in crossbridge kinetics are based on assumptions drawn from force kinetics – i.e., since relaxation is slower, crossbridge cycling must be slower. This conclusion may be correct, but the final force waveform is the end-product of several complicated processes, leaving open the possibility of contributions from alternative mechanisms.

There is also disagreement over the effect on calcium sensitivity. There is evidence that there is no change in [61], increased [34], or decreased calcium sensitivity [51]. It has been suggested that the effects of PKA and PKC phosphorylation are actually opposite and meant to balance each other *in vivo* [18]; however, there are data showing decreased calcium sensitivity during PKA [34] and PKC-activated phosphorylation [51].

Intracellular calcium transients recorded from S43A/S45A mice showed increases in diastolic and systolic calcium [57], but only at high extracellular calcium levels (3.5 mM). The effects at a more physiological concentration are less clear. Some other noted effects of cTnI phosphorylation at the PKC sites include its role in length-dependant activation [54], response to afterload [56], frequency [56] and length [54] and filament sliding speed [51].

Overall, it is clear that there remains disagreement and ambiguity regarding the effects of PKC-mediated phosphorylation of cTnI.

1.5 MATHEMATICAL MODEL BASED ANALYSES

Given the multifaceted, multivariate effects on the major links between calcium and force generation by PKC phosphorylation of cTnI, there needs to be an analysis of the data that is robust enough to uncover these effects. We will therefore employ a model-based analysis, where appropriate, which should provide stronger evidence of the specific effects of PKC-activated phosphorylation of cTnI on the calcium-force relationship.

Mathematical modeling is an indispensible tool in analyzing complex systems. As put by Rosenblueth and Wiener in 1945 [62],

> "No substantial part of the universe is so simple that it can be grasped and controlled without abstraction. Abstraction consists in replacing the part of the universe under consideration by a model of similar but simpler structure. Models… are thus a central necessity of scientific procedure."

Like the system being studied, a mathematical model must possess a certain degree of unpredictability. For a mathematical model or simulation, this characteristic is called "emergent properties".

Well designed models, in general, serve three purposes: descriptive, predictive, and explanative. A descriptive model has adequate complexity and appropriate design so that it can capture the important features of an observed behavior, i.e., it can describe a system. A predictive model can anticipate events which have not yet occurred or experimentally cannot be perceived, i.e., it can predict the state of a system. An explanative model has states, structure, or parameters which represent actual elements in the system and so it is possible for the model to clarify why the system responded a certain way, i.e., it can explain system behavior.

There are several types of mathematical models and evaluation methods: Markov models, Monte Carlo simulations, discrete event simulations, and others [63]. It is common to model biological systems as dynamic, state-based systems. Clearly, biological systems, despite overall homeostasis, are marked by continuous change, making them ideal dynamic systems. This means the model will most likely be characterized by differential equations. State-based, or compartment, models consist of a set of mutually exclusive and collectively exhaustive states. Transition from one state (i.e., State 1) to another (State 2) depends on a transition probability parameter and the population in State 1. This is similar to models of chemical kinetics, where the transition probability parameter is called a rate constant.

Once a type of model has been chosen, the model structure needs to be formed. This will be guided by two things: (1) the purpose the model is intended to fulfill, which will come from the research question or hypothesis, and (2) knowledge of the system (either from the literature or experiments). Structural decisions could include selection of inputs and outputs, states to include, relationships between elements, and hierarchies. Along with the structure, there will be a number of assumptions to be identified.

At the current pace of scientific advancement there is usually an over abundance of knowledge. The complexity of the model needs to match the use of the model. James Bassingthwaighte, a mathematical modeler, wrote, “A model… is simpler than the real thing. Like any simplification, it provides only a parsimonious and somewhat erroneous description” [64]. Given the purpose of the mathematical model, how much error between real life and the model is allowable? If this question is answered too conservatively, the model will be large, unmanageable, and probably useless. If the question is answered too liberally, the model will be so simple as to lack emergent properties.

Following the development of the model, it is necessary to validate it. Model validation ensures the model meets the most basic property described above: it is descriptive. The model needs to be compared to actual data to determine whether it can, to a reasonable degree, reproduce known data.

It may be necessary to return to a previous step if the model cannot be validated. This may mean rearranging the structure, reassessing the assumptions, or even returning to the initial research question. For the model-based analysis used in this project, we have selected the four-state model, which will be introduced, and its selection justified in **Section 7.2**.

1.6 CLINICAL RELEVANCE

Cardiovascular disease (CVD) is the number one killer in the United States and claims more lives each year than the next four leading causes combined [65]. Research shows that during end-stage heart failure, phosphorylation levels at all five sites on cTnI are abnormal [66-70], and that PKC itself is upregulated [70, 71]. Moreover, there is evidence that cTnI may represent an appropriate therapeutic target for possible heart failure treatments [72]. Understanding the effects of increased PKC phosphorylation of cTnI will help illuminate one piece of a complex and multivariate disease. This research will further our understanding of the effects of cTnI modification, a key step towards future development of treatment targets and schemes.

2.0 SPECIFIC AIMS

The TG-A mouse has provided valuable insights in understanding the impact of PKC phosphorylation of cTnI on cardiac function. It is not necessarily true that a constitutively phosphorylated system will behave opposite that of a non-phosphorylatable system.

Sakthivel *et al.* have created a transgenic mouse model with simulated constitutive phosphorylation of cTnI [41]. However, both PKC and PKA sites were constitutively phosphorylated in their model, making it difficult to separate their individual effects. Therefore, we created a new transgenic mouse model (TG-E) wherein the PKC sites, S43, S45, and T144 on cTnI were replaced with glutamic acids to simulate constitutive phosphorylation.

The overall research goal is to determine the effects of protein kinase C-mediated phosphorylation of cardiac troponin I, primarily using the TG-E transgenic mouse.

Initial Characterization: The TG-E transgenic mouse will express mutant cTnI (DNA and protein) without changes in total cTnI expression or histology.

Hypothesis 1: Increased cTnI phosphorylation at the PKC sites will result in systolic dysfunction and protection from ischemic contracture at the whole organ level.

Specific Aim 1a: Determine differences in *in vivo* cardiac function (echocardiography) in wild-type (WT, baseline) and TG-E (increased cTnI phosphorylation at the PKC sites) mice

Specific Aim 1b: Determine differences in *ex vivo* whole heart function (Langendorf) in WT (baseline) and TG-E (increased cTnI phosphorylation at the PKC sites) mice

Hypothesis 2: Increased cTnI phosphorylation at the PKC sites will result in depressed calcium-force and ATPase-force relationships (less force per calcium or ATP hydrolyzed).

Specific Aim 2a: Determine differences in the dynamic calcium-force relationship in intact papillary muscles under increased and baseline cTnI phosphorylation at the PKC sites (chronic and acute phosphorylation)

Specific Aim 2b: Determine differences in the static calcium-force and ATPase-force relationships under increased and baseline cTnI phosphorylation at the PKC sites

Hypothesis 3: A model-based analysis of data from Specific Aims 1 and 2 will provide an integrative interpretation of increased cTnI phosphorylation at the PKC sites.

Specific Aim 3a: Determine whether the four-state model can provide unique solutions

Specific Aim 3b: Using a model-based analysis, determine the myofilamental alterations caused by PKC-induced phosphorylation of cTnI

3.0 ANIMAL USE

All parts of this study were approved by the Institutional Animal Care and Use Committee (IACUC) of the University of Pittsburgh, and conform to the *Guide for the Care and Use of Laboratory Animals* published by the US National Institutes of Health (NIH Publication No. 85-23, revised 1996).

Animals were housed on a 12-hour light/dark cycle (7am-7pm), maintained at 68-74 ºF, and kept in AD Vent mouse caging (Alternative Design, Siloam Springs, AR). Animal care was provided by the University of Pittsburgh IACUC's support staff, which is supervised by a veterinarian.

Transgenic mice were bred and genotyped in house and wild-type FVB mice were purchased from Taconic (Germantown, NY).

4.0 EXPRESSION OF MUTANT CTNI DNA AND PROTEIN

4.1 INTRODUCTION

The TG-E transgenic mouse is a novel model, and this project represents the first work examining it. An initial characterization of the mouse at the DNA, RNA, protein, and cellular levels is necessary to confirm that the creation of the transgenic mouse was successful. Polymerase chain reaction (PCR) was used to identify positive mice. To confirm the sequence of the mutant cTnI, the PCR product was sequenced and compared to the original construct. To determine the success of the mutation at the mRNA level, reverse transcriptase PCR (RT-PCR) was used, but was unsuccessful because the primers were not specific enough to distinguish mutant cTnI mRNA from WT cTnI mRNA due to the high GC content. However, if the mutant protein is expressed, there must be mutant mRNA. The first attempt at protein quantification used the back-phosphorylation assay, which was not accurate enough to find differences. Instead, a phosphoprotein staining procedure was used. Overall protein expression was quantified using western analysis. Lastly, the histology of the S43E/S45E/T144 mice was compared to WT mice.

4.2 GENERATION OF TRANSGENIC MICE

There are two strains of transgenic mice that have mutated only the PKC phosphorylation sites on cTnI. The first is the S43A/S45A, unphosphorylatable mouse. This transgenic mouse was generated several years ago and much work has been done on it. This mouse will be referred to as the TG-A (for transgenic, mutated to alanines) mouse. The second strain is a novel transgenic mouse: S43E/S45E/T144E. This mouse will be referred to as the TG-E (transgenic, mutated to glutamates) mouse. The TG-E mouse is the focus of this study.

To create this mouse, the serine 43 and 45 and threonine 144 residues on cTnI were replaced with glutamic acid to simulate constitutive phosphorylation. The cDNA for this mutant cTnI was placed under the control of the cardiac specific α-myosin heavy chain promoter [73], using a Bluescript vector. Steps to create the transgenic mouse were similar to the creation of the TG-A mouse [57]. The transgene was injected into FVB (friendly virus type B) zygotes. Microinjected mouse embryos were then reimplanted into pseudo-pregnant FVB female mice.

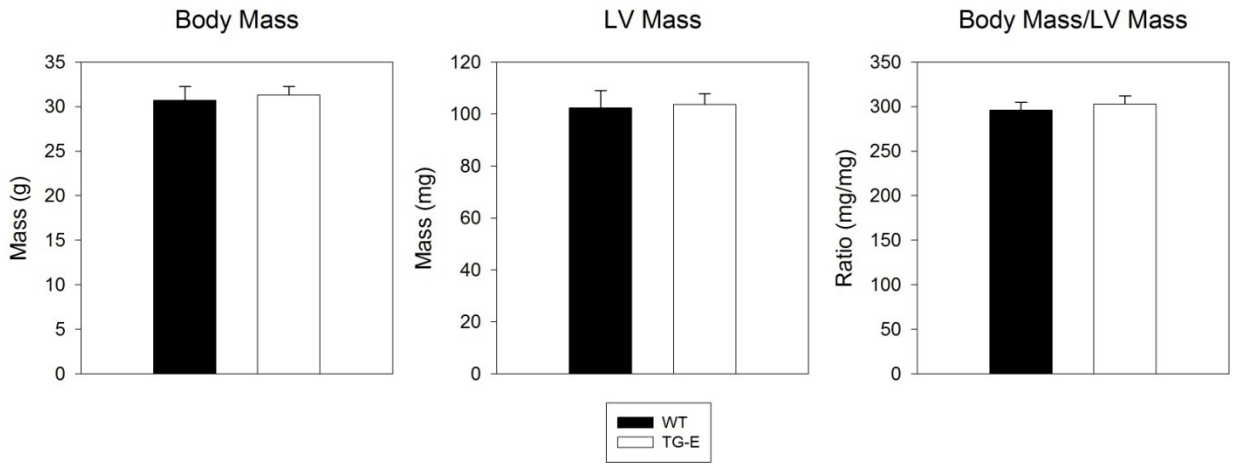

Figure 4-1. Wild type (WT) versus TG-E (TG-E) Mice Mass Comparison.

LV, left ventricular.

The TG-E mice showed no differences in body mass (WT: 30.7 ± 1.6 g, TG-E: 31.3 ± 1.0 g), left ventricular (LV) mass (WT: 102.4 ± 6.7 mg, TG-E: 103.7 ± 4.2 mg), or their ratio (WT: 296 ± 9, TG-E: 303 ± 9), as shown in **Figure 4-1**. The TG-E mice also showed no external signs of heart failure, including lethargy or differences in feeding.

4.3 METHODS

4.3.1 Polymerase Chain Reaction

PCR was performed to identify the TG-E mice. The DNA samples were isolated from tail clips taken from the mice at three weeks of age. The DNA was isolated using a Wizard Genomic DNA Purification Kit (Promega, Madison, WI) following the manufacturers published protocol. The two primers (Applied Biosystems, Foster City, CA) were: 5'-CCTTGTCTTGATTAATCTTGGC-3' (binds to the myosin heavy chain promoter) and 5'-CTCCTGCTTCGCAATCTGCAGC-3' (binds to cTnI sequence). PCR was run on a PCR Sprint Thermal Cycler (Thermo Fisher, Waltham, MA). Samples were then loaded on a 1% Agarose gel and run at 160 volts for 30 minutes. Gels were then imaged on a Kodak ImageStation IS2000R.

4.3.2 Sequencing

Three sequencing primers were used on the isolated DNA from the TG-E mice: 5' - CTACTTTCGTCGCTACGC -3' and 5' - GCCTTCCATGCCACTCAG -3', and an internal

primer: 5’ - CACCTCCCGGTTTTCCTT -3’. DNA sequencing was then carried out by the University of Pittsburgh genomics core.

TATA AAG GGG CTG GAG CGC TGA GAG CTG TCA GAC CGA GAT TTC
TCC ATC CCA GGT AAG AAG GAG TTT AGC GTG GGG GCT CTC CAA CCG
CAC CAG ACC TGT CCC CAC CTA GAG GGA AAG TGT CTT CCC TGG AAG
TGG GGC TCC TCC CAC CGG CCT GGG AAG TTC TCG GTG GCA GGA TGT
TTC TAC TGG ATG CCC CTT CCC TTC CAC TGC CTC CTC CCT CCC TTG
TCT TGA TTA ATC TTG GCT CTT AGT GTT CAG AAA GAT TTG CCC GGT
GCT GTC TAC TCC ATC TGT CTC TAC TCT CTC TGC CTT GCC TTC TTG
TGT GTT CTC CTT TTC CAC GTG TTT CTC ACT CCA CTG CCT CCC CCC
CCC CCT TCA TTT TTA TCC TTC CTT TCT TTC TGT GTC AGA ATG CTG
GGA ATC AAA CCC AGG GCT TCA TAC ACG TCA AGT AAG CAA TCT CCC
AGT GAG CCA AAG CTT

ATG GCT GAT GAA AGC AGC GAT GCG GCT GGG GAA CCG CAG CCT GCG
CCT GCT CCT GTC CGA CGC CGC TCC TCT GCC AAC TAC CGA GCC TAT
GCC ACC GAG CCA CAC GCC AAG AAA AAG TCT AAG ATC ***GAA*** GCC ***GAA***
AGA AAA CTT CAG TTG AAG ACT CTG ATG CTG CAG ATT GCG AAG CAG
GAG ATG GAA CGA GAG GCA GAA GAG CGA CGT GGA GAG AAG GGG CGC
GTT CTG AGG ACT CGT TGC CAG CCT TTG GAG TTG GAT GGG CTG GGC
TTT GAA GAG CTT CAG GAC TTA TGC CGA CAG CTT CAC GCT CGG GTG
GAC AAA GTG GAT GAA GAG AGA TAT GAC GTG GAA GCA AAA GTC ACC
AAG AAC ATC ACT GAG ATT GCA GAT CTG ACC CAG AAG ATC TAT GAC
CTC CGT GGC AAG TTT AAG CGG CCC ***GAA*** CTC CGA AGA GTG AGG ATC
TCT GCA GAT GCC ATG ATG CAG GCG CTG CTG GGG ACC CGG GCC AAG
GAA TCC TTG GAC CTG AGG GCC CAC CTC AAG CAG GTG AAG AAG GAG
GAC ATT GAG AAG GAA AAC CGG GAG GTG GGA GAC TGG CGC AAG AAT
ATC GAT GCA CTG AGT GGC ATG GAA GGC CGC AAG AAA AAG TTT GAG
GGC TGA

Figure 4-2. DNA Sequence from the TG-E Plasmid.

The sequence above the break is the alpha myosin heavy chain promoter, and the bottom sequence is the cardiac troponin I sequence. The grey box is the TATA box for transcription factor binding. Notice the cTnI sequence starts with ATG, the methionine start codon. The double underlined sections represent the binding sequence for the PCR primers, and the single underlined sequences are the binding sites for the sequencing primers. The bold italicized triplets represent the mutation sequences (GAA is glutamate) at amino acid positions 43, 45 and 144. The primers were selected so that the mutation sites at 43 and 45 would be sequenced.

Figure 4-2 shows the DNA sequence from the construct used to generate the mouse, and was utilized to develop the PCR and sequencing primers. The various primer binding locations are shown on the figure as underlined sections: double underlined for the PCR primers, and

singly underlined for the sequencing primers. The base pair mutations are shown in bold italicized font (the amino acid code used to incorporate glutamate into cTnI is GAA).

4.3.3 Myofibril Isolation

The heart was quickly excised from the mouse, and then placed in ice cold PBS, where the atria, as well as any other extra tissue, was removed. The ventricles were then cut into smaller sections, roughly eight to ten pieces, and placed in 10 mL of ice cold myofibrillar relax buffer (MRB) with 10 mM ethylenediaminetetraacetic acid (EDTA). The MRB consisted of: standard rigor buffer (SRB) plus phospocreatine (4 mM), adenosine triphosphate (ATP) (1 mM), 2,3-butanedione monoxime (BDM, inhibits crossbridge interaction) (50 mM), dithiothreitol (DTT, breaks disulfide bonds) (1 mM), and phenylmethylsulphonyl fluoride (PMSF, a protease inhibitor) (0.1 mM). Between 2 and 4 hearts are used for each sample. The tissue was then homogenized using a Biohomogenizer (Biospec Products Inc., Bartlesville, OK) on the low setting 5 times for 12 seconds each time. The sample was then spun down on a centrifuge (Sorvall RC-5, Thermo Scientific, Waltham, MA) at 5,000 rpms at 4 ^{o}C for ten minutes. The supernatant was discarded and the pellet was resuspended in 12 mL SRB plus 1% Triton X-100 (v/v) and allowed to sit on ice for 5 minutes. SRB consisted of: KCl (75 mM), imidazole (10 mM), $MgCl_2$ (2 mM), ethylene glycol tetraacetic acid (EGTA) (2 mM), and NaN_3 (1 mM). The sample was spun down, and the pellet was resuspended in SRB plus Triton X-100 two more times, and SRB alone three more times. The last time, the pellet was resuspended in 1-5 mL (depending on the number of hearts that are being used) SRB plus protease inhibitor cocktail (Sigma) which contained: AEBSF (104 mM), aprotinin (80 μM), leupeptin (2.1 mM), bestatin (3.6 mM), pepstatin A (1.5 mM), and E-64 (1.4 mM).

4.3.4 Phosphoprotein Stain

The percent replacement of endogenous cTnI with mutant cTnI in the TG-E mice was measured using a phosphoprotein stain. This protocol has been used to identify cardiac protein phosphorylation states by others [30, 69]. One set of myofibrils were treated with 20 mU PKA and 30 mU PKC at 37 ^{o}C for 2 hours to ensure all five phosphorylation sites in the WT mouse, and the remaining phosphorylation sites (two sites on the mutant cTnI and five sites on the endogenous cTnI) in the TG-E cTnI were maximally phosphorylated. A second set of myofibrils were untreated. These were then loaded on a 12.5% 8x10cm SDS-PAGE gel (1mm thickness). The gel was run for 60 minutes at 200V, fixed in 50% methanol and 10% acetic acid, then stained with Pro-Q diamond phosphoprotein stain (Invitrogen, Carlsbad, CA) [74] according to the manufacturer's protocol. The gel was visualized with a custom gel scanner with an excitation filter of 560 nm and an emission filter of 590 nm. The gel was subsequently stained with SYPRO ruby total protein stain (Invitrogen) to control for differences in loaded protein. Once the gel was stained and rinsed according to the manufacturer, the gel was excited with UV illumination and visualized with a 600 nm emission filter. Band intensity was quantified using densitometry with ImageJ software (National Institutes of Health, Bethesda, MD).

4.3.5 Phosphoprotein Data analysis

There were two goals in the analysis of the measured band intensity from the phosphoprotein stain. The first was the determination of the percent replacement in the TG-E mouse, and the second was the identification of the basal phosphorylation state of the WT and TG-E mice.

Let n = total number of cTnI molecules, assumed to be the same for wild-type (WT) or TG-E mice; f_M: fraction of mutant cTnI protein in TG-E mice; X_{WT} and X_{TG}: basal degree of cTnI phosphorylation for WT and TG-E mice, respectively (0: no phosphorylation, 1: full (maximal) phosphorylation); AP_{WT} and AP_{TG}: actual cTnI phosphorylation for WT and TG-E mice, respectively; TP_{WT} and TP_{TG}: total (= actual + pseudo) cTnI phosphorylation for WT and TG-E mice, respectively (note: for WT mice, $TP_{WT} = AP_{WT}$).

The phosphoprotein stain does not recognize pseudo-phosphorylation and therefore quantifies actual phosphorylation only. Actual cTnI phosphorylation under basal conditions for WT (AP_{WT_base}) and TG-E (AP_{TG_base}) mice can be written as:

$$AP_{WT\_base} = 5nX_{WT} \tag{4.1}$$

$$AP_{TG\_base} = 5n(1-f_m)X_{TG} + 2nf_mX_{TG} = (5-3f_m)nX_{TG} \tag{4.2}$$

Thus, actual cTnI phosphorylation under full (maximal) phosphorylation conditions (i.e., $X_{WT} = X_{TG} = 1$), for the two groups can be written as:

$$AP_{WT\_\max} = 5n \tag{4.3}$$

$$AP_{TG\_\max} = (5-3f_m)n \tag{4.4}$$

Dividing **Equation 4.4** by **Equation 4.3**, the fraction of mutant cTnI prtotein (f_m) can be written as ($R_{actual\_max} = \frac{AP_{TG\_\max}}{AP_{WT\_\max}}$):

$$f_m = \frac{5}{3}\left[1 - R_{actual\_\max}\right] \tag{4.5}$$

Dividing **Equation 4.2** by **Equation 4.1**, the ratio of actual phosphorylation under basal conditions, R_{actual_base} ($= \frac{AP_{TG\_base}}{AP_{WT\_base}}$), can be written as:

$$R_{actual\_base} = \frac{(5 - 3f_m)X_{TG}}{5X_{WT}} \tag{4.6}$$

Substituting f_m from **Equation 4.5**, **Equation 4.6** can be rewritten to express $\frac{X_{TG}}{X_{WT}}$ in terms of measured quantities (R_{actual_max} and R_{actual_base}) as:

$$\frac{X_{TG}}{X_{WT}} = \frac{R_{actual\_base}}{R_{actual\_max}} \tag{4.7}$$

Total cTnI phosphorylation levels (actual + pseudo) under basal conditions for the two groups are given by:

$$TP_{WT\_base} = 5nX_{WT} \tag{4.8}$$

$$TP_{TG\_base} = (5 - 3f_m)nX_{TG} + 3nf_m \tag{4.9}$$

Dividing **Equation 4.8** by **Equation 4.9**, the ratio of total phosphorylation, R_{total_base} can be written as:

$$R_{total\_base} = \frac{TP_{TG\_base}}{TP_{WT\_base}} = \frac{X_{TG}}{X_{WT}} + \frac{3f_m}{5}\left(\frac{1}{X_{WT}} - \frac{X_{TG}}{X_{WT}}\right) \tag{4.10}$$

This analysis makes two key assumptions. The first is assumption is there are only five phosphorylation sites on cTnI. This is most likely false (see **Section 1.4**), but is still a safe assumption because it is conservative. If you assume that there are six phosphorylation sites, instead of five, the fractional coefficient on Equation 4.5 becomes 6/3 instead of 5/3, leading to a larger estimation of f_m. Therefore, the more phosphorylation sites there are, the larger the percent replacement estimate.

The second assumption is more difficult. The cTnI was treated with high doses of PKA and PKC, and assumed that it was fully phosphorylated. It may be very difficult or nearly impossible, however, to fully phosphorylate cTnI. In order to test this possibility, we needed to

collaborate with an outside group, as we did not have the capabilities here. These data and analyses is shown in **Section 4.4**.

4.3.6 Western Blots

Immunoblotting (Western blots) was performed on cellular lysate and myofibrillar samples to quantify total cTnI protein and its myofilamental stoichiometry. The myofibrilar isolation protocol was slightly altered from **Section 4.2.3**. To prepare samples, the ventricular tissue was isolated from the excised heart and then homogenized in homogenizing buffer (75 mmol/L KCl, 10 mmol/L imidazole (pH 7.2), 2 mmol/L $MgCl_2$, 2 mmol/L EGTA, 1 mmol/L NaN_3, 4 mmol/L creatine phosphate, 1 mmol/L ATP, 50 mmol/L BDM, 1 mmol/L DTT, 0.1 mmol/L PMSF, 10 mmol/L EDTA) [75]. This was centrifuged and resuspended in standard rigor buffer plus 1% Triton X-100 (v/v) multiple times. The isolated pellet was the myofibrils, and the supernatant was the cell lysate. Myofibril and cell lysate samples were separated by SDS-PAGE (10% separating gel, Bio-Rad Laboratories, Hercules, CA). Separated proteins were then transferred to a nitrocellulose membrane (Bio-Rad), at 4 ºC at 90V for 90 minutes. The membrane was then placed in blocking buffer (Odyssey, LI-COR Biosciences Lincoln, NE) for 1 hour at room temperature. WT and TG-E myofibrils were treated with mouse monoclonal cTnI antibody (clone 19C7, Fitzgerald, Concord, MA) and mouse monoclonal β-actin antibody (Abcam, Cambridge, MA, USA). The entire cellular content (myofibrils plus supernatant) from the WT and TG-E mice were treated with mouse monoclonal cTnI antibody and mouse monoclonal GAPDH (glyceraldehyde 3-phosphate dehydrogenase) antibody (AbD Serotec, Raleigh, NC). Primary antibodies were visualized with IR-Dye 800 donkey anti-mouse secondary antibody (Rockland Immunochemicals, Gilbertsville, PA). All proteins were

visualized using an infrared western blot imaging system (Odyssey). Band intensity was quantified using densitometry using ImageJ software.

4.3.7 Hemotoxylin and Eosin Staining

Left ventricular tissue from wild-type (WT) and transgenic (TG-E) mice was fixed with 2% paraformaldehyde PBS at 4 °C for four hours, and then cryoprotected in 30% sucrose in PBS at 4 °C for at least 24 hours. The samples were submerged in OCT (Optimal Cutting Temperature) compound and frozen in isopentane over liquid N_2, and then sliced into 6 μm sections and placed on glass slides. Samples were then stored at -80 °C until they could be stained.

The samples were stained with 0.1% Mayers Hematoxylin solution (Sigma) and 0.5% alcoholic Eosin Y solution. After each stain, the sample was washed with ethanol. Samples were mounted and coversliped with Cytoseal XYL mounting medium (Fisher). Samples were visualized on a fluorescence microscope (Nikon Instruments Inc, Melville, NY). Analysis of images to determine myocyte size and number was done using MetaMorph software (Molecular Devices Corporation, Downington, PA).

4.4 RESULTS

4.4.1 PCR Results

PCR was run on every TG-E mouse that descended from the original founder mouse. The original plasmid was run on every gel as a positive control. Gels were run in duplicate. If there was any ambiguity, such as an unclear band, the sample was run a third or fourth time until two subsequent gels yielded clear results. Mice were only subjected to experiments if they were confirmed positive by two PCR runs.

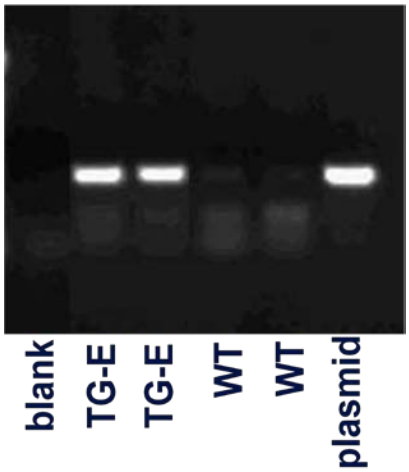

Figure 4-3. Representative PCR Gel

Figure 4-3 shows a representative agarose gel of PCR results. Since the primers only bind to the mutant DNA sequence, the presence of a band indicates the presence of the mutant DNA. The first lane on the left is the negative control, containing only loading buffer and PCR cocktail. The next two lanes were confirmed positive transgenic mice, the next two confirmed negative mice. The right lane is the plasmid for positive control.

4.4.2 DNA Sequencing Results

While the PCR data were intended to confirm the presence of the mutant cTnI DNA in the transgenic mice, it was important to confirm that the sequence of this DNA contained the specific point mutations at positions 43, 45 and 144.

Figure 4-4 and **Figure 4-5** compare the DNA from a transgenic mouse and the plasmid for the α-MHC promoter and cTnI, respectively. There is a high degree of homology (97% for the α-MHC promoter and 99% cTnI) between the plasmid and transgenic mouse sequences, indicating the presence of mutant DNA in the transgenic mice.

```
Sample  TCNTCCATCTGTNNCTACTCTCTCTGCCTTGCCTTCTTGTGTGTTCTCCTTTTCCACGTG
        :  :::::::::  ::::::::::::::::::::::::::::::::::::::::::::
Plasmid TACTCCATCTGTCTCTACTCTCTCTGCCTTGCCTTCTTGTGTGTTCTCCTTTTCCACGTG

Sample  TTTCTCACTCCACTGCCTCCCCCCCCCC-TTCATTTTTATCCTTCCTTTCTTTCTGTGTC
        :::::::::::::::::::::::::::: ::::::::::::::::::::::::::::::
Plasmid TTTCTCACTCCACTGCCTCCCCCCCCCCTTCATTTTTATCCTTCCTTTCTTTCTGTGTC

Sample  ANAATGCTGGGAATCAAACCCAGGGCTTCATACACGTCAAGTAAGCAATCTCCCAGTGAG
        : ::::::::::::::::::::::::::::::::::::::::::::::::::::::::::
Plasmid AGAATGCTGGGAATCAAACCCAGGGCTTCATACACGTCAAGTAAGCAATCTCCCAGTGAG

Sample  CCAAAGCTT
        :::::::::
Plasmid CCAAAGCTT
```

Figure 4-4. α-MHC Plasmid Sequence Versus Sequence from TG-E Mouse

The top sequence is from a PCR-confirmed positive TG-E mouse, and the bottom sequence is from the plasmid used to generate the mouse. There is greater than 97% agreement between the two sequences. If the nucleotide could not be reliably identified, the position was marked with an 'N' in the sample sequence..

More specifically, the TG-E mouse possesses the base pair sequence GAA, indicating glutamates, at sites 43 and 45 (indicated by the underlined sections in **Figure 4-5)**, indicating that the point mutations are expressed in the transgenic mouse's DNA. The third site, 144, was

too far downstream to confirm its presence by sequencing, and so we remain uncertain that it was mutated. However, it is unlikely that only two of the three mutated sites were expressed.

```
Sample  -----------------ATGGCTGATGAAAGCAGCGATGCGGCTGGGGAACCGCAGCCTG
                         ::::::::::::::::::::::::::::::::::::::::::::
Plasmid -----------------ATGGCTGATGAAAGCAGCGATGCGGCTGGGGAACCGCAGCCTG

Sample  CGCCTGCTCCTGTCCGACGCCGCTCCTCTGCCAACTACCGAGCCTATGCCACCGAGCCAC
        ::::::::::::::::::::::::::::::::::::::::::::::::::::::::::::
Plasmid CGCCTGCTCCTGTCCGACGCCGCTCCTCTGCCAACTACCGAGCCTATGCCACCGAGCCAC

Sample  ACNCCAAGAAAAAGTCTAAGATCGAAGCCGAAAGAAAACTTCAGTTGAAGACTCTGATGC
        :: ::::::::::::::::::::::::::::::::::::::::::::::::::::::::::
Plasmid ACGCCAAGAAAAAGTCTAAGATCGAAGCCGAAAGAAAACTTCAGTTGAAGACTCTGATGC

Sample  TGCAGATTGCGAAGCAGGAGA
        ::::::::::::::::::::
Plasmid TGCAGATTGCGAAGCAGGAGA
```

Figure 4-5. cTnI Sequence from Plasmid Versus TG-E mouse

The top sequence is from a PCR-confirmed positive TG-E mouse. It shows greater than 99% agreement with the plasmid sequence below it. The underlined sections (in the third line) represent the cTnI positions 43 and 45, which were mutated from serines to glutamates (GAA). The underlined sections show that the sample did incorporate the base pair changes.

4.4.3 Phosphoprotein Stain

Phosphorylation levels of maximally phosphorylated cTnI (PKA and PKC-treated) were used to calculate the fraction (f_M) of endogenous cTnI that has been replaced with the mutant form. First, the ratio of the intensity of the cTnI phosphoprotein stain to total cTnI protein stain for the WT (R_{WT}) and transgenic (R_{TG}) mice was calculated (**Figure 4-6**).

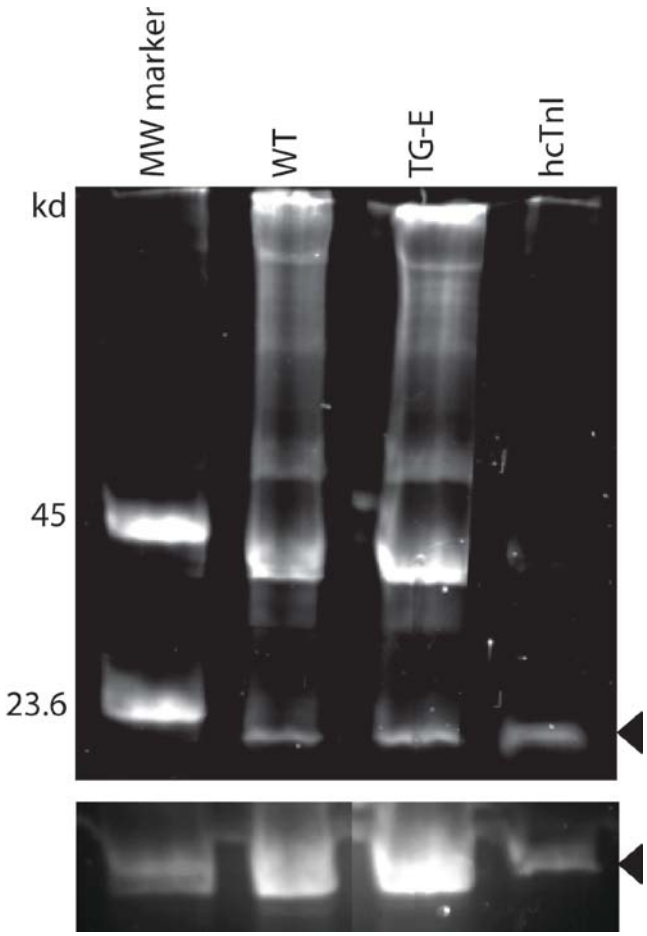

Figure 4-6. Phosphoprotein Assay on PKA and PKC Treated Samples

SDS-PAGE gel stained with Pro-Q Diamond phosphoprotein stain (top panel) and subsequently with SYPRO Ruby total protein stain (bottom panel). The arrow shows the cTnI bands in the WT, TG and hcTnI (human cardiac troponin I) lanes. Image was cropped to remove irrelevant lanes from same gel. WT and TG samples were treated with PKA and PKC. Band intensity of phosphoprotein stain (A.U.): WT = 113, TG-E = 144, and total protein stain: WT = 1047, TG-E = 1666. This yielded R_{WT} = 0.108, R_{TG} = 0.087, and thus a R_{actual_max} = 0.80, suggesting that there is 20% less phosphorylation in the TG-E sample.

The ratio of these two numbers ($R_{\text{actual\_max}} = R_{\text{TG}}/R_{\text{WT}}$) is the relative level of maximal phosphorylation of cTnI in the TG-E mice as a fraction of the maximal phosphorylation level of the cTnI in WT mice. Based on the measured value of $R_{\text{actual\_max}}$ (0.79 ± 0.02, n = 4) and **Equation 4.5**, the replacement of endogenous cTnI with mutant cTnI was 35.6 ± 3.7%.

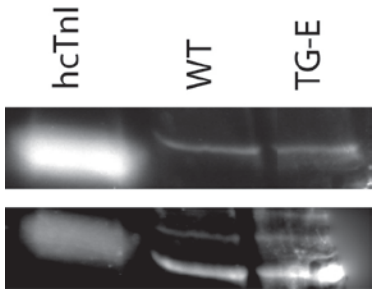

Figure 4-7. Phosphoprotein Assay on Untreated Samples

The procedure was also performed on untreated samples; the top panel is the phosphoprotein stain and the bottom panel is the total protein stain. Band intensity of the phosphoprotein stain (A.U.): WT = 30.5, TG-E = 21.0, and total protein stain: WT = 101, TG-E = 97. This yielded R_{WT} = 0.300, and R_{TG} = 0.216, and thus R_{actual_base} = 0.721, suggesting 27% less phosphorylation in the TG sample.

The phosphoprotein assay was used on a second set of myofibrils not treated with PKA or PKC to quantify the relative level of actual phosphorylation under the baseline condition in the TG-E mouse (**Figure 4-7**). The value of $R_{\text{actual\_base}}$ for the untreated samples was 0.75 ± 0.02 (n = 3). Given that $R_{\text{actual\_base}}$ (0.75 ± 0.02, n = 3) is not statistically different from $R_{\text{actual\_max}}$ (0.79 ± 0.02, n = 4), **Equation 4.7** shows that the basal degree of cTnI phosphorylation for WT and TG-E mice is equal. Thus, **Equation 4.10** can be simplified to yield:

$$R_{total\_base} = \frac{TP_{TG\_base}}{TP_{WT\_base}} = 1 + \frac{3 f_m}{5}\left(\frac{1}{X_{WT}} - 1\right) \tag{4.11}$$

Where TP_{WT_base} and TP_{TG_base} are total (= actual + pseudo) cTnI phosphorylation for WT and TG-E mice, respectively. It can be seen that R_{total_base} is greater than one (since $0 \le X_{WT} \le 1$ and $0 \le f_m \le 1$ by definition). This suggests that the TG-E mice have greater total phosphorylation than the WT mice.

4.4.4 Western Blots

While it has been shown that the physiological stoichiometry of myofilament proteins is maintained in other troponin mutants [76], it is important to examine cTnI expression due to the addition of the transgene in this mouse. A representative gel is shown in **Figure 4-8**.

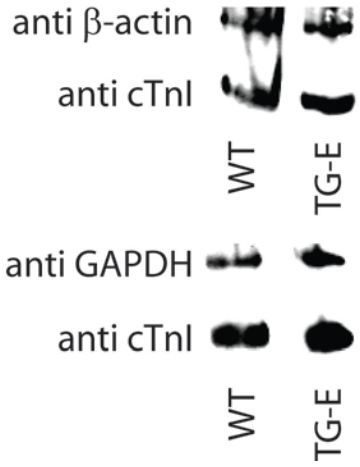

Figure 4-8. Western blot of TG-E versus WT samples

Western blot on myofibrils (top panel) and total cellular lysate (bottom panel), using monoclonal antibodies anti β-actin, anti cTnI (cardiac troponin I) and anti GAPDH (glyceraldehyde 3-phosphate dehydrogenase).

In the TG-E mouse, Western blots revealed that there were no differences in the ratio of the intensity of the cTnI and β-actin bands (WT: 1.54 ± 0.07, TG-E: 1.47 ± 0.19, n = 2, P = 0.65), or the cTnI to GAPDH bands (WT: 1.59 ± 0.17, TG-E: 1.43 ± 0.16, n = 2, P = 0.43), indicating that the mutant cTnI was incorporated into the myofilament in such a way that native stoichiometry was maintained.

4.4.5 Histology

The hematoxylin and eosin stained LV sections from WT (**Figure 4 -9A**) and TG-E samples (**Figure 4-9B**) showed similar cell area as a percent of total image area (WT: 81.5 ± 1.6 %, n = 2 animals, TG-E: 78.4 ± 0.4 %, n = 2 animals, *P* = NS) and a similar number of nuclei (WT: 111 ± 11, n = 2, TG-E: 111 ± 8, n = 2 animals, *P* = NS) in a 100 x 100 pixel segment of the image.

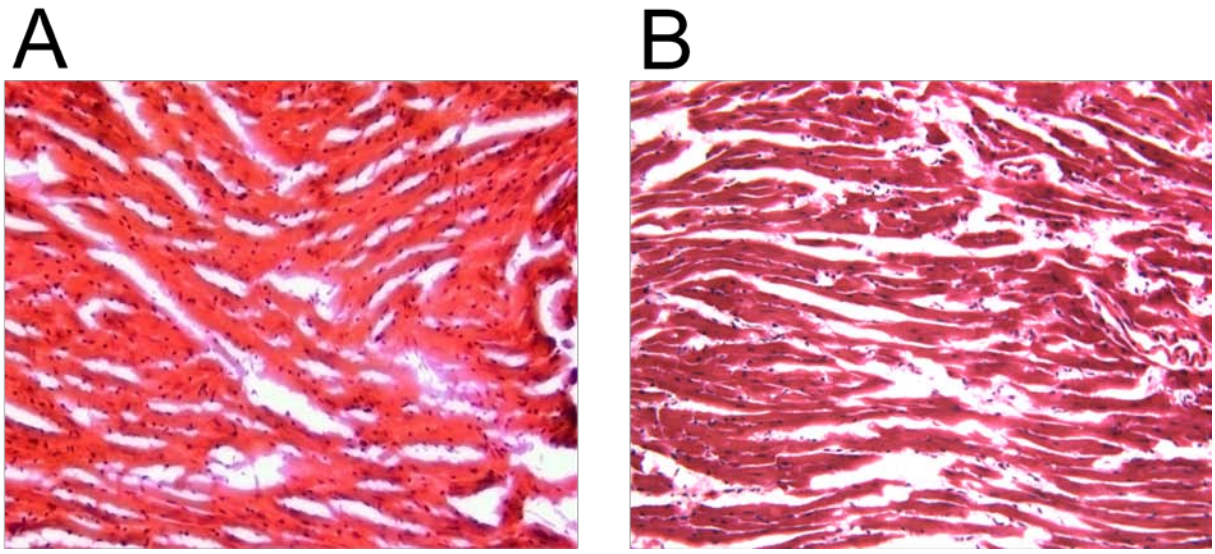

Figure 4-9. H&E Stained Sections from WT and TG-E mice

Hematoxylin and eosin stained sections from WT (panel A) and TG-E (panel B) mice. Magnification: 20X. Numerical analysis of cell area and number of nuclei showed no statistical differences.

These numerical data suggest that there are no histological abnormalities in the TG-E mice. Furthermore, the images show no obvious differences in cell shape or orientation.

4.5 2D-DIGE

The 2D-DIGE (Difference In Gel Electrophoresis) was done in collaboration with Dr. R. John Solaro, Chad Warren and the University of Illinois at Chicago Proteomics Core.

4.5.1 Methods

Two sets of samples were sent to University of Illinois at Chicago for analysis. The first set were WT myofibrils treated with PKA and PKC as described in **Section 4.2.4**. The second set were WT and TG-E liquid nitrogen frozen mouse tissue.

For the PKA and PKC treated myofibrils, samples were randomly labeled with fluorescent cyanine dyes (Cy2, Cy3, and Cy5) from GE Healthcare (Piscataway, NJ) to control for any dye differences. Protein samples were labeled by adding 100 pmoles of CyDye to 50 µg of protein and then quenched with 10 mM L-lysine [77]. The gel's first dimension was focused using the Protean IEF cell (BioRad, Hercules, CA) with pH 4-7 or 7-11 IPG strips. The samples were actively rehydrated at 50 V in 18 cm IPG strips pH 4-7, or 7-11NL 10-16 hrs with 80-120 µg of total protein (40 µg/channel). The focusing in the first dimension was achieved using a preset linear program: 250 V rapid ramping for 15 min, 10,000 V linear ramping for 3 hours, 10,000 V rapid ramping until 60,000 V•hours [78]. The strips were equilibrated and laid onto 12% SDS-PAGE gels [77, 79]. Gels were imaged with a Typhoon 9410 scanned at 100 µm and analyzed with PDQuest software (v7.1, BioRad, Hercules, CA).

In the case of the frozen mouse tissue samples, the liquid nitrogen frozen mouse tissue was homogenized twice in standard relax buffer (10 mmol/L Imidazole pH 7.2, 75 mmol/L KCL, 2 mmol/L $MgCl_2$, 2 mmol/L EDTA, and 1 mmol/L NaN_3) with 1% (v/v) Triton X-100 [75]. For

the untreated samples, the pellet was solubilized in UTC buffer (8 mol/L urea, 2 mol/L thiourea, and 4% (w/v) CHAPS). The phosphatase treated samples were washed twice in phosphatase buffer (25 mmol/L Tris-HCl pH7.0, 0.2 mmol/L $MnCl_2$, 0.1 mmol/L EDTA, 5 mmol/L DTT and mammalian protease inhibitors from Sigma 1:100) then resuspended in 50 μL phosphatase buffer plus PP1A (10 units) and $PP2A_1$ (0.1 unit) (Calbiochem). The samples were then allowed to incubate for 4 hrs at 37°C to completely de-phosphorylate the cTnI. After the incubation period, myofibrils were spun down and the supernatant was removed. The pellet was resuspended in UTC buffer. Protein (in UTC buffer) concentration was determined with an RC-DC assay kit (BioRad, Hercules, CA). Samples in UTC buffer (100 μg) were cleaned up with GE Healthcare's 2D clean-up kit (Piscataway, NJ) and then re-suspended in UTC buffer.

These samples were then labeled and run on 2D gels as described for the first set of samples; gels were then transferred on polyvinylidene fluoride (PVDF) membrane and analyzed as previously described [80]. The primary antibody used for cTnI was a pan monoclonal C5 1:5000 (Fitzgerald) and the secondary antibody was an anti-mouse-IgG (FAB) specific 1:100000 (Sigma).

4.5.2 Results

Two sets of samples were subjected to 2D-DIGE. The first samples were those run on the phosphoprotein stain, in order to determine the accuracy of our assumption that cTnI had been fully phosphorylated by the PKA and PKC treatment. The PKA and PKC treated samples (n=3) were never fully phosphorylated, and never reduced the unphosphorylated species to zero. A representative 2D-DIGE gel is shown in **Figure 4-10**. One of the key assumptions in the analysis of the phosphoprotein data is proven incorrect, and another analysis was needed.

Significantly increasing the dose of PKA and PKC treatment was unrealistic due to cost issues. One possible method was to treat the heart tissue with PKA and PKC activators before creating the myofibrils. However, given the success with 2D-DIGE, we decided to perform our analysis using this technique.

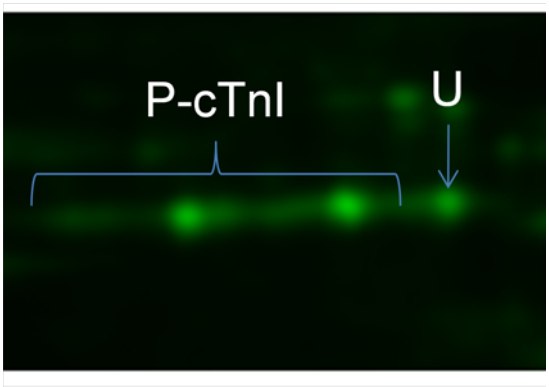

Figure 4-10. 2D-DIGE of PKA and PKC WT Myofibrils

Representative 2D-DIGE gel of myofibrils treated with PKA and PKC. P-cTnI: phosphorylated forms of cTnI, U: unphosphorylated form of cTnI.

Proteins from WT and TG-E myofibrils were separated using 2D-DIGE (**Figure 4-11A**). The 2D-DIGE gels were capable of separating the individual phospho-species of cTnI (U: unphosphorylated cTnI, P1: phosphorylated at one site, P2: two, P3: three, P4: four, P5: five sites). In TG-E samples, there was an additional spot near P3, indicated by an asterisk in **Figure 4-11A**, which was not present in the WT samples. We postulated that this spot represented mutant cTnI, given the mutant cTnI is pseudo-phosphorylated at three sites.

To confirm that this spot was constitutively pseudo-phosphorylated mutant cTnI, we treated WT and TG-E myofibrils with PP1A and $PP2A_1$ to de-phosphorylate cTnI (**Figure 4-11B**). The WT cTnI spot profile was reduced to only the U (unphosphorylated) spot, indicating complete dephosphorylation. In the phosphatase-treated TG-E samples, there were two spots: U

and mutant cTnI (indicated by an asterisk in **Figure 4-11B**). The ratio of the intensity of the mutant cTnI spot to the total intensity (i.e., sum of unphosphorylated (U) and mutant spots) represents the percent replacement, which was 7.2 ± 0.5% (n = 9, $P < 0.001$ versus no change, **Table 1**).

To verify the protein identity of the spots, membrane transfers of the 2D-DIGE gels were probed with a specific pan cTnI antibody. **Figure 4-11C** illustrates multiple spots in the untreated samples whereas only one spot is visible in the phosphatase-treated sample, a pattern similar to that in the 2D-DIGE gels (**Figures 4-11A** and **Figure 4-11B**, second panels). All six spots are not seen in this example due to low abundance of P4 and P5. The mutant cTnI spot was also confirmed by Western analysis (data not shown).

There were no differences in the relative spot intensities (U, P1-P5) of cTnI in the WT and TG-E samples, except the presence of the mutant cTnI spot (**Figure 4-11A** and **Table 1**). This indicates that the basal *actual* phosphorylation of cTnI was unchanged in the transgenic mouse. Moreover, there were no differences in the phosphorylation levels of cardiac troponin T (cTnT), tropomyosin (Tm), myosin regulatory light chain (RLC), or myosin binding protein C (MyBP-C) (**Figure 4-11D** and **Table 1**; n: WT = 4, TG-E = 4) .

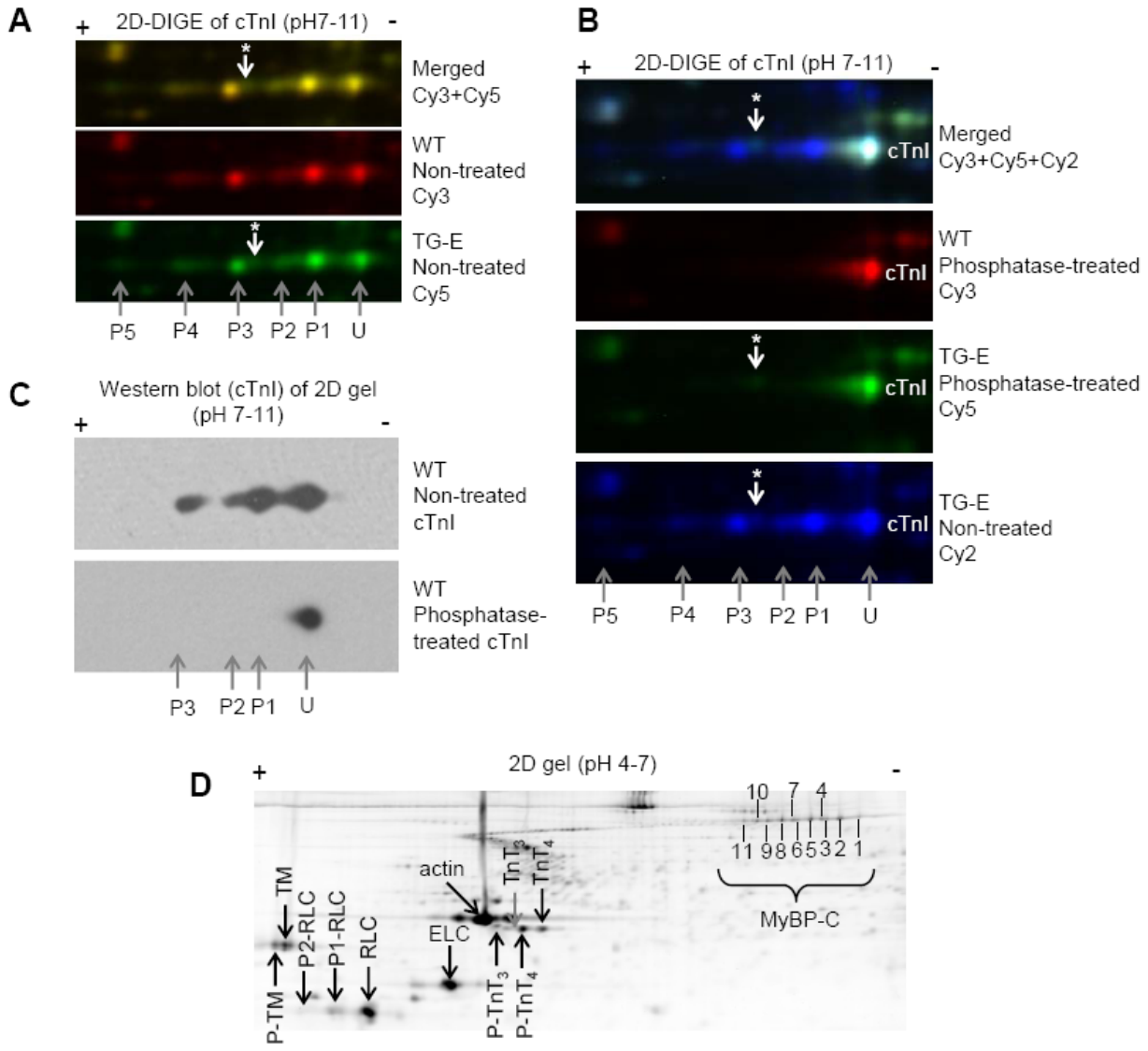

Figure 4-11. 2D-DIGE Data from WT and TG-E Samples

Analysis of cardiac troponin I (cTnI) by 2D-DIGE. *, mutant cTnI; P*x*, phosphorylated spot (where x = number of sites phosphorylated); U, un-phosphorylated spot. pH values indicate the strip that was used for the first dimension. Samples were labeled separately with different CyDyes and mixed to run in the same 2D gel. (A) Representative image of untreated WT and TG-E samples run on a 2D-DIGE gel that was utilized to determine phosphorylation levels of cTnI. Notice the mutant cTnI near the P3 spot. (B) Phosphatase treated (PP1A and $PP2A_1$) WT and TG-E samples and a non-treated TG-E sample. Percent replacement was 7.2 ± 0.5% expressed as mean ± S.E.M. (n=9). (C) Western blot analysis to verify cTnI spots and the complete de-phosphorylation of cTnI by PP1A and $PP2A_1$. Note: P4 and P5 are not shown due to low abundance, however with longer exposure time we positively identified these spots, but the others were saturated. (D) Representative 2D-DIGE gel (only one channel shown) utilized to determine phosphorylation levels of the sarcomeric proteins (n = 4). TM, tropomyosin; RLC, regulatory light chain; TnT_{3or4}, troponin T isoform 3 or 4; MyBP-C 1-11, myosin binding protein C spots labeled arbitrarily; and ELC, essential light chain.

Table 1. Quantification of Percent Replacement and Protein Phosphorylation

	WT	TG-E
REPLACEMENT	N/A	7.2 ±0.5%
TM-P	46.3±7.0%	36.5±4.7
RLC-P	19.5±1.2%	21.3±1.4%
cTnT-P	56.9±0.9%	56.3±0.6%
cTnI-P1	27.6±1.3%	27.3±1.6%
cTnI-P2	12.5±1.0%	13.2±0.9%
cTnI-P3	20.0±1.6%	19.2±1.4%
cTnI-P4	9.9±0.8%	10.1±0.5%
cTnI-P5	3.9±1.3%	4.1±0.5%
S1-MyBP-C/TOTAL	6.7±0.8%	6.2±0.4%
S2-MyBP-C/TOTAL	8.3±0.7%	7.3±0.9%
S3-MyBP-C/TOTAL	11.7±1.6%	11.5±1.3%
S4-MyBP-C/TOTAL	13.3±0.4%	12.8±0.7%
S5-MyBP-C/TOTAL	9.6±2.3%	11.8±1.7%
S6-MyBP-C/TOTAL	6.2±1.8%	4.7±1.6%
S7-MyBP-C/TOTAL	14.3±0.9%	13.9±0.6%
S8-MyBP-C/TOTAL	6.6±1.2%	6.1±1.1%
S9-MyBP-C/TOTAL	7.0±1.4%	8.4±0.8%
S10-MyBP-C/TOTAL	10.3±1.3%	11.0±1.5%
S11-MyBP-C/TOTAL	5.9±1.1%	6.4±0.7%

Values are expressed as mean ± S.E.M.. TM-P: phosphorylated tropomyosin, RLC-P: phosphorylated myosin regulatory light chain, cTnT-P: phosphorylated troponin T, cTnI-P – cTnI-P5: phosphorylated cTnI (at 1 – 5 sites), S1-S11-MyBP-C: myosin binding protein-C. Quantification of percent phosphorylation of the total indicated by P (n=4). The percent replacement of the mutant troponin I is labeled as replacement (n=9). The percent of myosin binding protein C spot of the total myosin binding protein C spots labeled as S1 through S11 n=4. Note: There were no significant differences between WT and TG-E.

4.6 SUMMARY

It was confirmed that the TG-E mice successfully incorporated the mutant DNA.

The analysis of the phosphoprotein stain was not a reliable assay for determining percent replacement of endogenous cTnI in the TG-E mouse. With the assistance of the University of Illinois at Chicago Proteomics core, we were able to determine the percent replacement using 2D-DIGE. The TG-E mice had 7.2 ± 0.5% replacement of endogenous cTnI with the mutant form.

Moreover, there were no differences in overall cTnI expression, phosphorylation of other myofilamental proteins, or histology. Overall, the mutant mouse was confirmed as a useful research tool, although the low expression of mutant cTnI may be of concern.

5.0 WHOLE ORGAN STUDIES

5.1 INTRODUCTION

Hypothesis 1: Increased cTnI phosphorylation at the PKC sites will result in systolic dysfunction and protection from ischemic contracture at the whole organ level.

Specific Aim 1a: Determine differences in *in vivo* cardiac function (echocardiography) in WT (baseline) and TG-E (increased cTnI phosphorylation at the PKC sites) mice

Specific Aim 1b: Determine differences in *ex vivo* whole heart function (Langendorf) in WT (baseline) and TG-E (increased cTnI phosphorylation at the PKC sites) mice

Non-invasive procedures allow the collection of data while minimizing the impact on the system. Imaging, such as echocardiography, can be used to determine function in the intact *in vivo* system, without possible artifacts from an artificial experimental condition. However, a minimally invasive procedure such as this does not isolate a single system, which can make it difficult to determine the nature of the observed functional effects.

The perfused isolated heart preparation was performed by Oscar Langendorf in 1897 (who lends his name to the procedure), and is still useful today [81]. Langendorf preparation

experiments have been done in the TG-A mouse [57, 60]. Those results will be discussed and compared to the results from the TG-E mouse.

5.2 METHODS

5.2.1 Echocardiography

The mice were anesthetized with isoflurane (1.5% isoflurane induction and maintenance with 100% oxygen) via nose cone. The depth of anesthesia was monitored by toe reflex (extension of limbs, supine positioning). Isoflurane was selected because it is a quickly reversible anesthetic; once administration is completed, the animal recovers quickly.

Once the plane of anesthesia was established, the animal was placed in a supine position on a warmed pad. The hair on the chest was removed using Nair® Lotion (Church & Dwight Co., Inc., Princeton, NJ) and prepared for echocardiographic examination. Echocardiography was used to take measurements of left ventricular dimensions (M-mode), pulmonary artery flow right above the pulmonary valve, and aortic flow just above the aortic valve (via Doppler imaging). Data were collected via a 13 MHz linear array probe (model 15L8, Acuson, Mountain View CA). Hemodynamic measurements were performed once on mice ranging from 4-6 months of age.

Upon completion of the echocardiographic examination, the chest was cleaned and wiped dry, and the animal was maintained on the warming pad until it had recovered. Then the animal was returned to its box and checked after ten minutes to confirm they were unaffected by the procedure.

5.2.2 Echocardiography: Data Analysis

The echocardiographic data were analyzed using Access Point (version 2.0, Freeland, LLC., Boulder, CO). Data were collected for three subsequent beats, and then averaged to obtain a single value per animal.

Measured variables from the M-mode 1-D data included: septal wall end-systolic thickness (SWESt), left ventricular end-systolic diameter (LVESd), posterior wall end-systolic thickness (PWESt), septal wall end-diastolic thickness (SWEDt), ventricular end-diastolic diameter (LVEDd), and posterior wall end-diastolic thickness (PWEDt). Fractional shortening (FS) was calculated from the measured M-mode data by **Equation 5.1**.

$$\mathrm{FS}(\%) = \left(\frac{\mathrm{LVEDd\text{-}LVESd}}{\mathrm{LVEDd}}\right) \times 100 \tag{5.1}$$

Measured variables from Doppler data included: cycle length (CL), systolic time, and time to peak. Peak to diastolic time was calculated on a beat to beat basis as systolic time minus time to peak.

Reading echocardiographic images is subjective, especially in mice where the structures of interest are quite small. In order to correct for subjectivity when reading the images, a second person (trained in reading echocardiography images) also analyzed a subset of the data (4 total, picked randomly: 2 WT and 2 TG-E), and was blinded to genotype. The error between the two readings, the intra-observer error [82], was calculated as the percent difference between the original reading and the second reading, as shown in **Table 2**.

There was very high intra-observer error in the septal wall thickness measurements during systole (74%) and diastole (60%), as well as posterior wall thickness during systole (19%) and diastole (22%). These measurements were only an order of magnitude greater than the

resolution of the images, and so it is of little surprise that the error was large. These measurements were removed from further analysis. The other measurements had low intra-observer errors (LVESd, LVEDd, cycle length, systolic time and diastolic time), and statistical analysis was performed on these.

Table 2. Echocardiographic Intra-Observer Error

	Error (n = 4)
M-Mode	
Systole	
Septal Wall Thickness (%)	74 ± 64
Ventricular Diameter (%)	5 ± 4
Posterior Wall Thickness (%)	19 ± 14
Diastole	
Septal Wall Thickness (%)	60 ± 70
Ventricular Diameter (%)	3 ± 2
Posterior Wall Thickness (%)	22 ± 10
Pulmonary Flow	
Cycle Length (%)	2 ± 1
Systolic Time (%)	6 ± 4
Time to Peak (%)	10 ± 5

	Error (n = 4)
M-Mode	
LVESd (%)	5 ± 4
LVEDd (%)	3 ± 2
Pulmonary Flow	
Cycle Length (%)	2 ± 1
Systolic Time (%)	6 ± 4
Time to Peak (%)	10 ± 5

Values are mean ± S.E.M.. Top table shows intra-observer errors for all measured parameters. Bottom table shows error for parameters that had error ≤ 10%, which were included for statistical analysis.

The top section in **Table 2** shows the error in all measured parameters, while the bottom section indicates the error in the measured parameters that had acceptable levels of intra-observer error.

5.2.3 Isolated Heart

Isolated heart preparations were similar to those we have done in the past [83]. Male WT FVB and TG-E mice of similar age (121 – 140 days) were used. The mice were anesthetized with an intraperitoneal injection of Avertin (2,2,2-tribromoethanol, 250 mg/kg body weight). Animals were then anticoagulated using 100 units of heparin. Once the heart was excised from the animal, the aorta was quickly cannulated, and the atria were removed. The heart was perfused in retrograde fashion at a constant pressure of 70-80 mmHg. Tissue culture medium (Media 199, Invitrogen, Carlsbad, CA) was used as the perfusate (1.8 mmol/L [Ca]). To this solution the following were added: creatine (5.0 mmol/L), taurine (4.8 mmol/L), carnitine (6.0 mmol/L), sodium pyruvate (2.5 mmol/L), insulin (8 µmol/L), and metoprolol (5.0 µmol/L, to eliminate pacing-induced catecholamine release). The solution was oxygenated with 95% O_2 and 5% CO_2, pH adjusted to 7.4, and temperature maintained at 37 ^{o}C. A balloon made from high density polyethylene (HDPE) was placed in the left ventricle through the mitral valve and secured with a suture though the left ventricular apex. A catheter-tip pressure transducer (MPC-500, Millar Instruments, Houston, TX) was used to measure left ventricular pressure. The balloon volume was altered using a thumb-screw controlled 100 µL micro-syringe (Hamilton Gas Tight, Reno, NV). Platinum pacing electrodes were placed on the heart, which was then paced at 4 Hz using a stimulator (Harvard Apparatus, Holliston, MA). Pressure data were digitized on-line at 500 Hz for later offline analysis.

When the experiment was complete, the heart was removed from the apparatus. The left and right ventricles were separated, blotted dry, and then weighed (see **Section 1.7** for results).

5.2.4 Isolated Heart: Protocols

A Frank Starling protocol was performed on all of the isolated hearts. A reference LV volume (V_{ref}, typically 10–12 µl) was set by adjusting the balloon volume to yield a LV end diastolic pressure of 5 mmHg. Pressure data were continuously recorded over a 2 minute period. The first 20 seconds corresponded to data at the reference volume, followed by a period wherein LV volume was increased in 2 µl increments to the point when developed pressure had reached its maximum value (V_{max}, **Figure 5-1**). The Frank Starling protocol alone was performed on one subset of experiments (WT: n = 6, transgenic, TG-E: n = 6).

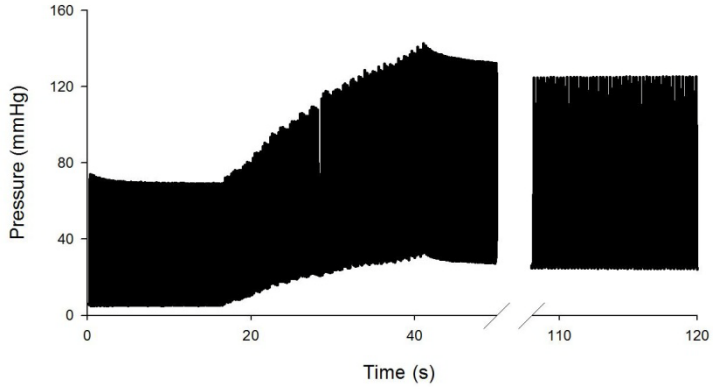

Figure 5-1. Frank Starling Protocol

Typical 2-minute recording of left ventricular (LV) pressure before, during, and after increase in LV volume. LV pressure increased with increments in LV volume. There was no change in pressure when LV volume was held constant at the highest value for 80 s. Used from [83] with permission.

In a second subset of the experiments (WT: n = 11, TG-E: n = 9), the Frank Starling protocol was performed, and then hearts were perfused as described above for a baseline period

of five minutes, after which retrograde aortic perfusion was halted for fifteen minutes, inducing global no-flow ischemia. Flow was then restored for twenty minutes which was called the reperfusion period. Pressure data were digitized at 100 Hz for the forty minute baseline-ischemia-reperfusion period.

In a third subset of the experiments (WT: n = 6, TG-E: n = 6), the Frank Starling protocol was performed, and then isolated hearts were treated with 1 μmol/L isoproterenol for ten minutes. A second Frank-Starling protocol was conducted on the heart post isoproterenol treatment.

5.2.5 Isolated Heart: Data analysis

In isolated heart experiments, individual cardiac cycles were first identified by using the spike in the pacer signal. Signal averaging over the cardiac cycle was then performed to reduce high-frequency random noise. Pressure data from five to seven steady state contractions at a given LV volume were averaged to yield a representative cycle. LV pressure waveforms were characterized by several amplitude and rate indices. Amplitude indices included end diastolic pressure (P_{ed}), peak systolic pressure (P_{sys}), and developed pressure ($P_{dev} = P_{sys} - P_{dia}$). Rate indices included maximal rate of rise (dP/dt_{max}), maximal rate of fall (dP/dt_{min}), rise time (T_{rise}), and relaxation time (T_{relax}). T_{relax} was defined as the time taken for developed pressure to decay from 75% to 25% of its maximum value. Similarly, T_{rise} was defined as the time taken for pressure to rise from 25% to 75% of its maximum value. Calculations of T_{relax} and T_{rise} were performed after the diastolic value of the pressure waveform was subtracted, such that each waveform rose from and declined to zero.

Wall stress (σ) was estimated using a thick-walled spherical model from **Equation 5.2** [84],

$$\sigma = \frac{P}{\left(1+\frac{M}{\rho V}\right)^{\frac{2}{3}}-1} \tag{5.2}$$

where P is pressure, M is the mass of the left ventricle, ρ is the density of muscle, which was assumed to be 1.05 g/ml, and V is the volume of the ventricle. **Equation 5.2** was used to calculate σ_{dev}, σ_{ed}, $d\sigma/dt_{max}$, and $d\sigma/dt_{min}$ by using P_{dev}, P_{ed}, dP/dt_{max} and dP/dt_{min} in place of P, respectively.

5.2.6 Isolated Heart: Statistical Analysis

For the isolated heart data, regression analysis with dummy variables was used to identify differences in various relationships between wild-type and transgenic groups: σ_{dev}–volume, $d\sigma/dt_{max}$–volume, T_{relax}–volume, $d\sigma/dt_{min}$–volume. Data were fit to the following linear regression model:

$$\boldsymbol{Y = b_0 + b_1 X + b_{0x} D + b_{1x} XD} \tag{5.3}$$

where Y is the response variable (σ_{dev}, $d\sigma/dt_{max}$, etc.), X is the predictor variable (volume), and D is the dummy variable, which differentiates between the control (WT: D = 0) and the treatment (TG-E: D = 1) groups, b_0 is the intercept and b_1 is the slope. If the values of b_{0X} and b_{1X} are statistically different from zero, the mutation had an effect on either the intercept (b_{0X}) or slope (b_{1X}) of the relationship [85].

5.3 RESULTS

5.3.1 Echocardiography

Sample images from the echocardiography studies are shown in **Figure 5-2.** The TG-E mice exhibited a decrease in fractional shortening (FS, WT: 50.7 ± 5.3, n=10, TG-E: 46.0 ± 5.6, n=10, see **Table 3**), but it was not statistically significant (P = 0.07). This decrease was not the result of diastolic dysfunction, as there were no differences in left ventricular end-diastolic diameter. The TG-E mice did show decreased contractility, however, evidenced by a greater left ventricular end-systolic diameter (WT: 1.66 ± 0.19, TG-E: 1.85 ± 0.25), which, like FS, was on the verge of statistical significance (P = 0.06). While the P-values for the differences in LVESd and EF are non-significant, their proximity to the threshold of significance is close.

The lack of differences in LVEDd also indicates that the mutation in TG-E did not lead to any detectable enlargement of the left ventricle, suggesting no cardiac hypertrophy. However, we cannot be certain since we were unable to accurately measure wall thickness.

The TG-E mice showed significantly increased cycle length and decreased heart rate (WT: 461 ± 31 bpm, TG-E; 426 ± 29 bpm, P = 0.02, **Table 3**). The increased cycle time came with an increased systolic time (WT: 65 ± 3 ms, TG-E: 68 ± 3 ms, P = 0.04). These changes were not due to the time to peak, or rise time, since that was actually shorter in the S43E/S45E/T144 mice. However, the peak to diastolic, relax time was longer in the TG-E mice (WT: 46 ± 3 ms, TG-E: 52 ± 4 ms, P = 0.001, **Table 3**).

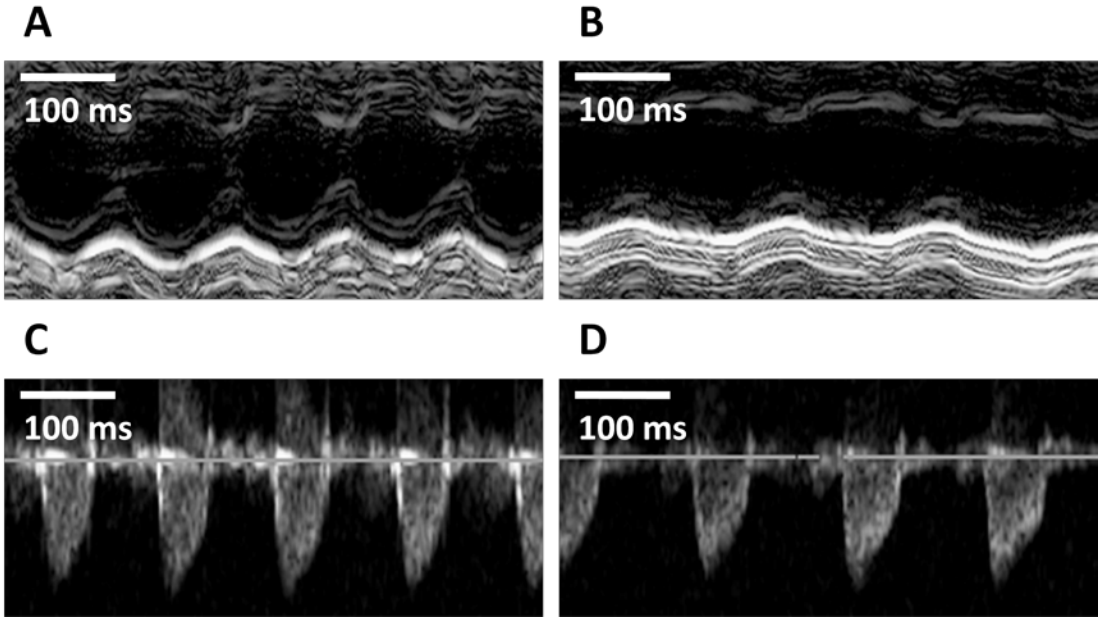

Figure 5-2. Echocardiographic Images from WT and TG-E mice

Representative images from WT (Panels A and C), and TG-E (Panels B and D) mice. Images are from 1-D M-mode of the left ventricle (Panels A and B) and Doppler of pulmonary arterial flow just outside the pulmonary valve (Panels C and D). The white horizontal bar represents 100 ms.

Table 3. Echocardiographic Indices from WT and TG-E Mice

	WT (n = 10)	TG-E (n = 10)	*P*-value
M-Mode			
LVESd (mm)	1.66 ± 0.19	1.85 ± 0.25	0.06
LVEDd (mm)	3.37 ± 0.22	3.42 ± 0.22	0.56
FS (%)	50.7 ± 5.3	46.0 ± 5.6	0.07
Pulmonary Flow			
Cycle Length (ms)	131 ± 9	141 ± 9	0.02
HR (bpm)	461 ± 31	426 ± 29	0.02
Systolic Time (ms)	65 ± 3	68 ± 3	0.04
Time to Peak (ms)	19 ± 2	16 ± 2	0.02
Peak to Diastolic (ms)	46 ± 3	52 ± 4	0.001

Data are mean ± S.E.M.. LVESd: left ventricular end-systolic diameter, LVEDd: left ventricular end-diastolic diameter, FS: fractional shortening, HR: heart rate.

5.3.2 Isolated Heart

5.3.2.1 Frank Starling Protocol

Pressure waveforms are shown for the Frank Starling protocol from a representative individual WT (**Figure 5-3A**) and TG-E (**Figure 5-3B**) animal. P_{dev} and P_{ed} were compiled for all animals (**Figure 5-4**).

The TG-E mice showed no differences passive or diastolic properties compared to WT mice. There were no statistical differences in P_{ed} (**Figure 5-4**, triangles) or σ_{ed} (data not shown) over the entire range of volumes studied.

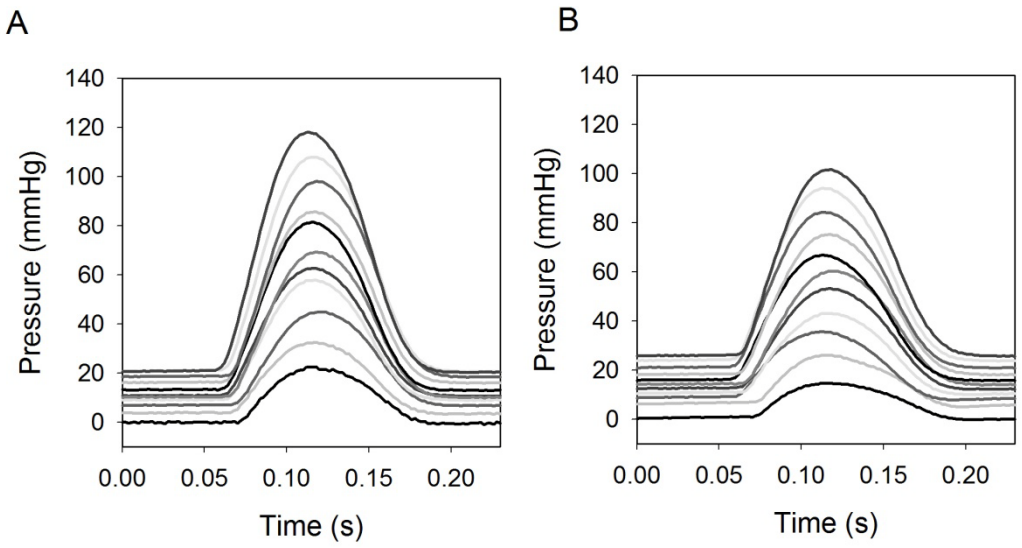

Figure 5-3. WT and TG-E Frank Starling Raw Data

Left ventricular (LV) pressure recordings for WT (A) and TG-E (B) mice as volume is increased from 12μL to V_{max}.

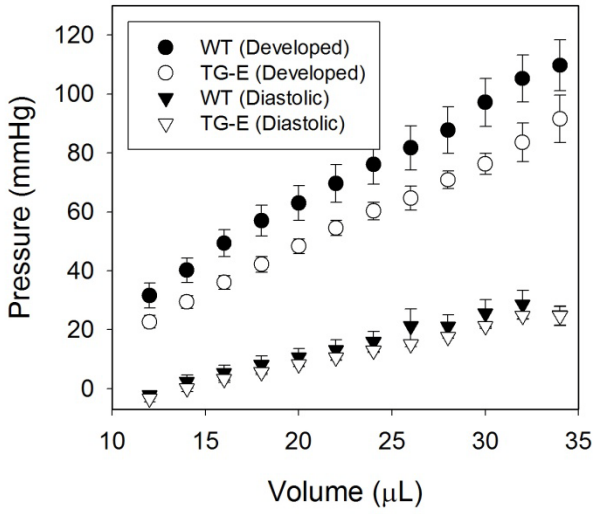

Figure 5-4. Compiled Developed and Diastolic Indices

Developed (circles) and diastolic (triangles) pressures for WT (closed) and TG-E (open) mice. Values are means ± S.E.M..

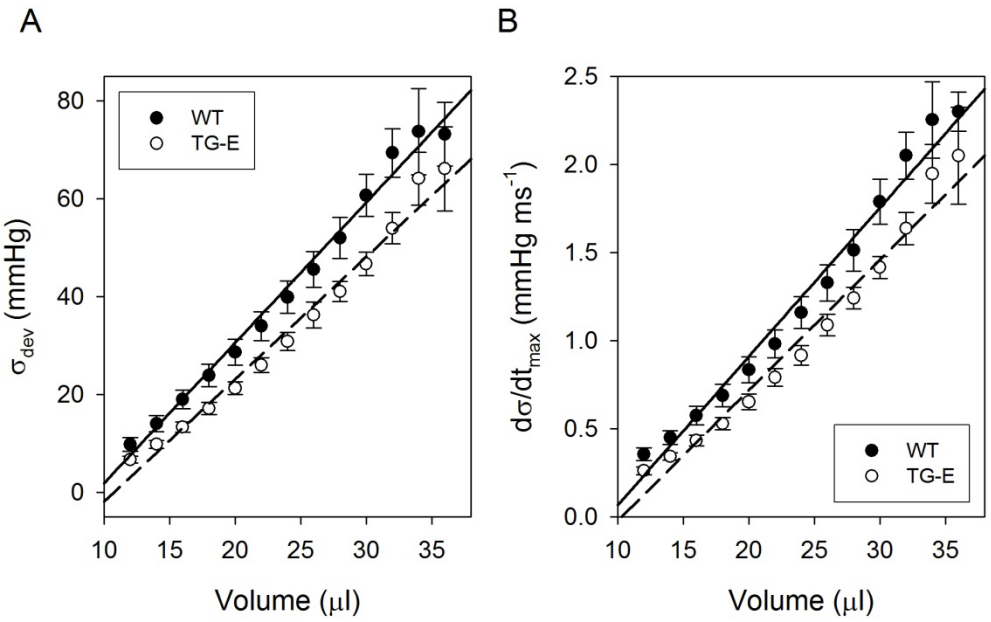

Figure 5-5. Stress-Volume Relationships for WT and TG-E Mice

Effects of altered LV volume on σ_{dev} (developed stress) (A), $d\sigma/dt_{max}$ (maximum time-derivative of stress) (B) in WT (closed) and TG-E (open) mice. The data were fitted to a linear trendline (WT: solid line, TG-E: dashed line). The slopes of the σ_{dev} – volume, and $d\sigma/dt_{max}$ – volume relationships for the TG-E mice were significantly lower (P<0.05) than in the WT data.

The TG-E mice exhibited reduced systolic function. The slope of the σ_{dev} – volume relationship was reduced in TG-E mice (WT: 2.9 ± 0.1 mmHg•µl^{-1}, n = 6, TG-E: 2.5 ± 0.1 mmHg•µl^{-1}, n = 6, P = 0.02), with no change in the intercept, indicating a 13% reduction in LV contractile state over all lengths (**Figure 5-5A**). Additionally, there was a decrease in the slope of the $d\sigma/dt_{max}$ – volume relationship (WT: 0.084 ± 0.004 mmHg•ms^{-1}•µl^{-1}, n = 6, TG-E: 0.074 ± 0.003 mmHg•ms^{-1}•µl^{-1}, n = 6, P = 0.03), with no change in the intercept, indicating a 12% decrease in the kinetic aspects of contraction (**Figure 5-5B**).

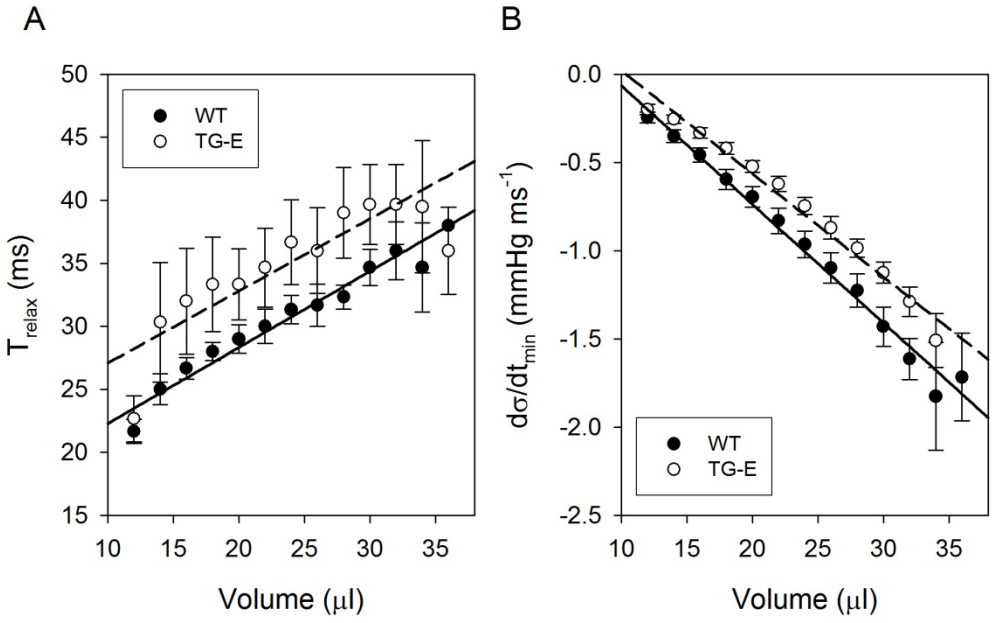

Figure 5-6. Relaxation Indices for WT and TG-E Mice

Effects of altered LV volume on T_{relax} (relaxation time from 75% to 25% peak developed pressure) (A), and $d\sigma/dt_{min}$ (minimum time-derivative of stress) (B) in WT (closed) and TG-E (open) mice. The data were fitted to a linear trendline (WT: solid line, TG-E: dashed line). The intercept of the T_{relax} – volume relationship for the TG-E mice was significantly greater (P<0.05) than for the WT data. The magnitude of the slope of the $d\sigma/dt_{min}$ – volume relationship for the TG-E mice was significantly lower (P<0.05) than for the WT data.

The TG-E mice exhibited slowed relaxation as evidenced by a parallel, upward shift of the T_{relax} – volume relationship (intercept values: WT: 24 ± 1 ms, n = 6, TG-E: 30 ± 2 ms, n = 6,

P = 0.005), with no change in the slope, indicating a 20% increase in the time for the LV to relax (**Figure 5-6A**). Moreover, there was a decrease in the magnitude of the slope of the $d\sigma/dt_{min}$ – volume relationship (WT: -0.067 ± 0.003 $mmHg \bullet ms^{-1} \bullet \mu l^{-1}$, n = 6, TG-E: -0.056 ± 0.003 $mmHg \bullet s^{-1} \bullet \mu l^{-1}$, n = 6, P = 0.03), with no change in the intercept, indicating a 16% reduction in the kinetic aspects of relaxation (**Figure 5-6B**).

5.3.2.2 Ischemia-Reperfusion Protocol

TG-E mice showed no differences in systolic (**Figure 5-7A**) or diastolic (**Figure 5-7B**) pressure with respect to WT mice during the entire time course of the ischemia-reperfusion experiments. Of particular interest are the similar increases in diastolic pressure immediately following reperfusion (**Figure 5-7B**, 2^{nd} vertical line), as this represents the degree of diastolic contracture (fold increase in diastolic pressure from baseline to reperfusion, WT: 4.6 ± 0.8, n = 9, TG-E: 3.9 ± 0.5, n = 11, P = 0.32).

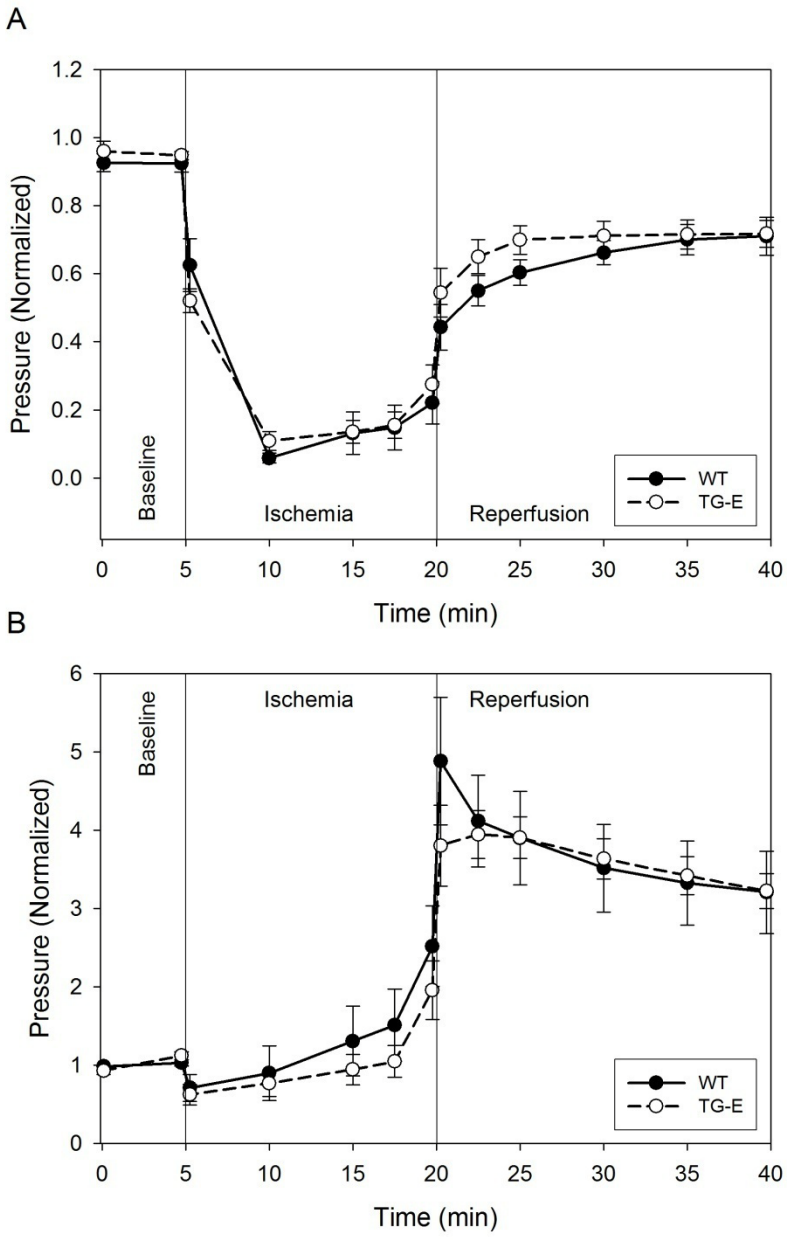

Figure 5-7. Data from Ischemia-Reperfusion Experiments

LV pressure from WT and TG-E mice during ischemia and reperfusion. At five minutes (first vertical line), coronary flow is reduced to zero and ischemia begins. At twenty minutes (second vertical line), flow is restored and reperfusion begins. Protocol lasts 40 minutes total. (A) Systolic pressures have been normalized to baseline values prior to ischemia. There were no statistical differences between WT (black) and TG-E (white) pressures. (B) Diastolic pressures have been normalized to baseline values prior to ischemia. The TG-E (white) mice showed no significant protection from diastolic contracture compared to WT (black). Data are mean ± S.E.M..

5.3.2.3 Isoproterenol Protocol

Treatment with 1 µM isoproterenol increased developed pressures to the same degree in both WT and TG-E mice (**Table 4**). The developed pressures after isoproterenol treatment, while not significantly different (P = 0.053), trended towards higher pressures in the WT (P_{dev} = 78 ± 6 mmHg) than in TG-E (P_{dev} = 62 ± 4 mmHg). Isoproterenol also shortened rise and relaxation times to the same degree in WT and TG-E animals (see **Table 4**).

Table 4. Effects of Isoproterenol Treatment

	WT (n = 7)	TG-E (n = 7)
ΔP_{dev} (mmHg)	28 ± 2	29 ± 3
$\Delta(dP/dt_{max})$ (mmHg•ms^{-1})	3.37 ± 0.35	3.20 ± 0.21
ΔT_{rise} (ms)	-14 ± 1	-14 ± 1
ΔT_{relax} (ms)	-68 ± 13	-56 ± 12

Data represent index value post-isoproterenol treatment minus pre-isoproterenol treatment. There were no significant differences between the WT and TG-E responses to isoproterenol treatment. Data are mean ± S.E.M..

5.4 INADVERTENTLY INDUCED HYPOXIA

Given that our perfusion medium (supplemented Media 199, see **Section 5.2.3**) has lower oxygen carrying capacity than blood, one needs to consider potentially confounding effects of hypoxia, especially at high LV volumes. In order to be certain we were not inducing ischemic effects in isolated hearts at high left ventricular volumes (at or near V_{max}), we performed an isolated mouse heart experiment wherein LV volume was fixed at a high level (end-diastolic pressure ~30 mmHg) and perfusate O_2 tension was measured with an ABL-5 Blood Gas

Analyzer (Radiometer, Copenhagen, Denmark) and reduced in stepwise fashion (controlled mixing of fully oxygenated and deoxygenated perfusate).

Raw LV pressure data at each of the oxygenation conditions from the experiment are illustrated in **Figure 5-8A**; the first recording is for the fully oxygenated condition (pO_2 = 921 mmHg). Developed (**Figure 5-8B**) and end-diastolic (**Figure 5-8C**) pressures are plotted as a function of pO_2. The initial 20% decrease in pO_2 from the baseline level (i.e., from 921 to 736) caused only a small (1.5%) drop in developed pressure.

Thus, it is unlikely that our baseline perfusate oxygenation status is on the verge of being a limiting factor for LV contractility. Furthermore, ischemia caused a significant rise in end-diastolic pressure (see **Section 5.3.2.2**). We did not observe similar increases in end-diastolic pressure at a fixed volume in the isolated heart experiments.

Moreover, while blood would be a better perfusion medium (efficient carrier and delivery of oxygen) than that used in this project, blood perfused mouse hearts showed values similar to ours [86]. In summary, we do not believe that ischemia was a confounding factor in our studies.

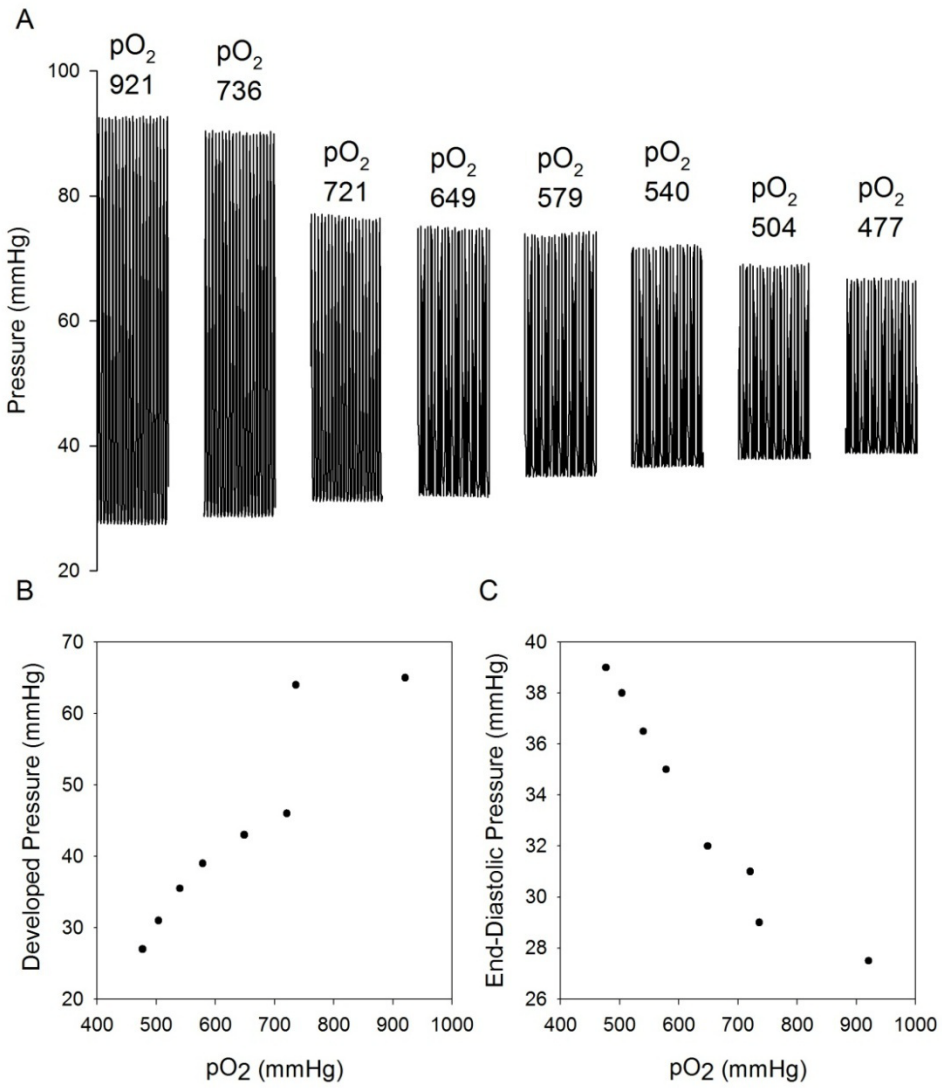

Figure 5-8. Effects of Reduced Oxygenation in an Isolated Heart

Isolated mouse heart data (LV pressure at fixed LV volume) obtained at various perfusate oxygenation levels. (A) Segments of raw pressure data at each perfusate oxygenation level. (B) Values of developed pressure at each pO_2. (C) Values of end-diastolic pressure at each pO_2 studied. This is data from one mouse, but several experiments confirmed these results.

5.5 SUMMARY

Hypothesis 1: Increased cTnI phosphorylation at the PKC sites will result in systolic dysfunction and protection from ischemic contracture at the whole organ level.

Compared to wild-type control mice, TG-E mice exhibited decreased systolic function in echocardiography studies (decreased fractional shortening, P=0.07) and isolated whole heart experiments (decreased developed pressure, P=0.02), with no evidence of diastolic dysfunction. Moreover, the TG-E mice exhibited slowed relaxation under echocardiography (increased peak to diastolic time, P=0.001) and isolated hearts (increased relaxation time, P=0.005). Compared to WT mice, the transgenic mice did not exhibit any additional protection from ischemic contracture.

6.0 FORCE-CALCIUM RELATIONSHIPS

6.1 INTRODUCTION

Hypothesis 2: Increased cTnI phosphorylation at the PKC sites will result in depressed calcium-force and ATP-force relationships (less force per calcium or ATP hydrolyzed).

Specific Aim 2a: Determine differences in the dynamic calcium-force relationship in intact papillary muscles under increased and baseline cTnI phosphorylation at the PKC sites (chronic and acute phosphorylation)

Specific Aim 2b: Determine differences in the static calcium-force and ATP-force relationships under increased and baseline cTnI phosphorylation at the PKC sites

The goal of Specific Aims 1a and 1b was to determine the functional effects of PKC phosphorylation of cTnI. The goal of Specific Aims 2a and 2b is to determine if these functional effects are mediated through changes in calcium handling, the myofilament response to calcium, or energetics.

6.1.1 Myofibrilar ATPase Measurement

In order to determine ATPase activity, we first used a myofibrilar ATPase assay. Myofibrils used in the ATPase assay were suspended in standard rigor buffer to a concentration of approximately 100μg/ml, and maximal Ca^{2+}-activated actomyosin ATPase activity was measured as described by Liou and Fuchs [87]. The reaction was initiated by the addition of 1mM MgATP and terminated after 10min by the addition of an equal volume of 2% SDS [88]. Samples were then measured for inorganic phosphate content [89].

The myofibrilar maximal ATPase activity assay showed no differences between the WT and TG-E samples (WT = 172.3 ± 11.2 nmol•mg^{-1}•min^{-1}, n= 12, TG-E: 171.6 ± 6 nmol•mg^{-1}•min^{-1}, n=12, see **Figure 6-1**).

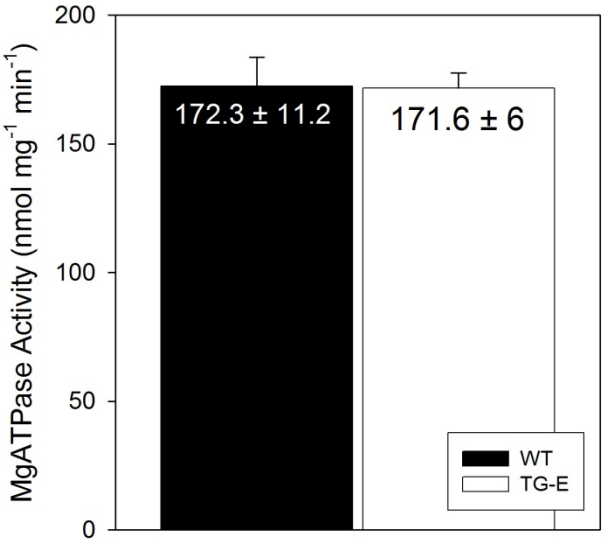

Figure 6-1. Myofibrilar Maximal ATPase Activity

Maximal calcium-activated ATPase activity for WT (black) and TG-E (white) myofibrils. No differences were seen in maximal ATPase activity in WT (172.3 ± 11.2 nmol mg^{-1} min^{-1}) versus TG (171.6 ± 6.0 nmol mg^{-1} min^{-1}) mice. Data are mean ± S.E.M..

Subsequent to this experiment, however, it was decided to directly compare ATPase activity to skinned fiber force generation. In order to make this comparison, the force and ATPase data needed to be collected simultaneously in the same fiber. Thus, this procedure was replaced with the skinned fiber ATPase assay described in **Section 6.2.4**.

6.2 METHODS

6.2.1 Isolated Papillary Muscle

Male FVB mice of similar age and body mass were anesthetized with inhaled isoflurane, and then cervically dislocated. The heart was quickly excised and placed in modified Krebs-Henseleit (KH) solution containing 30 mmol/L 2,3-butadione monoxime (BDM). The KH solution contained NaCl (141 mmol/L), Dextrose (50 mmol/L), $NaHCO_3$ (25 mmol/L), HEPES (5 mmol/L), KCl (5 mmol/L), NaH_2PO_4 (1.2 mmol/L), $MgSO_4$ (1 mmol/L) and $CaCl_2$ (2.0 mmol/L), pH adjusted to 7.35, and bubbled with 95% O_2, 5% CO_2. Thin papillary muscle strips of similar shape and size were dissected from the right ventricle and mounted by suturing the valve and ventricular tissue to a force transducer (Aurora Scientific Inc., Aurora, Ontario, Canada) and motor arm (Aurora Scientific Inc., Aurora, Ontario, Canada). The muscle was lowered into a constantly perfused bath containing KH solution and maintained at 37 ^{o}C, and paced at 2 Hz. Stimulation voltage and muscle length (L_{max}) were adjusted to obtain maximum developed force. The muscle was allowed to equilibrate for at least 30 minutes before performing the experimental protocol. Muscle diameter was recorded using a digital video

microscopy system (Ionoptix, Milton, MA), and cross-sectional area (mm^2) was calculated assuming cylindrical geometry.

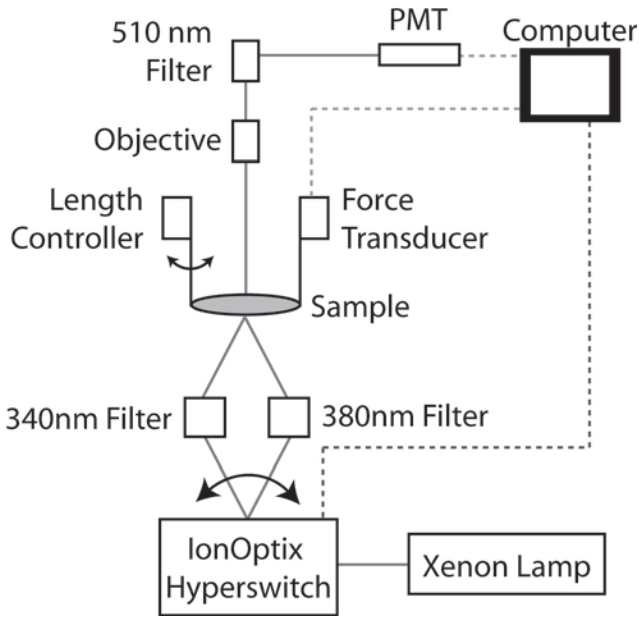

Figure 6-2. Schematic of Intracellular Calcium Imaging Setup

Schematic of the experimental setup used to collect simultaneous force and calcium fluorescence in isolated papillary muscles. The system starts with a xenon white light lamp (lower right hand corner of the schematic), which generates a wide frequency spectrum of excitation light. This light is passed to the Ionoptix Hyperswitch which rapidly switches the light pathway into two filters, a 340 nm wavelength and a 380 nm wavelength filter. These two alternating filtered wavelengths of light are then focused on the surface of the sample papillary muscle. The muscle is mounted between a force transducer and a length controller motor arm. The fluorescent dye loaded in the muscle, when excited, emits light at a wavelength of 510 nm. This light passes through a 510 nm filter and into a photomultiplier tube (PMT). The PMT passes a voltage signal (which is proportional to the amount of light that it detects) to the computer. The computer is also connected to the Hyperswitch, so it is able to differentiate between light emitted when the muscle is excited by 340 nm light versus 380 nm light. The computer also simultaneously measures the output signal from the force transducer.

Calcium measurements using fura-5F AM required a system capable of dual excitation, single emission measurements. An IonOptix Hyperswitch (Ionoptix) alternated between excitation frequencies of 340 and 380 nm at 1000 Hz. The setup also included an inverted microscope, a filter, and a pair of photomultiplier tubes (see **Figure 6-2**). The fluorescence was gathered from a small section from the center of the muscle with a 40X magnification objective

lens (LD Plan-NEOFLUA, Carl Zeiss MicroImaging, Inc., Thornwood, NY). Background fluorescence was recorded before dye loading. Fura-5F AM (50 μg) was dissolved in 25 μL dimethyl sulfoxide (DMSO) and 25 μL Pluronic. To this solution, 2.755 mL KH solution, 4.3 mg/L TPEN, and 5.0 mg/L cremophor were added. The muscle was diffusionally loaded by bathing the muscle with this solution for 30 minutes. The ratio of fluorescence emission from 340 nm excitation and 380 nm excitation, *R*, was calculated after subtracting background fluorescence.

Fluorescence calibration was performed after the experiment was complete. The first step was to end all metabolic activity in the muscle, so that calcium was no longer being actively transported. The muscle was bathed in a poisoning solution [90] for 10 minutes which completely removed its ability to generate force. The poisoning solution contained: KCl (140 mmol/L), HEPES (25 mmol/L), $MgCl_2$ (0.75 mmol/L), NaCN (2mmol/L), iodoacetic acid (0.5 mmol/L). After 10 minutes, the muscle was bathed in the saturating calcium calibration solution, which contained 1 mg of the calcium ionophore 4-BrA23187 (TefLabs, Austin, TX) dissolved in 50 μL DMSO added to 100 mL modified KH solution with 4 mM $CaCl_2$. The muscle was left in the saturating calcium calibration for ten minutes and then fluorescence was measured. The two fluorescence signals were: $S_{b\text{-}340}$ and $S_{b\text{-}380}$. Their ratio, $S_{b\text{-}340}/S_{b\text{-}380}$ is R_{max}. The muscle was then bathed in zero calcium calibration solution, which contained modified KH solution with 0 mM Ca, and 1 mM EGTA. After ten minutes, fluorescence was measured. The two fluorescence signals were $S_{f\text{-}340}$ and $S_{f\text{-}380}$. Their ratio, $S_{f\text{-}340}/S_{f\text{-}380}$ is R_{min}. These calibration coefficients were then used to calibrate calcium using **Equation 6.1** [91]. See **Appendix E**.

$$[Ca^{2+}]_i = K_d \left(\frac{S_{f-380}}{S_{b-380}}\right)\left(\frac{R-R_{min}}{R_{max}-R}\right) \tag{6.1}$$

where K_d is the dissociation constant for the fluorescent dye calcium binding. For fura-5F K_d is

assumed to be 400 nM, as indicated by the manufacturer [92], but can be determined experimentally [93, 94].

6.2.2 Isolated Papillary Muscle: Protocols

Muscle length was set to several values less than L_{max} by the computer controlled length controller. The complete length protocol included (as a percentage of L_{max}, and alternating with 100% L_{max}), 75%, 80%, 85%, 90%, 92%, 94%, 96%, 98%, 100%. Muscle length was normalized to L_{max} and 75% L_{max}, representing the full range of force producing lengths (sarcomere lengths of 2.4 μm and 1.7 μm).

The acute treatment protocol was performed at room temperature to decrease the possibility of muscle degradation during the chemical treatment. Moreover, calcium transients were not measured during this protocol – the length of time required to load the fluorescent dye and chemically treat the muscle was too long to yield reliable data by the end of the protocol. After the muscle equilibrating period, 1 μM propranolol (Sigma) was added to the papillary superperfusate solution, and the muscle was treated for 15 minutes. Following the first treatment, the muscle was superperfused with 1 μM propranolol plus 30 μM phenylephrine (Sigma) for 15 minutes.

We did not verify that this treatment increased PKC phosphorylation of cTnI. The concentration used here were taken directly from a previous study on mouse RV papillary muscles, in which it *was* shown that this treatment resulted in increased cTnI phosphorylation at the PKC sites [95].

6.2.3 Isolated Papillary Muscle: Data Analysis

In isolated papillary experiments, individual cycles were first identified by using the spike in the pacer signal. Signal averaging over the cycle was then performed to reduce high-frequency random noise. Force and fluorescence data from five to seven steady state contractions at a given length were averaged to yield a representative cycle. Force waveforms were characterized by several amplitude and rate indices. Amplitude indices included end diastolic force (F_{ed}), peak systolic force (F_{sys}), and developed force ($F_{dev} = F_{sys} - F_{dia}$). Rate indices included maximal rate of rise (dF/dt_{max}), and maximal rate of fall (dF/dt_{min}). The calcium transient was characterized in terms of R/R_{ed} (R_{ed}: fluorescence ratio at end-diastole), R_{sys}/R_{ed} (R_{sys}: peak systolic fluorescence) and dR/dt_{min}.

The effects of phenylephrine were determined by comparing force waveforms after propranolol treatment and after phenylephrine plus propranolol treatment.

6.2.4 Isolated Papillary Muscle: Statistical Analysis

For the papillary muscle data, regression analysis with dummy variables was used to identify differences in various relationships between the WT and TG-E groups: F_{dev}–length, dF/dt_{min}–length, R/R_{ed}–length, and dR/dt_{min}–length (see **Section 5.2.6**).

6.2.5 Skinned Fiber

The skinned fiber protocols were performed in collaboration with Dr. Murali Chandra (and his graduate student: Ranganath Mamidi) in the Department of Veterinary and Comparative Anatomy, Pharmacology and Physiology (*VCAPP*) at Washington State University.

Both the WT and TG-E mice were anesthetized with pentobarbital sodium (50 mg/kg body wt), and hearts were rapidly excised and immediately placed into ice-cold high relaxing (HR) solution containing (in mM) 20 MOPS, 53 KCl, 10 EGTA, 6.81 $MgCl_2$, 5.35 Na_2ATP, and 1.0 DTT. The pH was adjusted to 7.0 with KOH and a fresh cocktail of protease inhibitors (in μM: 4 benzamidine-HCl, 5 bestatin, 2 E-64, 10 leupeptin, 1 pepstatin, and 200 PMSF) were added to the fresh ice-cold buffered solutions. Papillary muscle fiber bundles were then carefully cut from the wall of the left ventricles of WT and TG-E mouse hearts. Thin muscle fiber bundles (~200 μm in width and ~2.0 mm in length) were dissected and were detergent skinned overnight using HR solution with 1% TritonX-100 to chemically permeabilize the muscle fiber preparations [96].

The detergent-skinned muscle fiber bundles were attached to the arm of a displacement motor (model 308B, Aurora Scientific Inc) on one end and to a force transducer (AE 801, Sensor One Technologies Corporation) on the other end using aluminum T-clips (Kem-Mil Co, Hayward, CA). The elliptical cross-sectional area of the muscle fiber was determined by measuring the width and thickness at three points along the length of the muscle fiber bundle. The muscle fiber bundle was immersed in a 15-μL bath containing activating solutions with different pCa ($-\log_{10}([Ca^{2+}])$). Activating solution in the bath was constantly stirred by means of a motor-driven vibration of a membrane positioned on the underside of the bath. Maximum activating solution (pCa 4.3) contained (in mM) 31 potassium propionate, 5.95 Na_2ATP, 6.61

$MgCl_2$, 10 EGTA, 10.11 $CaCl_2$, 50 BES (pH 7.0), 10 NaN_3, 0.9 NADH, and 10 phosphoenolpyruvate as well as 4 mg/ml pyruvate kinase (500 U/mg), 0.24 mg/ml lactate dehydrogenase (870 U/mg), and 20 μM A_2P_5, and a cocktail of protease inhibitors.

Isometric tension and ATPase activity were simultaneously measured at 20°C as described previously [97, 98]. Briefly, the tension developed at steady-state was measured by the force transducer and recorded using LabView software (National Instruments, Austin, TX). ATPase activity of the detergent-skinned muscle fiber bundles was measured by projecting near UV light through the muscle chamber. Light was split via a beam splitter (50/50) and intensities measured at 340 nm (sensitive to changes in NADH concentration) and at 410 nm (insensitive to changes in NADH concentration), which served as a reference signal. An analog divider and a log amplifier produced a signal proportional to the amount of ATP consumed in the muscle chamber solution. ATP regeneration from ADP was enzymatically coupled to the breakdown of phosphoenolpyruvate (PEP) by pyruvate kinase to pyruvate with a concomitant regeneration of ATP from ADP. This reaction is coupled to the synthesis of lactate from pyruvate catalyzed by lactate dehydrogenase during which process NADH is converted to NAD^+. The consumption of NADH is proportional to the amount of ATP consumed and was measured online by UV absorbance at 340 nm [98].

6.2.6 Skinned Fiber: Protocols

The sarcomere length of the muscle fiber bundle was adjusted to 2.2 μm using a He-Ne laser diffraction system [97]. The sarcomere length was readjusted to 2.2 μm after two cycles of full activation and relaxation to stabilize the resting sarcomere length throughout the later stages of the experiment [98].

The Ca^{2+} concentration of the activating solution was changed to produce steady-state force-generating activations at pCa 4.3, 5.3, 5.4, 5.5, 5.6, 5.7, 5.8, 5.9, 6.0, and 9.0 [99].

6.2.7 Skinned Fiber: Data Analysis

For skinned fiber experiments, normalized force or ATPase activity was calculated as the ratio of the measured quantity at a given pCa and the maximally activated value (i.e., at pCa = 4.33). Normalized force-pCa and ATPase-pCa data were fitted to a modified Hill equation (**Equation 6.2**) using a nonlinear regression algorithm (SigmaPlot, Systat Software Inc., San Jose, CA):

$$\frac{X}{X_{max}} = \frac{1}{1+10^{n_H(pCa\ 50 - pCa\ )}} \tag{6.2}$$

where X is a measured quantity (either force or ATPase activity) at a given pCa and X_{max} is the maximally activated value (i.e., at pCa = 4.33). Two parameters were estimated from normalized force-pCa data for each fiber: pCa_{50} (pCa required to produce normalized value of 50%) and the Hill coefficient (n_H, a measure of the steepness of the normalized force-pCa or ATPase-pCa curve, which characterizes the cooperative phenomena).

6.2.8 Skinned Fiber: Statistical Analysis

The force-pCa and ATPase-pCa data were analyzed using a standard t-test comparing F_{max}, $ATPase_{max}$, and the pCa_{50} and n_H values for both relationships.

6.3 RESULTS

6.3.1 Papillary Muscle: Results

6.3.1.1 Muscle Length Protocol

Representative raw fluorescence count data are shown for 340 nm excitation (**Figure 6-3A**), 380 nm excitation (**Figure 6-3B**) and their online calculated ratio (**Figure 6-3C**).

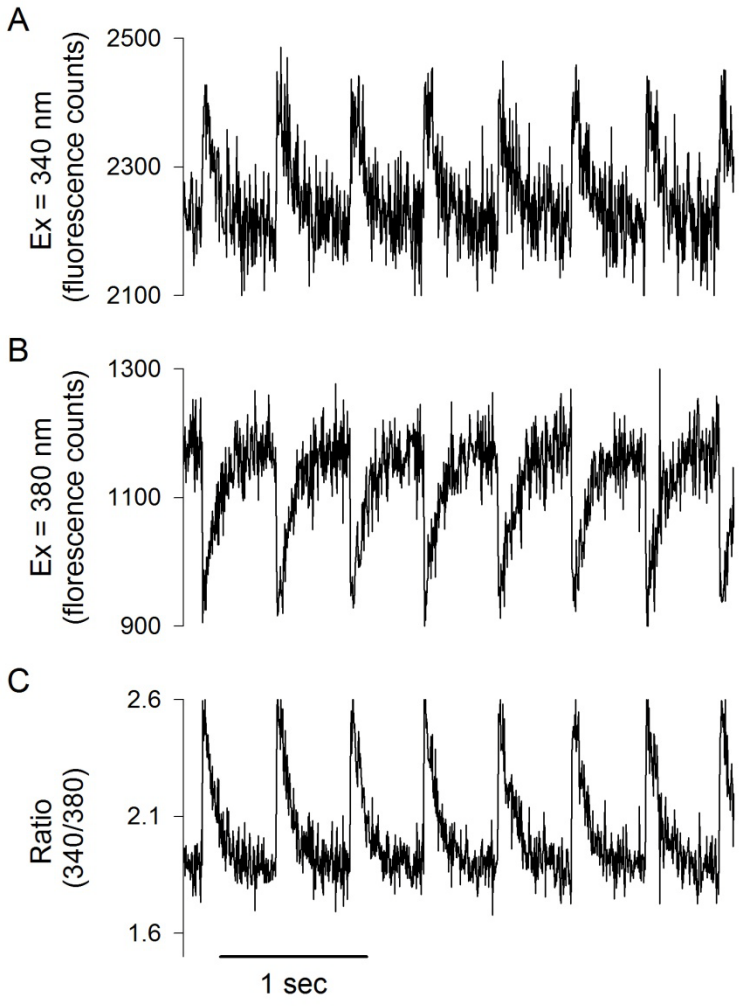

Figure 6-3. Raw Fluorescence Data from a WT Papillary Muscle

Raw fluorescence counts at excitation wavelengths of (A) 340 nm and (B) 380 nm. Also shown is the online calculated ratio of the two signals, 340/380. From one WT RV papillary muscle.

The raw fluorescence data are then averaged on a beat to beat basis (10-20 cycles). **Figure 6-4** shows representative force and calcium data from one WT and one TG-E experiment. The TG-E mice exhibited decreased force production, indicated by a downward shift of the developed force (F_{dev}) – length relationship (intercept values: WT: 1.88 ± 1.22 mN•mm^{-2}, n = 5, TG-E: -0.51 ± 0.35 mN•mm^{-2}, n = 6, *P* = 0.04, **Figure 6-5A** and **Table 5**).

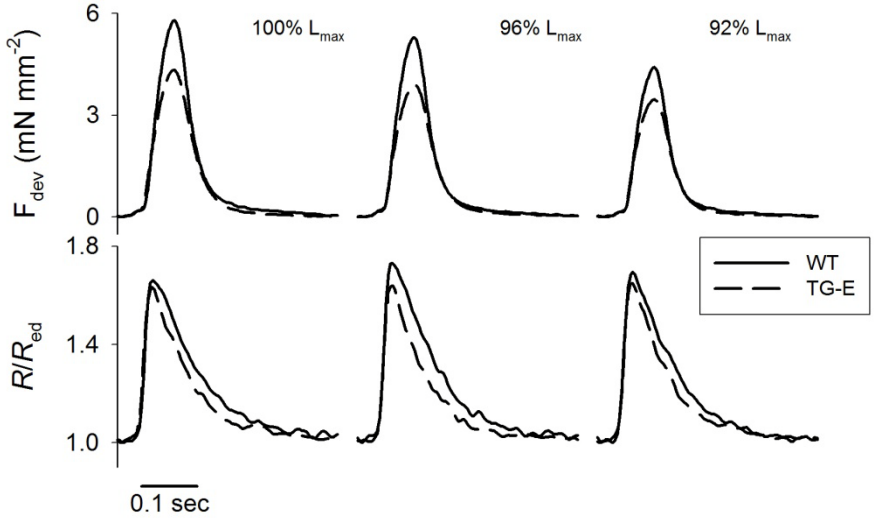

Figure 6-4. Raw Force and Calcium from WT and TG-E Papillary Muscles

Representative force (top) and calcium (bottom) data for WT (solid line) and TG-E (dashed line) mice at three lengths (100%, 96% and 92% of L_{max}).

Compared to the WT mice, there was slowed relaxation in the TG-E mice as evidenced by an upward shift in the dF/dt_{min} – length relationship (intercept values: WT: -55 ± 16 mN•mm^{-2}•s^{-1}, TG-E: 5 ± 8 mN•mm^{-2}•s^{-1}, *P* < 0.001, **Figure 6-5B** and **Table 5**).

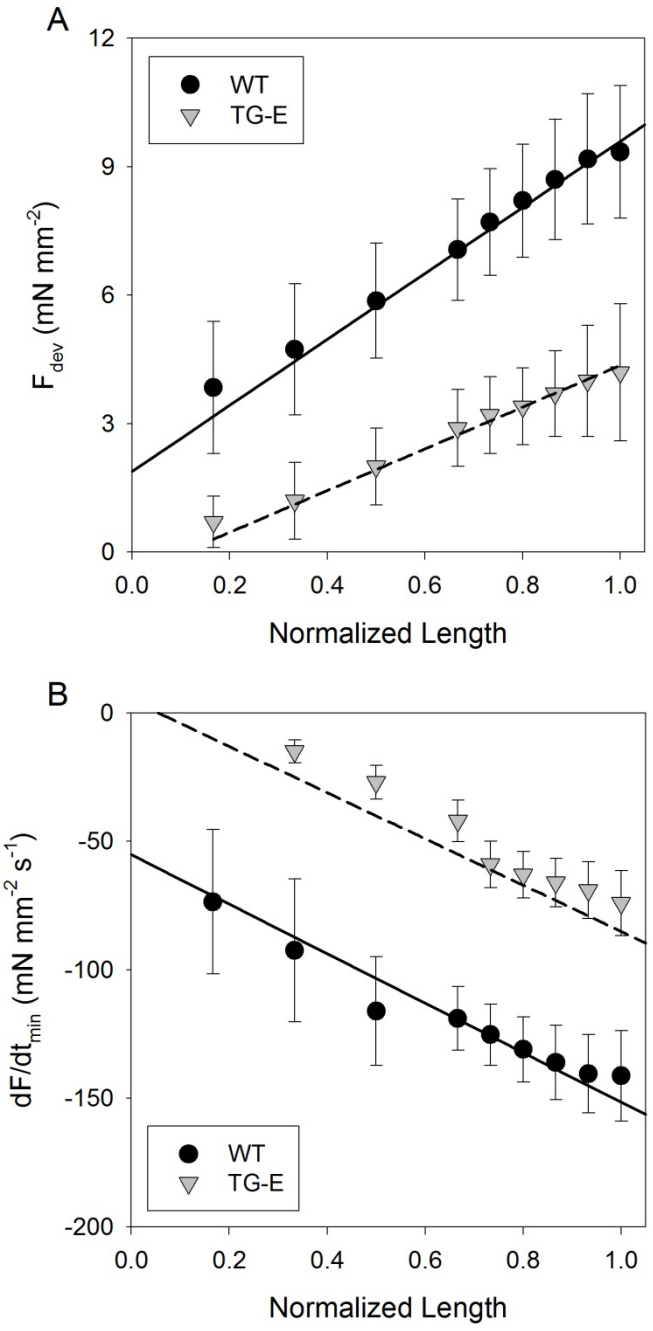

Figure 6-5. Force - Length Relationships in WT and TG-E Papillary Muscles

Force data from isolated papillary muscles. Effects of altered muscle length on developed force (F_{dev}) (A), dF/dt$_{min}$ (relaxation) (B) in WT (black circles) and TG-E (gray triangles) mice. The raw data were fitted to a linear trendline (WT: solid line, TG-E: dotted line). Compared to the WT data, the intercept of the F_{dev} – length relationship was significantly lower (P<0.05) and the intercept of the dF/dt$_{min}$ –length relationship was significantly higher (P<0.05) in the TG-E mice.

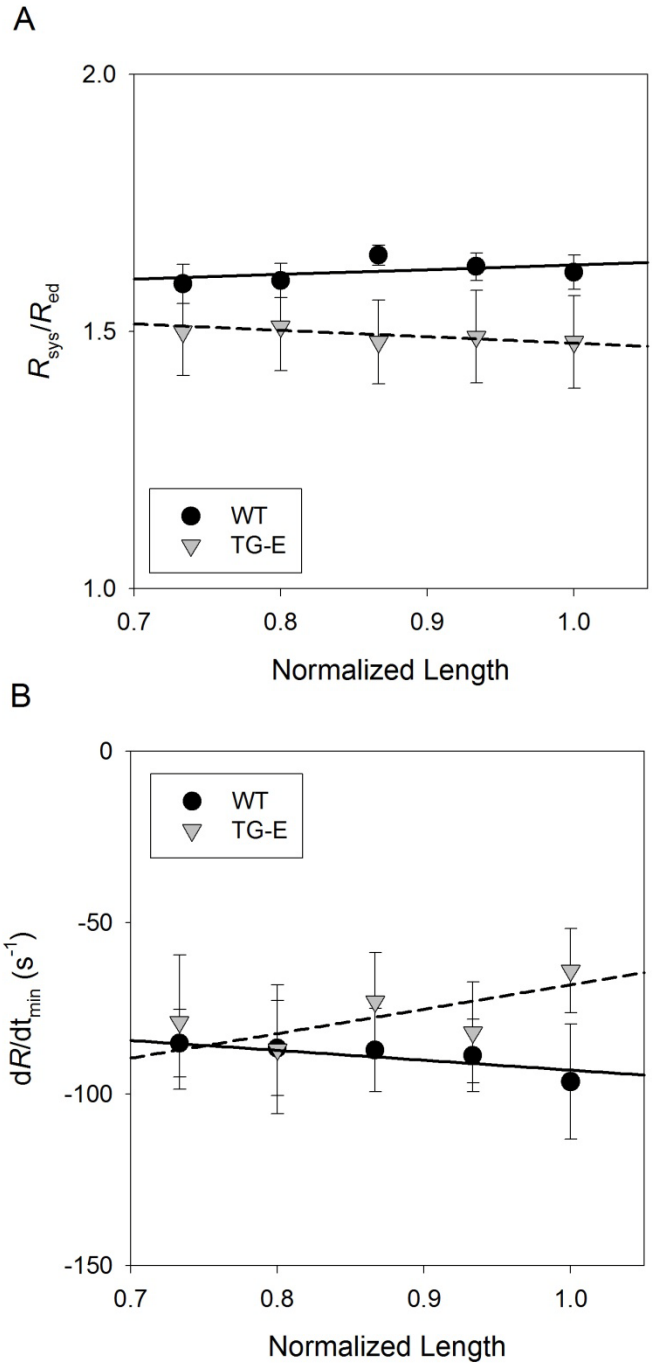

Figure 6-6. Calcium - Length Relationships in WT and TG-E Papillary Muscles

Intracellular calcium concentration $[Ca]_i$ data from isolated papillary muscles. $[Ca]_i$ is expressed as R (R = [emission fluorescence$_{340}$]/[emission fluorescence$_{380}$]) and is normalized by the end-diastolic value of R (R_{ed}). Effects of altered muscle length on R_{sys} (peak systolic R) normalized by R_{ed} (end-diastolic R) (A) and dR/dt_{min} (calcium relaxation) (B) in WT (black circles) and TG-E (gray triangles) mice. The raw data were fitted to a linear trendline (WT: solid line, TG-E: dashed line). There were no differences in the intercept or slope of the R_{sys}/R_{ed} – length, or dR/dt_{min} – length relationships between WT and TG-E.

In contrast, intracellular calcium concentration transients ($[Ca]_i$) were unaltered in TG-E mice, exhibiting no changes in the slope or intercept of the $[Ca]_i$ amplitude (as quantified by R_{sys}/R_{ed}) – length relationship (*P*-value: for slope = 0.53, for intercept = 0.83; **Figure 6-6A** and **Table 5**), or the relaxation (as quantified by dR/dt_{min}) – length relationship (*P*-value: for slope = 0.23, for intercept = 0.28; **Figure 6-6B** and **Table 5**).

If the slope of the length-parameter relationship is statistically different from zero, then length has an effect on that parameter. The WT and TG-E mice showed an effect of length on F_{dev} and dF/dt_{min} (increasing F_{dev} with increasing length, and increasing magnitude, i.e., more negative, of dF/dt_{min} with increasing length). However, there was no effect of length on R_{sys}/R_{ed} or dR/dt_{min} in the WT or TG-E mice. This is in agreement with our past findings ([83] and **Appendix A**), that length changes do not affect the calcium transient in mice.

Table 5. Slope and Intercept Values for Various Relationships in Papillary Muscles

	WT	TG-E	*P*-value
F_{dev} - Length	n = 40	n= 48	
Slope	7.7 ± 1.7	4.9 ± 0.5	0.0858
Intercept	1.9 ± 1.2	-0.5 ± 0.3	**0.0447**
dF/dt_{min} - Length	n = 40	n = 48	
Slope	-96.4 ± 22.6	-90.0 ± 11.5	0.793
Intercept	-55.1 ± 16.5	5.0 ± 8.4	**0.001**
R_{sys}/R_{ed} - Length	n = 28	n = 34	
Slope	0.09 ± 0.12	-0.13 ± 0.30	0.5361
Intercept	1.5 ± 0.1	1.6 ± 0.3	0.828
dR/dt_{min} - Length	n = 28	n = 34	
Slope	-28.8 ± 39.4	71.2 ± 67.0	0.2276
Intercept	-64.2 ± 33.1	-139.3 ± 56.3	0.2807

We did perform the standard calibration measurements after every papillary muscle experiment; however, we found that in approximately half of the experiments, the measured calibration values did not make physical sense (e.g., R_{min} measured at the end of the experiment below the background value measured at the beginning of the experiment or R_{max} measured at the end of the experiment close to some of the peak R values measured during the experiment). Therefore, we decided to report our calcium measurements in terms of uncalibrated fluorescence ratios, which should be valid for relative comparisons, if not for absolute values of calcium [100]. In about half of the experiments, the calibration values did make sense (n: WT = 3, TG-E = 3). Upon reviewing these subset of data, we found no significant difference in diastolic calcium between the WT and TG-E groups (WT= 401 ± 142 nM, TG-E = 524 ± 152 nM, *P* = 0.58). These values are similar to calibrated calcium levels reported in the past [57, 101].

6.3.1.2 Acute cTnI Phosphorylation Protocol

Figure 6-7 shows representative data from before and after phenylephrine treatment for a WT (**Figure 6-7A** and **B**) and TG-E (**Figure 6-7C** and **D**) mouse.

In the WT mice, treatment with 30 μM phenylephrine in the presence of 1 μM propranolol resulted in a decrease in F_{dev} (-22.2 ± 6.4%) compared to F_{dev} with 1 μM propranolol treatment alone (**Figure 6-8A**). There was also an increase in T_{relax} after phenylephrine treatment (15.9 ± 7.4%) compared to propranolol treatment (**Figure 6-8B**).

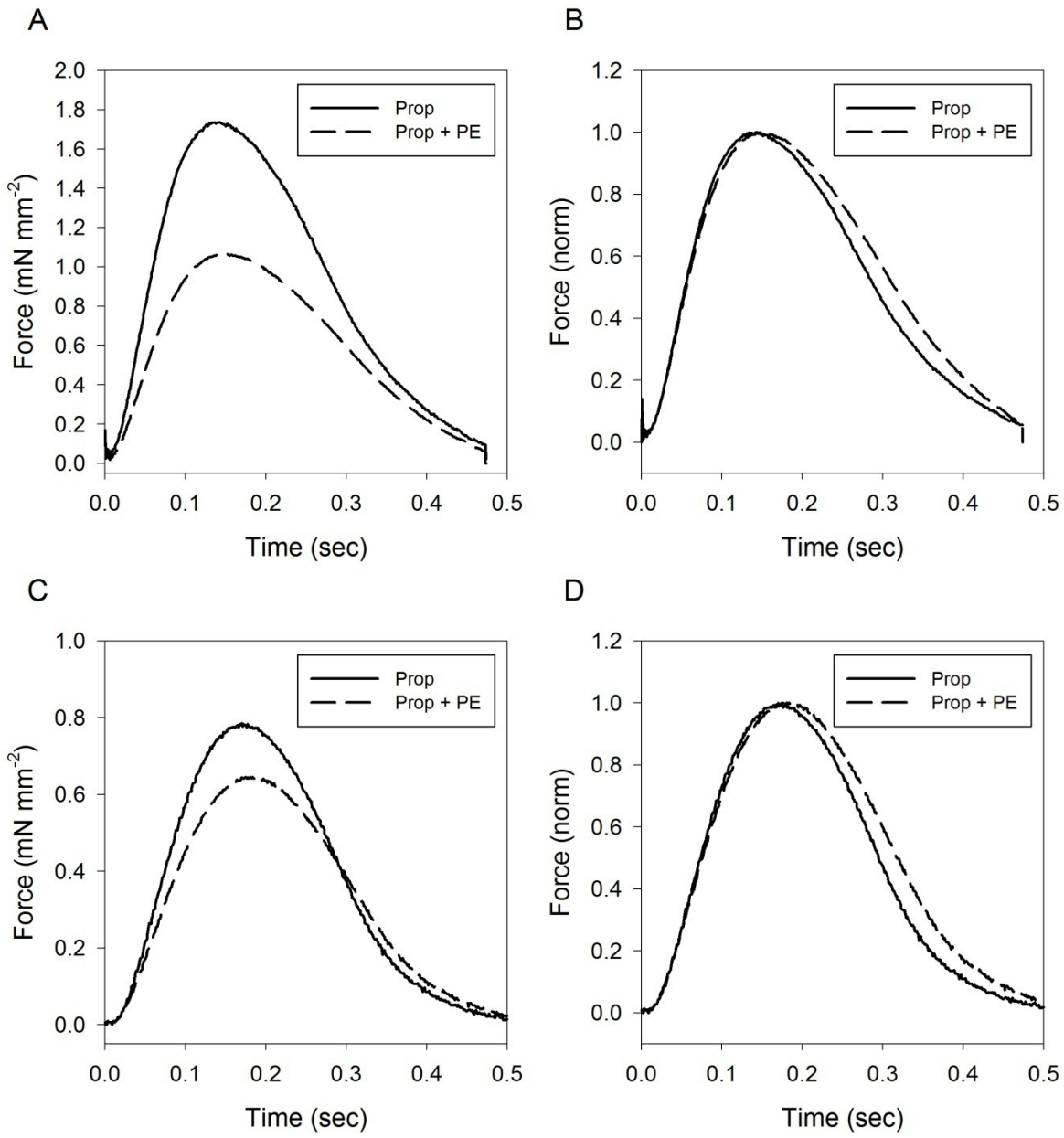

Figure 6-7. Representative Prop./PE Treatment Data

Comparison of developed force (panels A and C) and normalized force (panels B and D) after 1 μM propranolol (prop.) treatment (solid line) and after 1 μM propranolol plus 30 μM phenylephrine (PE) treatment (dashed line). Panels A and B are from a single WT mouse, and Panels C and D are from a single TG-E mouse. Both showed a decrease in developed force and an increase in relaxation time with PE treatment.

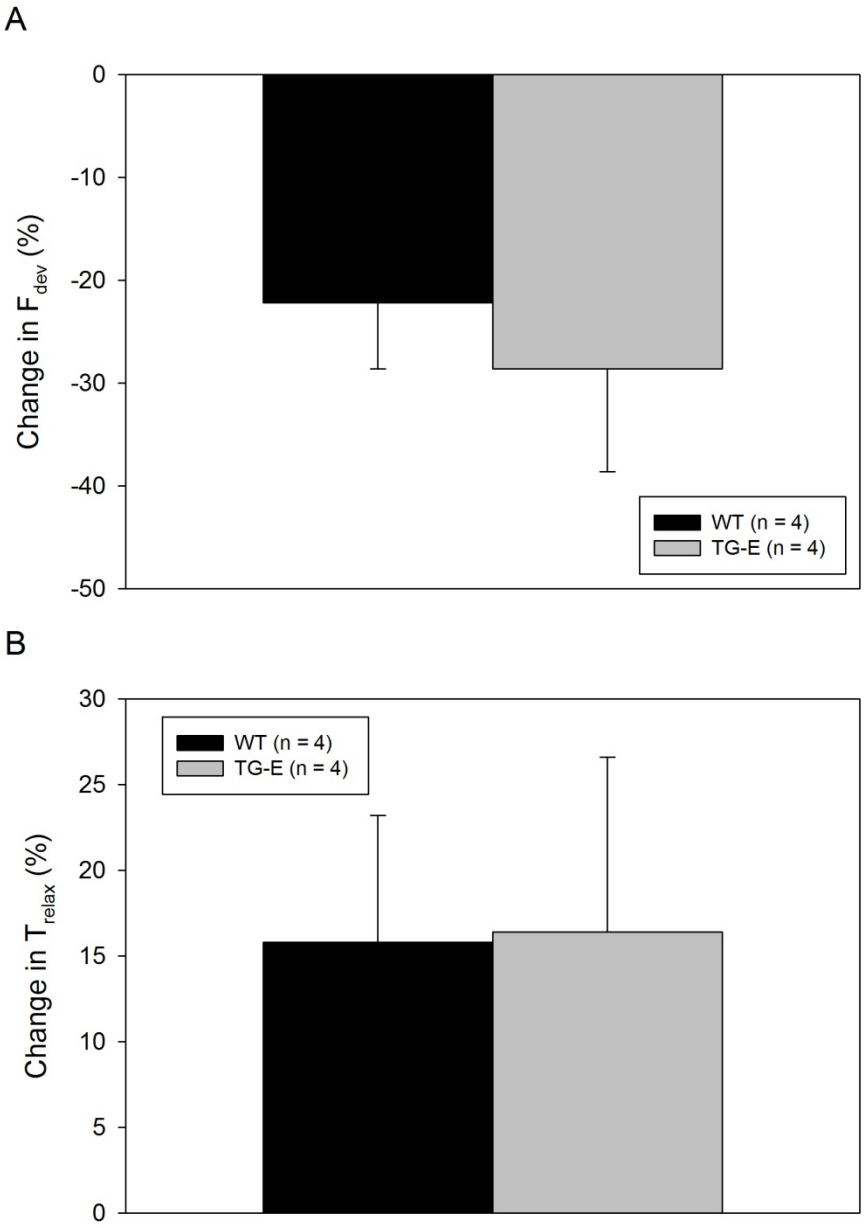

Figure 6-8. Effect of Phenylephrine Treatment

Percent change in F_{dev} (A) and T_{relax} (B) in WT (black) and TG-E (gray) mice after treatment of papillary muscle with phenylephrine in the presence of propranolol, compared to baseline (treatment with propranolol alone). Data are mean ± S.E.M..

The TG-E mice exhibited similar responses, showing a decrease in F_{dev} (-28.7 ± 10%, **Figure 6 -8A**) and an increase in T_{relax} (16.4 ± 10.2%) after phenylephrine and propranolol treatment, compared to propranolol treatment alone.

There were no differences between the WT and TG-E mice in the response to phenylephrine in the presence of propranolol, either in F_{dev} (*P*-value = 0.60) or T_{relax} (*P*-value = 0.97).

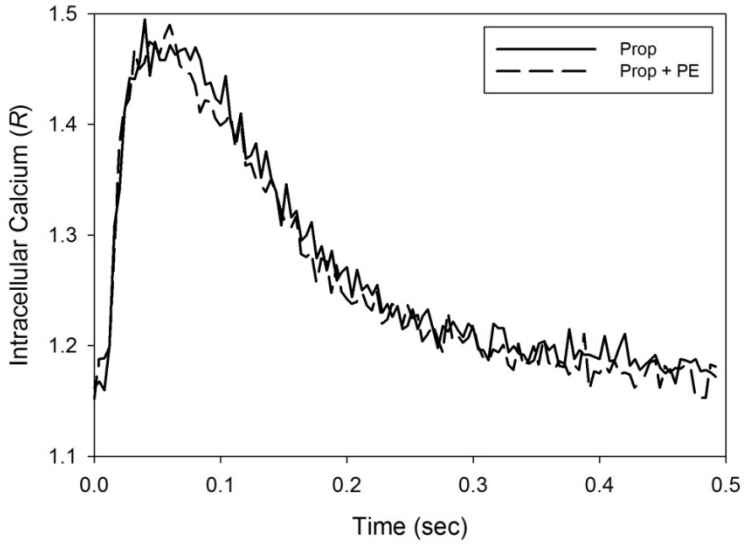

Figure 6-9. Calcium from Prop./PE Treatment Experiment

Intracellular calcium after 15 minutes of 1 μM propranolol (prop.) treatment (solid line) and after 5 minutes of 1 μM propranolol plus 30 μM phenylephrine (PE) treatment (dashed line).

In general, due to the length of the protocol, it was not possible to record calcium and force simultaneously under propranolol and phenylephrine conditions. However, in a few of the experiments, we were able to record calcium, so there is anecdotal evidence of no effect on the intracellular calcium transient with phenylephrine treatment, as can be seen in **Figure 6-9**. In this example, force has been reduced, with no change in intracellular calcium. The ability to record force and calcium simultaneously in these experiments was rare, so statistical evidence cannot be provided.

6.3.2 Skinned Fiber

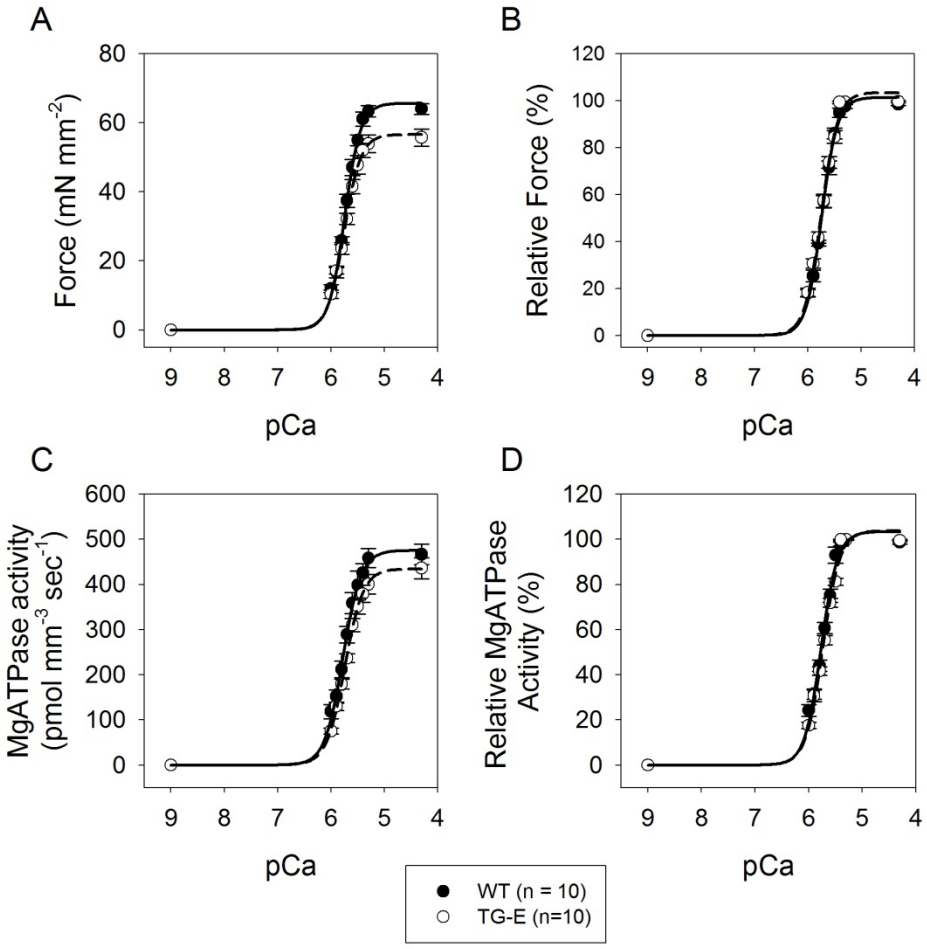

Figure 6-10. Data from WT and TG-E Skinned Fibers

Mechanical and energetic characteristics in skinned fibers from WT (closed circles) and TG-E (open circles) mice. (A) Absolute force data ($mN \cdot mm^{-2}$) showing WT mice have significantly higher F_{max} than TG-E mice. (B) Relative force data ($\%F_{max}$) showing that there is no difference in pCa_{50} (calcium sensitivity) or Hill coefficient (cooperativity) between the WT and TG-E mice. (C) Absolute ATPase activity ($pmol \cdot mm^{-3} \cdot sec^{-1}$) shows that WT mice have a higher, but not statistically significant maximal value. (D) Relative ATPase activity (%Max) shows no differences in pCa_{50} or n_H values between the WT and TG-E mice.

There was a 14% significant decrease in maximally activated force (F_{max}) in the TG-E mice (**Figure 6-10A** and **Table 6**). While there was a similar decrease (9%) in maximal ATPase activity (**Figure 6-10C** and **Table 6**), it was not statistically significant. The skinned fiber data were fit to the modified Hill equation (**Equation 6.1**). There were no differences in pCa_{50}

(calcium sensitivity) or Hill coefficient (n_H, cooperativity) for either the force-pCa (**Figure 6-10B and Table 6**) or ATPase-pCa relationships (**Figure 6-10D and Table 6**).

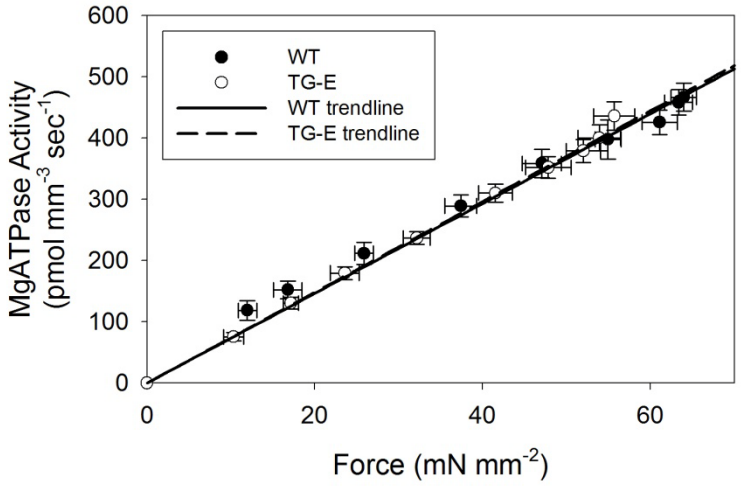

Figure 6-11. Tension Cost for WT and TG-E Skinned Fibers

There was no difference in the slope of the fitted linear regression, representing tension cost, between the two groups.

The force-ATPase activity relationship is a linear one, and its slope (when fit to linear regression) is defined as tension cost. There were no differences in tension cost between the WT (7.33 ± 0.13, R^2 = 0.97) and TG-E (7.41 ± 0.10, R^2 = 0.98) mice (**Figure 6-11** and **Table 6**).

Table 6. Summary of Data from Skinned Fiber Protocol

	WT (n=10)	TG-E (n=10)
Force - pCa		
F_{max} ($mN \bullet mm^{-2}$)	65.7 ± 1.6	56.6 ± 2.5 *
pCa_{50}	5.74 ± 0.01	5.76 ± 0.01
n_H	2.98 ± 0.13	2.84 ± 0.11
MgATPase - pCa		
Max ($pmol \bullet mm^{-3} \bullet sec^{-1}$)	477 ± 23	434 ± 23
pCa_{50}	5.77 ± 0.02	5.75 ± 0.01
n_H	2.60 ± 0.13	2.56 ± 0.07
Tension Cost	7.33 ± 0.13	7.41 ± 0.10

Values are mean ± S.E.M.. F_{max}: maximally activated force; n_H: Hill coefficient. * $P<0.05$ versus WT.

6.4 SUMMARY

Hypothesis 2: Increased cTnI phosphorylation at the PKC sites will result in depressed calcium-force and ATP-force relationships (less force per calcium or ATP usage).

In isolated papillary muscle experiments over a range of muscle lengths, the TG-E mouse (increased cTnI phosphorylation at the PKC sites) exhibited decreased F_{dev} and dF/dt_{min}, indicating negative inotropy and negative (slower) relaxation. There were no changes in the calcium transient amplitude (R_{sys}/R_{ed}) or relaxation (dR/dt_{min}) in the TG-E mouse, compared to the WT mouse.

Acute phosphorylation of cTnI using phenylephrine in the presence of propranolol had a negative inotropic and lusitropic effect in the WT mice. The TG-E mice showed a similar pattern. Due to the length of the protocol, it was not possible to perform chemical treatments in and measure intracellular calcium transients the same papillary muscle. However, anecdotal evidence shows there is no effect on the calcium transient.

In skinned fiber data, the TG-E mouse showed a decrease in maximal developed force, with no change in pCa_{50} or Hill coefficient. There was no change in pCa_{50} or Hill coefficient for the pCa – ATPase relationship. There was no change in the tension cost between the TG-E and WT mice.

7.0 MODEL-BASED ANALYSIS

7.1 INTRODUCTION

Hypothesis 3: A Model-based analysis of data from Specific Aims 1 and 2 will provide an integrative interpretation of increased cTnI phosphorylation at the PKC sites.

Specific Aim 3a: Determine whether the four-state model can provide unique solutions

Specific Aim 3b: Using a model-based analysis, determine the myofilamental alterations caused by PKC-induced phosphorylation of cTnI

The experimental evidence from Specific Aims 1a, 1b, 2a and 2b provide an extensive catalogue of functional effects of PKC-induced phosphorylation of cTnI. The goal here is to identify the underlying changes in myofilamental processes that can simultaneously explain all of our results. To do this, we require the use of a mathematical model-based analysis to integrate and interpret the experimental results. Before we can use the model in this way, however, we must provide evidence that the model is identifiable based on our input(s) and output(s).

7.2 METHODS

7.2.1 Model Selection

In lieu of developing an entirely new mathematical model, we set out first to determine if an existing model could meet our needs. The four-state model of myofilament activation was found to be a suitable model because its inputs and outputs matched our data, and it met the three criteria of a well-posed model set forth in **Section 1.5**: descriptive, predictive, and explanative. The four-state model is descriptive because it has adequate complexity and appropriate design to capture the important features of an observed behavior [102, 103]; predictive because after careful validation it can anticipate behavior that has not been observed [104]; and explanative because, being based upon actual elements in the physiological pathway, the model is capable of illuminating the causes of the behavior [105].

We have also used this model-based analysis for calcium and pressure data in WT mouse isolated hearts previously, see **Appendix A** and [83]. It has the appropriate design and level of complexity. For these reasons, we have selected this model for our data analysis.

7.2.2 Four-State Model

During diastole, actin and myosin are unbound and the muscle is relaxed (see **Section 1.1**). During systole, an action potential stimulates cardiac myocytes to allow extracellular calcium to enter the cell, which stimulates a huge secondary release of calcium from the sarcoplasmic reticulum. Calcium then binds to cardiac TnC and triggers a cascade that allows actin and myosin to form a crossbridge, the force generating unit of muscle.

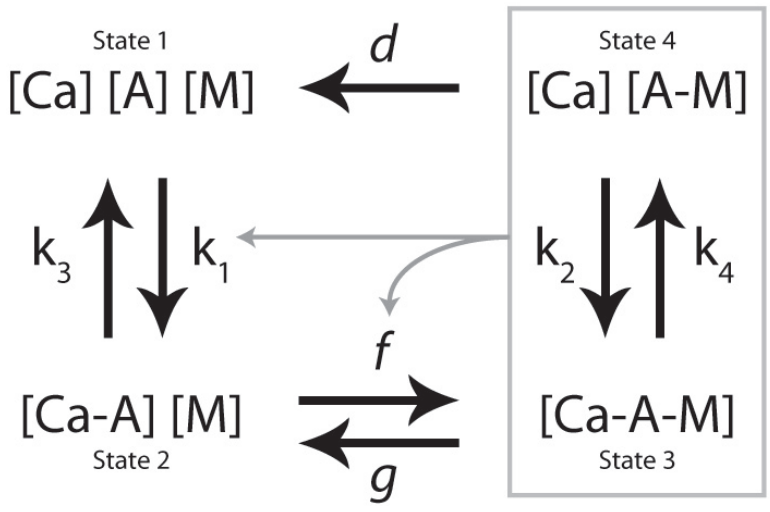

Figure 7-1. Schematic of the Four-State Model

The four –state model is a compartment model describing two non-force-generating states (States 1 and 2) and two force-generating states (States 3 and 4), and five individual species: actin, [A]; myosin [M]; calcium-bound actin [Ca-A]; calcium-bound crossbridge, [Ca-A-M]; calcium-free crossbridge, [A-M]. There are seven rate constants: k_1, k_2, k_3, k_4, f, g, and d.

This pathway of cardiac contraction is described in the four-state model and is shown in **Figure 7-1**. In State 1, calcium ([Ca]), actin ([A]) and myosin ([M]) are all in their unbound (diastolic) states. In State 2, calcium is bound to troponin on the thin filament ([Ca-A]), but actin and myosin have not formed a crossbridge. Movement between State 1 and State 2 is regulated by the parameters k_1 and k_3, representing the rate constants of calcium binding and release, respectively. State 3 is a force-generating state (converting from diastole to systole), and has calcium bound, and the strong crossbridge is formed ([Ca-A-M]). The classical f and g rate constants represent the binding and unbinding of actin and myosin, or the forming and breaking of the strongly bound crossbridge. State 4 ([A-M]) is a second force-generating state, in which calcium is dissociated from troponin (controlled by k_4) in the presence of a strongly bound crossbridge. Calcium can bind to TnC in State 4 (by rate constant k_2) to return to State 3. State 4 can convert to State 1 though the unbinding of actin and myosin and dissolution of the force-

generating crossbridge, described by rate constant *d*. There is no pathway directly from State 1 to State 4. A differential equation can be written for each species, yielding **Equations 7.1 – 7.5**.

$$\frac{d[A](t)}{dt} = -k_1[\text{Ca}](t)[A](t) + k_3[\text{Ca-}A](t) + d[A\text{-}M](t) \tag{7.1}$$

$$\frac{d[M](t)}{dt} = d[A\text{-}M](t) - f[\text{Ca-}A](t)[M](t) + g[\text{Ca-}A\text{-}M](t) \tag{7.2}$$

$$\frac{d[\text{Ca-}A](t)}{dt} = k_1[\text{Ca}](t)[A](t) - k_3[\text{Ca-}A](t) - f[\text{Ca-}A](t)[M](t) + g[\text{Ca-}A\text{-}M](t) \tag{7.3}$$

$$\frac{d[\text{Ca-}A\text{-}M](t)}{dt} = f[\text{Ca-}A](t)[M](t) + k_2[\text{Ca}](t)[A\text{-}M](t) - g[\text{Ca-}A\text{-}M](t) - k_4[\text{Ca-}A\text{-}M](t) \tag{7.4}$$

$$\frac{d[A\text{-}M](t)}{dt} = k_4[\text{Ca-}A\text{-}M](t) - d[A\text{-}M](t) - k_2[\text{Ca}](t)[A\text{-}M](t) \tag{7.5}$$

The model simulates cooperativity through a feedback mechanism of force generating crossbridges (State 3 and 4) on to the rate constants k_1 and *f*. This feedback is shown by the gray arrows in **Figure 7-1**. There are also two algebraic feedback equations, described by:

$$k_1(t) = \alpha_1\left([\text{Ca-}A\text{-}M](t) + [A\text{-}M](t)\right)^{\gamma_1} + \beta_1 \tag{7.6}$$

$$f(t) = \alpha_f\left([\text{Ca-}A\text{-}M](t) + [A\text{-}M](t)\right)^{\gamma_f} + \beta_f \tag{7.7}$$

The model output is force, and is the sum of the two force-generating states (**Equation 7.4** and **Equation 7.5**) times a scaling factor, and is shown in **Equation 7.8**:

$$F(t) = \gamma\left([\text{Ca-}A\text{-}M](t) + [A\text{-}M](t)\right) \tag{7.8}$$

Initial conditions represent the concentrations (per unit volume of sarcoplasm) at t=0 of each state prior to introduction of free calcium [102, 106]: $[\text{A}]_{t=0}$ = 70 μM, $[\text{M}]_{t=0}$ = 20 μM, $[\text{Ca-A}]_{t=0}$ = 0 μM, $[\text{Ca-A-M}]_{t=0}$ = 0 μM, $[\text{A-M}]_{t=0}$ = 0 μM.

We experimentally measured ATPase activity and estimated the tension cost. We adapted the four-state model to provide these data. **Equation 7.8** was used to calculate ATPase activity from the model predicted steady-state data.

$$\text{ATPase} = g * [\text{Ca-A-M}] + d * [\text{A-M}] \tag{7.8}$$

The parameter *d* has very little effect on the value of ATPase (see **Appendix D**), however, as the [A-M] state is much less populated than the [Ca-A-M] state. Thus, g is the primary effector of ATPase activity. The tension cost is calculated as the slope of the linear trendline associated with the steady-state force – ATPase relationship.

7.2.3 *A Priori* Identifiability

First we will define what an identifiable model is. We assume the model is defined by a system of differential equations:

$$\frac{dx_n(t)}{dt} = f\big(x_n(t), p_i, u_m(t)\big) \tag{7.9}$$

where x_n is an *n*-dimensional state variable, p_i is an *i*-dimensional parameter array, and u_m is an *m*-dimensional input vector. We also assume there is at least one output equation:

$$y_j(t) = g\big(x_n(t), p_i, u_m(t)\big) \tag{7.10}$$

where y_j is a *j*-dimensional output vector. We assume that there is some true, experimental output array of dimension *j*, Y_j. If the model is identifiable, there exists a unique, parameter set of dimension *i*, P_i. Thus, the goal of model optimization is to minimize $Y_j - y_j$ by altering p_i until it is equal to P_i. If this is possible, the model is identifiable.

Differential algebra allows the use of classical algebra techniques on a system with derivatives [107]. The system (1) is reduced using Ritt's pseudodivision algorithm into a

characteristic set. To reduce the system, the variables are first ranked, with the state variables and their derivatives ranked highest. When the system is being reduced, the highest ranked elements are preferentially eliminated from the equation set. When the set can no longer be reduced, it is called *autoreduced*. One of the equations in this characteristic set should contain only inputs, outputs and parameters:

$$f\left(y_j, \dot{y}_j, \ddot{y}_j, \dots, u_m, \dot{u_m}, \ddot{u_m}, \dots, p_i\right) = 0 \tag{7.11}$$

which is in a state-space form and represents the input-output relationships. The parameters are therefore a function of only the model inputs, outputs, and their derivatives, all known elements. The coefficients of **Equation 7.11** are extracted, and represent the *exhaustive summary*. The Buchberger algorithm is applied to the exhaustive summary, to obtain the Gröbner set [108]. This is analogous to finding the solution of a linear system using Gaussian elimination. If the parameters are uniquely identifiable then the model is *a priori* globally identifiable. If there are a finite number of possible parameter sets then the model is locally identifiable, and if there are an infinite number of parameter sets, the model is nonidentifiable.

This analysis assumes a fixed input function, noise-free input and output, and a given model structure.

7.2.3.1 Model Identifiability Using Differential Algebra: An Example

The details of this analysis are explained elsewhere [109, 110]. The use of differential algebra to determine whether a model is globally identifiable is easiest to describe through use of a simple example.

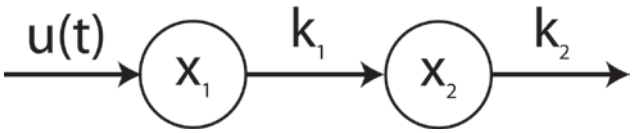

Figure 7-2. Schematic of Example Model

Consider a two compartment model (see **Figure 7.2**), with an input u(t) into state 1 (x_1), a transition rate constant of k_1 to state 2 (x_2) and rate constant of k_2 to a sink from state 2. The model output, y, is state 2, x_2. The model is described by the following two differential equations and one output equation.

$$\frac{dx_1(t)}{dt} = \dot{x_1}(t) = u(t) - k_1 x_1 \tag{7.12}$$

$$\frac{dx_2(t)}{dt} = \dot{x_2}(t) = k_1 x_1 - k_2 x_2 \tag{7.13}$$

$$y = x_2 \tag{7.14}$$

We will assign the following ranking system, which ranks the state variables highest, because our goal is to eliminate them first.

$$u < y < \dot{y} < \ddot{y} < x_1 < x_2 < \dot{x_1} < \dot{x_2} \tag{7.15}$$

The two differential equations and output equation are then ranked according to the highest input, output, or state variable in each equation. This yields:

$$-x_2 + y \quad \text{leader } x_2 \tag{7.16}$$

$$\dot{x_1} - u + k_1 x_1 \quad \text{leader } \dot{x}_1 \tag{7.17}$$

$$\dot{x_2} - k_1 x_1 + k_2 x_2 \quad \text{leader } \dot{x}_2 \tag{7.18}$$

The first step is to reduce the highest ordered equation, **Equation 7.18**. We will do this by using **Equation 7.16** and its derivative. When we do this, **Equation 7.18** becomes:

$$-k_1 x_1 + \dot{y} + k_2 y \quad \text{leader } x_1 \tag{7.19}$$

The system is now:

$$\dot{y} - k_1 x_1 + k_2 y \quad \text{leader } x_1 \tag{7.20}$$

$$x_2 + y \quad \text{leader } x_2 \tag{7.21}$$

$$\dot{x_1} - u + k_1 x_1 \quad \text{leader } \dot{x}_1 \tag{7.22}$$

The same technique is used, where **Equation 7.20** and its derivative are used to replace x_1 in **Equation 7.22**. When this is done, **Equation 7.22** becomes:

$$\ddot{y} + (k_1 + k_2)\dot{y} + k_2 y - k_1 u \quad \text{leader } \ddot{y} \tag{7.23}$$

The system is now:

$$\ddot{y} + (k_1 + k_2)\dot{y} + k_1 k_2 y - k_1 u \quad \text{leader } \ddot{y} \tag{7.24}$$

$$-k_1 x_1 + \dot{y} + k_2 y \quad \text{leader } x_1 \tag{7.25}$$

$$x_2 + y \quad \text{leader } x_2 \tag{7.26}$$

This system can no longer be further reduced, and is said to be autoreduced. This is known at the model's *characteristic set*. **Equation 7.24** contains no state variables, and represents the model's input-output relationship. The coefficients of **Equation 7.24** are extracted, and represent the *exhaustive summary*.

$$k_1 + k_2 \qquad k_1 k_2 \qquad k_1 \tag{7.27}$$

The next step is to determine if k_1 and k_2 be uniquely identified from the exhaustive summary. The Buchberger algorithm is applied to the exhaustive summary to obtain the Gröbner set. For this simple example, it is possible to do this analysis by hand. First, we assume that the true, unique value for k_1 is α and for k_2 is β, which provides the following:

$$k_1 + k_2 - \alpha - \beta = 0 \tag{7.28}$$

$$k_1 k_2 - \alpha\beta = 0 \tag{7.29}$$

$$k_1 - \alpha = 0 \tag{7.30}$$

Clearly, it is possible to solve this system for $k_1 = \alpha$ and $k_2 = \beta$. This technique has been automated in a program known as DAISY (Differential Algebra for Identifiability of SYstems).

DAISY (version 1.4) was written by G.Bellu, M.P.Saccomani, S.Audoly and L.D'Angio, and is copyrighted by University of Cagliari and University of Padova, Italy. We have received permission from the authors to use it here. The program runs in Reduce, an algebraic computer program (version 3.8, Konrad-Zuse-Zentrum für Informationstechnik Berlin (ZIB), Berlin, Germany).

Obtaining the Gröbner set can be extremely computationally intensive, making it difficult or impossible to solve. Moreover, this analysis becomes significantly more computationally intensive with even minor increases in complexity. In order to assuage this problem DAISY uses a set of pseudo-randomly selected values for each parameter, to simplify the symbolic algebra. So in the above example, the program may select $k_1 = 25$ and $k_2 = 27$. The system is solved, and the Gröbner set is obtained, showing uniquely identified parameters. Therefore, for this example, DAISY would report that it is globally identifiable.

DAISY was used to determine the *a priori* identifiability of other models of cardiac function, as shown in **Appendix B**.

7.2.3.2 DAISY and the Four-State Model

DAISY was used to determine the *a priori* identifiability of the four-state model. The model first must be in its most reduced form, which it is not as described above. The five differential equations can be reduced to the following three differential equations and one output equation.

$$\frac{d[A](t)}{dt} = -k_1[\text{Ca}](t)[A](t) + k_3(-[A](t) + [A\text{-}M](t) + 50) + d(-[M](t) - [\text{Ca-}A\text{-}M](t) + 20) \quad (7.31)$$

$$\frac{d[M](t)}{dt} = d(-[M](t) - [\text{Ca-}A\text{-}M](t) + 20) - f(-[A](t) + [A\text{-}M](t) + 50)[M](t) + g[\text{Ca-}A\text{-}M](t) \quad (7.32)$$

$$\frac{d[\text{Ca-}A\text{-}M](t)}{dt} = f(-[A](t) + [A\text{-}M](t) + 50)[M](t) + k_2[\text{Ca}](t)(-[M](t) - [\text{Ca-}A\text{-}M](t) + 20) - g[\text{Ca-}A\text{-}M](t) - k_4[\text{Ca-}A\text{-}M](t) \quad (7.33)$$

$$F(t) = \gamma(-[M](t) + 20) \quad (7.34)$$

The model input is [Ca](t), and the model output is F(t). The exponents on the feedback equations (**Equation 7.6 and 7.7**), γ_1 and γ_f, are not estimated, and their values are assumed to obtain appropriate cooperativity, and have previously been assigned values of 0.5 and 2, respectively [102]. Here we use values of 1.25 and 1 (**Section 7.3.3**), because they resulted in n_H values that closely matched our experimental data. There are nine free parameters to estimate: α_1, β_1, k_2, k_3, k_4, α_f, β_f, d, and g. The scaling factor γ is not included as a free parameter.

DAISY cannot handle exponent values which are not whole numbers, so there is an issue with **Equation 7.6** if γ_1 is 0.5, or 1.25. We tested the instance when γ_1 is 0.5, and in this case, we made the following substitution for the feedback variable:

$$k_1(t) = \alpha_1 x_4(t) + \beta_1 \quad (7.35)$$

Where $x_4(t)$ is the new model output, and introduced in:

$$[M](t) = x_4^2(t) + 20 \quad (7.36)$$

We have performed identifiability analysis with and without the feedback equations (in which case there are seven free parameters).

7.2.4 Automated Optimization

Automated parameter estimation was performed using built-in Matlab functions (version 2009a, The Mathworks, Natick, MA). These included *lsqcurvefit* (which uses the Levenberg-Marquadt and Newton methods) and the Genetic Algorithm. Each parameter was bounded by zero as a minimum, but was given no maximum bound.

7.3 RESULTS

7.3.1 *A Priori* Identifiability

The identifiability analysis of the four-state model turned out to be computationally expensive. Each variation took hours to run, and the exhaustive summary for the most complicated model was over 150,000 characters long.

Table 7. Results of Identifiability Analysis

Model	# State Var.	# Outputs	# Paramters	Observable	Identifiable
4-state Model	----------				
Without Feedback	3	1	7	✓	Globally
Linear Feedback	3	1	9	✓	Globally
$\gamma_1 = 0.5, \gamma_f = 2$	3	1	9	✓	Globally

Each variation was both algebraically observable and globally identifiable.

7.3.2 Automated Optimization

Automated optimization was unable to calculate parameters with reasonable standard errors. A representative optimized parameter set is shown in **Table 8**. The R^2 for the fit is high; however, the standard error of each parameter exceeds the actual value estimated for that parameter. The ± standard error values in **Table 8** (and **Table 9**) are the 5% confidence limits of estimation calculated from the Jacobian matrix (not to confuse them with S.E.M. from experimental observations). The *P*-value compares the parameter to zero, and no parameter was significantly different from zero.

Table 8. Parameter Estimates from Levenberg-Marquadt Algorithm

Parameter	Value	*P* - value
k_2	99.0 ± 299	N.S.
k_3	5.70 ± 319	N.S.
k_4	407 ± 687	N.S.
g	434 ± 4210	N.S.
d	137 ± 394	N.S.
α_1	1.58 ± 4.24	N.S.
β_1	0.145 ± 0.344	N.S.
α_f	0 .00 ± 5.16	N.S.
β_f	35.2 ± 107	N.S.
R^2	0.995	

This was a typical result, and indicates that automated optimization cannot reliably identify the unique solution, despite the identifiability analysis indicating that the four-state model was *a priori* globally identifiable (see **Section 7.3.1**). It is a bit of a misnomer to refer to it as "identifiability analysis", however, since it does not determine if the unique parameter set is

identifiable. Instead, identifiability analysis determines whether a unique parameter set *exists* for a given input-output pair and model structure [111]. It is an important analysis to do, even if the model is not being used for the inverse problem. In this case, that unique parameter set was not attainable using a variety of automated procedures.

Why was the model theoretically identifiable but not practically identifiable by automated optimization procedures? There are many challenges in numerical parameter optimization (see **Section 8.7.1**), but a sensitivity analysis of the four-state model (see **Appendix D**) revealed some important details. A number of the model parameters had only a small effect on the time-varying data. However, when the model was used to simulate steady-state force-pCa data, these parameters had a larger effect (**Table 21**).

In order to further explore this idea, we used the four-state model to generate synthetic dynamic data using a known parameter set, and applied automated optimization to determine whether it was possible to recover the parameter set from this synthetic data.

One of the assumptions made by the DAISY differential algebra analysis is a noise free data set. Intracellular calcium transients are associated with a fair amount of noise due to the nature of the measuring technique. Even signal averaging can only reduce the noise, not eliminate it. Therefore, we used a model to approximate the time-varying calcium transient. The model input is described by **Equation 7.37**:

$$[Ca]_i(t) = A(1 - e^{-Bt})(e^{-Ct}) \tag{7.37}$$

where A = 1.739 μM, B = 205.89 s^{-1}, and C = 30.52 s^{-1}.

Parameter optimization on the synthetic dynamic data alone showed that the parameters associated with largest sensitivity for the dynamic data (k_3, *g*, and *d:* see **Table 2 1**) were accurately estimated, and associated with reasonable standard error values (**Table 9**, see values

highlighted in gray), while those associated with low sensitivity were less accurately estimated and associated with large standard errors. Nonetheless, the overall model fit was very good (R^2 > 0.99, **Table 9** and **Figure 7-3**).

Table 9. Values for Parameter Estimation on Synthetic Data

Parameter	Synthetic Data	Fit to Dyamic Synthetic Data	Fit to Dynamic + Steady State Synthetic Data
k_2	25	3.42 ± 144	24.6 ± 0.044
k_3	84	93.3 ± 13.3	86.2 ± 0.176
k_4	84	80.0 ± 55.9	82.9 ± 0.147
g	205.3	201 ± 76.3	206 ± 0.349
d	44.6	42.5 ± 4.07	44.0 ± 0.067
α_1	2	1.50 ± 15.9	2.04 ± 0.003
β_1	3	2.63 ± 15.0	3.05 ± 0.003
α_f	0.15	0.130 ± 1.18	0.150 ± 0.001
β_f	0.7	0.839 ± 4.78	0.705 ± 0.001
R^2	N/A	> 0.99	> 0.99

We then generated synthetic steady-state data using the same parameter set used to create the synthetic dynamic data. For the steady state data, constant levels of calcium were used as input. Automated parameter optimization was used to fit both dynamic and steady-state data simultaneously, which resulted in accurate estimation of all model parameters and standard error values several orders of magnitude smaller than those associated with parameters fit to only the dynamic data (Table 9). The overall model fit using the combined data was excellent (R^2 > 0.99, **Table 9** and **Figure 7-3**).

These findings indicated that the difficulty in using parameter estimation on the experimental data arose because the input/output pair for the twitch contraction lacked the necessary informational content. To compensate for this, the model should be fit to dynamic and

steady-state data simultaneously. However, dynamic and steady-state experimental data were not collected under the same conditions and so they could not be paired. Therefore, another form of model-based analysis was required.

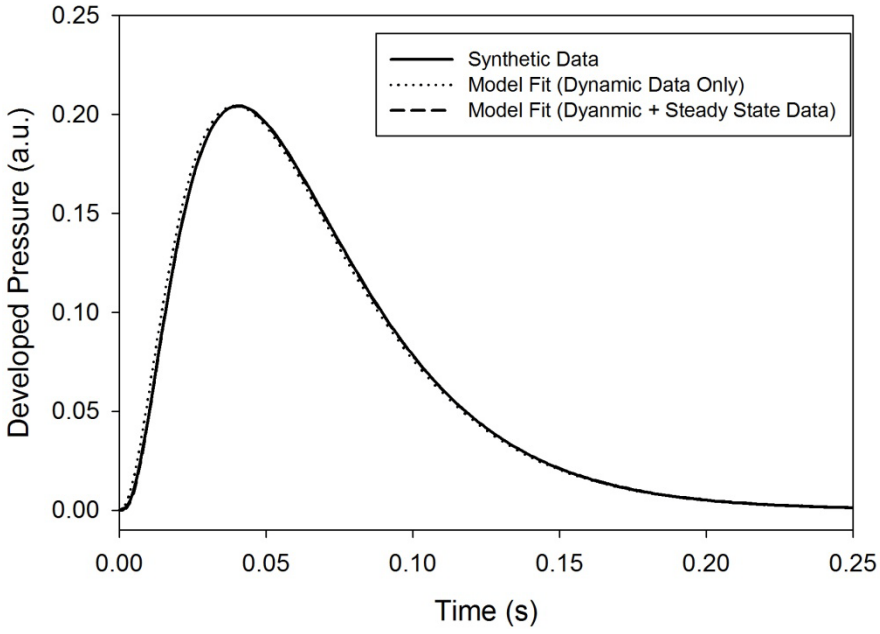

Figure 7-3. Synthetic and Model-Fit Pressure Waveform

Pressure waveforms (arbitrary units) for model-generated synthetic data (solid line) and model-based fits (parameter optimization) to dynamic data only (dotted line) or dynamic and steady-state data simultaneously (dashed line).

7.3.3 Model-Based Interpretation of Experimental Data

Instead of trying to fit the whole raw data set, we attempted to simulate the dynamic and steady-state functional differences between the WT and TG-E mice identified here (see **Section 5** and **Section 6**). The goal was to first identify a "baseline" parameter set that created data similar to the WT mice, and then determine the minimum number of parameters required to simultaneously recapitulate all of the differences in the TG-E mouse. In order to do this, we

wrote a Matlab program which could simultaneously calculate time-varying and steady-state data (see **Appendix C**).

We identified three changes in the TG-E mouse that we wished to recreate: a decrease in peak developed force/pressure (see **Section 5. 3.2.1** and **Section 6.3. 1.1**), an increase in relaxation time (see **Section 5.3.2.1** and **Section 6.3.1.1)**, and a decrease in F_{max} (see **Section 6.3.2**). There were also three indices that should not be significantly altered between the groups: pCa_{50}, the Hill coefficient, and the tension cost (see **Section 6.3.2**).

We also simplified the system by determining if any parameters could be estimated from our experimental data. The slope of the force–ATPase activity relationship is an estimate of the tension cost, and represents the rate constant of cross-bridge detachment (g) [112, 113]. The TG-E mice exhibited no change in tension cost compared to WT mice (see **Section 6.3 .2**), implying unaltered g in the TG-E mouse.

The relationship between g and tension cost as defined by Brenner [112] applies to the two state model used in that paper. In the four-state model used here, tension cost and g are not synonymous. As discussed above, model parameter d also affects steady-state ATPase; but its contribution relative to the effects of g is small (7.8% (average over all activation levels) of the total ATPase rate calculation, see Sensitivity Analysis in **Appendix D**).

Since there were no differences in the intracellular calcium transients in the WT and TG-E mice (see **Section 6.3.1.1**), we used the same simulated transient as the input for both.

The first step was to identify a baseline parameter set. We used estimated parameters from past work with the four-state model [83, 102-105], making slight alterations to match the WT data. The following parameters were used for the baseline: α_1 ($\mu M^{-2} \bullet s^{-1}$) = 2.0, β_1

($\mu M^{-1} \bullet s^{-1}$) = 3, α_f ($\mu M^{-2} \bullet s^{-1}$) = 0.15, β_f ($\mu M^{-1} \bullet s^{-1}$) = 0.7, k_2 ($\mu M^{-1} \bullet s^{-1}$) = 25, k_3 (s^{-1}) = 84, k_4 (s^{-1}) = 84, g (s^{-1}) = 205.3, d (s^{-1}) = 44.6, γ_1 = 1.25, and γ_f = 1.

Decreasing the value of *f* (23%) predicted the observed decrease in maximum twitch force and F_{max} but no change in relaxation time under twitching conditions. However, we experimentally observed an increase in relaxation time. There must be a parameter (or set of parameters), altered simultaneously with *f*, that would produce decreased magnitude of contraction (both under twitching and steady-state conditions), increased relaxation time, and no change in calcium sensitivity or tension cost. We focused on parameters that would maintain the activation state: (1) increased calcium binding (i.e., increase k_1), and (2) decreased crossbridge dissolution in the absence of cTnC-bound calcium (i.e., decreased *d*). Although the first perturbation can produce slowed relaxation, it was unable to reconcile all of the experimental observations.

The second perturbation (a decrease in *f* by 23% and a decrease in *d* by 35%) was able to reproduce the time-varying experiment observations (see **Figure 7-4**), the steady state experiment observations (see **Figure 7-5**) and the tension cost estimate (see **Figure 7-6**). The magnitude of these changes closely mirrored the results observed in the isolated heart (14% negative inotropy, 20% negative lusitropy) and skinned fiber (14% decrease in F_{max}, less than 2% change in pCa_{50}, n_H, and tension cost).

These magnitudes acted as a guide. The goal here was not to identify exact parameter values, but identify a plausible solution which explained the major findings of our experiments. It is necessary to point out that there is no mathematical proof that this is a unique solution. However, we systematically varied all model parameters and found only one solution. Moreover,

there is some experimental evidence to corroborate changes in these parameters (see **Section 8.7**).

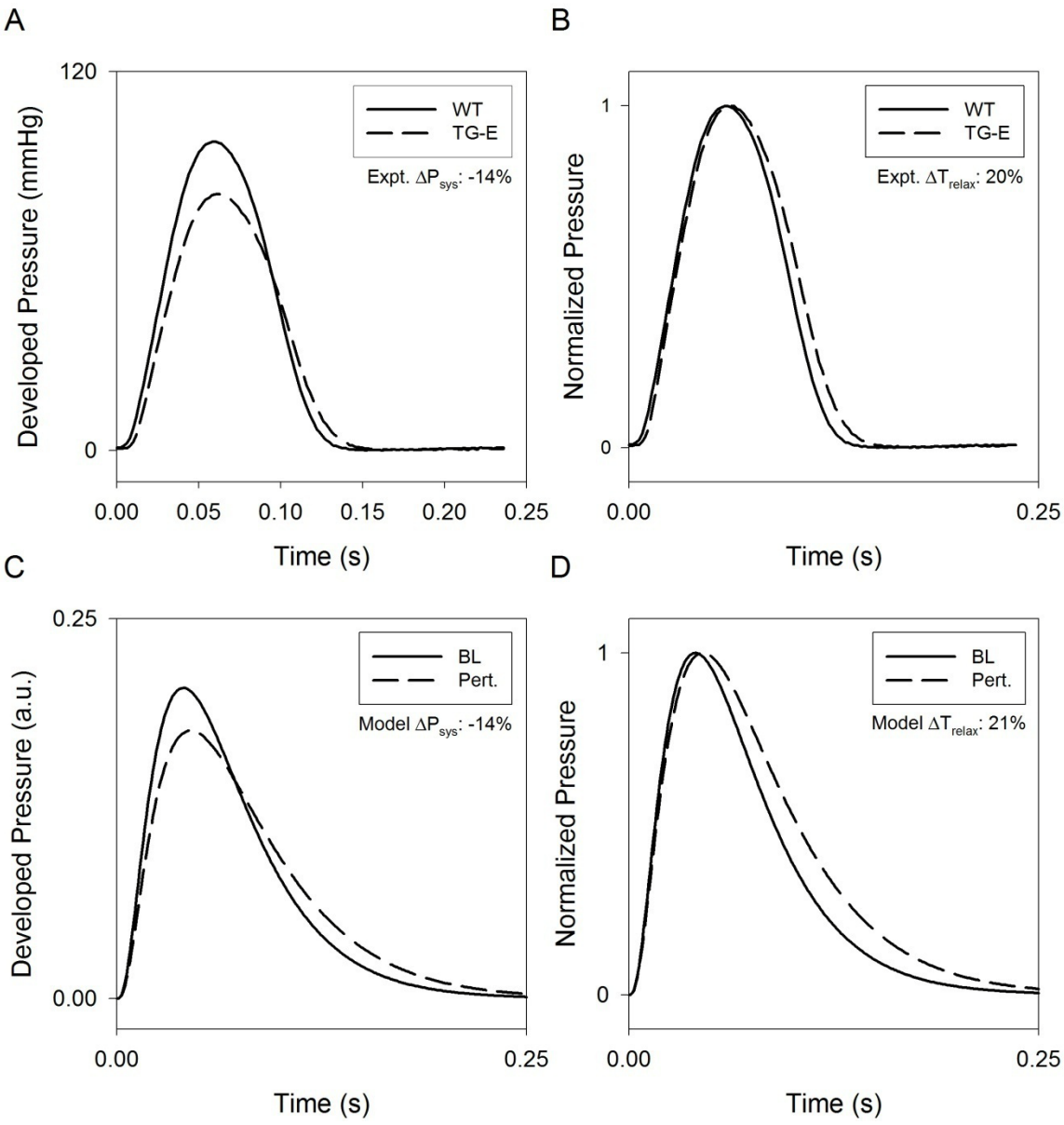

Figure 7-4. Experimental and Model Calculated Pressure Waveforms

Experimental (A,B) and Model (C, D) derived pressure data, shown as absolute values (A, C) and normalized values (B, D) from WT/BL (baseline) (solid) and TG-E/Pert. (perturbation) (dashed) data. Percent change between the WT/BL and TG/Pert. indices shown below the legend in appropriate panels.

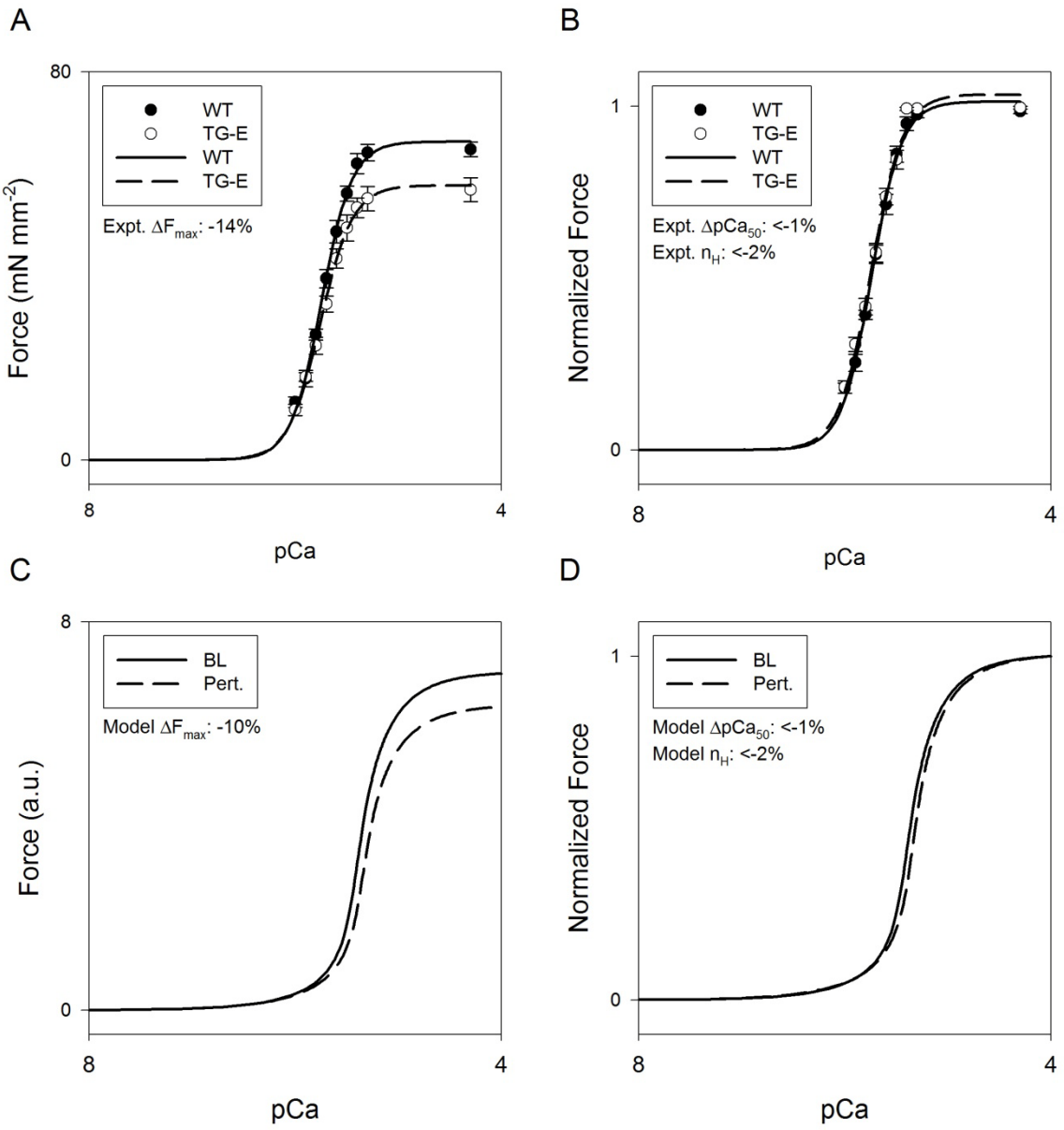

Figure 7-5. Experimental and Model Calculated pCa-Force Plots

Experimental (A,B) and Model (C, D) derived stead-state data, shown as absolute values (A, C) and normalized values (B, D) from WT/BL (baseline) (solid) and TG-E/Pert. (perturbation) (dashed) data. Percent change between the WT/BL and TG/Pert. indices shown below the legend in appropriate panels.

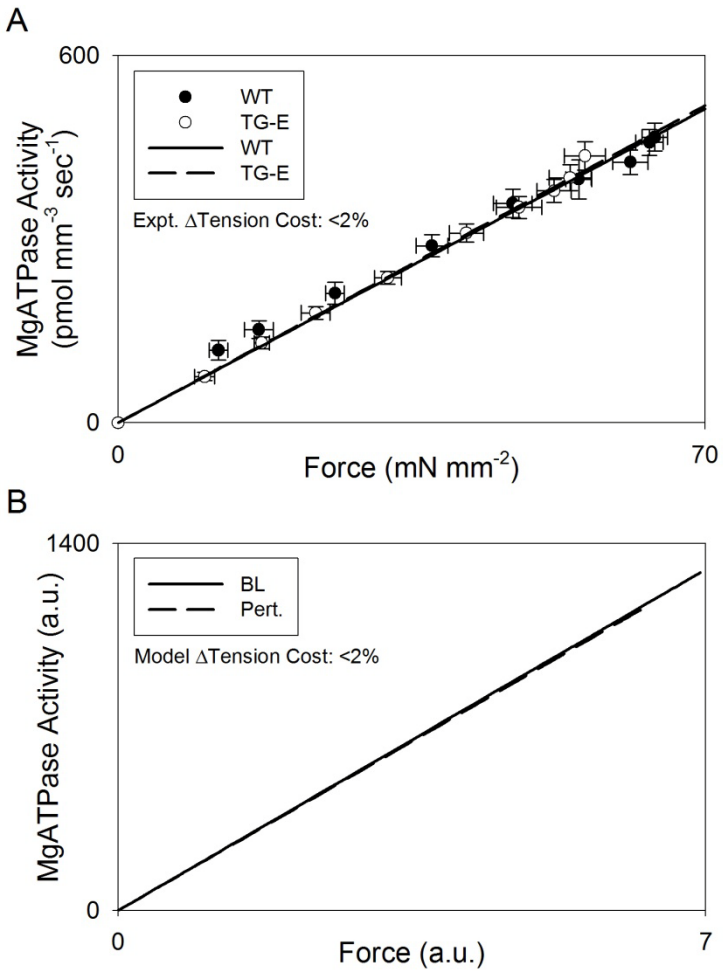

Figure 7-6. Experimental and Model Calculated Force-ATPase Relationships

Experimental (A) and Model (B) derived tension cost, from WT/BL (baseline) (solid) and TG-E/Pert. (perturbation) (dashed) data. Percent change between the WT/BL and TG/Pert. indices shown below the legend in appropriate panels.

We chose to model the isolated heart data for three reasons: (1) the isolated heart experiment represents more physiological conditions compared to the isolated papillary muscle experiment, (2) there was a great deal of variability in the papillary muscle data, and (3) data from isolated heart and skinned fiber preparations were quantitatively consistent (e.g., magnitudes of ΔP_{dev} at V_{max} and ΔF_{max} were similar).

The experimental data and the model-based analysis suggest that the TG-E mouse has two altered myofilament processes: decreased *f* and a calcium-independent persistence of the active state.

7.4 SUMMARY

The differential algebra tool DAISY found the four-state model to be *a priori* globally identifiable, although automated optimization proved to be unreliable. We decided to conduct *in silico* experiments to identify what parameters would recreate our experimental observations.

The model-based analysis revealed that the experimental observations in TG-E mice could be reproduced by two simultaneous perturbations: a decrease in the rate constant of crossbridge dissolution (*f*) and an increase in calcium-independent persistence of the myofilament active state (*d*).

8.0 DISCUSSION

8.1 HYPOTHESES

Hypothesis 1: Increased cTnI phosphorylation at the PKC sites will result in systolic dysfunction and protection from ischemic contracture at the whole organ level

The results presented in **Section 5.3.1** and **Section 5.3.2.1** show that the TG-E mice exhibited systolic dysfunction, evidenced by an increased LVESd in echocardiographic data, and a decreased peak developed pressure in isolated heart data. The results of the ischemia-reperfusion experiments (**Section 5.3.2.2**) indicated that the TG-E mice have no added protection from ischemic contracture, compared to WT mice.

Part of hypothesis 1 is supported by our results: increased cTnI phosphorylation at the PKC sites *does* result in systolic dysfunction. However, the second half of the thesis has been disproven: increased cTnI phosphorylation at the PKC sites *does not* result in protection from ischemic contracture at the whole organ level.

Hypothesis 2: Increased cTnI phosphorylation at the PKC sites will result in depressed calcium-force and ATP-force relationships (less force per calcium or ATP hydrolyzed).

In **Section 6.3.1.1** the TG-E mice had decreased developed force, with no change in intracellular calcium, indicating less twitch force per unit calcium compared to WT mice. The results in **Section 6.3.2** showed that there was a reduction in F_{max} for fixed calcium levels, also

indicating depressed calcium-force relationship. In this same section, there was no change in the ATPase-force relationship (the tension cost) between the WT and TG-E mice. Protocol length restricted our ability to record intracellular calcium during acute phosphorylation experiments.

Our results support the first part of hypothesis 2, indicating that increased cTnI phosphorylation at the PKC sites *does* result in depressed calcium-force relationship. However, we have found that there is *no change* in the ATPase-force relationship.

Hypothesis 3: A model-based analysis of data from Specific Aims 1 and 2 will provide an integrative interpretation of increased cTnI phosphorylation at the PKC sites.

The results of the identifiability analysis (**Section 7.3.1**) indicate that the four-state model we selected for the model-based analysis is capable of providing unique solutions from the data. The model-based analysis was able to recreate the negative inotropy, negative lusitropy, decrease in F_{max} with no change in pCa_{50} or the tension cost that were experimentally observed in the TG-E mice (**Section 7.3.2**). All of these results were recreated with two model parameter perturbations.

Thus, a model-based analysis of data from Specific Aims 1 and 2 *did* provide an integrative interpretation of increased cTnI phosphorylation at the PKC sites.

8.2 INITIAL CHARACTERIZATION

The TG-E mouse showed a 7.2% replacement of endogenous cTnI with mutant cTnI. There were no differences in the level of other phosphorylated species of cTnI (unphosphorylated and one through five sites phosphorylated). Therefore, there is an increase in total phosphorylation of cTnI at the PKC sites: the summation of basal phosphorylation

(unchanged in TG-E mice) and pseudo-phosphorylation (increased by 7.2% in TG-E mice). Recent evidence indicates that basal *in vivo* cTnI phosphorylation at the PKC sites is very low [38, 114]. Thus, the percent replacement in our TG mice, although small, may represent a physiologically relevant level of increased PKC cTnI phosphorylation.

The other mouse model, TG-A (serine 43 and 45 mutated to alanine), showed a ~50% replacement of endogenous cTnI by the mutant cTnI [61]. Thus, the TG-E and TG-A mice represent cTnI phosphorylation changes in opposite directions and of differing magnitudes. However, given the low basal phosphorylation state, a higher replacement of non-phosphorylatable sites would be required to observe functional effects.

There were also no alterations in phosphorylation of Tm, TnT, ELC or MyBP-C, indicating that the observed effects were from cTnI PKC phosphorylation alone.

Transgenic mouse models are not a panacea; there can be some limitations associated with these models. For example, it is important to verify that the observed functional effects are due to changes made in the transgene (i.e., PKC phosphorylation of cTnI in our case), and not an unintentional side-effect of inserting the transgene. It is possible that when the mutant cTnI transgene randomly inserted into the genome it split the coding region for another protein, changing the transgenic animal in an unforeseen and unpredictable manner. Usually, this possibility is eliminated by studying multiple lines, where the transgene would have randomly inserted into different locations in each line. Unfortunately, we only had one line for our transgenic mouse. This is a limitation of the study, which we partially addressed by examining the phosphorylation status of other key myofilamental proteins (see **Section 4.5.2**) and performing acute phosphorylation experiments (see **Section 6.3.1.2**). While not a replacement for multiple transgenic lines, since we cannot completely eliminate the possibility that the

transgene altered or eliminated an important gene during its incorporation, the results of these two experiments provide reasonable evidence that the functional effects we observed were most likely due to the mutation (i.e., increased PKC phosphorylation of cTnI), and not a side effect of the creation of the transgenic mouse.

8.3 CONTRACTION AND RELAXATION

There was evidence of reduced contraction in the TG-E mice compared to WT mice at all levels studied: (1) echocardiographic studies revealed decreased LVESd, (2) isolated heart studies showed depressed developed pressures over the entire volume range, (3) intact papillary muscles exhibited lower developed force over the entire set of lengths, and (4) skinned fibers showed significantly lower F_{max}. In reconstituted fibers where cTnI PKC phosphorylation sites were rendered constitutively pseudo-phosphorylated, a decrease in F_{max} was also seen [51]. The TG-A mouse model showed an increase in developed pressures at high extracellular calcium levels (3.5 mmol/L [Ca]) [60]. Together with previous data, the new transgenic model supports the hypothesis that phosphorylation of cTnI by PKC lowers the ability of the myocardium to generate active force, under both dynamic and steady-state activations.

In echocardiographic, isolated heart and intact papillary experiments, TG-E mice also showed negative lusitropy when compared to control mice. This is consistent with the results of Pi *et al.,* who treated wild-type mice with the PKC activator ET-1 and observed an increase in relaxation time (negative lusitropy) [55]. Furthermore, in their transgenic animal, in which all 5 cTnI phosphorylation sites were replaced with alanines, the effects of ET-1 were severely

blunted. These results, combined with the results presented here, suggest that phosphorylation of the PKC sites on cTnI has a negative lusitropic effect.

By that same logic, the TG-A mouse would be expected to exhibit positive lusitropy. Contrary to this, however, our own work in isolated hearts provides no evidence of change [60]. In the TG-A mouse, the T144 is not mutated to an unphosphorylatable alanine, leaving its phosphorylation level near baseline levels. It is possible that phosphorylation at position T144 on cTnI is primarily responsible for PKC-induced slowing of relaxation. If this were true, then it follows that the TG-A mouse may not show differences compared to WT mice.

8.4 ISOLATED HEART AND ECHOCARDIOGRAPHY

8.4.1 Heart Rate

Echocardiographic data showed that the TG-E mice had a lower heart rate (mild bradycardia) compared to the WT mice (see **Section 5.3.1**). Given the interplay between heart rate and heart failure [115], there was a concern that the mutation resulted solely in a depressed heart rate, and all other functional effects were a long-term consequence of this reduced heart rate. When WT mice were subjected to acute phosphorylation treatment, the functional changes mimicked those seen in the TG-E mouse (see **Section 6.3.1.2**). The WT mice, however, had never been exposed to reduced heart rates, making it unlikely that our observations in the TG-E mouse were a response to chronic bradycardia.

8.4.2 Response to Ischemia

TG-A mice have shown increased susceptibility to ischemic contracture [57]. This was based on a significant increase in diastolic pressures compared to WT mice during the ischemic and reperfusion periods in isolated hearts, as shown in **Figure 8-1**. Based on these results, we expected that constitutive phosphorylation of these sites might confer protection from ischemic contracture. However, our data did not support this expectation (see **Figure 5-7**, **Section 5.3.2.2**).

We did not treat either WT or TG-E mice with anything to control phosphorylation. Therefore the WT myocardium was free to respond to stresses as it would under normal conditions. In the case of ischemia/reperfusion injury, it would attempt to protect itself by upregulating PKC [116]. Because the WT and TG-E mice had similar responses to ischemia/reperfusion, we hypothesized that the phosphorylation state of cTnI in the two strains may have been similar as well.

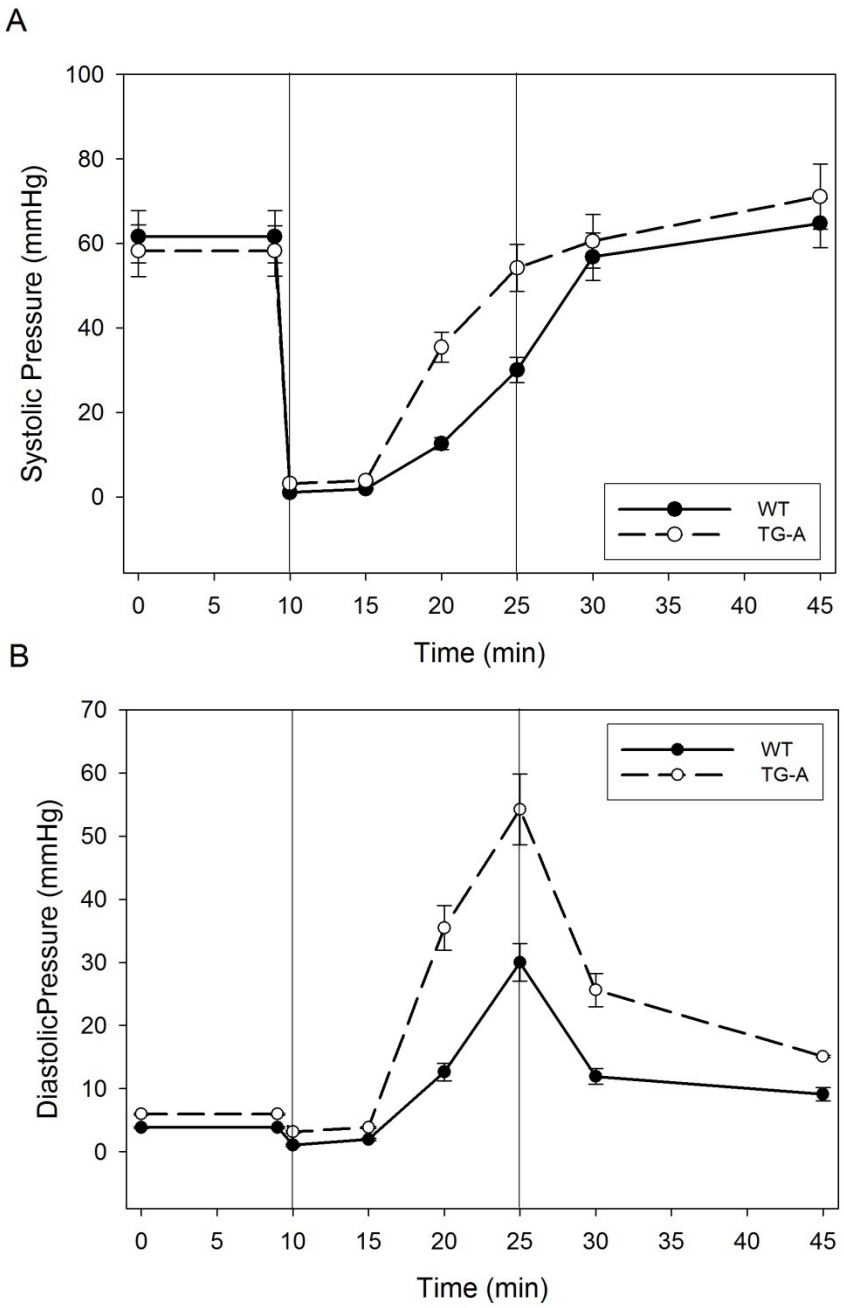

Figure 8-1. WT vs. TG-A Response to Ischemia-Reperfusion

LV pressure from WT and TG-A mice during ischemia and reperfusion, modified from [57]. At five minutes (first vertical line), coronary flow is reduced to zero and ischemia begins. At twenty minutes (second vertical line), flow is restored and reperfusion begins. Protocol lasts 40 minutes total. (A) Systolic pressures. There were no statistical differences between WT (black) and TG-A (white) pressures. (B) Diastolic pressures. The TG-A (white) mice showed significant susceptibility to diastolic contracture compared to WT (black). Data are mean ± S.E.M..

8.4.3 Response to β-adrenergic Stimulation

The TG-E and WT mice responded similarly to isoproterenol (1μmol/L) infusion: an increase in developed pressure and a decrease in rise and relaxation times. β-adrenergic stimulation acts through cAMP mediated activation of PKA-activated pathways. Specifically, PKA phosphorylates specific sites on cTnI (S23 and S24) and cellular calcium handling proteins (e.g., sarcoplasmic reticulum ATPase pump, L-type calcium channels), which result in positive inotropy and faster relaxation [31, 33, 117]. These results show that the mutation we introduced in cTnI did not affect these PKA-dependent pathways, suggesting that β- and α- adrenergic stimulation of cTnI are distinct, and may not have any interaction in their effects on cardiac function.

8.5 ISOLATED PAPILLARY MUSCLE

8.5.1 Intracellular Calcium Transients

There were no differences in intracellular calcium amplitude or relaxation between the WT and TG-E mice, or with PKC activation through phenylephrine treatment. We have previously seen in the TG-A mice that there were also no differences in intracellular calcium at normal extracellular calcium levels [57]. Others have also shown that there are no changes in intracellular calcium with PKC phosphorylation of cTnI [55, 58].

There are several limitations in the methodology of measuring intracellular calcium transients. An intact papillary muscle is a live system, and it is difficult to reliably measure an

intracellular process without disrupting the system. In order to detect intracellular calcium, fura must bind to it, which it does because fura is derived from the calcium chelator BAPTA [91]. The problem is that intracellular calcium buffering can occur, specifically with fura-2 [118], which has a high binding affinity for calcium (k_d = 224 nM). Moreover, the high binding affinity can slow its dissociation from calcium during the relaxation (descending) phase of the calcium transient, leading to a perceived increase in relaxation times compared to measurements using other calcium indicators [119]. In order to reduce the impact of these limitations, we used an alternate form of fura-2, fura-5F, which has a higher k_d value (400 nM), and thus dissociates from calcium more readily.

Another limitation is compartmentalization, which arises from the loading method used here. We used the acetoxymethylester (AM) form of fura, which is cell-permeant and can diffuse across membranes. Once the dye is in the cytoplasm, nonspecific esterases hydrolyze the AM form, removing its ability to move across the membrane and activating the calcium sensitive dye. However, it is possible for the dye to enter other intracellular organelles before it is activated, removing its ability to measure cytoplasmic calcium. It is estimated that up to 29% of fura-2 could be compartmentalized [120], particularly in the mitochondria [121]. This makes it difficult to determine absolute levels of intracellular calcium (see **Section 6.1.1.1**), but should not affect our ability to compare intracellular calcium transients that were collected under identical experimental conditions.

Lastly, this is a measurement of intracellular free calcium, not calcium bound to troponin C. We assume that the free calcium and TnC-bound calcium follow the same time path, but it is not necessarily true. Suppose we observe an increase in relaxation time of the free calcium transient and assume this means elongation of bound TnC calcium; this is a legitimate

assumption, but the observation could also indicate faster dissociation of calcium from TnC, thus increasing the free form of calcium. In fact, there are many intracellular pathways that can increase or decrease free calcium concentration. There is currently no way to definitively measure the calcium which activates the myofilament, and so care must be taken while analyzing data from intracellular free calcium transients.

8.5.2 Acute Phosphorylation

The goal of the acute cTnI phosphorylation experiments was to extend the results of Montgomery *et al.* [95]. In that study, right ventricular papillary muscles from WT FVB and TG-A mice were treated with 30 μM phenylephrine in the presence of 1 μM propranolol. They found that there was a 62% reduction in peak twitch force in the WT mice, and only a 45% reduction in the TG-A mice. They attribute this blunted response to the inability of PKC to phosphorylate the alanines on the mutant cTnI expressed in the TG-A mice.

We decided to use phenylephrine with propranolol as well, due to its common usage as an α_1-adrenergic stimulator in mice [122-124]. We observed a negative inotropic response in the WT mice, as well as a negative lustropic response. While we had hypothesized that the TG-E mouse would have a blunted response to α_1-adrenergic stimulation, the mice responded similarly to the WT mice, showing negative inotropy and lusitropy of comparable magnitude.

The difference in response between the TG-A and TG-E mice compared to the WT mice is likely due to the large difference in expression of the transgenic cTnI. The TG-A mice exhibited approximately 50% replacement of endogenous cTnI with the mutant cTnI [61]. Thus, the alanines on the mutant cTnI would be fairly effective at blocking the PKC phosphorylation activated by the α_1-adrenergic stimulation.

However, the TG-E mice have only 7.2% replacement of endogenous cTnI (see **Section 4.4.2**). While the glutamates that replaced the serines are just as effective as the alanines at blocking phosphorylation, there are not nearly as many of them. In fact, almost 93% of the PKC phosphorylation sites are free to be phosphorylated. Thus, it is unlikely there would be a significant difference between the WT and TG-E mice in their response to α_1-adrenergic stimulation.

The response itself fits in well with our other findings. In the echocardiographic, isolated heart, and isolated papillary data, we found that the TG-E mice had decreased force production and slowed relaxation compared to the WT mice. It is important to verify that these effects arise from actual PKC phosphorylation of cTnI, and not from another possible source arising from the formation of the transgenic mice. The fact that the acute treatment resulted in these same responses provides this evidence.

The limitation of this study stems from PKC's ability to phosphorylate other myofilamental proteins (see **Section 1.2**), and so the effects observed may be due to phosphorylation of proteins other than cTnI. However, this seems unlikely given the agreement of these data with the transgenic data.

8.6 SKINNED FIBERS

8.6.1 Calcium Sensitivity

The TG-E mice did not exhibit differences in calcium sensitivity compared to WT mice. Burkart *et al.* conducted experiments on detergent-extracted cardiac fibers reconstituted with

three forms of mutant cTnI that were pseudo phosphorylated at the PKC sites: S43E/S45E, S43E/S45E/T144E, and T144E [51]. They showed that S43E/S45E and S43E/S45E/T144E fibers exhibited similar decreases in calcium sensitivity. However, there was no change in calcium sensitivity in T144E fibers, suggesting that phosphorylation at this site plays no role. This is inconsistent with data from Wang *et al.* in which chemical phosphorylation of T144 by PKC-βII resulted in increased calcium sensitivity [125].

The reconstituted fibers studied by Burkart *et al.* showed a much higher replacement of endogenous cTnI with the mutant form (70-97%) than was present in our TG-E mouse. Wang *et al.* found that PKC-βII caused a 20-50% incorporation of radiolabeled phosphate, which was much closer to the level of phosphorylation simulated by our mutant cTnI. This suggests calcium sensitivity may be affected differently at very high, possibly non-physiologic, levels of PKC phosphorylation of cTnI.

Since our model simulates phosphorylation at all three PKC sites, it is possible there are two offsetting effects on calcium sensitivity; a decrease in calcium sensitivity due to the (pseudo)phosphorylation at S43/S45 and an increase in calcium sensitivity in response to the (pseudo)phosphorylation at T144. This possibility raises the question: if PKC phosphorylates all three positions, what is the purpose of mutually offsetting effects at the different sites? One possibility is that certain PKC isoforms only phosphorylate or preferentially phosphorylate a given residue, resulting in unequal phosphorylation on the three sites. For example, PKC-βII [125] and tyrosine-phosphorylated PKCδ [126] preferentially phosphorylate T144.

8.6.2 ATPase Activity

We observed a decrease in maximal ATPase activity of approximately 9%, although this was not quite statistically significant. Pyle *et al*. saw a decrease in ATPase activity and F_{max}, leading to no change in tension cost in WT papillary muscles treated with phenylephrine plus propranolol [61].

8.7 INTEGRATIVE AND MODEL-BASED INTERPRETATION

8.7.1 Parameter Identifiability Challenges

Analysis with DAISY revealed that the four-state model is globally identifiable, but there are many obstacles when identifying the unique parameter set in practice. In the case of the four-state model, we discovered the issue involved the informational content of our input/output pair. However, in general, additional difficulties can arise from the complexity of the solution space. If the solution space is discontinuous, an automated optimization algorithm may generate errors when it attempts to find solutions in these areas. More complicated procedures, like Genetic Algorithms, however, can avoid this problem because they search for multiple solutions at the same time.

The solution space may also contain many local minima and basins of attraction. These can lead an optimization algorithm to find a solution which does not represent the global minima. In order to find the true global minima, much iteration may be required to be certain that the best solution has actually been found.

If the experimental data the model is trying to fit involves multiple processes with varying time constants, the error function may not produce reasonable values. The pressure waveform from an isolated heart has a fast decay period followed by a relatively steady-state diastolic period. The method of calculation of the error between the model and experimental data becomes very important. Assume the error is represented by the vertical difference (in the y-direction) between the waveforms. In this case, if the fast decay period is shifted by only a small degree in the x-direction, the error value would be very large, considering only a small parameter change may be necessary to improve the fit. However, if the error is represented by the horizontal difference (in the x-direction) between the waveforms, a small difference during the diastolic period would results in very large errors. It is very difficult to accurately represent the error between the data and the model in situations like this.

8.7.2 Site Specificity

While the experimental data were explained by a simultaneous decrease in model parameters *g* and *d*, it is possible to model the effects of each change independently. The four-state model indicated that an independent decrease in *d* was associated with an increase in calcium sensitivity and slowed relaxation. As discussed earlier, experimental data suggest that T144 phosphorylation causes an increase in calcium sensitivity [125] and is primarily responsible for slowed relaxation (see **Section 8.3**). Burkart *et al*. [51] found that reconstituted detergent-extracted cardiac fibers mutating S43/S45 and S43/S45/T144 to glutamates caused a depression in maximal force, but mutating only T144 resulted in no significant change in F_{max}. There was even a slight, though non-significant, increase in maximal force in the T144E mutant,

which we saw in the model when only *d* was altered. For these reasons, it is tempting to attribute the decrease in *d* to T144 phosphorylation.

Likewise, the model indicated that an independent decrease in *f* was associated with a decrease in calcium sensitivity, no change in relaxation, negative inotropy, and decreased maximal ATPase activity. Experimental data suggest that phosphorylation of S43 and S45 results in decreased calcium sensitivity [51], no change in relaxation [60], and negative inotropy [60]. Thus, it is possible that the decrease in *f* is a result of S43 and S45 phosphorylation.

This is also supported by a recent paper by Mathur *et al*. [127], in which they studied the effects of three mutant cTnI's (S45E, S43E/S45E and S43E/S45E/T144E) expressed in an isolated actin/myosin system. They found that the S45E mutation alone was sufficient to lower the ATPase rate, which is consistent with phosphorylation at S43/S45 resulting in a decrease in *f*. This also supports the hypothesis that T144 phosphorylation causes the change in *d*, which has little affect on the ATPase rate.

8.7.3 Biophysical Basis for Model-Based Interpretations

There is evidence that the introduction of negative charges at S43 and S45 stabilizes the N-terminus region and increases the interaction of the inhibitory region with actin [128]. This leads to a stabilization of the inactive form of actin [127]. If the phosphorylation of cTnI at the PKC sites stabilized the inactive form of actin, when myosin binds to it, it is less likely to hydrolyze ATP and generate force. In the four-state model, there is no pathway for inactive actin and so it is possible that a stabilization of inactive actin could be manifested in the model as a decrease in *f*.

There is also evidence that T144, but not S43 or S45, phosphorylation alters the interaction of cTnI with cTnC at the Ca^{2+} binding site [129]. Our model-based hypothesis is that T144 phosphorylation is responsible for a calcium-independent persistence of the myofilament active state. This could be mediated through altered interaction with cTnC and its interaction with calcium binding. While this is a tenuous connection, it provides a plausible explanation for our theory. Unfortunately, however, there is a paucity of work done on the T144 site.

We had assumed that *f, g,* and *d* represent the kinetic rate constants for formation and dissolution of force-generating crossbridges. However, this is a simplification of reality. The parameters *f, g,* and *d* are actually a mean field approximation of spatially distributed and interacting individual contractile units, the totality of which manifest as the "mean" rate constants of crossbridge formation and dissolution. It is likely that the overall (mean) values of *f, g,* and *d*. are determined by spatial distribution, organization, and interaction of these individual units, in addition to the kinetic rate constants of the individual units. One can imagine a situation where two mice have identical overall expression of a mutant myofilament protein, but different spatial distribution. It is possible that these two mice would have different values of *f, g,* or *d*.

In the end, the precise biophysical basis for the altered myofilament properties remains unknown. Although, given that the model parameters represent several biochemical processes lumped together, there exist many possible explanations for the model-based findings.

8.7.4 Functional "Gain"

The low level of mutant cTnI expression (7-8%, see **Section 4.5.2**) was unexpected, but resulted in significant functional effects. If the myofilament is visualized as many force-generating units working in parallel and series, it is difficult to envision how a change in 8% of

these units could result in the overall phenotype we observed. However, there are several possible explanations for the high functional “gain” of PKC phosphorylation of cTnI.

The first possibility is that the mutant cTnI had differential transmural expression. There is evidence that myosin isoforms are differentially expressed through the ventricular wall [130], so it is possible that the mutant cTnI was expressed at higher levels in either the endocardium or epicardium. This would result in a higher than 8% expression in a specific location and could produce large global functional effects.

It is also possible that a minority of mutant cTnI affect a much larger area by influencing neighboring functional units arranged in series or parallel. In skeletal muscle, it has been suggested that cooperative interaction can be sensed along the entire length of the thin filament [131]. It is also possible that the mutant cTnI may have changed the myofilament lattice spacing, altering the crossbridge kinetics (a mechanism observed for MyBP-C [132]) in an area surrounding a single mutant cTnI.

9.0 CONCLUSIONS

9.1 TAKE HOME MESSAGES

- Despite low integration of mutant protein, TG mice show significant functional changes, indicating high sensitivity of cardiac contraction to PKC cTnI phosphorylation.
- Increased PKC phosphorylation of cTnI resulted in decreased magnitude of contraction (decreased fractional shortening in echocardiographic data, decreased developed pressure in isolated hearts, decreased developed force in isolated papillary muscles, and decreased maximally activated force in skinned fibers).
- Increased PKC phosphorylation of cTnI resulted in slowed relaxation (longer peak to diastolic time in echocardiographic data, longer relaxation time in isolated hearts, and decreased magnitude of dF/dt_{min} in isolated papillary muscles).
- Increased PKC phosphorylation of cTnI resulted in no changes in calcium sensitivity, cooperativity, tension cost, or intracellular calcium transient (magnitude or relaxation).
- Identifiability analysis on the four-state model found it to be *a priori* globally identifiable; however, automated optimization was not effective.
- The model-based analysis revealed that the experimental observations in TG-E mice could be reproduced by two simultaneous perturbations: a decrease in *f* and an increase in calcium-independent persistence of the myofilament active state.

- Based on our data and data from the literature, we speculate that the effects of PKC-mediated cTnI phopshorylation are site-specific (S43/S45 *vs*. T144).

9.2 CLINICAL IMPLICATIONS

As covered in **Section 1.6** , PKC phosphorylation of cTnI may be involved in heart failure, either as a cause, a consequence, or compensation. The work done here shows several effects which depress cardiac function in a transgenic animal with increased phosphorylation of cTnI at the PKC sites. Nonetheless, the mouse did not appear to degenerate into heart failure, showing no cardiac hypertrophy (evidenced by no change in LVEDd, see **Section 5.3.1**) or external signs of depressed cardiac function such as lethargy or differences in eating patterns. This suggests that an ~8% increase in PKC phosphorylation of cTnI does not cause heart failure. Therefore, if PKC over-phosphorylation of cTnI is a cause or stimulating event for heart failure, it is at higher levels.

There may be utility in blocking PKC phosphorylation of cTnI in humans during heart failure as a treatment scheme [72, 133, 134]. Cardiac TnI is a useful target for therapy because of specificity of its expression in cardiac tissues, as evidenced by its use as a diagnostic marker for myocardial ischemia. As we have shown here, increased PKC phosphorylation of cTnI is associated with many negative effects, and blocking this pathway would help to assuage these. Moreover, there is high “gain” on the functional effect of phosphorylation at these sites.

The effects of PKC phosphorylation of cTnI are not all bad; there are beneficial effects as well. For example, PKC phosphorylation of cTnI exerts cardioprotective effects during ischemia-reperfusion injury (see **Section 5.3.2.2**), most likely through a decrease in myofilament ATPase

[135] (see **Section 6.3.2**). Thus, non-specific blocking of PKC phosphorylation of cTnI may not be a clinically viable strategy. More work is required to determine whether the positive and negative effects of PKC phosphorylation of cTnI follow different signaling pathways and if so, whether it is possible to selectively block pathways that produce negative effects.

9.3 FUTURE WORK

The quanitification of mutant mRNA in the transgenic mouse was unsuccessful in our earlier attempts. While we proved that the mutant protein was expressed (see **Section 4.5.2**), quantifying the mutant mRNA might help identify the cause of the low mutant protein expression. We originally used primers that would bind to the mutant cTnI sequence, but not the endogenous one, by targeting the mutated sites (S43, S45 or T144). However, it is possible to take advantage of the untranslated 3' region or introns to differentiate between the mutant and endogenous protein. Thus, the two ends of the endogenous cTnI sequence could be used to generate primers, and the RT-PCR products differentiated by weight.

While we performed acute phosphorylation experiments in papillary muscles (see **Section 6.2.2**), it would also be useful to treat skinned fibers with a PKC activator. Then it is possible to compare the change in F_{max} in the acute phosphorylation treatment fibers (if there is one) to the observed change in the transgenic fibers.

One of the findings of the modeling portion of this work is that the four-state model, while *a prior* globally identifiable, requires an information-rich data set (see **Section 7.3.2**). It is possible to increase the information content of the data set by providing paired dynamic and steady-state data. There are two experiments that could provide these data: skinned fibers with

caged calcium (dynamic response to activation level) and skinned fibers with length perturbations (dynamic response to length changes). Both of these experiments could be done on skinned fibers that had already produced steady-state (force-pCa and ATPase-pCa) data.

Caged calcium allows calcium to be near-instantly mobilized or chelated through flash photolysis [136, 137]. By nearly instantaneously decreasing or increasing the concentration of calcium available to the myofilament, we generate "step-inputs" into the system. Analyzing "step-input" responses can provide dynamic data that are simple to interpret. Length perturbations are made to a skinned fiber by stretching or shortening the fiber by a small amount (~1% total length), which creates a spike in force production, a return to a value near baseline, and then an approach to a new steady-state value [138]. This type of dynamic data comes at a trade-off, however, since muscle length would have to be incorporated into the model, which would increase its complexity.

One of the conjectures put forth here is the site specificity between S43/S45 and T144. It would be helpful to create additional transgenic mice expressing each of the mutant cTnIs used by Burkart *et al.* [51]. Experiments on these mice could help to clarify these issues.

There are also a number of hypotheses generated by this work that may be possible to test experimentally, but were outside the purview of this project. The first deals with the phosphorylation status of cTnI during ischemia/reperfusion. Since there was no difference between the WT and TG-E mice, we hypothesized that their phosphorylation status was similar. Flash freezing the heart in liquid nitrogen and then using 2D-DIGE to check the level of phosphorylation (see **Section 4.4**) could confirm this hypothesis.

The model-based hypotheses would also be useful to test. Specifically, investigating the biophysical basis for these effects – how does cTnI phosphorylation result in the effects in

crossbridge cycling that the model-based interpretation identified? Possible avenues of research including examining lattice spacing [35] and structural dynamics using FRET [139]. They are difficult to test, and few reliable techniques currently exist. In the future, new techniques may be available to test these hypotheses.

Given the utility of this transgenic mouse in understanding heart failure, it would be interesting to cross this mouse with a true heart failure model, and compare the phenotypes of the TG-E + heart failure mouse, TG-E mouse, heart failure mouse, and WT mouse. Does the increase in PKC phosphorylation of cTnI exacerbate the heart failure phenotype or is it more complicated than that? It would also be interesting to cross the heart failure mouse with a transgenic mouse in which the PKC phosphorylation sites on cTnI were unphosphorylatable.

There is no doubt of the utility of the mouse model for studying cardiac physiology and disease [140], but, obviously, a mouse is not a man. Care must be exercised when applying findings from a mouse to human cardiovascular function and disease [141]. One can question the extrapolation of mouse studies to humans, so future studies could focus on larger mammals.

APPENDIX A

PRESSURE-CALCIUM RELATIONSHIPS IN PERFUSED MOUSE HEARTS

While not directly related to the overall goals of this project, we were interested in the pressure-calcium relationships in WT mouse hearts. The following text and figures are modified from [83], and used here with permission.

The mouse heart has several distinguishing features compared to larger mammals, including an *in-vivo* heart rate of approximately 600 beats per minute [141]. Consequently, calcium handling in the mouse myocardium is also different from mammals with longer cardiac cycles. There exists an almost complete dependence on the sarcoplasmic reticulum to provide the calcium for myocyte contraction [1, 142]. Gao *et al.* [94] have characterized calcium cycling and contractile activation in mouse myocardium. They described a positive force-frequency relationship in isolated mouse myocardium, though the increase in force was greater than that expected from the underlying increase in intracellular free calcium, suggesting "frequency dependent sensitization" of the myofilaments. Their findings also showed that mouse myofilament had decreased calcium sensitivity and increased cooperativity under steady-state activation relative to other species.

Length-dependent activation in the mouse may have unique features as well. Typically, there are two components of length-dependent activation that are distinguishable from their temporal patterns of responses [143, 144]. The fast-acting early component is due to increased calcium sensitivity of the myofilament, and is the basis for the Frank-Starling relationship. The slow-acting late component is due to an increase in the calcium transient. Reyes *et al.* [145] have studied *in-vivo* hemodynamics in the anesthetized mouse using a conductance catheter to obtain pressure-volume loops. They demonstrated that increasing end-diastolic volume by aortic constriction resulted in an immediate increase in contractility. However, there was no further augmentation in contractility up to 7 minutes after the increase in load, suggesting that the late component of length-dependent activation was not operative in the mouse. Calcium transients were not measured in this study, and therefore the potential role of intracellular free calcium in the absence of the late component remains speculative.

The purpose of this study was to characterize the relationship between pressure and intracellular free calcium in the perfused mouse heart. Specifically, we were interested in the following questions: (1) Can peak developed pressure change significantly with a minimal change in the peak systolic intracellular free calcium?, (2) Is the late component of length-dependent activation absent?, and (3) What are the determinants of pressure relaxation? Two perturbations were used to alter pressure: changes in ventricular volume at a fixed stimulation interval (Frank-Starling protocol) and single-beat changes in stimulation interval at a fixed ventricular volume (mechanical restitution protocol). We used the isolated perfused mouse heart preparation and the calcium-sensitive fluorescent dye rhod-2 to record pairs of left ventricular (LV) pressure and intracellular free calcium concentration ($[Ca]_i$). This allowed us a more

physiological assessment of murine myocardium compared to isolated tissue studies, as well as measurements of $[Ca]_i$ that are not possible with *in vivo* studies.

METHODS

Isolated perfused hearts experiments were performed as described in **Section 5.2.3**. The Frank-Starling protocol was performed as described in **Section 5.2.4**.

Fluorescence measurements. Methods to measure intracellular free calcium from the perfused mouse heart using the calcium sensitive fluorescent dye rhod-2 have previously been described in detail [146, 147]. In this study, several equipment modifications from the original descriptions have been made, which include use of a spectrofluorometer equipped with a 150 watt Xenon light source and 2 photomultiplier units (Photon Technology International, Lawrenceville, NJ). The heart was situated in a water-jacketed chamber kept at 37 ^oC, and placed against the optical window. Heart motion was prevented by an anterior-to-posterior stabilizer as well as two lateral stabilizers. Three light guides (3 mm core) were coupled to the surface of the mouse heart by placing them within 1 mm of a glass window of the heart warming chamber: one for excitation light, one to collect fluorescence emission, and one to collect reflected light that was used in the calibration of the fluorescence signal. The excitation and fluorescence emission light guides were placed in a horizontal plane and at 30^o and 70^o, respectively, with respect to the plane of the glass window. The light guide for reflected light was placed 45^o above the horizontal plane and at 70^o with respect to the glass window.

After baseline measurements, 100 μg of rhod-2 was loaded through the coronary perfusate, and after 20 minutes, fluorescence and absorbance measurements were taken. Fluorescence time-based scans were performed with excitation at 524 nm and emission at 589

nm, and a long pass filter (550 nm) placed in the emission light pathway. Fluorescence data were digitized on-line at 500 Hz for later off-line analysis. To account for dye washout, absorbance was calculated from a reflectance scan at 500 – 600 nm taken after each time-based fluorescence scan. At the end of the experiment the heart was tetanized with a bolus of 20 mM $CaCl_2$ with 10 μM cyclopiazonic acid (Sigma Chemical Co., St. Louis, MO) to determine the maximum fluorescence (F_{max}).

Quantification of the relative amount of rhod-2 in the heart was done by taking the ratio of reflectance at 524 nm (R_{524}, rhod-2 sensitive) to 589 nm (R_{589}, rhod-2 insensitive). Rhod-2 absorbance (A) was calculated according to the following formula [146, 148]:

$$A = \log\left\{\frac{\left(\frac{R_{524}}{R_{589}}\right)_0}{\left(\frac{R_{524}}{R_{589}}\right)_{rhod2}}\right\} \tag{A.1}$$

where subscripts "0" and "rhod2" indicate the reflectance ratio before and after dye loading, respectively. Intracellular free calcium was calculated using the following formula:

$$[Ca^{2+}]_i = \frac{\left(\frac{K_d(F_t - F_0)}{A_t}\right)}{\left(\frac{F_{max} - F_0}{A_{max}}\right) - \left(\frac{F_t - F_0}{A_t}\right)} \tag{A.2}$$

where K_d is the dissociation constant for rhod-2 and calcium (710 nM), F_t and A_t are fluorescence and dye absorbance at time t, F_0 is the fluorescence before dye loading, and F_{max} and A_{max} are maximal fluorescence obtained from the tetanized heart and dye absorbance just prior to tetanizing the heart, respectively.

Mechanical restitution protocol. All measurements were obtained in this protocol with LV volume set at V_{max} (identified in the Frank-Starling protocol). Pressure and fluorescence data

were recorded for steady-state contractions at the control pacing interval of 240 ms (i.e., control pulse interval, CPI) and for a test contraction with a single-beat perturbation of the pacing interval (i.e., test pulse interval, TPI). To achieve a range of pressure and calcium pairs, data were collected at four values of TPI (200, 400, 600, and 800 ms) and with the test contraction deployed in three ways: after a steady-state contraction (**Figure 9-1A**), after one extra-systole at 100 ms (**Figure 9-1B**), and after two extra-systoles at 100 and 200 ms (**Figure 9-1C**). Each experimental condition (i.e., a combination of TPI value and mode of deployment) was repeated 4 – 5 times.

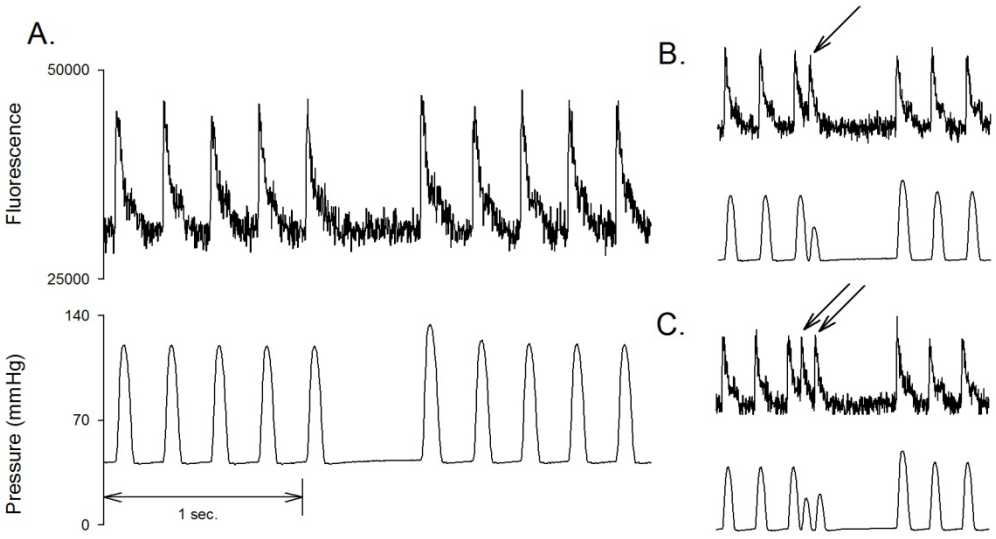

Figure 9-1. Example of Mechanical Restitution Protocol

Examples of fluorescence and left ventricular (LV) pressure data obtained during mechanical restitution protocols. **A**, **B**, and **C** correspond to protocol 1 (test pulse interval = 600 ms, no extra systole), protocol 2 (test pulse interval = 600 ms, 1 extra-systole indicated by arrow), and protocol 3 (test pulse interval = 600 ms, 2 extra-stimuli indicated by arrows), respectively. Following a prolonged test pulse interval there was potentiation of both LV pressure and systolic calcium with respect to the steady-state contractions.

Data analysis. Individual cardiac cycles were first identified using the spike in the pacer signal. Signal averaging over the cardiac cycle was then performed to reduce high-frequency random noise, especially in the calcium fluorescence signal. For the Frank-Starling protocol,

pressure and fluorescence data from 5-7 steady-state contractions at a given LV volume were averaged to yield a representative cycle. For the mechanical restitution protocol, up to 5 of the repeated measurements of each experimental condition were averaged to yield one representative cycle each for control and test contractions. LV pressure and calcium waveforms were characterized by several amplitude and rate indices. Amplitude indices included diastolic pressure (P_{dia}) and calcium ($[Ca]_{i\text{-}dia}$), peak systolic pressure (P_{sys}) and calcium ($[Ca]_{i\text{-}sys}$), and developed pressure ($P_{dev} = P_{sys} - P_{dia}$) and calcium ($[Ca]_{i\text{-}dev} = [Ca]_{i\text{-}sys} - [Ca]_{i\text{-}dia}$). Rate indices included maximal rate of rise (dP/dt_{max}, $d[Ca]_i/dt_{max}$), maximal rate of fall (dP/dt_{min}, $d[Ca]_i/dt_{min}$), rise time ($T_{rise\text{-}P}$, $T_{rise\text{-}Ca}$), and relaxation time ($T_{relax\text{-}P}$, $T_{relax\text{-}Ca}$). T_{relax} was defined as the time taken for developed pressure (or calcium) to decay from 75% to 25% of its maximum value. Similarly, T_{rise} was defined as the time taken for pressure (or calcium) to rise from 25% to 75% of its maximum value. Finally, the calcium area ($[Ca]_{i\text{-}area}$) was calculated as the area under the calcium transient. Calculations of T_{relax}, T_{rise}, and $[Ca]_{i\text{-}area}$ were performed after subtracting the diastolic value of pressure (or calcium) waveform, such that each waveform rose from and declined to zero.

Data are expressed as mean ± S.E.M.. Repeated measures analysis of variance and Tukey's HSD post hoc test were used to evaluate the effects of acute changes in LV volume loading on pressure and calcium variables, the effects of time on these variables, and the effects of stimulus interval in the mechanical restitution data. To relate percentage changes from baseline values in two variables, linear regression analysis was performed with the constraint of zero intercept.

RESULTS

Frank-Starling protocol. An example of the Frank-Starling protocol data from one heart is illustrated in **Figure 9-2**, showing marked changes in pressure with little change in the calcium transient. In 8 hearts, P_{sys} increased from 62.3 ± 5.5 mmHg to 120.2 ± 9.0 when LV volume was raised from 16.5±0.3 μL to 30.6±0.3 μL.

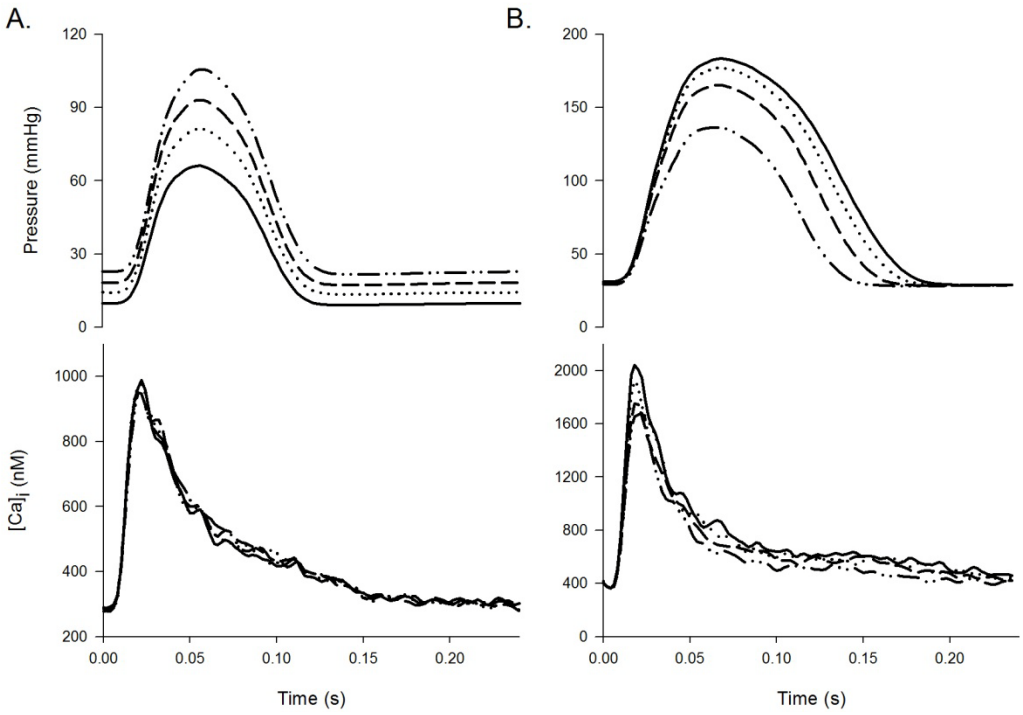

Figure 9-2. Example Pressure and Calcium Waveforms

Examples of averaged LV pressure and intracellular free calcium transient ($[Ca]_i$) data during a cardiac cycle from the Frank-Starling (**A**) and mechanical restitution (**B**) protocols. **A**: As LV volume was increased, there were significant changes in the LV pressure without any accompanying changes in $[Ca]_i$. **B**: During single-beat alterations in pacing interval at a fixed volume, both LV pressure and $[Ca]_i$ changed.

As illustrated in **Figure 9-3**, P_{dia}, P_{dev} (**9-3A**), $(dP/dt)_{max}$, and $(dP/dt)_{min}$ significantly increased (all $P<0.05$) and $T_{relax\text{-}P}$ or $T_{rise\text{-}P}$ (**9-3B**) were unchanged with increments in LV volume. Thus, changes in LV volume simply scaled the developed pressure waveform, without

any significant alterations in its morphology. In contrast, there were no significant changes in any of the indices calculated from calcium transients (**Figure 9-3C** and **Figure 9-3D**).

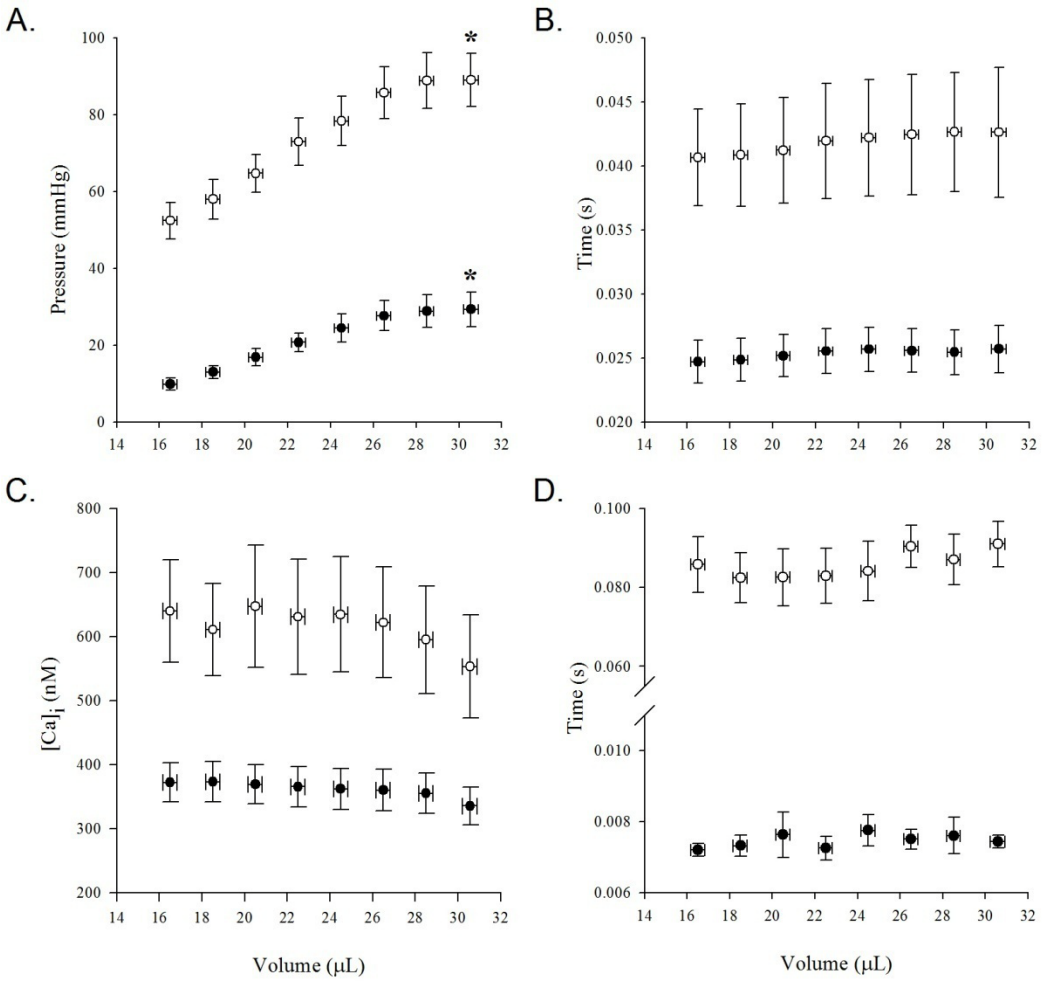

Figure 9-3. Effects of Altered LV Volume

Effects of altered LV volume on indices of pressure (**A** and **B**) and $[Ca]_i$ (**C** and **D**). With increments in LV volume, LV end-diastolic pressure (●) and developed pressure (○) significantly increased (**A**), with no changes in either pressure rise time (●) or pressure relaxation time (○) (**B**). In contrast, neither the magnitude (**C**; ●: diastolic $[Ca]_i$, ○: developed $[Ca]_i$) nor the morphology (**D**; ●: $[Ca]_i$ rise time, ○: $[Ca]_i$ relaxation time) were altered with increments in LV volume. Data are mean ± S.E.M. *: $P<0.05$ for ANOVA with repeated measures.

At 10 minutes after the increase in LV volume to V_{max}, there was a small, but significant, decrease in P_{dev} and P_{dia} (6% and 8% respectively, both $P<0.05$) (**Figure 9-4A**). None of the

$[Ca]_i$ indices (e.g., $[Ca]_{i\text{-}sys}$, $[Ca]_{i\text{-}dia}$, $T_{relax\text{-}Ca}$) changed significantly over this time (**Figure 9-4B** and **Figure 9-4C**).

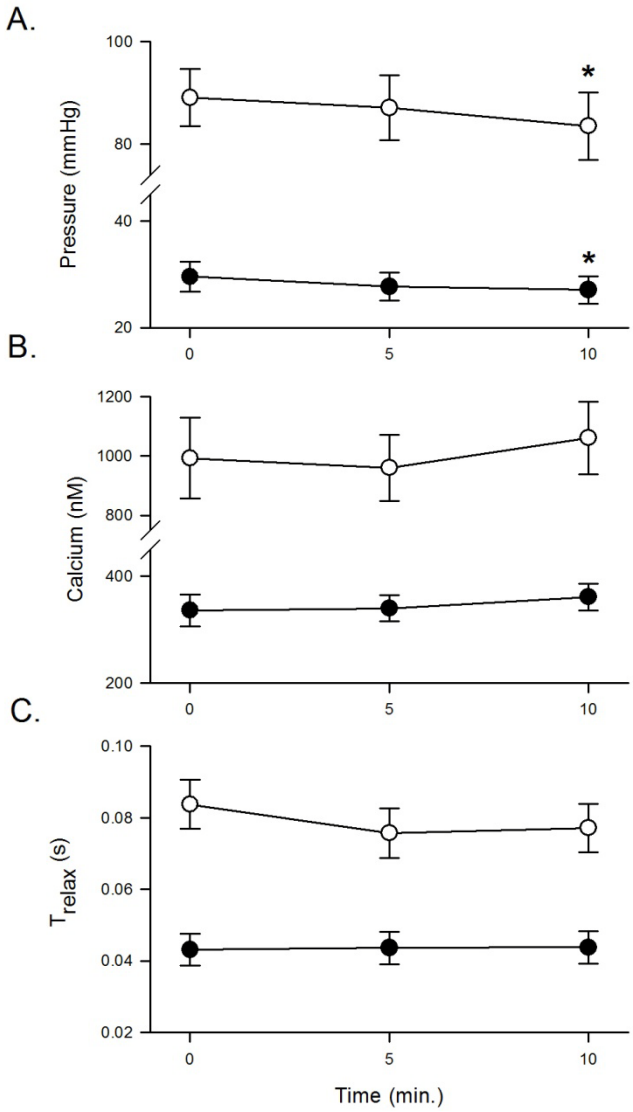

Figure 9-4. Effects of Sustained Volume

Effects of sustained volume over a 10-minute period. **A**: LV developed pressure (○) and LV end-diastolic pressure (●). **B**: systolic $[Ca]_i$ (○) and diastolic $[Ca]_i$ (●). **C**: $[Ca]_i$ relaxation time (○) and LV pressure relaxation time (●). There were small, but significant, decrements in LV developed and end-diastolic pressures over the 10-minute period, though there were no changes in any of the $[Ca]_i$ indices or LV pressure relaxation time. Data are mean ± S.E.M. *: $P<0.05$ ANOVA with repeated measures.

Mechanical restitution protocol. An example of the mechanical restitution protocol data from one heart is illustrated in **Figure 9-1B**, showing marked changes in pressure due to TPI alterations at a fixed LV volume. As summarized in **Table 10**, an increase in TPI increased P_{sys}, P_{dev} , $(dP/dt)_{max}$, $(dP/dt)_{min}$, and $T_{relax\text{-}P}$. For example, with respect to the control beat values, P_{sys}, P_{dev}, $(dP/dt)_{max}$, $(dP/dt)_{min}$, and $T_{relax\text{-}P}$ increased at TPI = 600 ms by 23.8±1.2% (P<0.01), 31.3±1.2% (P<0.01), 28.0±1.4% (P<0.01), 7.8±1.1% (P<0.01), and 21.2±1.9% (P<0.01), respectively.

Unlike the results from the Frank-Starling protocol, there were significant changes in $[Ca]_i$ dynamics, along with small, but significant, changes in $[Ca]_i$ peak magnitude. As illustrated in **Table 10**, an increase in TPI increased $[Ca]_{i\text{-}sys}$, $[Ca]_{i\text{-}dev}$, $T_{relax\text{-}Ca}$, and $[Ca]_{i\text{-}area}$. For example, with respect to the control beat values, $[Ca]_{i\text{-}sys}$, $[Ca]_{i\text{-}dev}$, $T_{relax\text{-}Ca}$, and $[Ca]_{i\text{-}area}$ increased at TPI = 600 ms by 7.4±1.4% (P<0.01), 10.6±1.8% (P<0.01), 30.0±5.5% (P<0.01), and 29.2±2.2% (P<0.01), respectively. TPI did not affect $T_{rise\text{-}Ca}$; it remained very fast under all conditions ($T_{rise\text{-}Ca}$ = 8±1 ms). Given that $[Ca]_{i\text{-}area}$ increased much more than $[Ca]_{i\text{-}sys}$, the major contributor to the area increase was the prolonged time of calcium transient decay (i.e., increased $T_{relax\text{-}Ca}$). These results indicate that the increase in developed pressure with increasing TPI is associated with a small, but significant, increase in peak systolic calcium and marked prolongation of both pressure and calcium relaxation.

Table 10. Mechanical Restitution Data

	Interval (ms)			
	200	240 (control)	400	600
Pressure data				
P_{sys} (mmHg)	102.9 ± 4.3	106.5 ± 4.0	123.9 ± 4.7†	133.3 ± 5.1†
P_{dia} (mmHg)	28.5 ± 1.7	28.4 ± 1.7	29.2 ± 1.7†	29.6 ± 1.9†
P_{dev} (mmHg)	74.4 ± 4.2	78.1 ± 4.0	94.7 ± 4.9†	103.8 ± 5.5†
dP/dt_{max} (mmHg•s^{-1})	3028 ± 138	3108 ± 123	3657 ± 148†	3960 ± 155†
dP/dt_{min} (mmHg•s^{-1})	-1916 ± 107	-1982 ± 102	-2148 ± 105†	-2159 ± 105†
T_{rise-P} (ms)	26.2 ± 1.0†	26.7 ± 1.0	27.1 ± 1.1	27.2 ± 1.2
$T_{relax-P}$ (ms)	43.1 ± 2.9	43.8 ± 3.0	49.0 ± 3.6†	53.6 ± 4.4†
Calcium data				
$[Ca]_{i-sys}$ (nM)	948 ± 59*	990 ± 63	1009 ± 63	1094 ± 72†
$[Ca]_{i-dia}$ (nM)	365 ± 14*	381 ± 15	375 ± 15	394 ± 15
$[Ca]_{i-dev}$ (nM)	582 ± 54	610 ± 57	633 ± 58	700 ± 66†
$[Ca]_{i-area}$ (nM•s)	24.8 ± 2.3	25.3 ± 2.1	29.8 ± 2.7†	34.0 ± 2.9†
$T_{rise-Ca}$ (ms)	8.3 ± 0.3	8.4 ± 0.4	8.2 ± 0.4	8.3 ± 0.4
$T_{relax-Ca}$ (ms)	79.9 ± 4.2	82.5 ± 3.6	91.6 ± 5.2	105.9 ± 5.1†

Values are means ± S.E.M.. P_{sys}: LV peak systolic pressure; P_{dia}: LV diastolic pressure; P_{dev}: LV developed pressure; dP/dt_{max}: maximal rate of rise of LV pressure; dP/dt_{min}: maximal rate of fall of LV pressure; T_{rise-P}: LV pressure rise time; ; $T_{relax-P}$: LV pressure fall time; $[Ca]_{i-sys}$: peak systolic intracellular free calcium; $[Ca]_{i-dia}$: diastolic intracellular free calcium; $[Ca]_{i-dev}$: developed intracellular free calcium; $[Ca]_{i-area}$: area under the intracellular free calcium transient; $T_{rise-Ca}$: calcium rise time; ; $T_{relax-Ca}$: calcium fall time. (Note: Limited data were available at TPI = 800 ms because there was often a spontaneous contraction before the desired stimulation interval. Therefore, data for this TPI are not included in this Table; though they are included **Figures 9-5 through 9-7**.) *P<0.05, †P<0.01, versus 240 ms pacing interval, Tukey's HSD post-hoc test if repeated measures ANOVA showed a significant difference.

As mentioned earlier, the three TPI deployment modes (**Figure 9-1**) were used merely to create a wide variety of pressure and calcium pairs. Clearly, changes in pressure at a given TPI are not expected to be the same for the three TPI deployment modes. This is the reason for the relatively large standard errors in **Table 10**. Instead of pooling data by TPI, we plotted

percentage changes in rise and relaxation times against the corresponding percentage change in P_{dev} and $[Ca]_{i\text{-}dev}$ for all experiments and all conditions within an experiment (i.e., 4 TPI settings and 3 TPI deployment modes). This was done to assess whether changes in waveform morphology were related to the changes in waveform magnitude. All percentage changes were computed with respect to the control beat values (i.e., steady-state contractions at pacing interval of 240 ms).

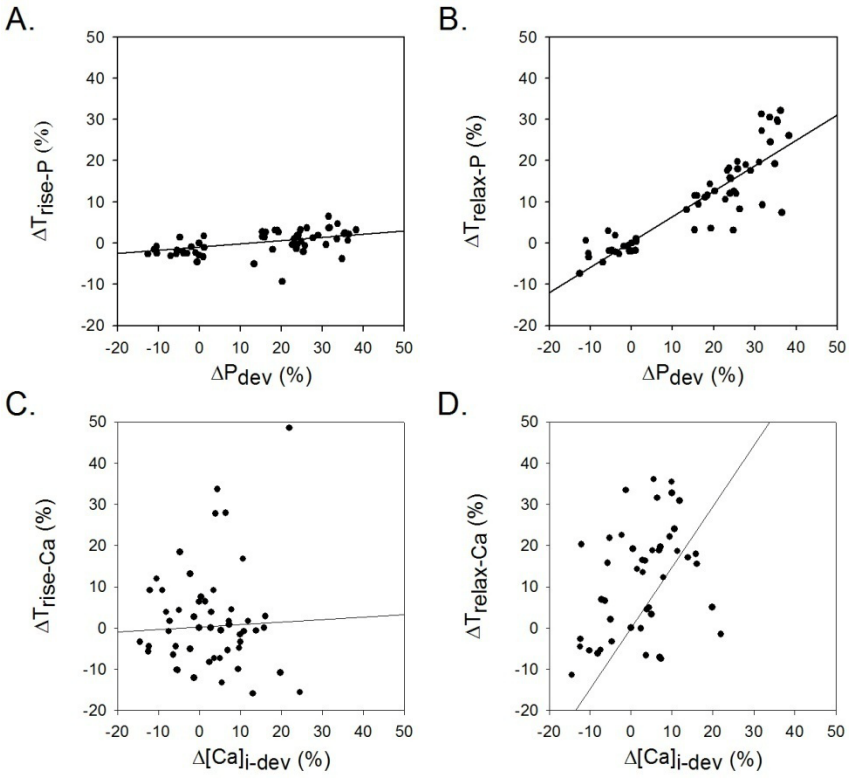

Figure 9-5. Analysis of Mechanical Restitution Data

Analysis of mechanical restitution data from all experiments to examine morphological changes in LV pressure and $[Ca]_i$ signals individually. **A** and **B**: Percentage changes in LV pressure rise ($\Delta T_{rise\text{-}P}$) and relaxation ($\Delta T_{relax\text{-}P}$) times with respect to the control beat values are plotted as a function of the percentage change in LV developed pressure (ΔP_{dev}). $\Delta T_{rise\text{-}P}$ was independent of ΔP_{dev} (**A**; slope = 0.05, P<0.001). In contrast, $\Delta T_{relax\text{-}P}$ increased with increasing ΔP_{dev} (**B**; slope = 0.63, P<0.001), indicating relative slowing of pressure relaxation. **C** and **D**: Percentage changes in $[Ca]_i$ rise ($\Delta T_{rise\text{-}Ca}$) and relaxation ($\Delta T_{relax\text{-}Ca}$) times with respect to the control beat values are plotted as a function the percentage change in developed $[Ca]_i$ ($\Delta[Ca]_{i\text{-}dev}$). $\Delta T_{rise\text{-}Ca}$ was independent of $\Delta[Ca]_{i\text{-}dev}$ (**C**; slope = 0.07, P=0.73). In contrast, $\Delta T_{relax\text{-}Ca}$ increased with increasing $\Delta[Ca]_{i\text{-}dev}$ (**D**; slope = 1.48, P<0.001), indicating relative slowing of calcium relaxation.

As P_{dev} increased, there was no change in $T_{rise\text{-}P}$ (**Figure 9-5A**) and $T_{relax\text{-}P}$ increased (**Figure 9-5B**). Similar correlations existed for the calcium data as well (**Figure 9-5C** and **Figure 9-5D**), i.e., invariant $T_{rise\text{-}Ca}$ (**Figure 9-5C**) and increasing $T_{relax\text{-}Ca}$ (**Figure 9-5D**) with increments in $[Ca]_{i\text{-}dev}$. There was greater variability in the calcium data, which is attributable to lower signal-to-noise ratio associated with fluorescence-based calcium measurements.

The percentage change in $T_{relax\text{-}P}$ ($\Delta T_{relax\text{-}P}$) was positively correlated to the percentage change in $T_{relax\text{-}Ca}$ ($\Delta T_{relax\text{-}Ca}$) (**Figure 9-6**, R^2=0.53; P<0.001), indicating that the slower pressure relaxation can be explained in terms of the slower calcium relaxation. To examine how percentage changes in P_{dev} (ΔP_{dev}) are related to changes in various indices of $[Ca]_i$, ΔP_{dev} is plotted against percentage changes in three selected indices of $[Ca]_i$ (**Figure 9-7**): $\Delta[Ca]_{i\text{-}sys}$, $\Delta T_{relax\text{-}Ca}$, and $\Delta[Ca]_{i\text{-}area}$. While each of the three relationships had a significant positive correlation, the slope of ΔP_{dev}-$\Delta[Ca]_{i\text{-}sys}$ relationship (2.30, **Figure 9-7A**) was significantly greater than that of ΔP_{dev}-$\Delta T_{relax\text{-}Ca}$ relationship (0.96, **Figure 9-7B**) or ΔP_{dev}-$\Delta[Ca]_{i\text{-}area}$ relationship (0.93, **Figure 9-7C**). Thus, TPI-induced changes in developed pressure are associated with small changes in peak systolic calcium and large changes in $[Ca]_{i\text{-}area}$ (almost 1:1) that are mostly due to the marked prolongation of calcium relaxation. Furthermore, slower pressure relaxation is mostly attributable to this prolongation of calcium relaxation.

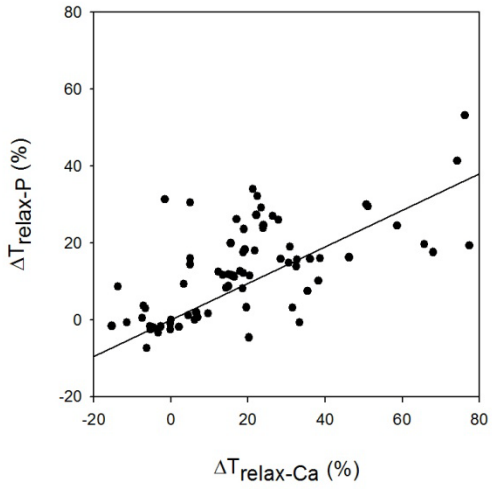

Figure 9-6. Pressure versus Calcium Relaxation

Analysis of mechanical restitution data from all experiments to examine the relationship between morphological changes in LV pressure and $[Ca]_i$ signals. The percentage change in LV pressure relaxation ($\Delta T_{relax\text{-}P}$) was positively correlated with the percentage change in $[\Delta Ca]_i$ relaxation ($T_{relax\text{-}Ca}$): slope = 0.48, R^2 = 0.53, P<0.001.

DISCUSSION

Our data demonstrate unique features of the calcium-pressure relationship in the intact mouse heart. During the length-dependent increase in contraction, left ventricular developed pressure increased immediately, but the secondary rise seen in larger mammals was absent. None of the indices of pressure waveform shape or the calcium transient (magnitude and/or waveform shape including relaxation) were altered significantly. Single-beat changes in stimulus interval at a fixed ventricular volume also produced marked changes in developed pressure. However, an increase in pressure in this case was associated with marked increases in pressure and calcium relaxation times and a small, but significant, rise in the peak of the calcium transient. Finally, pressure relaxation was load-independent and primarily governed by calcium relaxation (removal).

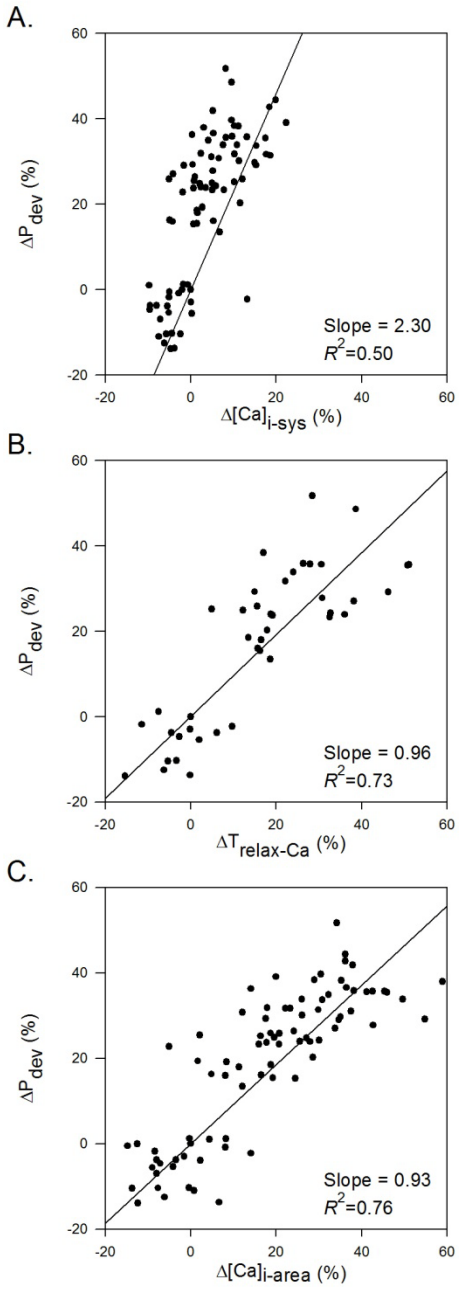

Figure 9-7. Determinants of Developed Pressure

Analysis of mechanical restitution data from all experiments to examine how the percentage change in LV developed pressure (ΔP_{dev}) is related to percentage changes in various indices of $[Ca]_i$. **A**: $\Delta P_{dev} - \Delta[Ca]_{i\text{-}sys}$ (changes in peak systolic $[Ca]_i$). **B**: $\Delta P_{dev} - \Delta T_{relax\text{-}Ca}$ (changes in $[Ca]_i$ relaxation time). **C**: $\Delta P_{dev} - \Delta[Ca]_{i\text{-}area}$ (change in area under the calcium transient). While ΔP_{dev} was positively correlated with all three $\Delta[Ca]_i$ indices, the slope of $\Delta P_{dev} - \Delta[Ca]_{i\text{-}sys}$ relationship was significantly greater than the slopes of the other two relationships.

Pressure modulation via changes in muscle length. Studies in isolated muscles from rats and cats have shown that increases in muscle length produce an immediate increase in force, though no change in the peak of the calcium transient, followed by slow increases in calcium and force that are similar in both magnitude and time course (1). Todaka *et al.* [149] have observed a similar pattern of response in the canine, blood-perfused isolated heart; following the immediate increase in pressure resulting from myocardial stretch, pressure and intracellular free calcium rose slowly for three minutes. In contrast to these studies, Reyes *et al.* [145], who studied *in vivo* hemodynamics in the mouse, showed that there was no secondary (late) increase in contractility (pressure) following an increase in left ventricular end-diastolic volume brought about by aortic constriction. Our data are consistent with these observations and add to the study of Reyes *et al.* by showing that the constant pressure is accompanied by an absence of changes in the intracellular free calcium transient over a 10-minute period.

The explanation for the difference between the mouse and other mammalian hearts could be based on the aforementioned limited dependence upon sarcolemmal calcium transport. Alvarez *et al.* [144] demonstrated that the secondary increase in force and calcium in rat ventricular trabeculae is related to activation of the Na^+/H^+ exchanger, which increases intracellular sodium and leads to an increase in intracellular calcium. However, since sarcolemmal calcium transport in the mouse plays such a small role in excitation-contraction coupling [2, 142], this sarcolemmal mechanism of the secondary increase in intracellular calcium may not be operative in the mouse, leading to a lack in augmentation of the calcium transient found in other species. Additionally, a tertiary decrease has been observed following the secondary rise that returned calcium and pressure levels to the pre-secondary-rise levels [149]. The mechanism for this tertiary drop is not understood, but if the time courses of the late-phase-

rise and tertiary drop are comparable in the mouse, these two phenomena can offset each other, resulting in no late changes in calcium.

Pressure modulation via transient changes in stimulation interval. Wier and Yue [150] have described the relationship between calcium and force during transient alterations of stimulation interval in isolated ferret papillary muscles. They demonstrated a linear relationship between force and peak intracellular free calcium, with an increase in peak intracellular free calcium of 1 μM producing a large increase in force of 0.03 $N \bullet mm^{-2}$. Moreover, they showed that the percentage increase in peak force was nearly equal to the percentage increase in peak calcium, indicating a one-to-one relative increase over a wide range (several times the baseline values). While we also saw large increases in peak pressure (up to 50%), the maximum increase in peak calcium was only 20%. In other words, an increase in systolic calcium was associated with an increase in developed pressure of much greater magnitude (**Figure 9-7A**). This observation of high calcium-pressure "gain" is consistent with significantly greater cooperativity (Hill coefficient = 9.9) reported by Gao *et al*. [94] in constantly activated mouse myocardium as compared to that of larger mammals. They also reported that that the positive force-frequency relationship (FFR) in mouse myocardium was accompanied by relatively small changes in intracellular free calcium for stimulation frequencies above 2 Hz, a phenomenon they referred to as "frequency-dependent sensitization of myofilaments."

Our results show that P_{dev} and $[Ca]_{i\text{-}area}$ in the mouse increase almost one-to-one (**Figure 9-7C**). The increased $[Ca]_{i\text{-}area}$ is only slightly modulated by the increased peak; instead, a slowed decay of the calcium transient is the major contributor (**Figure 9-7B**). This observation supports the premise that the temporal pattern of the calcium transient, not just the peak, significantly influences developed pressure in the mouse heart. Slower decay of the calcium transient may be

due to one or more of the following: (1) the rate of calcium uptake is near maximal under baseline conditions so that the calcium transient amplitude would be higher and calcium decay would be slower when more calcium is released (as would be expected for a contraction with increased pacing interval); (2) sarcoplasmic reticulum calcium uptake is reduced; and/or (3) there is increased troponin C calcium binding [151] due to increased myofilament calcium sensitivity. All of these postulated mechanisms of delayed decay of the calcium transient are likely to increase pressure, as there is prolonged calcium binding to troponin C and consequent prolonged actomyosin crossbridge interactions.

Developed pressure and calcium. Our data indicate that significant changes in LV peak developed pressure can occur in the mouse heart with little or no change in peak of the calcium transient. This behavior in the mouse heart is quite different from what has been reported for higher mammals [143, 149, 152]. This lack of peak calcium variation may be a result of calcium cycling functioning at near maximal capacity at baseline in the mouse heart. We recognize that β-adrenergic agonists can significantly increase peak intracellular free calcium in the isolated mouse heart [46]. However, given its high baseline heart rate and limited ability to increase heart rate via sympathetic activation, indicating high basal sympathetic tone [153], this physiological mechanism may not be available to the mouse *in-vivo*. Our observation of high calcium-pressure gain and increased cooperativity reported by others [94] can be considered as compensatory responses to offset the limited ability for modulating calcium transient amplitude in the mouse heart.

Determinants of pressure relaxation. Increased load prolongs force relaxation in mammalian ventricular muscle preparations [154]. Specifically, an increase in developed stress, brought about by an increase in muscle stretch, is associated with prolonged relaxation in

isolated, isovolumically contracting ferret hearts [155] and in isosarcometrically contracting isolated rat trabeculae [156]. Two potential mechanisms have been postulated for this prolongation of pressure (force) relaxation: (1) changes in calcium transient, particularly its prolonged relaxation, and (2) existence of cooperative feedback mechanisms, including crossbridge-myofilamental activation cooperativity and crossbridge-crossbridge cooperativity [155-157]. In contrast to these observations from other mammalian species, we did not observe any load-dependent changes in calcium transients or pressure waveform morphology in the Frank-Starling protocol. In agreement with these findings, Reyes *et al.* [145] have shown that afterload increases in the *in-vivo* mouse model do not affect active relaxation.

We did observe prolonged pressure relaxation with increasing developed pressure in the mechanical restitution protocol (**Figure 9-5B**). However, this prolongation can be attributed to slower decay of the calcium transient (**Figure 9-6**). This observation, together with results from the Frank-Starling protocol, indicates that pressure (force) relaxation in the mouse is primarily governed by calcium removal; crossbridge-mediated control of relaxation, typically seen other mammalian species, is either absent (minimal) or operating near saturation under the baseline conditions. Given the increased cooperativity of constantly activated mouse myocardium (Hill coefficient = 9.9) (12), the latter possibility is more likely. Teleologically, this load-independence of pressure relaxation may help maintain cardiac function in the setting of high heart rates.

Model-based analysis. A model-based analysis was performed to obtain additional insights into the dynamics of pressure-calcium relationships. Specifically, the four-state model (see **Section 7.2.2**) was used to predict the pressure waveform for a given calcium transient and model parameters.

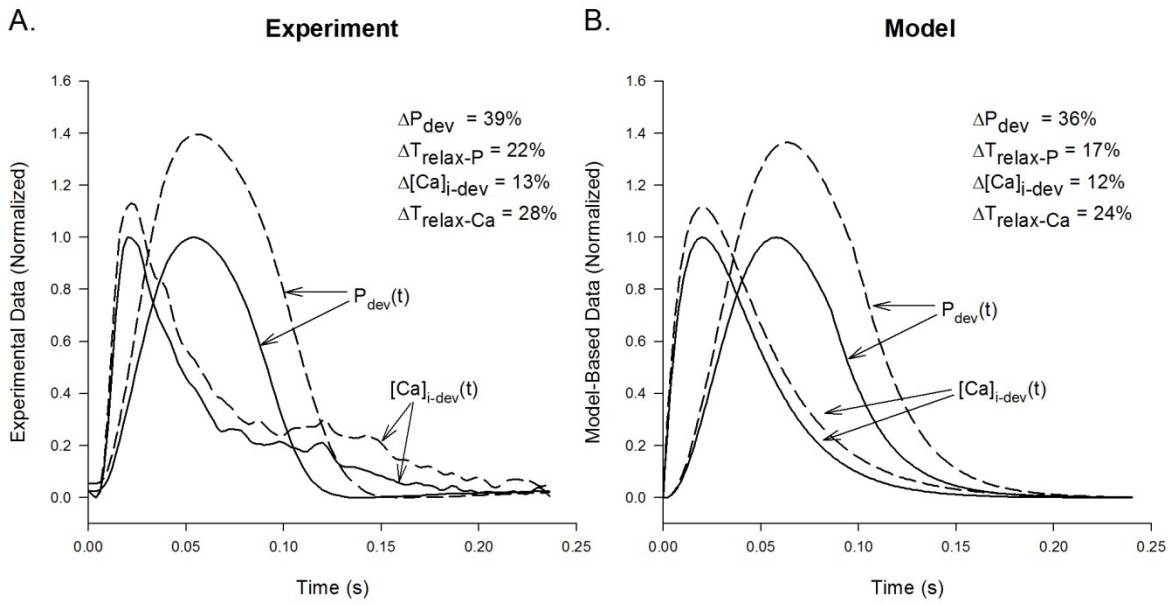

Figure 9-8. Model-Based Interpretation: Mechanical Restitution Protocol

Comparison of the model-based prediction and experimentally measured data obtained with the mechanical restitution protocol. **A**: Experimentally measured LV developed pressure waveform, $P_{dev}(t)$ and developed $[Ca]_i$ waveform, $[Ca]_{i\text{-}dev}(t)$ (solid lines: control pacing interval of 240 ms; dashed lines: test pulse interval of 600 ms). Data are normalized by the peak value of each signal under the control condition. When the pacing interval was transiently increased to 600 ms, both pressure and $[Ca]_i$ changed as indicated. $\Delta[Ca]_{i\text{-}dev}$: change in developed $[Ca]_i$; $\Delta T_{relax\text{-}Ca}$: change in $[Ca]_i$ relaxation time; ΔP_{dev}: change in LV developed pressure; $\Delta T_{relax\text{-}P}$: change in pressure relaxation time. **B**: Model-based analysis (solid lines: control pacing interval of 240 ms; dashed lines: test pulse interval of 600 ms). Experimentally measured pressure and calcium data for the control condition were first used to estimate the calcium input function and the four-state model parameters (see Appendix). When the calcium input function was altered to match experimentally observed data, the model pressure output reproduced experimentally observed alterations in the developed pressure waveform, without any need to change the four-state model parameters.

In the mechanical restitution protocol there were changes in the magnitude and shape of calcium and pressure waveforms (**Figure 9-8A**). Given the similarity in directional changes in the indices of calcium and pressure transients, we hypothesized that the changes in the pressure waveform were due entirely to changes in the calcium transient. Specifically, with respect to the control condition, $[Ca]_{i\text{-}dev}$, $T_{relax\text{-}Ca}$, P_{dev}, and $T_{relax\text{-}P}$ increased at TPI of 600 ms by 13%, 28%, 39%, and 22%, respectively. When the magnitude and relaxation of the model-input calcium transient were altered to match experimentally observed changes during altered stimulation

interval, the model output reproduced experimentally observed alterations in the developed pressure waveform (**Figure 9-8B**) without any perturbations in the model parameters. These results support our hypothesis and indicate that there is no need to invoke any changes in the dynamic processes that link calcium to pressure (i.e., model parameters) to reconcile observed calcium-pressure data from the mechanical restitution protocol. However, one cannot rule out the possibility of multiple, mutually offsetting changes in model parameters on the basis of this analysis.

In the Frank-Starling protocol there were no changes in the calcium transient, but the developed pressure increased significantly (101%), while $T_{rise\text{-}P}$ and $T_{relax\text{-}P}$ increased by modest amounts (8% and 5%, respectively) (**Figure 9-9A**). From the modeling perspective, if the input to the system (calcium transient) is not changing and the output (pressure transient) is then the parameters describing the system must be changing. In other words, certain model parameters are volume- or stretch-dependent. Based on the results of Shimizu *et al*. [104], the following model parameters were considered to be stretch-dependent: (1) two parameters (K_3 and K_4) corresponding to calcium dissociation from troponin C, (2) two parameters corresponding to crossbridge formation (f) and dissolution (g'), and (3) the gain parameter (γ) that converts molar concentration of force generating states to pressure (force).

Effects of changes in stretch-dependent model kinetic parameters (i.e., categories (1) and (2) listed above) are illustrated in **Figure 9-9B**. Data from Shimizu *et al.* [104] were used to alter these model parameter values. While this perturbation increased developed pressure by an appropriate amount (109%), it also increased $T_{rise\text{-}P}$ and $T_{relax\text{-}P}$ by 14% and 94%, respectively, which is inconsistent with the experimental observations (especially for the change in $T_{relax\text{-}P}$).

Effects of an increase in the gain parameter (γ) are illustrated in **Figure 9-9C**. We see a simple amplification of the pressure waveform by 100%, with no change in either $T_{rise\text{-}P}$ or $T_{relax\text{-}P}$. Clearly, this perturbation satisfactorily captures both the magnitude and temporal features of the pressure response to increased volume. Although the physiologic meaning of this gain parameter is not entirely understood, an increase in its value may indicate an increase in force generated per cross-bridge. Unfortunately, if we accept that changes in LV volume (muscle length) only affect this gain parameter, the model fails to reproduce length-dependent changes in the steady-state force-pCa relationship observed in the mouse myocardium [35, 158]. We are unable to identify specific mechanisms that can simultaneously reproduce both the length-dependent changes in force-pCa and the disconnect between increased P_{dev} and $T_{relax\text{-}P}$. Further studies are necessary to explain this unique length-dependent behavior in the mouse heart.

Conclusions. The mouse myocardium appears to be unique in that significant changes in peak developed pressure can occur with little or no change in the peak of the calcium transient. In addition, unlike other mammalian species, pressure relaxation is load-independent and primarily governed by calcium removal. Thus, although genetically engineered mouse models are commonly used to study cardiac structure-function relationships, caution must be exercised while extrapolating findings from these models to the human setting.

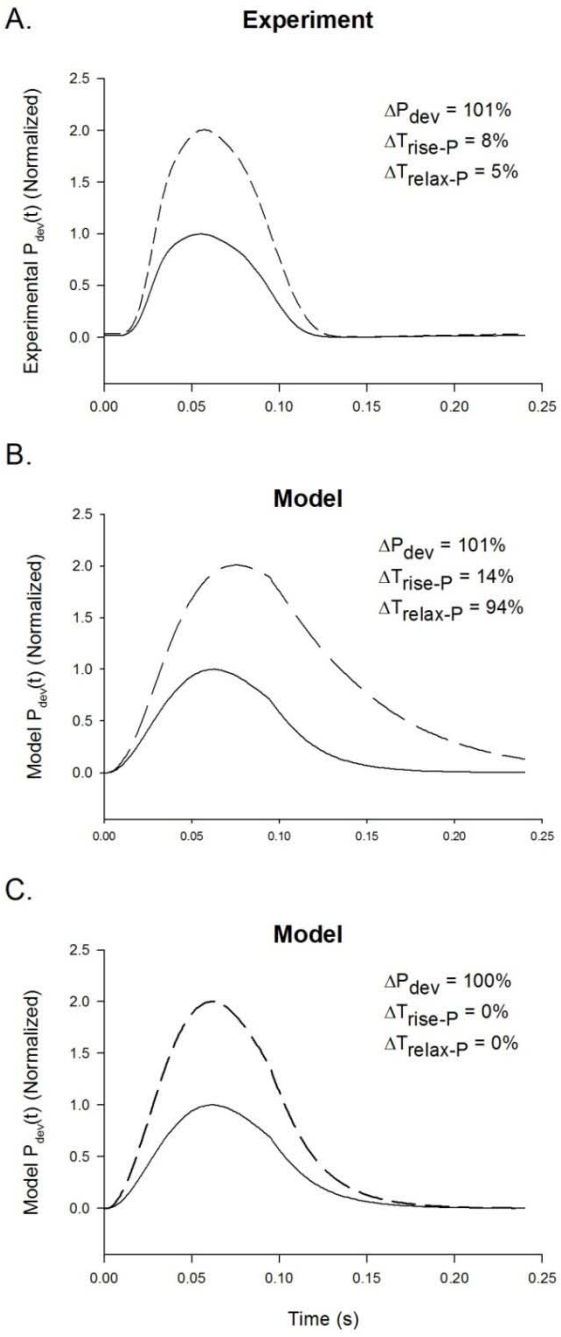

Figure 9-9. Model-Based Interpretation: Frank Starling Protocol

Comparison of the model-based prediction and experimentally measured data obtained with the Frank-Starling protocol. **A**: Experimentally measured LV developed pressure waveform, $P_{dev}(t)$, at two LV volumes: low (solid line) and high (dashed line). Data are normalized by the peak developed pressure (P_{dev}) at low volume. P_{dev} doubled with the increase in LV volume, with little changes in pressure rise (T_{rise-P}) and relaxation ($T_{relax-P}$) times and $[Ca]_i$ (not shown). **B, C**: Model-based analysis. Experimentally measured pressure and calcium data for the low volume condition were first used to estimate the calcium input function and the four-state model parameters. Model-based prediction of changes in $P_{dev}(t)$ when the stretch-dependent kinetic parameters were altered (**B**) and when the stretch-dependent gain parameter was altered (**C**) (see text).

APPENDIX B

IDENTIFIABILITY IN OTHER MODELS

In addition to the four-state model, DAISY (see **Section 7.2.3.1**) was used to determine the identifiability in other models of cardiovascular function.

Model #1. Windkessel Models

Using analogous electrical circuits to model the arterial system is an old concept, described by Hales in 1733. By assuming pressure analogous to voltage and blood flow analogous to current, the Windkessel model is a robust and ubiquitous technique used to study arterial systems [159]. One of the simplest forms is the three-element Windkessel, which consists of a total arterial resistance (*R*), a total arterial compliance (*C*) and a characteristic impedance (*r*), as shown in **Figure 9-10A**. The model is described by one differential equation, **Equation B.1**, and one output equation, **Equation B.2**.

$$\frac{dP_C(t)}{dt} = -\frac{1}{CR_P}P_C(t) + \frac{1}{C}Q_{ao}(t) \tag{B.1}$$

$$P_{ao}(t) = P_C(t) + rQ_{ao}(t) \tag{B.2}$$

where P_C is a state variable for pressure across the capacitor, Q_{ao} is the aortic flow (model input) and P_{ao} is the aortic pressure (model output). Total arterial resistance can be estimated from the input and output, so there are only two free parameters to be estimated: *r* and *C*.

There is a variation of this 3-element Windkessel where the characteristic impedance (r) is in series with the compliance. This is shown in **Figure 9-10B**.

By combining the two 3-element Windkessel models, we obtain a 4-element Windkessel shown in **Figure 9-10C**. It is important to note that this form of Windkessel is not regularly used, and is only shown here as an extension of the 3-element Windkessel models.

While the three-element Windkessel models capture many of the major characteristics of the aortic pressure and flow relationship, greater fidelity comes from adding additional elements. For example, the 5-element Windkessel adds the effects of blood inertance [160] and a more complicated structure (**Figure 9-10D**). The model is described by three differential equations and one output equation.

$$\frac{dP_{C_1}(t)}{dt} = \frac{1}{C_1} Q_{ao\,(t)} - \frac{1}{C_1} Q_L(t) \tag{B.3}$$

$$\frac{dQ_L(t)}{dt} = -\frac{1}{L} P_{C_2}(t) - \frac{1}{L} P_{C_1}(t) \tag{B.4}$$

$$\frac{dP_{C_2}(t)}{dt} = \frac{1}{C_2} Q_L(t) - \frac{1}{RC_2} P_{C_2}(t) \tag{B.5}$$

$$P_{ao}(t) = P_{C_1}(t) + rQ_{ao}(t) \tag{B.6}$$

where P_{C1}, P_{C2}, and Q_L are the state variables, P_{ao} is the output, and Q_{ao} in the input. There are five free parameters to be estimated: r, R, C_1, C_2, and L.

Similar to the two 3-element Windkessel models shown, there are multiple arrangements of the 5-element Windkessel; one such variation is shown in **Figure 9-10E**.

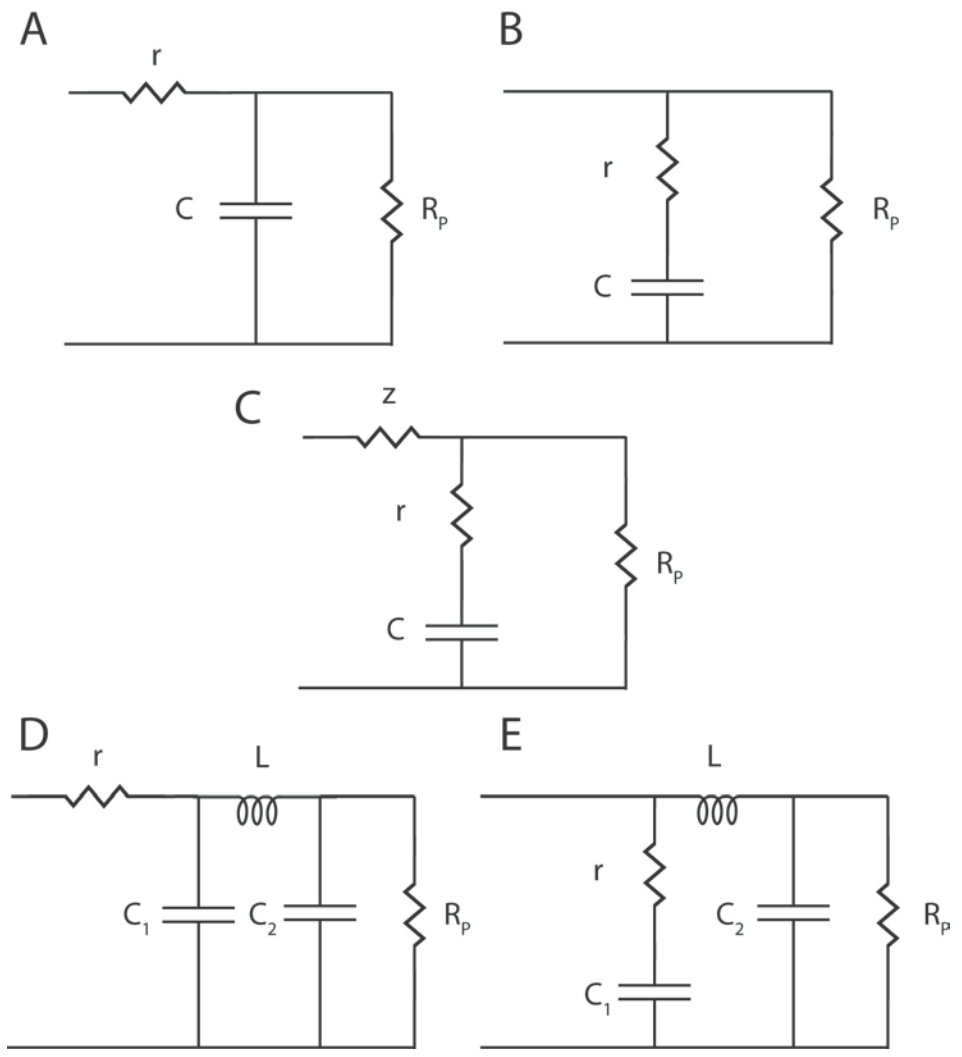

Figure 9-10. Windkessel Models

Schematics of Windkessel model variations. There are two 3-element (A and B), one 4-element (C) and two 5-element (D and E) Windkessel models.

Model #2: Stiffness Model.

Cardiac muscle responds to changes in length with alterations in force development, by the so called force-length relationship (FLR). A common experiment involves altering muscle length sinusoidally, and observing the resultant sinusoidal force response. The ratio of the magnitudes of the force response and length perturbation at each sinusoid frequency represents the complex stiffness at that particular frequency. The complex stiffness over a wide range of

frequencies (experimentally this is done by a length "chirp", a sinusoid of continuously increasing frequency) is a useful indicator of a muscle's dynamic FLR.

The stiffness model was developed to analyze chirp data from skinned fibers in the time domain, and is based on system of two force producing dynamics: recruitment and distortion of crossbridges. The model has been rigorously validated [161], and used for parameter estimation [162, 163], but has never been tested for identifiability. The model itself is a black box model described by two differential equations, **Equations B.11** represents the recruitment dynamics, **Equation B.12** represents the distortion dynamics, and the output equation is **Equation B.13**:

$$\frac{d\eta(t)}{dt} = -b[\eta(t) - \Delta L(t)] \tag{B.11}$$

$$\frac{dx(t)}{dt} = -cx(t) + \frac{d\Delta L(t)}{dt} \tag{B.12}$$

$$\Delta F = E_0\eta(t) + E_\infty x(t) \tag{B.13}$$

where η(t) is the recruitment variable, x(t) is the distortion variable, ΔL is the length change (model input), and ΔF is the force change (model output). There are four free parameters to be estimated: E_0, E_∞, *b*, and *c*.

Model #3: Three State Model.

It is possible to group cardiac contraction/relaxation processes into three main categories: 1) activator calcium, 2) myofilament activation, and 3) myofilament contraction. There are no experimental techniques to reliably measure myofilament properties, and so their measurement is handled indirectly, through identifying model parameter values. There exist several models of myofilament function that can be used for this approach, often taking the form of compartment or state models. The three-state examined here was developed to analyze the effects of acidosis [164], and is shown in **Figure 9-11**. It is described by the following three differential equations,

$$\frac{dX_{CO}}{dt} = -\left(f + k_{off} + k_{on}[Ca]_i\right)X_{CO} + (d - k_{on}[Ca]_i)X_{CN} - k_{on}[Ca]_i X_{CF} - k_{on}[Ca]_i X_T \quad \text{(B.14)}$$

$$\frac{dX_{CN}}{dt} = fX_{CO} - (d + h)X_{CN} \quad \text{(B.15)}$$

$$\frac{dX_{CF}}{dt} = hX_{CN} - gX_{CF} \quad \text{(B.16)}$$

The input is the intracellular calcium concentration, $[Ca]_i$ (either a time time-dependent transient, or a steady state value) and the output is X_{CF}, which is proportional to force. There are seven free parameters to estimate: k_{off}, k_{on}, f, d, g, h, and X_T.

The model can also include a feedback algebraic equation, which will decrease k_{off} when the value of X_{cf}, force producing crossbridges, gets larger. This feedback attempts to describe the concept of cooperativity in the model. The feedback equation is:

$$k_{off} = \frac{k_{off,0}}{1+\beta X_{cf}^2} \quad \text{(B.17)}$$

Where $k_{off,0}$ is the baseline value of k_{off}, and β is a cooperatively parameter. This removes one free parameter (k_{off}), but introduces two, increasing the number of free parameters to eight.

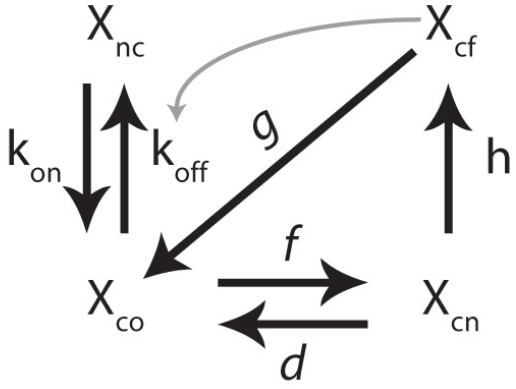

Figure 9-11. Schematic of Three-State Model

RESULTS AND DISCUSSION

A total of eight models (not including the four-state model) were run through DAISY to determine identifiability. The results obtained from DAISY can be seen in **Table 11**.

Table 11. Results of Identifiability Analysis

Model	# State Var.	# Outputs	# Paramters	Observable	Identifiable
3-element Windkessel	----------	----------	----------	----------	----------
Variant 1	1	1	2	✓	Globally
Variant 2	1	1	3	✓	Globally
4-element Windkessel	1	1	4	✓	Non
5-element Windkessel	----------	----------	----------	----------	----------
Variant 1	3	1	5	✓	Globally
Variant 2	3	1	5	✓	Globally
Stiffness Model	2	1	4	✓	Globally
3 state Model	----------	----------	----------	----------	----------
Without Feedback	3	1	7	✓	Globally
With Feedback	3	1	8	✓	Globally

The models that are tested for *a priori* identifiability using DAISY, along with the number of state variables, measured outputs, free parameters to estimate, whether it is algebraically observable and identifiable.

All of the models were found to be globally identifiable, except the 4-element Windkessel. This particular model is a variation created for this study, and there is no evidence of its prior use. These results suggest that models of cardiovascular function which are functionally identifiable (have been successfully used in parameter identification) are *a priori* identifiable using DAISY. It is important to note that a positive result from the *a priori* model identifiability analysis constitutes a necessary, but not sufficient, condition for successful parameter identification from real input-output data. In summary, DAISY is a very useful tool for conducting *a priori* model identifiability analysis. Such an analysis, performed prior to conducting extensive experiments, is likely to help optimize model structure and/or experimental design.

APPENDIX C

MATLAB PROGRAMS

MODEL ANALYSIS – MAIN PROGRAM

```
clear
close all

% Program that uses the four-state model, with variations in the
% model parameters to help forward-fit the solution to data
% Developed 10/08 by Jonathan Kirk, revised 5/09
% Developed for S43E/S45E/T144E manuscript data analysis

%% Parameter Sets
K2 = 25;
K3 = 84;
K4 = 84;
g = 205.3;
alpha_K1 = 2.0;
beta_K1 = 3;
alpha_f = 0.15;
beta_f = 0.7;
d = 44.6;

% Baseline Set
Params(1) = K2;
Params(2) = K3;
Params(3) = K4;
Params(4) = g;
Params(5) = alpha_K1;
Params(6) = beta_K1;
Params(7) = alpha_f;
Params(8) = beta_f;
Params(9) = d;

% Perturbation One
Params2(1) = K2;
Params2(2) = K3;
Params2(3) = K4;
```

```
Params2(4) = g;
Params2(5) = alpha_K1;
Params2(6) = beta_K1;
Params2(7) = alpha_f;
Params2(8) = beta_f * 0.77;
Params2(9) = d;

% Perturbation Two
Params3(1) = K2;
Params3(2) = K3;
Params3(3) = K4;
Params3(4) = g;
Params3(5) = alpha_K1;
Params3(6) = beta_K1;
Params3(7) = alpha_f;
Params3(8) = beta_f*0.77;%0.77;
Params3(9) = d*0.65;%*0.65;

%% Steady state solutions
Ca_array1 = 0.01:0.01:.1;
Ca_array2 = 0.2:0.1:10;
Ca_array3 = 11:1:100;
Ca_array = [Ca_array1 Ca_array2 Ca_array3];
Yo = [70,20,0,0,0];

Timef = 0:0.001:0.5;
Inputs = 0;
F = zeros(1,length(Ca_array));
F2 = zeros(1,length(Ca_array));
F3 = zeros(1,length(Ca_array));
%% Baseline

for i = 1:length(Ca_array)
Params(10) = Ca_array(i);
[T,Y] = ode45(@B_Model3,Timef,Yo,[],Inputs,Params);
F(i) = Y(length(Timef),4)+Y(length(Timef),5);
state41(i) = Y(length(Timef),4);
state51(i) = Y(length(Timef),5);
MgATP11(i) = Params(4)*state41(i);
MgATP12(i) = Params(9)*state51(i);
end

%% Perturbation One

for i = 1:length(Ca_array)
Params2(10) = Ca_array(i);
[T,Y] = ode45(@B_Model3,Timef,Yo,[],Inputs,Params2);
F2(i) = Y(length(Timef),4)+Y(length(Timef),5);
state42(i) = Y(length(Timef),4);
state52(i) = Y(length(Timef),5);
MgATP21(i) = Params2(4)*state42(i);
MgATP22(i) = Params2(9)*state52(i);
end

%% Perturbation Two
```

```
for i = 1:length(Ca_array)
Params3(10) = Ca_array(i);
[T,Y] = ode45(@B_Model3,Timef,Yo,[],Inputs,Params3);
F3(i) = Y(length(Timef),4)+Y(length(Timef),5);
state43(i) = Y(length(Timef),4);
state53(i) = Y(length(Timef),5);
MgATP31(i) = Params3(4)*state43(i);
MgATP32(i) = Params3(9)*state53(i);
end

%% Calculate SS Indices

% Calculates Fmax, pCa50 and Hill Coefficient from force values
Fmax1 = max(F);
halfmax1 = findnearest((Fmax1)/2,F);
pCa1 = -log10(Ca_array(halfmax1)*10^-6);
nH1 = max(gradient(F/Fmax1,log10(Ca_array)));

Fmax2 = max(F2);
halfmax2 = findnearest((Fmax2)/2,F2);
pCa2 = -log10(Ca_array(halfmax2)*10^-6);
nH2 = max(gradient(F2/Fmax2,log10(Ca_array)));

Fmax3 = max(F3);
halfmax3 = findnearest((Fmax3)/2,F3);
pCa3 = -log10(Ca_array(halfmax3)*10^-6);
nH3 = max(gradient(F3/Fmax3,log10(Ca_array)));

% Calculates Max ATPase, pCa50 and Hill coefficient from ATPase values
MgATP1 = (MgATP11 + MgATP12);
MgATP2 = (MgATP21 + MgATP22);
MgATP3 = (MgATP31 + MgATP32);

ATPmax1 = max(MgATP1);
halfmaxATP1 = findnearest((ATPmax1)/2,MgATP1);
ATPpCa1 = -log10(Ca_array(halfmaxATP1)*10^-6);
ATPnH1 = max(gradient(MgATP1/ATPmax1,log10(Ca_array)));

ATPmax2 = max(MgATP2);
halfmaxATP2 = findnearest((ATPmax2)/2,MgATP2);
ATPpCa2 = -log10(Ca_array(halfmaxATP2)*10^-6);
ATPnH2 = max(gradient(MgATP2/ATPmax2,log10(Ca_array)));

ATPmax3 = max(MgATP3);
halfmaxATP3 = findnearest((ATPmax3)/2,MgATP3);
ATPpCa3 = -log10(Ca_array(halfmaxATP3)*10^-6);
ATPnH3 = max(gradient(MgATP3/ATPmax3,log10(Ca_array)));

% Collect values into result arrays
data_static = [Fmax1 Fmax2 Fmax3;pCa1 pCa2 pCa3;nH1 nH2 nH3];
data_ATP = [ATPmax1 ATPmax2 ATPmax3;ATPpCa1 ATPpCa2 ATPpCa3;ATPnH1 ATPnH2
ATPnH3];

%% Dynamic Calcium Solution
```

```
% Simulation of calcium transient
A = 1.739;
B = 205.89;
C = 30.52;
t = 0:0.0001:0.25;
Ca = A.*(1-exp(-B.*t)).*(exp(-C.*t));

% Specifices Time Dependent
Params(10) = 1;
Params2(10) = 1;
Params3(10) = 1;
Timef2 = 0:0.001:0.25;
Inputs = [t' Ca'];

% Runs Differential Equations for three parameter sets
[T1,Y1] = ode45(@B_Model3,Timef2,Yo,[],Inputs,Params);
[T2,Y2] = ode45(@B_Model3,Timef2,Yo,[],Inputs,Params2);
[T3,Y3] = ode45(@B_Model3,Timef2,Yo,[],Inputs,Params3);

% Force is addition of two states
F1d = Y1(:,4)+Y1(:,5);
F2d = Y2(:,4)+Y2(:,5);
F3d = Y3(:,4)+Y3(:,5);

% Developed force
DevP1 = max(F1d);
DevP2 = max(F2d);
DevP3 = max(F3d);

% Diastolic values (should be close to zero)
Dia1 = F1d(length(F1d));
Dia2 = F2d(length(F2d));
Dia3 = F3d(length(F3d));

% Time to max
time_max1 = find(F1d == DevP1);
time_max2 = find(F2d == DevP2);
time_max3 = find(F3d == DevP3);

%% Rise/relax time for baseline

rise_phase1 = F1d(1:time_max1);
t25_1 = findnearest(DevP1*0.25,rise_phase1);
t75_1 = findnearest(DevP1*0.75,rise_phase1);
rise_time1 = T1(t75_1) - T1(t25_1);

relax_phase1 = F1d(time_max1:length(F1d));
t25_1 = findnearest(DevP1*0.25,relax_phase1);
t75_1 = findnearest(DevP1*0.75,relax_phase1);
relax_time1 = T1(t25_1) - T1(t75_1);

%% Rise/relax for Perturbation One
rise_phase2 = F2d(1:time_max2);
t25_2 = findnearest(DevP2*0.25,rise_phase2);
```

```
t75_2 = findnearest(DevP2*0.75,rise_phase2);
rise_time2 = T2(t75_2) - T2(t25_2);

relax_phase2 = F2d(time_max2:length(F2d));
t25_2 = findnearest(DevP2*0.25,relax_phase2);
t75_2 = findnearest(DevP2*0.75,relax_phase2);
relax_time2 = T2(t25_2) - T2(t75_2);

%% Rise/relax for Perturbation Two
rise_phase3 = F3d(1:time_max3);
t25_3 = findnearest(DevP3*0.25,rise_phase3);
t75_3 = findnearest(DevP3*0.75,rise_phase3);
rise_time3 = T3(t75_3) - T3(t25_3);

relax_phase3 = F3d(time_max3:length(F3d));
t25_3 = findnearest(DevP3*0.25,relax_phase3);
t75_3 = findnearest(DevP3*0.75,relax_phase3);
relax_time3 = T3(t25_3) - T3(t75_3);

%% Collect Data

P_title = ['   Set 1     ' 'Set 2     ' 'Set 3    '];
Parameter_set = [Params' Params2' Params3'];

disp(P_title)
disp(Parameter_set)
disp(data_static)

s_change = [(Fmax3 - Fmax1)/Fmax1 (pCa3-pCa1)/pCa1 (nH3-nH1)/nH1];
S_title = ['   Fmax      ' 'pCa50     ' 'nH    '];
disp(S_title)
disp(s_change)

data_dynamic = [DevP1 DevP2 DevP3;rise_time1 rise_time2
rise_time3;relax_time1 relax_time2 relax_time3];
disp(data_dynamic)

p_change = [(DevP3 - DevP1)/DevP1 (rise_time3-rise_time1)/rise_time1
(relax_time3-relax_time1)/relax_time1];
D_title = ['   DevP      ' 'RiseT     ' 'RelaxT    '];
disp(D_title)
disp(p_change)

ATP_title = ['   ATPmax     ' 'pCa50     ' 'nH    '];
data_ATP = [ATPmax1 ATPmax2 ATPmax3;ATPpCa1 ATPpCa2 ATPpCa3;ATPnH1 ATPnH2
ATPnH3];
ATP_change = [(ATPmax3 - ATPmax1)/ATPmax1 (ATPpCa3 - ATPpCa1)/ATPpCa1 (ATPnH3
- ATPnH1)/ATPnH1];
disp(ATP_title)
disp(ATP_change)

TensionCost1 = (MgATP1(length(MgATP1))-MgATP1(1))/(F(length(F))-F(1));
TensionCost3 = (MgATP3(length(MgATP3))-MgATP3(1))/(F3(length(F3))-F3(1));
```

```
%% Plot Twitch and Steady State Data
figure
colormap gray

subplot(221),plot(log10(Ca_array*10^-6),F,'k',log10(Ca_array*10^-6),F2,'--
k',log10(Ca_array*10^-6),F3,':k','LineWidth',2)
legend('BL','Pert. 1','Pert. 2','Location','NorthWest')
title('Absolute Force-pCa plot')
xlabel('pCa')
ylabel('Force')

subplot(222),plot(log10(Ca_array*10^-6),F/Fmax1,'k',log10(Ca_array*10^-
6),F2/Fmax2,'k--', ...
    log10(Ca_array*10^-6),F3/Fmax3,':k','LineWidth',2)
legend('BL','Pert. 1','Pert. 2','Location','NorthWest')
title('Normalized Force-pCa plot')
xlabel('pCa')
ylabel('Normalized Force')

subplot(223),
plot(T1,F1d,'k',T2,F2d,'--k',T3,F3d,':k','LineWidth',2)
legend('BL','Pert. 1','Pert. 2')
title('Absolute Force Twitch Plot')
xlabel('Time (s)')
ylabel('Force')
v = axis;
axis([0 0.25 v(3) v(4)])

subplot(224),
plot(T1,F1d/DevP1,'k',T2,F2d/DevP2,'--k',T3,F3d/DevP3,':k','LineWidth',2)
legend('BL','Pert. 1','Pert. 2')
title('Normalized Force Twitch Plot')
xlabel('Time (s)')
ylabel('Normalized Force')
v = axis;
axis([0 0.25 v(3) v(4)])

%% Plot Feedback values
figure

subplot(131)
plot(F1d,
Params(5).*F1d.^0.5+Params(6),'k',F3d,Params3(5).*F3d.^0.5+Params3(6),':k','L
ineWidth',2)
legend('Baseline','Pert. 2','Location','SouthEast')
title('K1 feedback, twitch')
xlabel('Force Generating States')
ylabel('K1')

subplot(132)
plot(F1d,
Params(7).*F1d.^1.5+Params(8),'k',F3d,Params3(7).*F3d.^1.5+Params3(8),'k:','L
ineWidth',2)
legend('Baseline','Pert. 2','Location','SouthEast')
title('f feedback, twitch')
```

```
xlabel('Force Generating States')
ylabel('f')

subplot(133)
plot(F1d,
Params(9).*F1d.^1.0+Params(10),'k',F3d,Params3(9).*F3d.^1.0+Params3(10),'k:',
'LineWidth',2)
legend('Baseline','Pert. 2','Location','East')
title('d feedback, twitch')
xlabel('Force Generating States')
ylabel('d')

%% Plot Steady State Data by force generating state
figure
set(gcf,'DefaultAxesColorOrder',[0 0 0;0 0 0;0 0 0;.6 .6 .6;.6 .6 .6;.6 .6
.6;])

subplot(121)
plot(T1,F1d,T1,Y1(:,4),'--',T1,Y1(:,5),':',T3,F3d,T3,Y3(:,4),'--
',T3,Y3(:,5),':','LineWidth',2)
legend('Total BL','State4 BL','State5 BL', ...
    'Total Pert. 2','State4 Pert. 2','State5 Pert 2')
title('State 4 and State 5 during twitch')
xlabel('Time (s)')
ylabel('Force')
colormap gray

subplot(122)
plot(log10(Ca_array*10^-6),F,log10(Ca_array*10^-6),state41,'--
',log10(Ca_array*10^-6),state51,':', ...
    log10(Ca_array*10^-6),F3,log10(Ca_array*10^-6),state43,'--
',log10(Ca_array*10^-6),state53,':','LineWidth',2)
legend('Total WT','WT State4','WT State5','Total TG','TG State4','TG
State5','Location','Northwest')
title('State 4 and State 5 during SS')
xlabel('pCa')
ylabel('Force')

%% Feedback by time
figure

subplot(131)
plot(T1,
Params(5).*F1d.^0.5+Params(6),'k',T3,Params3(5).*F3d.^0.5+Params3(6),':k','Li
neWidth',2)
legend('Baseline','Pert. 2','Location','NorthEast')
title('K1 feedback, twitch')
xlabel('Time (s)')
ylabel('K1')
v = axis;
axis([0 0.25 v(3) v(4)])

subplot(132)
```

```
plot(T1,
Params(7).*F1d.^1.5+Params(8),'k',T3,Params3(7).*F3d.^1.5+Params3(8),'k:','Li
neWidth',2)
legend('Baseline','Pert. 2','Location','NorthEast')
title('f feedback, twitch')
xlabel('Time (s)')
ylabel('f')
v = axis;
axis([0 0.25 v(3) v(4)])

subplot(133)
plot(T1,
Params(9).*F1d.^1.0+Params(10),'k',T3,Params3(9).*F3d.^1.0+Params3(10),'k:','
LineWidth',2)
legend('Baseline','Pert. 2','Location','East')
title('d feedback, twitch')
xlabel('Time (s)')
ylabel('d')
v = axis;
axis([0 0.25 v(3) v(4)])

%% ATPase Results

figure
set(gcf,'DefaultAxesColorOrder',[0 0 0;0 0 0;0 0 0;.6 .6 .6;.6 .6 .6;.6 .6
.6;])
colormap gray

subplot(221),plot(log10(Ca_array*10^-6),MgATP11+MgATP12,log10(Ca_array*10^-
6),MgATP11,'--',log10(Ca_array*10^-6),MgATP12,':', ...
    log10(Ca_array*10^-6),MgATP31+MgATP32,log10(Ca_array*10^-6),MgATP31,'--
',log10(Ca_array*10^-6),MgATP32,':','LineWidth',2)
legend('Total BL','BL State4','BL State5','Total Pert.','Pert. State4','Pert.
State5','Location','Northwest')
title('ATPase Activity')
xlabel('pCa')
ylabel('ATPase Activity')

subplot(222),plot(log10(Ca_array*10^-
6),MgATP1/ATPmax1,'k',log10(Ca_array*10^-6),MgATP2/ATPmax2,'k--', ...
    log10(Ca_array*10^-6),MgATP3/ATPmax3,':k','LineWidth',2)
legend('BL','Pert. 1','Pert. 2','Location','NorthWest')
title('Normalized MgATP-pCa plot')
xlabel('pCa')
ylabel('Normalized ATPase')

subplot(223), plot(F,MgATP1,'k',F3,MgATP3,'k--
',F,(F'\MgATP1')*F,'k',F3,(F3'\MgATP3')*F3,'k--')
    legend('BL','Pert. 2')
    xlabel('Force')
    ylabel('MgATP')
```

MODEL ANALYSIS – B_MODEL3.M

```
function Sysdot = B_Model3(t,Sys,Inputs,Params)
```

```
% Equation function, called by ode45 from main program

% Re establish the parameter set
K2 = Params(1);
K3 = Params(2);
K4 = Params(3);
g = Params(4);
alpha_K1 = Params(5);
beta_K1 = Params(6);
alpha_f = Params(7);
beta_f = Params(8);
d = Params(9);

% Calculate the feedback parameters
K1 = alpha_K1*(Sys(4) + Sys(5))^1.25 + beta_K1;
f = alpha_f*(Sys(4) + Sys(5)) + beta_f;

% Is it dynamic or steady state?
Ca = Params(10);
if length(Inputs) > 2
Calcium = Inputs(:,2);
Timeca = Inputs(:,1);
Ca = interp1(Timeca,Calcium,t);
end

% Differential equations describing the model
Sysdot(1,:) = -K1*Ca*Sys(1) + K3*Sys(3) + d*Sys(5); %dTnCAdt
Sysdot(2,:) = d*Sys(5) - f*Sys(3)*Sys(2) + g*Sys(4); %dMdt
Sysdot(3,:) = K1*Ca*Sys(1) - K3*Sys(3) - f*Sys(3)*Sys(2) + g*Sys(4);
%dCa_TnCAdt
Sysdot(4,:) = (f*Sys(3)*Sys(2) + K2*Ca*Sys(5) - (g+K4)*Sys(4)); %dCa_TnCA_Mdt
Sysdot(5,:) = (K4*Sys(4) - d*Sys(5) - K2*Ca*Sys(5)); %dTnCA_Mdt
```

MODEL ANALYSIS – FINDNEAREST.M

```
function [r,c,V] = findnearest(srchvalue,srcharray,bias)

% Usage:
% Find the nearest numerical value in an array to a search value
% All occurances are returned as array subscripts
%
% Output:
%
% For 2D matrix subscripts (r,c) use:
%
%       [r,c] = findnearest(srchvalue,srcharray,gt_or_lt)
%
%
% To also output the found value (V) use:
%
%       [r,c,V] = findnearest(srchvalue,srcharray,gt_or_lt)
%
%
% For single subscript (i) use:
```

```
%
%         i   = findnearest(srchvalue,srcharray,gt_or_lt)
%
%
% Inputs:
%
%    srchvalue = a numerical search value
%    srcharray = the array to be searched
%    bias      = 0 (default) for no bias
%                -1 to bias the output to lower values
%                 1 to bias the search to higher values
%                (in the latter cases if no values are found
%                 an empty array is ouput)
%
%
% By Tom Benson (2002)
% University College London
% t.benson@ucl.ac.uk

if nargin<2
    error('Need two inputs: Search value and search array')
elseif nargin<3
    bias = 0;
end

% find the differences
srcharray = srcharray-srchvalue;

if bias == -1   % only choose values <= to the search value

    srcharray(srcharray>0) =inf;

elseif bias == 1  % only choose values >= to the search value

    srcharray(srcharray<0) =inf;

end

% give the correct output
if nargout==1 | nargout==0

    if all(isinf(srcharray(:)))
        r = [];
    else
        r = find(abs(srcharray)==min(abs(srcharray(:))));
    end

elseif nargout>1
    if all(isinf(srcharray(:)))
        r = [];c=[];
    else
        [r,c] = find(abs(srcharray)==min(abs(srcharray(:))));
    end

    if nargout==3
```

```
        V = srcharray(r,c)+srchvalue;
    end
end
```

APPENDIX D

FOUR-STATE SENSITIVITY ANALYSIS

The following tables (**Table 12** through **Table 20**) show the effects of changes in the parameters of the four-state model on the each of the calculated parameters (steady-state and time-varying). Each table shows the effects of changes for an individual parameter. Sensitivity for a continuous relationship is described by:

$$S_X^Y = \frac{\delta Y/Y}{\delta X/X} \tag{D.1}$$

where S_X^Y is the sensitivity of Y to X. **Equation D.1** can be converted for use with discreet data, which we have used for the tables below:

$$S_X^Y = \frac{\Delta Y/Y}{\Delta X/X} \tag{D.2}$$

The average and S.E.M. sensitivity values in **Table 2 1** were calculated from the sensitivity values over 50% to 150% of the baseline value of the parameter.

Table 12. Effect of Changes in k_2

Parameter	5%	10%	50%	75%	BL	125%	150%	200%	1000%
k_2	***1.25***	***2.5***	***12.5***	***18.75***	***25***	***31.25***	***37.5***	***50***	***250***
k_3	84	84	84	84	84	84	84	84	84
k_4	84	84	84	84	84	84	84	84	84
g	205.3	205.3	205.3	205.3	205.3	205.3	205.3	205.3	205.3
α_1	2	2	2	2	2	2	2	2	2
β_1	3	3	3	3	3	3	3	3	3
α_f	0.15	0.15	0.15	0.15	0.15	0.15	0.15	0.15	0.15
β_f	0.7	0.7	0.7	0.7	0.7	0.7	0.7	0.7	0.7
d	44.6	44.6	44.6	44.6	44.6	44.6	44.6	44.6	44.6
Indices									
F_{max}	10.07	9.39	7.27	6.99	6.93	6.90	6.88	6.85	6.78
pCa_{50}	5.54	5.54	5.46	5.41	5.37	5.34	5.31	5.27	5.15
n_H	3.69	3.69	2.89	2.45	2.15	1.97	1.87	1.75	1.58
TC	152	170	196	199	200	201	202	203	205
P_{dev}	0.215	0.214	0.210	0.207	0.204	0.202	0.200	0.196	0.166
T_{rise}	0.012	0.012	0.013	0.013	0.013	0.012	0.012	0.012	0.011
T_{relax}	0.048	0.048	0.048	0.048	0.049	0.049	0.049	0.05	0.052
Δ (% from BL)									
F_{max}	45.2	35.5	4.9	0.8	0.0	-0.5	-0.8	-1.2	-2.2
pCa_{50}	3.2	3.2	1.7	0.8	0.0	-0.5	-1.1	-1.8	-3.9
n_H	71.4	71.3	34.3	13.8	0.0	-8.3	-13.3	-18.8	-26.5
TC	-24.0	-15.3	-2.3	-0.8	0.0	0.5	0.8	1.3	2.3
P_{dev}	5.1	4.8	2.5	1.2	0.0	-1.1	-2.2	-4.2	-19.0
T_{rise}	-7.7	-7.7	0.0	0.0	0.0	-7.7	-7.7	-7.7	-15.4
T_{relax}	-2.0	-2.0	-2.0	-2.0	0.0	0.0	0.0	2.0	6.1
Sensitivity									
F_{max}	-0.48	-0.39	-0.10	-0.03	0.00	-0.02	-0.02	-0.01	0.00
pCa_{50}	-0.03	-0.04	-0.03	-0.03	0.00	-0.02	-0.02	-0.02	0.00
n_H	-0.75	-0.79	-0.69	-0.55	0.00	-0.33	-0.27	-0.19	-0.03
TC	0.25	0.17	0.05	0.03	0.00	0.02	0.02	0.01	0.00
P_{dev}	-0.05	-0.05	-0.05	-0.05	0.00	-0.05	-0.04	-0.04	-0.02
T_{rise}	0.08	0.09	0.00	0.00	0.00	-0.31	-0.15	-0.08	-0.02
T_{relax}	0.02	0.02	0.04	0.08	0.00	0.00	0.00	0.02	0.01

Table 13. Effects of Changes in k_3

Parameter	5%	10%	50%	75%	BL	125%	150%	200%	1000%
k_2	25	25	25	25	25	25	25	25	25
k_3	***4.2***	***8.4***	***42***	***63***	***84***	***105***	***126***	***168***	***840***
k_4	84	84	84	84	84	84	84	84	84
g	205.3	205.3	205.3	205.3	205.3	205.3	205.3	205.3	205.3
α_1	2	2	2	2	2	2	2	2	2
β_1	3	3	3	3	3	3	3	3	3
α_f	0.15	0.15	0.15	0.15	0.15	0.15	0.15	0.15	0.15
β_f	0.7	0.7	0.7	0.7	0.7	0.7	0.7	0.7	0.7
d	44.6	44.6	44.6	44.6	44.6	44.6	44.6	44.6	44.6
Indices									
F_{max}	9.46	9.01	7.26	6.99	6.93	6.88	6.82	6.71	4.66
pCa_{50}	6.40	6.30	5.74	5.52	5.37	5.24	5.14	4.96	4.26
n_H	2.32	2.48	2.80	2.43	2.15	1.99	1.88	1.78	2.30
TC	201	200	200	200	200	200	200	200	200
P_{dev}	1.019	0.833	0.350	0.258	0.204	0.169	0.144	0.111	0.023
T_{rise}	0.031	0.027	0.016	0.014	0.013	0.011	0.011	0.01	0.007
T_{relax}	0.087	0.099	0.054	0.051	0.049	0.049	0.049	0.048	0.049
Δ (% from BL)									
F_{max}	36.4	30.0	4.7	0.8	0.0	-0.8	-1.6	-3.2	-32.8
pCa_{50}	19.2	17.4	7.0	2.9	0.0	-2.3	-4.3	-7.6	-20.6
n_H	7.6	15.4	30.1	13.0	0.0	-7.7	-12.5	-17.3	6.7
TC	0.2	0.1	0.0	0.0	0.0	0.0	0.0	0.0	0.0
P_{dev}	398.5	307.3	71.2	26.3	0.0	-17.3	-29.6	-45.9	-88.8
T_{rise}	138.5	107.7	23.1	7.7	0.0	-15.4	-15.4	-23.1	-46.2
T_{relax}	77.6	102.0	10.2	4.1	0.0	0.0	0.0	-2.0	0.0
Sensitivity									
F_{max}	-0.38	-0.33	-0.09	-0.03	0.00	-0.03	-0.03	-0.03	-0.04
pCa_{50}	-0.20	-0.19	-0.14	-0.12	0.00	-0.09	-0.09	-0.08	-0.02
n_H	-0.08	-0.17	-0.60	-0.52	0.00	-0.31	-0.25	-0.17	0.01
TC	0.00	0.00	0.00	0.00	0.00	0.00	0.00	0.00	0.00
P_{dev}	-4.19	-3.41	-1.42	-1.05	0.00	-0.69	-0.59	-0.46	-0.10
T_{rise}	-1.46	-1.20	-0.46	-0.31	0.00	-0.62	-0.31	-0.23	-0.05
T_{relax}	-0.82	-1.13	-0.20	-0.16	0.00	0.00	0.00	-0.02	0.00

Table 14. Effects of Changes in k_4

Parameter	5%	10%	50%	75%	BL	125%	150%	200%	1000%
k_2	25	25	25	25	25	25	25	25	25
k_3	84	84	84	84	84	84	84	84	84
k_4	***4.2***	***8.4***	***42***	***63***	***84***	***105***	***126***	***168***	***840***
g	205.3	205.3	205.3	205.3	205.3	205.3	205.3	205.3	205.3
α_1	2	2	2	2	2	2	2	2	2
β_1	3	3	3	3	3	3	3	3	3
α_f	0.15	0.15	0.15	0.15	0.15	0.15	0.15	0.15	0.15
β_f	0.7	0.7	0.7	0.7	0.7	0.7	0.7	0.7	0.7
d	44.6	44.6	44.6	44.6	44.6	44.6	44.6	44.6	44.6
Indices									
F_{max}	6.77	6.78	6.85	6.89	6.93	6.98	7.05	7.42	11.80
pCa_{50}	5.14	5.15	5.25	5.31	5.37	5.42	5.47	5.54	5.80
n_H	1.58	1.59	1.77	1.93	2.15	2.43	2.74	3.34	5.75
TC	205	205	203	201	200	199	198	195	165
P_{dev}	0.140	0.144	0.172	0.189	0.204	0.219	0.232	0.254	0.384
T_{rise}	0.009	0.009	0.011	0.012	0.013	0.012	0.013	0.014	0.014
T_{relax}	0.042	0.043	0.048	0.049	0.049	0.049	0.049	0.049	0.047
Δ (% from BL)									
F_{max}	-2.4	-2.2	-1.2	-0.6	0.0	0.6	1.7	7.0	70.2
pCa_{50}	-4.3	-4.1	-2.1	-1.1	0.0	1.0	1.9	3.2	8.0
n_H	-26.4	-25.9	-18.0	-10.2	0.0	12.8	27.3	55.2	167.0
TC	2.4	2.3	1.3	0.6	0.0	-0.6	-1.2	-2.4	-17.3
P_{dev}	-31.5	-29.8	-15.8	-7.6	0.0	7.0	13.3	24.3	87.9
T_{rise}	-30.8	-30.8	-15.4	-7.7	0.0	-7.7	0.0	7.7	7.7
T_{relax}	-14.3	-12.2	-2.0	0.0	0.0	0.0	0.0	0.0	-4.1
Sensitivity									
F_{max}	0.02	0.02	0.02	0.02	0.00	0.02	0.03	0.07	0.08
pCa_{50}	0.05	0.05	0.04	0.04	0.00	0.04	0.04	0.03	0.01
n_H	0.28	0.29	0.36	0.41	0.00	0.51	0.55	0.55	0.19
TC	-0.03	-0.03	-0.03	-0.02	0.00	-0.02	-0.02	-0.02	-0.02
P_{dev}	0.33	0.33	0.32	0.30	0.00	0.28	0.27	0.24	0.10
T_{rise}	0.32	0.34	0.31	0.31	0.00	-0.31	0.00	0.08	0.01
T_{relax}	0.15	0.14	0.04	0.00	0.00	0.00	0.00	0.00	0.00

Table 15. Effects of Changes in *g*

Parameter	5%	10%	50%	75%	BL	125%	150%	200%	1000%
k_2	25	25	25	25	25	25	25	25	25
k_3	84	84	84	84	84	84	84	84	84
k_4	84	84	84	84	84	84	84	84	84
g	**10.265**	**20.53**	**102.65**	**153.975**	**205.3**	**256.625**	**307.95**	**410.6**	**2053**
α_1	2	2	2	2	2	2	2	2	2
β_1	3	3	3	3	3	3	3	3	3
α_f	0.15	0.15	0.15	0.15	0.15	0.15	0.15	0.15	0.15
β_f	0.7	0.7	0.7	0.7	0.7	0.7	0.7	0.7	0.7
d	44.6	44.6	44.6	44.6	44.6	44.6	44.6	44.6	44.6
Indices									
F_{max}	18.80	17.82	11.63	8.94	6.93	5.47	4.41	3.06	0.43
pCa_{50}	6.10	6.05	5.72	5.54	5.37	5.24	5.13	5.00	4.85
n_H	4.51	4.80	4.93	3.30	2.15	1.57	1.27	0.99	0.68
TC	11	21	101	151	200	250	300	399	1990
P_{dev}	0.685	0.613	0.328	0.252	0.204	0.172	0.148	0.116	0.026
T_{rise}	0.017	0.016	0.013	0.013	0.013	0.012	0.012	0.011	0.011
T_{relax}	0.046	0.046	0.048	0.048	0.049	0.049	0.049	0.05	0.051
Δ (% from BL)									
F_{max}	171.1	157.0	67.7	28.9	0.0	-21.1	-36.4	-55.8	-93.9
pCa_{50}	13.6	12.7	6.6	3.2	0.0	-2.4	-4.4	-6.7	-9.6
n_H	109.6	122.8	128.9	53.4	0.0	-26.8	-41.1	-53.8	-68.5
TC	-94.3	-89.4	-49.6	-24.8	0.0	24.8	49.7	99.3	894.0
P_{dev}	234.8	199.9	60.4	23.4	0.0	-16.0	-27.6	-43.4	-87.4
T_{rise}	30.8	23.1	0.0	0.0	0.0	-7.7	-7.7	-15.4	-15.4
T_{relax}	-6.1	-6.1	-2.0	-2.0	0.0	0.0	0.0	2.0	4.1
Sensitivity									
F_{max}	-1.80	-1.74	-1.35	-1.16	0.00	-0.84	-0.73	-0.56	-0.10
pCa_{50}	-0.14	-0.14	-0.13	-0.13	0.00	-0.10	-0.09	-0.07	-0.01
n_H	-1.15	-1.36	-2.58	-2.14	0.00	-1.07	-0.82	-0.54	-0.08
TC	0.99	0.99	0.99	0.99	0.00	0.99	0.99	0.99	0.99
P_{dev}	-2.47	-2.22	-1.21	-0.93	0.00	-0.64	-0.55	-0.43	-0.10
T_{rise}	-0.32	-0.26	0.00	0.00	0.00	-0.31	-0.15	-0.15	-0.02
T_{relax}	0.06	0.07	0.04	0.08	0.00	0.00	0.00	0.02	0.00

Table 16. Effects of Changes in α_1

Parameter	5%	10%	50%	75%	BL	125%	150%	200%	1000%
k_2	25	25	25	25	25	25	25	25	25
k_3	84	84	84	84	84	84	84	84	84
k_4	84	84	84	84	84	84	84	84	84
g	205.3	205.3	205.3	205.3	205.3	205.3	205.3	205.3	205.3
α_1	***0.1***	***0.2***	***1***	***1.5***	***2***	***2.5***	***3***	***4***	***20***
β_1	3	3	3	3	3	3	3	3	3
α_f	0.15	0.15	0.15	0.15	0.15	0.15	0.15	0.15	0.15
β_f	0.7	0.7	0.7	0.7	0.7	0.7	0.7	0.7	0.7
d	44.6	44.6	44.6	44.6	44.6	44.6	44.6	44.6	44.6
Indices									
F_{max}	5.89	6.12	6.76	6.87	6.93	6.97	7.02	7.21	9.30
pCa_{50}	4.77	4.80	5.10	5.24	5.37	5.47	5.55	5.68	4.00
n_H	0.79	0.84	1.29	1.67	2.15	2.76	3.46	5.08	4.84
TC	200	200	200	200	200	200	200	200	200
P_{dev}	0.195	0.195	0.199	0.202	0.204	0.207	0.210	0.216	0.375
T_{rise}	0.012	0.012	0.012	0.012	0.013	0.013	0.013	0.012	0.018
T_{relax}	0.05	0.05	0.049	0.049	0.049	0.048	0.048	0.048	0.042
Δ (% from BL)									
F_{max}	-15.1	-11.7	-2.5	-0.9	0.0	0.6	1.2	4.0	34.2
pCa_{50}	-11.1	-10.6	-5.0	-2.3	0.0	1.9	3.5	5.8	-25.5
n_H	-63.1	-61.1	-40.1	-22.5	0.0	28.0	60.5	135.8	124.8
TC	0.0	0.0	0.0	0.0	0.0	0.0	0.0	0.0	0.0
P_{dev}	-4.8	-4.5	-2.6	-1.3	0.0	1.3	2.7	5.5	83.3
T_{rise}	-7.7	-7.7	-7.7	-7.7	0.0	0.0	0.0	-7.7	38.5
T_{relax}	2.0	2.0	0.0	0.0	0.0	-2.0	-2.0	-2.0	-14.3
Sensitivity									
F_{max}	0.16	0.13	0.05	0.04	0.00	0.02	0.02	0.04	0.04
pCa_{50}	0.12	0.12	0.10	0.09	0.00	0.08	0.07	0.06	-0.03
n_H	0.66	0.68	0.80	0.90	0.00	1.12	1.21	1.36	0.14
TC	0.00	0.00	0.00	0.00	0.00	0.00	0.00	0.00	0.00
P_{dev}	0.05	0.05	0.05	0.05	0.00	0.05	0.05	0.06	0.09
T_{rise}	0.08	0.09	0.15	0.31	0.00	0.00	0.00	-0.08	0.04
T_{relax}	-0.02	-0.02	0.00	0.00	0.00	-0.08	-0.04	-0.02	-0.02

Table 17. Effects of Changes in β_1

Parameter	5%	10%	50%	75%	BL	125%	150%	200%	1000%
k_2	25	25	25	25	25	25	25	25	25
k_3	84	84	84	84	84	84	84	84	84
k_4	84	84	84	84	84	84	84	84	84
g	205.3	205.3	205.3	205.3	205.3	205.3	205.3	205.3	205.3
α_1	2	2	2	2	2	2	2	2	2
β_1	***0.15***	***0.3***	***1.5***	***2.25***	***3***	***3.75***	***4.5***	***6***	***30***
α_f	0.15	0.15	0.15	0.15	0.15	0.15	0.15	0.15	0.15
β_f	0.7	0.7	0.7	0.7	0.7	0.7	0.7	0.7	0.7
d	44.6	44.6	44.6	44.6	44.6	44.6	44.6	44.6	44.6
Indices									
F_{max}	6.91	6.91	6.92	6.93	6.93	6.94	6.95	6.96	7.28
pCa_{50}	5.10	5.17	5.29	5.33	5.37	5.40	5.43	5.49	6.00
n_H	33.24	19.10	3.63	2.60	2.15	1.90	1.73	1.53	1.06
TC	200	200	200	200	200	200	200	200	201
P_{dev}	0.010	0.020	0.101	0.153	0.204	0.256	0.309	0.413	2.056
T_{rise}	0.012	0.012	0.012	0.012	0.013	0.013	0.013	0.013	0.013
T_{relax}	0.049	0.049	0.049	0.049	0.049	0.049	0.049	0.048	0.049
Δ (% from BL)									
F_{max}	-0.4	-0.4	-0.2	-0.1	0.0	0.1	0.2	0.3	4.9
pCa_{50}	-4.9	-3.7	-1.4	-0.7	0.0	0.6	1.2	2.4	11.8
n_H	1444.1	787.2	68.8	20.8	0.0	-11.8	-19.5	-28.8	-50.5
TC	0.0	0.0	0.0	0.0	0.0	0.0	0.0	0.0	0.2
P_{dev}	-95.1	-90.2	-50.4	-25.3	0.0	25.4	50.9	102.1	905.5
T_{rise}	-7.7	-7.7	-7.7	-7.7	0.0	0.0	0.0	0.0	0.0
T_{relax}	0.0	0.0	0.0	0.0	0.0	0.0	0.0	-2.0	0.0
Sensitivity									
F_{max}	0.00	0.00	0.00	0.00	0.00	0.00	0.00	0.00	0.01
pCa_{50}	0.05	0.04	0.03	0.03	0.00	0.02	0.02	0.02	0.01
n_H	-15.20	-8.75	-1.38	-0.83	0.00	-0.47	-0.39	-0.29	-0.06
TC	0.00	0.00	0.00	0.00	0.00	0.00	0.00	0.00	0.00
P_{dev}	1.00	1.00	1.01	1.01	0.00	1.02	1.02	1.02	1.01
T_{rise}	0.08	0.09	0.15	0.31	0.00	0.00	0.00	0.00	0.00
T_{relax}	0.00	0.00	0.00	0.00	0.00	0.00	0.00	-0.02	0.00

Table 18. Effects of Changes in α_f

Parameter	5%	10%	50%	75%	BL	125%	150%	200%	1000%
k_2	25	25	25	25	25	25	25	25	25
k_3	84	84	84	84	84	84	84	84	84
k_4	84	84	84	84	84	84	84	84	84
g	205.3	205.3	205.3	205.3	205.3	205.3	205.3	205.3	205.3
α_1	2	2	2	2	2	2	2	2	2
β_1	3	3	3	3	3	3	3	3	3
α_f	***0.0075***	***0.015***	***0.075***	***0.1125***	***0.15***	***0.1875***	***0.225***	***0.3***	***1.5***
β_f	0.7	0.7	0.7	0.7	0.7	0.7	0.7	0.7	0.7
d	44.6	44.6	44.6	44.6	44.6	44.6	44.6	44.6	44.6
Indices									
F_{max}	3.70	3.82	5.00	5.93	6.93	7.96	8.93	10.66	17.67
pCa_{50}	5.25	5.25	5.28	5.31	5.37	5.43	5.51	5.62	6.10
n_H	0.97	1.00	1.26	1.57	2.15	3.29	5.67	12.36	8.73
TC	200	200	200	200	200	200	200	200	200
P_{dev}	0.197	0.198	0.201	0.203	0.204	0.206	0.208	0.212	0.303
T_{rise}	0.012	0.012	0.012	0.012	0.013	0.013	0.013	0.013	0.014
T_{relax}	0.05	0.05	0.049	0.049	0.049	0.049	0.049	0.049	0.044
Δ (% from BL)									
F_{max}	-46.7	-45.0	-27.9	-14.6	0.0	14.7	28.8	53.7	154.8
pCa_{50}	-2.1	-2.1	-1.7	-1.1	0.0	1.2	2.6	4.7	13.6
n_H	-55.0	-53.8	-41.7	-26.9	0.0	52.9	163.2	474.2	305.6
TC	0.0	0.0	0.0	0.0	0.0	0.0	0.0	0.0	0.0
P_{dev}	-3.5	-3.3	-1.9	-0.9	0.0	1.0	1.9	3.9	48.1
T_{rise}	-7.7	-7.7	-7.7	-7.7	0.0	0.0	0.0	0.0	7.7
T_{relax}	2.0	2.0	0.0	0.0	0.0	0.0	0.0	0.0	-10.2
Sensitivity									
F_{max}	0.49	0.50	0.56	0.58	0.00	0.59	0.58	0.54	0.17
pCa_{50}	0.02	0.02	0.03	0.04	0.00	0.05	0.05	0.05	0.02
n_H	0.58	0.60	0.83	1.08	0.00	2.11	3.26	4.74	0.34
TC	0.00	0.00	0.00	0.00	0.00	0.00	0.00	0.00	0.00
P_{dev}	0.04	0.04	0.04	0.04	0.00	0.04	0.04	0.04	0.05
T_{rise}	0.08	0.09	0.15	0.31	0.00	0.00	0.00	0.00	0.01
T_{relax}	-0.02	-0.02	0.00	0.00	0.00	0.00	0.00	0.00	-0.01

Table 19. Effects of Changes in β_f

Parameter	5%	10%	50%	75%	BL	125%	150%	200%	1000%
k_2	25	25	25	25	25	25	25	25	25
k_3	84	84	84	84	84	84	84	84	84
k_4	84	84	84	84	84	84	84	84	84
g	205.3	205.3	205.3	205.3	205.3	205.3	205.3	205.3	205.3
α_1	2	2	2	2	2	2	2	2	2
β_1	3	3	3	3	3	3	3	3	3
α_f	0.15	0.15	0.15	0.15	0.15	0.15	0.15	0.15	0.15
β_f	***0.035***	***0.07***	***0.35***	***0.525***	***0.7***	***0.875***	***1.05***	***1.4***	***7***
d	44.6	44.6	44.6	44.6	44.6	44.6	44.6	44.6	44.6
Indices									
F_{max}	1.23	2.17	5.17	6.17	6.93	7.57	8.11	9.00	14.48
pCa_{50}	4.32	4.46	5.06	5.24	5.37	5.47	5.55	5.66	6.22
n_H	1.69	1.46	1.82	2.02	2.15	2.24	2.29	2.34	2.07
TC	200	200	200	200	200	200	200	200	200
P_{dev}	0.010	0.020	0.102	0.153	0.204	0.256	0.309	0.415	2.690
T_{rise}	0.012	0.012	0.012	0.012	0.013	0.013	0.013	0.012	0.017
T_{relax}	0.05	0.05	0.049	0.049	0.049	0.048	0.048	0.048	0.043
Δ (% from BL)									
F_{max}	-82.2	-68.8	-25.4	-11.1	0.0	9.1	16.9	29.8	108.8
pCa_{50}	-19.5	-17.0	-5.8	-2.4	0.0	1.9	3.5	5.4	15.9
n_H	-21.4	-32.1	-15.3	-6.1	0.0	3.9	6.4	8.8	-3.6
TC	0.0	0.0	0.0	0.0	0.0	0.0	0.0	0.0	0.1
P_{dev}	-95.0	-90.0	-50.1	-25.1	0.0	25.3	50.9	102.9	1215.8
T_{rise}	-7.7	-7.7	-7.7	-7.7	0.0	0.0	0.0	-7.7	30.8
T_{relax}	2.0	2.0	0.0	0.0	0.0	-2.0	-2.0	-2.0	-12.2
Sensitivity									
F_{max}	0.87	0.76	0.51	0.44	0.00	0.37	0.34	0.30	0.12
pCa_{50}	0.21	0.19	0.12	0.10	0.00	0.08	0.07	0.05	0.02
n_H	0.23	0.36	0.31	0.24	0.00	0.16	0.13	0.09	0.00
TC	0.00	0.00	0.00	0.00	0.00	0.00	0.00	0.00	0.00
P_{dev}	1.00	1.00	1.00	1.01	0.00	1.01	1.02	1.03	1.35
T_{rise}	0.08	0.09	0.15	0.31	0.00	0.00	0.00	-0.08	0.03
T_{relax}	-0.02	-0.02	0.00	0.00	0.00	-0.08	-0.04	-0.02	-0.01

Table 20. Effects of Changes in *d*

Parameter	5%	10%	50%	75%	BL	125%	150%	200%	1000%
k_2	25	25	25	25	25	25	25	25	25
k_3	84	84	84	84	84	84	84	84	84
k_4	84	84	84	84	84	84	84	84	84
g	205.3	205.3	205.3	205.3	205.3	205.3	205.3	205.3	205.3
α_1	2	2	2	2	2	2	2	2	2
β_1	3	3	3	3	3	3	3	3	3
α_f	0.15	0.15	0.15	0.15	0.15	0.15	0.15	0.15	0.15
β_f	0.7	0.7	0.7	0.7	0.7	0.7	0.7	0.7	0.7
d	***2.23***	***4.46***	***22.3***	***33.45***	***44.6***	***55.75***	***66.9***	***89.2***	***446***
Indices									
F_{max}	6.99	6.98	6.96	6.95	6.93	6.92	6.91	6.88	6.54
pCa_{50}	5.80	5.72	5.49	5.42	5.37	5.33	5.29	5.24	5.00
n_H	3.15	3.12	2.50	2.29	2.15	2.06	1.98	1.87	1.35
TC	199	199	200	200	200	201	201	202	212
P_{dev}	0.361	0.333	0.246	0.221	0.204	0.192	0.182	0.167	0.114
T_{rise}	0.023	0.021	0.015	0.013	0.013	0.012	0.011	0.011	0.009
T_{relax}	0	0.077	0.068	0.055	0.049	0.046	0.043	0.041	0.039
Δ (% from BL)									
F_{max}	0.9	0.7	0.4	0.2	0.0	-0.2	-0.4	-0.7	-5.7
pCa_{50}	8.0	6.6	2.4	1.0	0.0	-0.7	-1.4	-2.3	-6.7
n_H	46.4	45.1	16.1	6.5	0.0	-4.5	-8.1	-13.3	-37.2
TC	-0.4	-0.5	-0.4	-0.2	0.0	0.2	0.4	0.7	5.9
P_{dev}	76.7	63.1	20.1	8.2	0.0	-6.1	-10.9	-18.1	-44.2
T_{rise}	76.9	61.5	15.4	0.0	0.0	-7.7	-15.4	-15.4	-30.8
T_{relax}	-100.0	57.1	38.8	12.2	0.0	-6.1	-12.2	-16.3	-20.4
Sensitivity									
F_{max}	-0.01	-0.01	-0.01	-0.01	0.00	-0.01	-0.01	-0.01	-0.01
pCa_{50}	-0.08	-0.07	-0.05	-0.04	0.00	-0.03	-0.03	-0.02	-0.01
n_H	-0.49	-0.50	-0.32	-0.26	0.00	-0.18	-0.16	-0.13	-0.04
TC	0.00	0.01	0.01	0.01	0.00	0.01	0.01	0.01	0.01
P_{dev}	-0.81	-0.70	-0.40	-0.33	0.00	-0.25	-0.22	-0.18	-0.05
T_{rise}	-0.81	-0.68	-0.31	0.00	0.00	-0.31	-0.31	-0.15	-0.03
T_{relax}	1.05	-0.63	-0.78	-0.49	0.00	-0.24	-0.24	-0.16	-0.02

Table 21. Index Sensitivity to All Parameters

	Indices (Steady State Data)				Indices (Time Varying Data)		
Parameter	F_{max}	pCa_{50}	n_H	TC	P_{dev}	T_{rise}	T_{relax}
k_2	-0.04 ± 0.04	-0.03 ± 0.01	-0.46 ± 0.19	0.03 ± 0.01	-0.05 ± 0	-0.12 ± 0.15	0.03 ± 0.04
k_3	-0.05 ± 0.03	-0.11 ± 0.03	-0.42 ± 0.17	0 ± 0	-0.94 ± 0.38	-0.42 ± 0.15	-0.09 ± 0.11
k_4	0.03 ± 0	0.04 ± 0	0.46 ± 0.09	-0.02 ± 0	0.29 ± 0.02	0.08 ± 0.29	0.01 ± 0.02
g	-1.02 ± 0.29	-0.11 ± 0.02	-1.65 ± 0.84	0.99 ± 0	-0.83 ± 0.3	-0.12 ± 0.15	0.03 ± 0.04
α_1	0.03 ± 0.01	0.08 ± 0.01	1.01 ± 0.19	0 ± 0	0.05 ± 0	0.12 ± 0.15	-0.03 ± 0.04
β_1	0 ± 0	0.03 ± 0	-0.77 ± 0.45	0 ± 0	1.01 ± 0	0.12 ± 0.15	0 ± 0
α_f	0.58 ± 0.01	0.04 ± 0.01	1.82 ± 1.11	0 ± 0	0.04 ± 0	0.12 ± 0.15	0 ± 0
β_f	0.41 ± 0.08	0.09 ± 0.02	0.21 ± 0.08	0 ± 0	1.01 ± 0.01	0.12 ± 0.15	-0.03 ± 0.04
d	-0.01 ± 0	-0.04 ± 0.01	-0.23 ± 0.07	0.01 ± 0	-0.3 ± 0.08	-0.23 ± 0.15	-0.44 ± 0.25

Average sensitivity was calculated as the average sensitivity over 50% to 150% of the baseline value of the parameter.

APPENDIX E

CALCIUM CALIBRATION EQUATION DERIVATION

The calibration equation for the fluorescence recorded during measurement of intracellular calcium transients with fura-2 (or its derivatives) is shown in **Equation E.1**:

$$[Ca^{2+}]_i = K_d \left(\frac{S_{f-380}}{S_{b-380}}\right)\left(\frac{R-R_{min}}{R_{max}-R}\right) \quad \text{(E.1)}$$

This equation is presented in the literature many times, and is well known [100]. While it has been partially derived in the literature [91], we will derive it here in full as a reference.

We will begin by setting up the chemical equilibria of fura binding to calcium.

$$C_f + Ca^{2+} \underset{k_{-l}}{\overset{k_l}{\rightleftharpoons}} C_b$$

Figure 9-12. Fura Binding to Calcium

In **Figure 9-12**, C_f is concentration of free dye, Ca^{2+} is concentration of calcium, C_b is concentration of bound dye, k_l is the binding constant and k_{-l} is the unbinding constant. The following relationships can be made:

$$C_b = \frac{k_l C_f Ca^{2+}}{k_{-l}} \quad \text{(E.2)}$$

$$k_d = \frac{k_{-l}}{k_l} \tag{E.3}$$

$$C_b = \frac{C_f Ca^{2+}}{k_d} \tag{E.4}$$

where k_d is the dye dissociation constant.

There are two excitation wavelengths for fura dyes: λ_1 = 340 nm, and λ_2 = 380 nm. Fluorescence at each wavelength is composed of bound dye and free dye (bound dye increases fluorescence primarily at 340 nm and free dye increases fluorescence primarily at 380 nm), leading to four fluorescence intensities: S_{f1} (free dye at λ_1), S_{f2} (free dye at λ_2), S_{b1} (bound dye at λ_1), and S_{b2} (bound dye at λ_2). Therefore, there are two total fluorescences, one at each wavelength:

$$F_1 = S_{f1} C_f + S_{b1} C_b \tag{E.5}$$

$$F_2 = S_{f2} C_f + S_{b2} C_b \tag{E.6}$$

The ratio of the total fluorescence at 340 nm excitation over 380 nm excitation represents the fluorescence ratio R:

$$R = \frac{F_1}{F_2} = \frac{S_{f1} C_f + S_{b1} C_b}{S_{f2} C_f + S_{b2} C_b} \tag{E.7}$$

The vales of C_b in **Equation E.7** can be replaced with **Equation E.4** to yield:

$$R = \frac{S_{f1} + S_{b1} \frac{Ca^{2+}}{k_d}}{S_{f2} + S_{b2} \frac{Ca^{2+}}{k_d}} \tag{E.8}$$

which can be rearranged:

$$R\left(S_{f2} + S_{b2} \frac{Ca^{2+}}{k_d}\right) = S_{f1} + S_{b1} \frac{Ca^{2+}}{k_d} \tag{E.9}$$

$$RS_{f2} - S_{f1} = \frac{Ca^{2+}}{k_d}(S_{b1} - RS_{b2}) \tag{E.10}$$

$$\frac{Ca^{2+}}{k_d} = \frac{RS_{f2} - S_{f1}}{S_{b1} - RS_{b2}} \tag{E.11}$$

Two new parameters can be defined:

$$R_{min} = \frac{S_{f1}}{S_{f2}} \tag{E.12}$$

$$R_{max} = \frac{S_{b1}}{S_{b2}} \tag{E.13}$$

In order to introduce these two parameters into **Equation E.11**, the following multiplication is introduced:

$$\frac{Ca^{2+}}{k_d} = \frac{RS_{f2} - S_{f1}}{S_{b1} - RS_{b2}} \left(\frac{{}^{1}/_{S_{f2}S_{b2}}}{{}^{1}/_{S_{f2}S_{b2}}} \right) \tag{E.14}$$

which can be rearranged:

$$\frac{Ca^{2+}}{k_d} = \frac{{}^{1}/_{S_{b2}} - \left(R - \frac{S_{f1}}{S_{f2}} \right)}{{}^{1}/_{S_{f2}} - \left(\frac{S_{b1}}{S_{b2}} - R \right)} \tag{E.15}$$

Inserting **Equation E.12** and **Equation E.13** and rearranging yields the calibration equation:

$$Ca^{2+} = K_d \left(\frac{S_{f2}}{S_{b2}} \right) \left(\frac{R - R_{min}}{R_{max} - R} \right) \tag{E.16}$$

BIBLIOGRAPHY

1. **Bers, D.M.**, Calcium fluxes involved in control of cardiac myocyte contraction. *Circ Res*, 2000. 87(4): p. 275-81.

2. **Bers, D .M.**, Excitation-Contraction Coupling and Cardiac Contractile Force. Developments in Cardiovascular Medicine. 2001, New York, NY: Springer.

3. **Perry, S.V.**, Vertebrate tropomyosin: distribution, properties and function. *J Muscle Res Cell Motil*, 2001. 22(1): p. 5-49.

4. **Cooke, R.**, Actomyosin interaction in striated muscle. *Physiol Rev*, 1997. 77(3): p. 671-97.

5. **Maughan, D.W.**, Kinetics and energetics of the crossbridge cycle. *Heart Fail Rev*, 2005. 10(3): p. 175-85.

6. **Puceat, M. and G. Vassort**, Signalling by protein kinase C isoforms in the heart. *Mol Cell Biochem*, 1996. 157(1-2): p. 65-72.

7. **Sabri, A. and S.F. Steinberg**, Protein kinase C isoform-selective signals that lead to cardiac hypertrophy and the progression of heart failure. *Mol Cell Biochem*, 2003. 251(1-2): p. 97-101.

8. **Takai, Y., A. Kishimoto, Y. Iwasa, Y. Kawahara, T. Mori, and Y. Nishizuka**, Calcium-dependent activation of a multifunctional protein kinase by membrane phospholipids. *J Biol Chem*, 1979. 254(10): p. 3692-5.

9. **Kuo, J.F., R.G. Andersson, B.C. Wise, L. Mackerlova, I. Salomonsson, N.L. Brackett, N. Katoh, M. Shoji, and R.W. Wrenn**, Calcium-dependent protein kinase: widespread occurrence in various tissues and phyla of the animal kingdom and comparison of effects of phospholipid, calmodulin, and trifluoperazine. *Proc Natl Acad Sci U S A*, 1980. 77(12): p. 7039-43.

10. **Steinberg, S.F.**, Structural basis of protein kinase C isoform function. *Physiol Rev*, 2008. 88(4): p. 1341-78.

11. **Wu, S .C. an d R .J. S olaro**, Protein kinase c zeta : A novel regulator of both phosphorylation and de-phosphorylation of cardiac sarcomeric proteins. *J Biol Chem*, 2007.

12. **Mohamed, A.S., J.D. Dignam, and K.K. Schlender**, Cardiac myosin-binding protein C (MyBP-C): identification of protein kinase A and protein kinase C phosphorylation sites. *Arch Biochem Biophys*, 1998. 358(2): p. 313-9.

13. **Xiao, L ., Q . Zhao, Y . Du, C . Y uan, R .J. S olaro, an d P.M. B uttrick**, PKCepsilon increases phosphorylation of the cardiac myosin binding protein C at serine 302 both in vitro and in vivo. *Biochemistry*, 2007. 46(23): p. 7054-61.

14. **Tong, C.W., J.E. Stelzer, M.L. Greaser, P.A. Powers, and R.L. Moss**, Acceleration of crossbridge kinetics by protein kinase A phosphorylation of cardiac myosin binding protein C modulates cardiac function. *Circ Res*, 2008. 103(9): p. 974-82.

15. **Noland, T .A., Jr . an d J.F. K uo**, Phosphorylation of cardiac myosin light chain 2 by protein kinase C and myosin light chain kinase increases Ca(2+)-stimulated actomyosin MgATPase activity. *Biochem Biophys Res Commun*, 1993. 193(1): p. 254-60.

16. **Venema, R.C., R.L. Raynor, T.A. Noland, Jr., and J.F. Kuo**, Role of protein kinase C in the phosphorylation of cardiac myosin light chain 2. *Biochem J*, 1993. 294 (Pt 2): p. 401-6.

17. **Noland, T.A., Jr., R.L. Raynor, and J.F. Kuo**, Identification of sites phosphorylated in bovine cardiac troponin I and troponin T by protein kinase C and comparative substrate activity of synthetic peptides containing the phosphorylation sites. *J Biol Chem*, 1989. 264(34): p. 20778-85.

18. **Layland, J., R.J. Solaro, and A.M. Shah**, Regulation of cardiac contractile function by troponin I phosphorylation. *Cardiovasc Res*, 2005. 66(1): p. 12-21.

19. **Jobsis, F .F. an d M .J. O'Connor**, Calcium release and reabsorption in the sartorius muscle of the toad. *Biochem Biophys Res Commun*, 1966. 25(2): p. 246-52.

20. **Wickenden, A .D., R . Kaprielian, Z . Kassiri, J.N . T soporis, R . T sushima, G .I. Fishman, an d P .H. B ackx**, The role of action potential prolongation and altered intracellular calcium handling in the pathogenesis of heart failure. *Cardiovasc Res*, 1998. 37(2): p. 312-23.

21. **Beuckelmann, D .J., M . N abauer, an d E . Erdmann**, Intracellular calcium handling in isolated ventricular myocytes from patients with terminal heart failure. *Circulation*, 1992. 85(3): p. 1046-55.

22. **Beuckelmann, D .J., M . N abauer, C . Kruger, an d E . E rdmann**, Altered diastolic [Ca2+]i handling in human ventricular myocytes from patients with terminal heart failure. *Am Heart J*, 1995. 129(4): p. 684-9.

23. **Del M onte, F., C .M. Johnson, A .C. S tepanek, A .A. D oye, an d J. K. Gwathmey**, Defects in calcium control. *J Card Fail*, 2002. 8(6 Suppl): p. S421-31.

24. **Chang, K .C., J.H . S chreur, M .W. We iner, an d S .A. C amacho**, Impaired Ca2+ handling is an early manifestation of pressure-overload hypertrophy in rat hearts. *Am J Physiol*, 1996. 271(1 Pt 2): p. H228-34.

25. **Solaro, R.J.**, Is calcium the 'cure' for dilated cardiomyopathy? *Nat Med*, 1999. 5(12): p. 1353-4.

26. **Camacho, S .A., R. B randes, V .M. F igueredo, an d M .W. We iner**, Ca2+ transient decline and myocardial relaxation are slowed during low flow ischemia in rat hearts. *J Clin Invest*, 1994. 93(3): p. 951-7.

27. **Saini, H .K. and N.S. D halla**, Defective calcium handling in cardiomyocytes isolated from hearts subjected to ischemia-reperfusion. *Am J Physiol Heart Circ Physiol*, 2005. 288(5): p. H2260-70.

28. **Stefenelli, T ., J. Wi kman-Coffelt, S .T. Wu , a nd W.W. P armley**, Calcium-dependent fluorescence transients during ventricular fibrillation. *Am Heart J*, 1990. 120(3): p. 590-7.

29. **Varian, K .D., S . R aman, an d P .M. Jan ssen**, Measurement of myofilament calcium sensitivity at physiological temperature in intact cardiac trabeculae. *Am J Physiol Heart Circ Physiol*, 2006. 290(5): p. H2092-7.

30. **Varian, K .D. an d P .M. Jan ssen**, Frequency-dependent acceleration of relaxation involves decreased myofilament calcium sensitivity. *Am J Physiol Heart Circ Physiol*, 2007. 292(5): p. H2212-9.

31. **Takimoto, E., D.G. Soergel, P.M. Janssen, L.B. Stull, D.A. Kass, and A.M. Murphy**, Frequency- and afterload-dependent cardiac modulation in vivo by troponin I with constitutively active protein kinase A phosphorylation sites. *Circ Res*, 2004. 94(4): p. 496-504.

32. **Yasuda, S ., P . C outu, S . Sadayappan, J. R obbins, and J .M. Met zger**, Cardiac transgenic and gene transfer strategies converge to support an important role for troponin I in regulating relaxation in cardiac myocytes. *Circ Res*, 2007. 101(4): p. 377-86.

33. **Kentish, J.C ., D .T. McCloskey, J. L ayland, S . P almer, J. M. L eiden, A .F. M artin, and R.J. Solaro**, Phosphorylation of troponin I by protein kinase A accelerates relaxation and crossbridge cycle kinetics in mouse ventricular muscle. *Circ Res*, 2001. 88(10): p. 1059-65.

34. **Pi, Y., D. Zhang, K.R. Kemnitz, H. Wang, and J.W. Walker**, Protein kinase C and A sites on troponin I regulate myofilament Ca^{2+} sensitivity and ATPase activity in the mouse myocardium. *J Physiol*, 2003. 552(Pt 3): p. 845-57.

35. **Konhilas, J.P., T.C. Irving, B.M. Wolska, E.E. Jweied, A.F. Martin, R.J. Solaro, and P.P. de Tombe**, Troponin I in the murine myocardium: influence on length-dependent activation and interfilament spacing. *J Physiol*, 2003. 547(Pt 3): p. 951-61.

36. **Kajiwara, H., S. Morimoto, N. Fukuda, I. Ohtsuki, and S. Kurihara**, Effect of troponin I phosphorylation by protein kinase A on length-dependence of tension activation in skinned cardiac muscle fibers. *Biochem Biophys Res Commun*, 2000. 272(1): p. 104-10.

37. **Buscemi, N., D.B. Foster, I. Neverova, and J.E. Van Eyk**, p21-activated kinase increases the calcium sensitivity of rat triton-skinned cardiac muscle fiber bundles via a mechanism potentially involving novel phosphorylation of troponin I. *Circ Res*, 2002. 91(6): p. 509-16.

38. **Zabrouskov, V., Y. Ge, J. Schwartz, and J.W. Walker**, Unraveling molecular complexity of phosphorylated human cardiac troponin I by top down electron capture dissociation/electron transfer dissociation mass spectrometry. *Mol Cell Proteomics*, 2008. 7(10): p. 1838-49.

39. **You, B., G. Yan, Z. Zhang, L. Yan, J. Li, Q. Ge, J.P. Jin, and J. Sun**, Phosphorylation of cardiac troponin I by mammalian sterile 20-like kinase 1. *Biochem J*, 2008.

40. **Haworth, R.S., F. Cuello, T.J. Herron, G. Franzen, J.C. Kentish, M. Gautel, and M. Avkiran**, Protein kinase D is a novel mediator of cardiac troponin I phosphorylation and regulates myofilament function. *Circ Res*, 2004. 95(11): p. 1091-9.

41. **Sakthivel, S., N.L. Finley, P.R. Rosevear, J.N. Lorenz, J. Gulick, S. Kim, P. VanBuren, L.A. Martin, and J. Robbins**, In vivo and in vitro analysis of cardiac troponin I phosphorylation. *J Biol Chem*, 2005. 280(1): p. 703-14.

42. **Noland, T.A., Jr., R.L. Raynor, N.M. Jideama, X. Guo, M.G. Kazanietz, P.M. Blumberg, R.J. Solaro, and J.F. Kuo**, Differential regulation of cardiac actomyosin S-1 MgATPase by protein kinase C isozyme-specific phosphorylation of specific sites in cardiac troponin I and its phosphorylation site mutants. *Biochemistry*, 1996. 35(47): p. 14923-31.

43. **Kobayashi, T., X. Yang, L.A. Walker, R.B. Van Breemen, and R.J. Solaro**, A non-equilibrium isoelectric focusing method to determine states of phosphorylation of cardiac troponin I: identification of Ser-23 and Ser-24 as significant sites of phosphorylation by protein kinase C. *J Mol Cell Cardiol*, 2005. 38(1): p. 213-8.

44. **McClellan, G., A. Weisberg, and S. Winegrad**, Effect of endothelin-1 on actomyosin ATPase activity. Implications for the efficiency of contraction. *Circ Res*, 1996. 78(6): p. 1044-50.

45. **Pi, Y., R. Sreekumar, X. Huang, and J.W. Walker**, Positive inotropy mediated by diacylglycerol in rat ventricular myocytes. *Circ Res*, 1997. 81(1): p. 92-100.

46. **MacGowan, G.A., C. Du, and A.P. Koretsky**, High calcium and dobutamine positive inotropy in the perfused mouse heart: myofilament calcium responsiveness, energetic economy, and effects of protein kinase C inhibition. *BMC Physiol*, 2001. 1: p. 12.

47. **Jideama, N.M., T.A. Noland, Jr., R.L. Raynor, G.C. Blobe, D. Fabbro, M.G. Kazanietz, P.M. Blumberg, Y.A. Hannun, and J.F. Kuo**, Phosphorylation specificities of protein kinase C isozymes for bovine cardiac troponin I and troponin T and sites within these proteins and regulation of myofilament properties. *J Biol Chem*, 1996. 271(38): p. 23277-83.

48. **Shistik, E., T. Ivanina, Y. Blumenstein, and N. Dascal**, Crucial role of N terminus in function of cardiac L-type Ca2+ channel and its modulation by protein kinase C. *J Biol Chem*, 1998. 273(28): p. 17901-9.

49. **Dorn, G.W., 2nd and T. Force**, Protein kinase cascades in the regulation of cardiac hypertrophy. *J Clin Invest*, 2005. 115(3): p. 527-37.

50. **Sumandea, M.P., W. G. Pyle, T. Kobayashi, P.P. de Tombe, and R.J. Solaro**, Identification of a functionally critical protein kinase C phosphorylation residue of cardiac troponin T. *J Biol Chem*, 2003. 278(37): p. 35135-44.

51. **Burkart, E.M., M.P. Sumandea, T. Kobayashi, M. Nili, A.F. Martin, E. Homsher, and R.J. Solaro**, Phosphorylation or glutamic acid substitution at protein kinase C sites on cardiac troponin I differentially depress myofilament tension and shortening velocity. *J Biol Chem*, 2003. 278(13): p. 11265-72.

52. **Noland, T.A., Jr., X. Guo, R.L. Raynor, N.M. Jideama, V. Averyhart-Fullard, R.J. Solaro, and J.F. Kuo**, Cardiac troponin I mutants. Phosphorylation by protein kinases C and A and regulation of Ca^{2+}-stimulated MgATPase of reconstituted actomyosin S-1. *J Biol Chem*, 1995. 270(43): p. 25445-54.

53. **Westfall, M.V., A.M. Lee, and D.A. Robinson**, Differential contribution of troponin I phosphorylation sites to the endothelin-modulated contractile response. *J Biol Chem*, 2005. 280(50): p. 41324-31.

54. **Tachampa, K., H. Wang, G.P. Farman, and P.P. de Tombe**, Cardiac troponin I threonine 144: role in myofilament length dependent activation. *Circ Res*, 2007. 101(11): p. 1081-3.

55. **Pi, Y., K.R. Kemnitz, D. Zhang, E.G. Kranias, and J.W. Walker**, Phosphorylation of troponin I controls cardiac twitch dynamics: evidence from phosphorylation site mutants expressed on a troponin I-null background in mice. *Circ Res*, 2002. 90(6): p. 649-56.

56. **Bilchick, K.C., J.G. Duncan, R. Ravi, E. Takimoto, H.C. Champion, W.D. Gao, L.B. Stull, D.A. Kass, and A.M. Murphy**, Heart failure-associated alterations in troponin I phosphorylation impair ventricular relaxation-afterload and force-frequency responses and systolic function. *Am J Physiol Heart Circ Physiol*, 2007. 292(1): p. H318-25.

57. **MacGowan, G.A., C. Du, D.B. Cowan, C. Stamm, F.X. McGowan, R.J. Solaro, A.P. Koretsky, and P.J. Del Nido**, Ischemic dysfunction in transgenic mice expressing troponin I lacking protein kinase C phosphorylation sites. *Am J Physiol Heart Circ Physiol*, 2001. 280(2): p. H835-43.

58. **Takeishi, Y., G. Chu, D.M. Kirkpatrick, Z. Li, H. Wakasaki, E.G. Kranias, G.L. King, and R.A. Walsh**, In vivo phosphorylation of cardiac troponin I by protein kinase CβII decreases cardiomyocyte calcium responsiveness and contractility in transgenic mouse hearts. *J Clin Invest*, 1998. 102(1): p. 72-8.

59. **Roman, B.B., P.H. Goldspink, E. Spaite, D. Urboniene, R. McKinney, D.L. Geenen, R.J. Solaro, and P.M. Buttrick**, Inhibition of PKC phosphorylation of cTnI improves cardiac performance in vivo. *Am J Physiol Heart Circ Physiol*, 2004. 286(6): p. H2089-95.

60. **MacGowan, G.A., C. Evans, T.C. Hu, D. Debrah, S. Mullet, H.H. Chen, C.F. McTiernan, A.F. Stewart, A.P. Koretsky, and S.G. Shroff**, Troponin I protein kinase C phosphorylation sites and ventricular function. *Cardiovasc Res*, 2004. 63(2): p. 245-55.

61. **Pyle, W.G., M.P. Sumandea, R.J. Solaro, and P.P. De Tombe**, Troponin I serines 43/45 and regulation of cardiac myofilament function. *Am J Physiol Heart Circ Physiol*, 2002. 283(3): p. H1215-24.

62. **Rosenblueth, A. and N. Wiener**, The Role of Models in Science. *Philosophy of Science*, 1945. 12(4): p. 316-321.

63. **Roberts, M.S. and F.A. Sonnenberg**, Decision Modeling Techniques, in *Decision Making in Health Care*, G.B. Chapman and F.A. Sonnenberg, Editors. 2003, Cambridge University Press: Cambridge, UK. p. 20-64.

64. **Bassingthwaighte, J.B.**, Using computer models to understand complex systems. *Physiologist*, 1985. 28(5): p. 439-42.

65. **Rosamond, W., K. Flegal, G. Friday, K. Furie, A. Go, K. Greenlund, N. Haase, M. Ho, V. Howard, B. Kissela, S. Kittner, D. Lloyd-Jones, M. McDermott, J. Meigs, C. Moy, G. Nichol, C.J. O'Donnell, V. Roger, J. Rumsfeld, P. Sorlie, J. Steinberger, T. Thom, S. Wasserthiel-Smoller, and Y. Hong**, Heart disease and stroke statistics--2007

update: a report from the American Heart Association Statistics Committee and Stroke Statistics Subcommittee. *Circulation,* 2007. 115(5): p. e69-171.

66. **Bodor, G.S., A.E. Oakeley, P.D. Allen, D.L. Crimmins, J.H. Ladenson, and P.A. Anderson**, Troponin I phosphorylation in the normal and failing adult human heart. *Circulation,* 1997. 96(5): p. 1495-500.

67. **van der Velden, J., Z. Papp, R. Zaremba, N.M. Boontje, J.W. de Jong, V.J. Owen, P.B. Burton, P. Goldmann, K. Jaquet, and G.J. Stienen**, Increased Ca2+-sensitivity of the contractile apparatus in end-stage human heart failure results from altered phosphorylation of contractile proteins. *Cardiovasc Res,* 2003. 57(1): p. 37-47.

68. **Zakhary, D.R., C.S. Moravec, R.W. Stewart, and M. Bond**, Protein kinase A (PKA)-dependent troponin-I phosphorylation and PKA regulatory subunits are decreased in human dilated cardiomyopathy. *Circulation,* 1999. 99(4): p. 505-10.

69. **Messer, A.E., A.M. Jacques, and S.B. Marston**, Troponin phosphorylation and regulatory function in human heart muscle: dephosphorylation of Ser23/24 on troponin I could account for the contractile defect in end-stage heart failure. *J Mol Cell Cardiol,* 2007. 42(1): p. 247-59.

70. **Bowling, N., R.A. Walsh, G. Song, T. Estridge, G.E. Sandusky, R.L. Fouts, K. Mintze, T. Pickard, R. Roden, M.R. Bristow, H.N. Sabbah, J.L. Mizrahi, G. Gromo, G.L. King, and C.J. Vlahos**, Increased protein kinase C activity and expression of Ca2+-sensitive isoforms in the failing human heart. *Circulation,* 1999. 99(3): p. 384-91.

71. **Vlahos, C.J., S.A. McDowell, and A. Clerk**, Kinases as therapeutic targets for heart failure. *Nat Rev Drug Discov,* 2003. 2(2): p. 99-113.

72. **Day, S.M., M.V. Westfall, E.V. Fomicheva, K. Hoyer, S. Yasuda, N.C. La Cross, L.G. D'Alecy, J.S. Ingwall, and J.M. Metzger**, Histidine button engineered into cardiac troponin I protects the ischemic and failing heart. *Nat Med,* 2006. 12(2): p. 181-9.

73. **Subramaniam, A., W.K. Jones, J. Gulick, S. Wert, J. Neumann, and J. Robbins**, Tissue-specific regulation of the α-myosin heavy chain gene promoter in transgenic mice. *J Biol Chem,* 1991. 266(36): p. 24613-20.

74. **Steinberg, T.H., B.J. Agnew, K.R. Gee, W.Y. Leung, T. Goodman, B. Schulenberg, J. Hendrickson, J.M. Beechem, R.P. Haugland, and W.F. Patton**, Global quantitative phosphoprotein analysis using Multiplexed Proteomics technology. *Proteomics,* 2003. 3(7): p. 1128-44.

75. **Solaro, R.J., D.C. Pang, and F.N. Briggs**, The purification of cardiac myofibrils with Triton X-100. *Biochim Biophys Acta,* 1971. 245(1): p. 259-62.

76. **Lim, C.C., H. Yang, M. Yang, C.K. Wang, J. Shi, E.A. Berg, D.R. Pimentel, J.K. Gwathmey, R.J. Hajjar, M. Helmes, C.E. Costello, S. Huo, and R. Liao**, A novel mutant cardiac troponin C disrupts molecular motions critical for calcium binding affinity and cardiomyocyte contractility. *Biophys J*, 2008. 94(9): p. 3577-89.

77. **Warren, C.M., G.M. Arteaga, S. Rajan, R.P. Ahmed, D.F. Wieczorek, and R.J. Solaro**, Use of 2-D DIGE analysis reveals altered phosphorylation in a tropomyosin mutant (Glu54Lys) linked to dilated cardiomyopathy. *Proteomics*, 2008. 8(1): p. 100-5.

78. **Scruggs, S.B., A.C. Hinken, A. Thawornkaiwong, J. Robbins, L.A. Walker, P.P. de Tombe, D.L. Geenen, P.M. Buttrick, and R.J. Solaro**, Ablation of ventricular Myosin regulatory light chain phosphorylation in mice causes cardiac dysfunction in situ and affects neighboring myofilament protein phosphorylation. *J Biol Chem*, 2009. 284(8): p. 5097-106.

79. **Fritz, J.D., D.R. Swartz, and M.L. Greaser**, Factors affecting polyacrylamide gel electrophoresis and electroblotting of high-molecular-weight myofibrillar proteins. *Anal Biochem*, 1989. 180(2): p. 205-10.

80. **Layland, J., A.C. Cave, C. Warren, D.J. Grieve, E. Sparks, J.C. Kentish, R.J. Solaro, and A.M. Shah**, Protection against endotoxemia-induced contractile dysfunction in mice with cardiac-specific expression of slow skeletal troponin I. *Faseb J*, 2005. 19(9): p. 1137-9.

81. **Skrzypiec-Spring, M., B. Grotthus, A. Szelag, and R. Schulz**, Isolated heart perfusion according to Langendorff---still viable in the new millennium. *J Pharmacol Toxicol Methods*, 2007. 55(2): p. 113-26.

82. **Sahn, D.J., A. DeMaria, J. Kisslo, and A. Weyman**, Recommendations regarding quantitation in M-mode echocardiography: results of a survey of echocardiographic measurements. *Circulation*, 1978. 58(6): p. 1072-83.

83. **Macgowan, G.A., J.A. Kirk, C. Evans, and S.G. Shroff**, Pressure-calcium relationships in perfused mouse hearts. *Am J Physiol Heart Circ Physiol*, 2006. 290(6): p. H2614-24.

84. **Berger, D.S., K. Vlasica, C.M. Quick, K.A. Robinson, and S.G. Shroff**, Ejection has both positive and negative effects on left ventricular isovolumic relaxation. *Am J Physiol*, 1997. 273(6 Pt 2): p. H2696-707.

85. **Wu, Y., A.H. Tobias, K. Bell, W. Barry, M. Helmes, K. Trombitas, R. Tucker, K.B. Campbell, and H.L. Granzier**, Cellular and molecular mechanisms of systolic and diastolic dysfunction in an avian model of dilated cardiomyopathy. *J Mol Cell Cardiol*, 2004. 37(1): p. 111-9.

86. **Eberli, F.R., F. Sam, S. Ngoy, C.S. Apstein, and W.S. Colucci**, Left-ventricular structural and functional remodeling in the mouse after myocardial infarction: assessment

with the isovolumetrically-contracting Langendorff heart. *J Mol Cell Cardiol*, 1998. 30(7): p. 1443-7.

87. **Liou, Y .M. a nd F . F uchs**, Pyrene-labeled cardiac troponin C. Effect of Ca2+ on monomer and excimer fluorescence in solution and in myofibrils. *Biophys J*, 1992. 61(4): p. 892-901.

88. **Grabarek, Z ., R .Y. T an, J. Wan g, T . T ao, and J. G ergely**, Inhibition of mutant troponin C activity by an intra-domain disulphide bond. *Nature*, 1990. 345(6271): p. 132-5.

89. **Fiske, C.H. an d Y. Subbarow**, The Colorimetric Determination of Phosphorus. *J Biol Chem*, 1925. 66(2): p. 375-400.

90. **Gao, W.D., D. Atar, P.H. Backx, an d E. Marban**, Relationship between intracellular calcium and contractile force in stunned myocardium. Direct evidence for decreased myofilament Ca2+ responsiveness and altered diastolic function in intact ventricular muscle. *Circ Res*, 1995. 76(6): p. 1036-48.

91. **Grynkiewicz, G., M. Poenie, and R.Y. Tsien**, A new generation of Ca2+ indicators with greatly improved fluorescence properties. *J Biol Chem*, 1985. 260(6): p. 3440-50.

92. **Molecular_Probes**, *Product Information: Fura and Indo Ratiometric Calcium Indicators*, in *http://probes.invitrogen.com/media/pis/mp01200.pdf*. 2005.

93. **Gao, W.D ., P .H. B ackx, M . A zan-Backx, an d E . Marban**, Myofilament Ca2+ sensitivity in intact versus skinned rat ventricular muscle. *Circ Res*, 1994. 74(3): p. 408-15.

94. **Gao, W.D., N.G. Perez, and E. Marban**, Calcium cycling and contractile activation in intact mouse cardiac muscle. *J Physiol*, 1998. 507 (Pt 1): p. 175-84.

95. **Montgomery, D .E., B .M. Wol ska, W.G . Pyle, B .B. R oman, J. C. Dowell, P .M. Buttrick, A.P. Koretsky, P. Del Nido, and R.J. Solaro**, alpha-Adrenergic response and myofilament activity in mouse hearts lacking PKC phosphorylation sites on cardiac TnI. *Am J Physiol Heart Circ Physiol*, 2002. 282(6): p. H2397-405.

96. **Chandra, M., M.L. Tschirgi, S.J. Ford, B.K. Slinker, and K.B. Campbell**, Interaction between myosin heavy chain and troponin isoforms modulate cardiac myofiber contractile dynamics. *Am J Physiol Regul Integr Comp Physiol*, 2007. 293(4): p. R1595-607.

97. **Chandra, M., V.L. Rundell, J.C. Tardiff, L.A. Leinwand, P.P. De Tombe, an d R.J. Solaro**, Ca(2+) activation of myofilaments from transgenic mouse hearts expressing R92Q mutant cardiac troponin T. *Am J Physiol Heart Circ Physiol*, 2001. 280(2): p. H705-13.

98. **de Tombe, P.P. and G.J. Stienen**, Protein kinase A does not alter economy of force maintenance in skinned rat cardiac trabeculae. *Circ Res*, 1995. 76(5): p. 734-41.

99. **Fabiato, A. and F. Fabiato**, Calculator programs for computing the composition of the solutions containing multiple metals and ligands used for experiments in skinned muscle cells. *J Physiol (Paris)*, 1979. 75(5): p. 463-505.

100. **Takahashi, A., P. Camacho, J.D. Lechleiter, and B. Herman**, Measurement of intracellular calcium. *Physiol Rev*, 1999. 79(4): p. 1089-125.

101. **Tong, C.W., R.D. Gaffin, D.C. Zawieja, and M. Muthuchamy**, Roles of phosphorylation of myosin binding protein-C and troponin I in mouse cardiac muscle twitch dynamics. *J Physiol*, 2004. 558(Pt 3): p. 927-41.

102. **Baran, D., K. Ogino, R. Stennett, M. Schnellbacher, D. Zwas, J.P. Morgan, and D. Burkhoff**, Interrelating of ventricular pressure and intracellular calcium in intact hearts. *Am J Physiol*, 1997. 273(3 Pt 2): p. H1509-22.

103. **Burkhoff, D.**, Explaining load dependence of ventricular contractile properties with a model of excitation-contraction coupling. *J Mol Cell Cardiol*, 1994. 26(8): p. 959-78.

104. **Shimizu, J., K. Todaka, and D. Burkhoff**, Load dependence of ventricular performance explained by model of calcium-myofilament interactions. *Am J Physiol Heart Circ Physiol*, 2002. 282(3): p. H1081-91.

105. **Rhodes, S.S., K.M. Ropella, S.H. Audi, A.K. Camara, L.G. Kevin, P.S. Pagel, and D.F. Stowe**, Cross-bridge kinetics modeled from myoplasmic [Ca^{2+}] and LV pressure at 17°C and after 37°C and 17°C ischemia. *Am J Physiol Heart Circ Physiol*, 2003. 284(4): p. H1217-29.

106. **Peterson, J.N., W.C. Hunter, and M.R. Berman**, Estimated time course of Ca2+ bound to troponin C during relaxation in isolated cardiac muscle. *Am J Physiol*, 1991. 260(3 Pt 2): p. H1013-24.

107. **Forsman, K.**, *Constructive Commutative Algebra in Nonlinear Control Theory, Linköping Studies in Science and Technology, Dissertation, No. 261*, in *Department of Electrical Engineering*. 1992, Linköping University: Linköping, Sweden.

108. **Forsman, K. and T. Glad**. *Constructive algebraic geometry in nonlinear control*. in *Decision and Control, 1990., Proceedings of the 29th IEEE Conference on*. 1990.

109. **Audoly, S., G. Bellu, L. D'Angio, M.P. Saccomani, and C. Cobelli**, Global identifiability of nonlinear models of biological systems. *IEEE Trans Biomed Eng*, 2001. 48(1): p. 55-65.

110. **Bellu, G., M.P. Saccomani, S. Audoly, and L. D'Angio**, DAISY: a new software tool to test global identifiability of biological and physiological systems. *Comput Methods Programs Biomed*, 2007. 88(1): p. 52-61.

111. **Cobelli, C. and J.J. DiStefano, 3rd**, Parameter and structural identifiability concepts and ambiguities: a critical review and analysis. *Am J Physiol*, 1980. 239(1): p. R7-24.

112. **Brenner, B.**, Effect of Ca^{2+} on cross-bridge turnover kinetics in skinned single rabbit psoas fibers: implications for regulation of muscle contraction. *Proc Natl Acad Sci U S A*, 1988. 85(9): p. 3265-9.

113. **de Tombe, P.P., A. Belus, N. Piroddi, B. Scellini, J.S. Walker, A.F. Martin, C. Tesi, and C. Poggesi**, Myofilament calcium sensitivity does not affect cross-bridge activation-relaxation kinetics. *Am J Physiol Regul Integr Comp Physiol*, 2007. 292(3): p. R1129-36.

114. **Sancho Solis, R., Y. Ge, and J.W. Walker**, Single amino acid sequence polymorphisms in rat cardiac troponin revealed by top-down tandem mass spectrometry. *J Muscle Res Cell Motil*, 2008. 29(6-8): p. 203-12.

115. **Shusterman, V., I. Usiene, C. Harrigal, J.S. Lee, T. Kubota, A.M. Feldman, and B. London**, Strain-specific patterns of autonomic nervous system activity and heart failure susceptibility in mice. *Am J Physiol Heart Circ Physiol*, 2002. 282(6): p. H2076-83.

116. **Saurin, A.T., D.J. Pennington, N.J. Raat, D.S. Latchman, M.J. Owen, and M.S. Marber**, Targeted disruption of the protein kinase C epsilon gene abolishes the infarct size reduction that follows ischaemic preconditioning of isolated buffer-perfused mouse hearts. *Cardiovasc Res*, 2002. 55(3): p. 672-80.

117. **Turnbull, L., J.F. Hoh, R.I. Ludowyke, and G.H. Rossmanith**, Troponin I phosphorylation enhances crossbridge kinetics during beta-adrenergic stimulation in rat cardiac tissue. *J Physiol*, 2002. 542(Pt 3): p. 911-20.

118. **Neher, E.**, The use of fura-2 for estimating Ca buffers and Ca fluxes. *Neuropharmacology*, 1995. 34(11): p. 1423-42.

119. **Baylor, S.M. and S. Hollingworth**, Measurement and Interpretation of Cytoplasmic [Ca2+] Signals From Calcium-Indicator Dyes. *News Physiol Sci*, 2000. 15: p. 19-26.

120. **Blatter, L.A. and W.G. Wier**, Intracellular diffusion, binding, and compartmentalization of the fluorescent calcium indicators indo-1 and fura-2. *Biophys J*, 1990. 58(6): p. 1491-9.

121. **Steinberg, S.F., J.P. Bilezikian, and Q. Al-Awqati**, Fura-2 fluorescence is localized to mitochondria in endothelial cells. *Am J Physiol*, 1987. 253(5 Pt 1): p. C744-7.

122. **Tanaka, H., S. Manita, T. Matsuda, M. Adachi, and K. Shigenobu**, Sustained negative inotropism mediated by alpha-adrenoceptors in adult mouse myocardia: developmental conversion from positive response in the neonate. *Br J Pharmacol*, 1995. 114(3): p. 673-7.

123. **MacGowan, G.A., J. Rager, S.G. Shroff, and M.A. Mathier**, In vivo alpha-adrenergic responses and troponin I phosphorylation: anesthesia interactions. *J Appl Physiol*, 2005. 98(4): p. 1163-70.

124. **Dunaway, S., Q. Yu, and D.F. Larson**, Effect of acute alpha adrenergic stimulation on cardiac function. *Perfusion*, 2007. 22(4): p. 289-92.

125. **Wang, H., J.E. Grant, C.M. Doede, S. Sadayappan, J. Robbins, and J.W. Walker**, PKC-βII sensitizes cardiac myofilaments to Ca^{2+} by phosphorylating troponin I on threonine-144. *J Mol Cell Cardiol*, 2006. 41(5): p. 823-33.

126. **Sumandea, M.P., V.O. Rybin, A.C. Hinken, C. Wang, T. Kobayashi, E. Harleton, G. Sievert, C.W. Balke, S.J. Feinmark, R.J. Solaro, and S.F. Steinberg**, Tyrosine phosphorylation modifies protein kinase C δ-dependent phosphorylation of cardiac troponin I. *J Biol Chem*, 2008. 283(33): p. 22680-9.

127. **Mathur, M.C., T. Kobayashi, and J.M. Chalovich**, Negative Charges at Protein Kinase C Sites of Troponin I Stabilize the Inactive State of Actin. *Biophys J*, 2007.

128. **Solaro, R.J., P. Rosevear, and T. Kobayashi**, The unique functions of cardiac troponin I in the control of cardiac muscle contraction and relaxation. *Biochem Biophys Res Commun*, 2007.

129. **Finley, N.L. and P.R. Rosevear**, Introduction of negative charge mimicking protein kinase C phosphorylation of cardiac troponin I. Effects on cardiac troponin C. *J Biol Chem*, 2004. 279(52): p. 54833-40.

130. **Stelzer, J.E., H.S. Norman, P.P. Chen, J.R. Patel, and R.L. Moss**, Transmural variation in myosin heavy chain isoform expression modulates the timing of myocardial force generation in porcine left ventricle. *J Physiol*, 2008. 586(Pt 21): p. 5203-14.

131. **Brandt, P.W., M.S. Diamond, J.S. Rutchik, and F.H. Schachat**, Co-operative interactions between troponin-tropomyosin units extend the length of the thin filament in skeletal muscle. *J Mol Biol*, 1987. 195(4): p. 885-96.

132. **Colson, B.A., T. Bekyarova, M.R. Locher, D.P. Fitzsimons, T.C. Irving, and R.L. Moss**, Protein kinase A-mediated phosphorylation of cMyBP-C increases proximity of myosin heads to actin in resting myocardium. *Circ Res*, 2008. 103(3): p. 244-51.

133. **Day, S.M., M.V. Westfall, and J.M. Metzger**, Tuning cardiac performance in ischemic heart disease and failure by modulating myofilament function. *J Mol Med*, 2007. 85(9): p. 911-21.

134. **Scruggs, S.B., L.A. Walker, T. Lyu, D.L. Geenen, R.J. Solaro, P.M. Buttrick, and P.H. Goldspink**, Partial replacement of cardiac troponin I with a non-phosphorylatable mutant at serines 43/45 attenuates the contractile dysfunction associated with PKCε phosphorylation. *J Mol Cell Cardiol*, 2006. 40(4): p. 465-73.

135. **Pyle, W.G., Y. Chen, and P.A. Hofmann**, Cardioprotection through a PKC-dependent decrease in myofilament ATPase. *Am J Physiol Heart Circ Physiol*, 2003. 285(3): p. H1220-8.

136. **Brown, E.B., J.B. Shear, S.R. Adams, R.Y. Tsien, and W.W. Webb**, Photolysis of caged calcium in femtoliter volumes using two-photon excitation. *Biophys J*, 1999. 76(1 Pt 1): p. 489-99.

137. **Lenart, T.D., J.M. Murray, C. Franzini-Armstrong, and Y.E. Goldman**, Structure and periodicities of cross-bridges in relaxation, in rigor, and during contractions initiated by photolysis of caged Ca2+. *Biophys J*, 1996. 71(5): p. 2289-306.

138. **Campbell, K.B. and M. Chandra**, Functions of stretch activation in heart muscle. *J Gen Physiol*, 2006. 127(2): p. 89-94.

139. **Xing, J., M. Chinnaraj, Z. Zhang, H.C. Cheung, and W.J. Dong**, Structural studies of interactions between cardiac troponin I and actin in regulated thin filament using Forster resonance energy transfer. *Biochemistry*, 2008. 47(50): p. 13383-93.

140. **Molkentin, J.D. and J. Robbins**, With great power comes great responsibility: using mouse genetics to study cardiac hypertrophy and failure. *J Mol Cell Cardiol*, 2009. 46(2): p. 130-6.

141. **Kass, D.A., J.M. Hare, and D. Georgakopoulos**, Murine cardiac function: a cautionary tail. *Circ Res*, 1998. 82(4): p. 519-22.

142. **Li, L., G. Chu, E.G. Kranias, and D.M. Bers**, Cardiac myocyte calcium transport in phospholamban knockout mouse: relaxation and endogenous CaMKII effects. *Am J Physiol*, 1998. 274(4 Pt 2): p. H1335-47.

143. **Allen, D.G. and S. Kurihara**, The effects of muscle length on intracellular calcium transients in mammalian cardiac muscle. *J Physiol*, 1982. 327: p. 79-94.

144. **Alvarez, B.V., N.G. Perez, I.L. Ennis, M.C. Camilion de Hurtado, and H.E. Cingolani**, Mechanisms underlying the increase in force and Ca(2+) transient that follow stretch of cardiac muscle: a possible explanation of the Anrep effect. *Circ Res*, 1999. 85(8): p. 716-22.

145. **Reyes, M., G.L. Freeman, D. E scobedo, S . L ee, M.E. S teinhelper, an d M .D. Feldman**, Enhancement of contractility with sustained afterload in the intact murine heart: blunting of length-dependent activation. *Circulation*, 2003. 107(23): p. 2962-8.

146. **Du, C., G.A. MacGowan, D.L. Farkas, and A.P. Koretsky**, Calcium measurements in perfused mouse heart: quantitating fluorescence and absorbance of Rhod-2 by application of photon migration theory. *Biophys J*, 2001. 80(1): p. 549-61.

147. **MacGowan, G.A., C. Du, V. Glonty, J.P. Suhan, A.P. Koretsky, and D.L. Farkas**, Rhod-2 based measurements of intracellular calcium in the perfused mouse heart: cellular and subcellular localization and response to positive inotropy. *J Biomed Opt*, 2001. 6(1): p. 23-30.

148. **Del N ido, P .J., P. Glynn, P . B uenaventura, G . S alama, an d A .P. Koretsky**, Fluorescence measurement of calcium transients in perfused rabbit heart using rhod 2. *Am J Physiol*, 1998. 274(2 Pt 2): p. H728-41.

149. **Todaka, K ., K . O gino, A . G u, an d D . Burkhoff**, Effect of ventricular stretch on contractile strength, calcium transient, and cAMP in intact canine hearts. *Am J Physiol*, 1998. 274(3 Pt 2): p. H990-1000.

150. **Wier, W. G. an d D .T. Yue**, Intracellular calcium transients underlying the short-term force-interval relationship in ferret ventricular myocardium. *J Physiol*, 1986. 376: p. 507-30.

151. **Hajjar, R .J., U . S chmidt, P . H elm, an d J.K . G wathmey**, Ca++ sensitizers impair cardiac relaxation in failing human myocardium. *J Pharmacol Exp Ther*, 1997. 280(1): p. 247-54.

152. **Maier, L .S., P . B arckhausen, J. We isser, I . Aleksic, M . B aryalei, an d B . P ieske**, Ca(2+) handling in isolated human atrial myocardium. *Am J Physiol Heart Circ Physiol*, 2000. 279(3): p. H952-8.

153. **Georgakopoulos, D. and D. Kass**, Minimal force-frequency modulation of inotropy and relaxation of in situ murine heart. *J Physiol*, 2001. 534(Pt. 2): p. 535-45.

154. **Brutsaert, D.L., N.M. de Clerck, M.A. Goethals, and P.R. Housmans**, Relaxation of ventricular cardiac muscle. *J Physiol*, 1978. 283: p. 469-80.

155. **Tobias, A .H., B .K. S linker, R .D. K irkpatrick, an d K .B. C ampbell**, Mechanical determinants of left ventricular relaxation in isovolumically beating hearts. *Am J Physiol*, 1995. 268(1 Pt 2): p. H170-7.

156. **Campbell, K.B., M.V. Razumova, R.D. Kirkpatrick, and B.K. Slinker**, Myofilament kinetics in isometric twitch dynamics. *Ann Biomed Eng*, 2001. 29(5): p. 384-405.

157. **Janssen, P .M. an d W.C . H unter**, Force, not sarcomere length, correlates with prolongation of isosarcometric contraction. *Am J Physiol*, 1995. 269(2 Pt 2): p. H676-85.

158. **Cazorla, O., Y. Wu, T.C. Irving, and H. Granzier**, Titin-based modulation of calcium sensitivity of active tension in mouse skinned cardiac myocytes. *Circ Res*, 2001. 88(10): p. 1028-35.

159. **Toy, S.M., J. Melbin, and A. Noordergraaf**, Reduced models of arterial systems. *IEEE Trans Biomed Eng*, 1985. 32(2): p. 174-6.

160. **Stergiopulos, N ., B .E. Westerhof, an d N . We sterhof**, Total arterial inertance as the fourth element of the windkessel model. *Am J Physiol*, 1999. 276(1 Pt 2): p. H81-8.

161. **Campbell, K .B., M. C handra, R .D. K irkpatrick, B .K. S linker, an d W.C. H unter**, Interpreting cardiac muscle force-length dynamics using a novel functional model. *Am J Physiol Heart Circ Physiol*, 2004. 286(4): p. H1535-45.

162. **Campbell, K .B., Y . Wu, A .M. S impson, R.D. K irkpatrick, S .G. S hroff, H .L. Granzier, a nd B .K. Sl inker**, Dynamic myocardial contractile parameters from left ventricular pressure-volume measurements. *Am J Physiol Heart Circ Physiol*, 2005. 289(1): p. H114-30.

163. **Chandra, M ., M .L. Tschirgi, I . R ajapakse, an d K .B. C ampbell**, Troponin T modulates sarcomere length-dependent recruitment of cross-bridges in cardiac muscle. *Biophys J*, 2006. 90(8): p. 2867-76.

164. **Berger, D.S., S.K. Fellner, K.A. Robinson, K. Vlasica, I.E. Godoy, and S.G. Shroff**, Disparate effects of three types of extracellular acidosis on left ventricular function. *Am J Physiol*, 1999. 276(2 Pt 2): p. H582-94.